A dynamical systems analysis of vortex pinch-off

Thesis by

Clara O'Farrell

In Partial Fulfillment of the Requirements

for the Degree of

Doctor of Philosophy

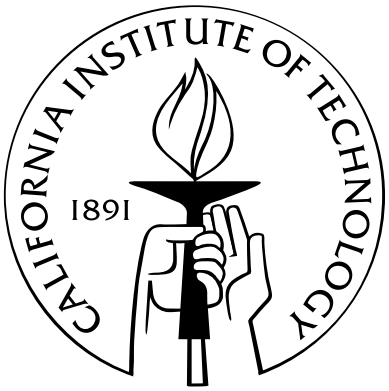

California Institute of Technology

Pasadena, California

2013

(Defended April 29, 2013)

Acknowledgments

This thesis is the product of five years spent at Caltech, interacting and collaborating with—and most importantly learning from—an outstanding community of scientists. To thank them all and grant them the credit they deserve would take longer than this section allows, but I hope their contributions are given a fair representation in the better portions of this text. Any mistakes herein, however, are my own and reflect only my own shortcomings.

The principal influence on this thesis has been that of my advisor, Professor John Dabiri, who is probably not aware of just how grateful I am for his guidance over the past five years. John has an uncanny gift for telling the forest from the trees, and I'm certain that his influence is evident in the more inspired sections of the text. I am still surprised at how often a chat with John provided answers to problems I had struggled with for days, research or otherwise.

I have also benefitted considerably from the expertise in experimental and theoretical vortex dynamics of Professors Mory Gharib and Tony Leonard, respectively. Both kindly took the time to offer input throughout this process, for which I am extremely grateful. I am similarly indebted to the members of my committee from CDS, who were kind enough to participate in the production of a thesis completely outside of their field of interest.

Throughout the years, the members of the Biological Propulsion Lab have offered input and advice at countless group meetings, and I am sure they can identify their own contri-

butions to this text. For these, I am grateful to: Drs. Jeff Peng, Lydia Ruiz, Kakani Katija, Kelly Sutherland, Matthias Kinzel, and Janna Nawroth; Messrs. Robert Whittlesey and Daniel Araya; and Ms. Monica Martinez Ortiz. In particular, Mr. Robert Whittlesey was instrumental in helping set up the experiments discussed herein. Ms. Martha Salcedo kept operations running at the Dabiri Lab, for which we probably don't thank her enough.

During my time at Caltech, I was funded by the Betty and Gordon Moore Foundation, as well as by an NSF Graduate Research Fellowship, which provided much freedom. Portions of this work were also funded by Office of Naval Research awards N000140810918 and N000141010137 to Professor Dabiri.

Dr. Federico Domenichini was kind enough to offer access to his simulations for non-axisymmetric vortex rings, which are discussed in Chapter 3. Similarly, Dr. Stefan Kern and Professor Petros Koumoustakos kindly shared their simulations of an anguilliform swimmer. Brad St. John, Ali Kiani, and Joe Haggerty were responsible for the construction of the non-axisymmetric nozzles used for the experiments described in the text.

Finally, I am most grateful to my family, especially Eduardo, Susana, Inés and Paz O'Farrell, who have been extremely supportive since the day I decided to forego common sense and move to the US to become a scientist. I would probably have given up a long time ago, were it not for their support and that of the many excellent friends I have had the good fortune to make in this country: Bernardo, Agostina, Jakob, Fay, Claire, Daniel, Amara, Melissa, Sarah, Arielle, Eric, Dave, Shyh Chang, Robert, and Julie, to name a few. And as for Francisco and Po, they've become my family here, and the past few months have shown that I could not have done it without them.

Abstract

Vortex rings constitute the main structure in the wakes of a wide class of swimming and flying animals, as well as in cardiac flows and in the jets generated by some moss and fungi. However, there is a physical limit, determined by an energy maximization principle called the Kelvin-Benjamin principle, to the size that axisymmetric vortex rings can achieve. The existence of this limit is known to lead to the separation of a growing vortex ring from the shear layer feeding it, a process known as 'vortex pinch-off', and characterized by the dimensionless vortex formation number. The goal of this thesis is to improve our understanding of vortex pinch-off as it relates to biological propulsion, and to provide future researchers with tools to assist in identifying and predicting pinch-off in biological flows.

To this end, we introduce a method for identifying pinch-off in starting jets using the Lagrangian coherent structures in the flow, and apply this criterion to an experimentally generated starting jet. Since most naturally occurring vortex rings are not circular, we extend the definition of the vortex formation number to include non-axisymmetric vortex rings, and find that the formation number for moderately non-axisymmetric vortices is similar to that of circular vortex rings. This suggests that naturally occurring vortex rings may be modeled as axisymmetric vortex rings. Therefore, we consider the perturbation response of the Norbury family of axisymmetric vortex rings. This family is chosen to model vortex rings of increasing thickness and circulation, and their response to prolate shape perturba-

tions is simulated using contour dynamics. Finally, the response of more realistic models for vortex rings, constructed from experimental data using nested contours, to perturbations which resemble those encountered by forming vortices more closely, is simulated using contour dynamics. In both families of models, a change in response analogous to pinch-off is found as members of the family with progressively thicker cores are considered. We posit that this analogy may be exploited to understand and predict pinch-off in complex biological flows, where current methods are not applicable in practice, and criteria based on the properties of vortex rings alone are necessary.

Contents

List of Figures

List of Symbols

Latin characters

A Cross-sectional area of the core of a vortex ring, page 7

A' Cross-sectional area of $\delta\xi$, page 8

$A_{1,2}$ Cross-sectional area of one of the vortices in a Pierrehumbert dipole, page 106

A_j Area of the jth region in multiple contour dynamics, page 137

A_{cruise} Amplitude of oscillation of wing or tail during cruise, page 15

∂A Boundary of a Norbury vortex, page 105

$\partial A_{1,2}$ Boundary of the two cores in a Pierrehumbert dipole, page 106

a Ratio of the equivalent diameter of the zero-vorticity patch to that of the constant-vorticity patch in the annular vortices of Dritschel (1986), page 139

$\mathbf{a}$ Vector potential, page 6

a_j Fourier coefficients describing the boundary of a Norbury or Pierrehumbert vortex, page 109

a'_j Fourier coefficients describing the boundary of a perturbed Norbury or Pierrehumbert vortices, page 109

b Scalar constant in definition of the Lamb-Chaplygin dipole, page 142

D Nozzle diameter, page 3

D_{eq} Equivalent diameter of non-circular nozzles, page 61

d Length of the perturbation simulating a shear layer, page 161

E Kinetic energy, page 7

$\bar{E}$ Dimensionless energy for the Norbury and Pierrehumbert families, page 123

E^* Impulse-normalized energy, page 10

E^*_{lim} Limiting value of the impulse-normalized energy for steady vortex rings, page 10

E^*_{piston} Impulse-normalized energy supplied by the piston-cylinder apparatus, page 10

$E(k)$ Complete elliptic integral of the second kind, page 111

$\mathbf{e}_\phi$ Unit vector in the azimuthal direction, page 7

$\mathbf{e}_r$ Unit vector in the radial direction, page 8

$\mathbf{e}_z$ Unit vector in the longitudinal direction, page 8

F Impulse-constrained energy, page 8

f Oscillating frequency of wing or tail, page 15

H Length of the rectilinear segment in Domenichini's nozzles, page 54

h Ratio of the length of the flat segment to the diameter of the circular segment in Domenichini's nozzles, page 54

I Impulse, page 7

i Imaginary unit, page 110

J_0 Bessel function of the first kind of order 0, page 142

J_1 Bessel function of the first kind of order 1, page 142

$K(k)$ Complete elliptic integral of the first kind, page 111

$\Delta\ell$ Contour length of the vortex tail or filament after one eddy turnover, page 120

L Length of the column of fluid ejected during vortex formation, page 2

N Number of Fourier coefficients describing the boundary of a Norbury or Pierrehumbert vortex, page 109

n Number of regions in multiple-contour dynamics, page 137

$\mathbf{n}$ Approximate normal to a ridge in the FTLE field, page 30

R Ring radius (Norbury) or half the dipole spacing (Pierrehumbert), page 105

r Radial coordinate in cylindrical coordinate system, page 6

Re Reynolds number based on the nozzle (equivalent) diameter and mean piston speed, page 25

Re_Γ Reynolds number based on the vortex ring circulation, page 25

$\mathbf{S}$ Rate of strain tensor (symmetric part of $\nabla\mathbf{u}$), page 30

s Coordinate along the oblique DPIV plane, page 66

s' Parametric coordinate along the length of the contour for the axisymmetric contour dynamics formulation, page 111

St Strouhal number, page 15

T Integration time for FTLE computation, page 25

T^* Formation time based on the diameter of the circular portion of the nozzles in Domenichini's, page 95

$\hat{T}$ Vortex formation time, page 4

$\hat{T}_{model}$ Formation time at which to extract vortex models, page 151

t Dimensional time in seconds, page 4

t^* Dimensionless time for contour dynamics simulations of the Norbury and Pierrehumbert families, page 113

t_0 Time at initiation of particle trajectories, page 25

U Unperturbed speed of steadily translating vortex ring or dipole, page 7

$\bar{U}$ Average velocity of the nested-contour models for the Lamb dipole, page 149

U_c Time derivative of z_c^*, page 113

U_{cruise} Forward velocity of the animal during cruise, page 15

U_p Instantaneous piston velocity, page 4

$\overline{U}_p$ Running average of the piston velocity, page 4

$\mathbf{u}$ Fluid velocity, page 6

u_x x-component of the velocity, page 111

u_y y-component of the velocity, page 111

u_z Longitudinal component of the velocity, page 6

u_r Radial component of the velocity, page 6

u_ϕ Azimuthal component of the velocity, page 6

w Width of the perturbation simulating a shear layer, page 161

x Abscissa in Cartesian coordinates, page 63

$\mathbf{x}$ Position vector, page 6

y Ordinate in Cartesian coordinates, page 63

y' Modified radial coordinate, page 7

z Longitudinal coordinate in cylindrical and Cartesian coordinate systems, page 6

z Position in the complex domain, page 110

z_c Unperturbed vorticity centroid, page 113

z_c^* Departure of vorticity centroid from the unperturbed vorticity centroid, page 113

Greek characters

α Ratio of the mean core radius to the ring radius (Norbury) or half the dipole spacing (Pierrehumbert), page 105

Γ Circulation, page 4

$\bar{\Gamma}$ Dimensionless circulation for the Norbury and Pierrehumbert families, page 123

$\Gamma_{desired}$ Desired circulation in the model vortex ring, page 151

Γ_{ring} Vortex ring circulation, page 4

γ Multiplicative constant introduced to preserve circulation in perturbed vortices, page 107

δ Size of a perturbation introduced to Norbury or Pierrehumbert vortices, page 109

ϵ Size of a perturbation to Hill's spherical vortex, page 107

ζ Polar angle in the coordinate system for Hill's spherical vortex, page 108

η Polar angle in the coordinate system for Norbury and Pierrehumbert vortices, page 108

η_w Polar angle at which the shear layer perturbation intersects the unperturbed vortex outline, page 161

θ Angle of the outward-pointing normal to the linear segment, relative to the symmetry axis, page 111

κ Local curvature, page 61

κ_{max} Maximum local curvature in a non-axisymmetric nozzle, page 59

κ_{min} Minimum local curvature in a non-axisymmetric nozzle, page 59

λ Scalar constant indicating the degree of asymmetry in the Lamb-Chaplygin dipole, page 144

ν Kinematic viscosity, page 25

ξ Vorticity density, page 7

ξ_{max} Maximum vorticity density inside the core of an experimental vortex ring, page 153

ρ Radius in the polar coordinate system for Hill's spherical vortex, page 108

ϱ Density, page 6

σ Radius in the polar coordinate system for Norbury and Pierrehumbert vortices, page 108

$\sigma_{t_0}^{T}$ The finite-time Lyapunov exponent, page 26

τ Dimensionless time for analyzing annular vortices, normalized according to Dritschel (1986), page 139

ϕ Azimuthal coordinate in cylindrical coordinate system, page 6

$\phi_{t_0}^{t_0+T}$ Flow map that maps fluid particles from their initial position at t_0 to their position a time T later, page 25

ψ Stokes streamfunction, page 7

Ω Constant for piecewise-constant or piecewise-linear vorticity distributions, page 104

Ω_0 Vorticity at the center of the vortex ring core (axisymmetric), or of the positively signed vortex core (two dimensions), page 112

Ω_j Increment in ω (two-dimensional) or ξ (axisymmetric) across a contour in nested-contour dynamics, page 137

ω Scalar out-of-plane vorticity in two dimensions and in the axisymmetric case, page 7

ω_{max} Maximum vorticity, page 31

Chapter 1

Introduction

1.1 Vortex rings and their formation

Vortex rings are a recurring feature in a wide class of biological, atmospheric, and engineering flows. These vortex rings occur naturally in a variety of settings, and their beneficial properties have been harnessed for a number of engineering applications. Under certain conditions, erupting volcanoes can produce visible vortex rings (Johnston-Lavis, 1890), and birds have been observed to exploit the vortex rings which appear in the atmosphere when the ground is heated intensely (Cone, 1962; Pennycuick, 1971). Vortex rings are also found in the discharge of blood from the atria into the ventricles in the human heart (Domenichini *et al.*, 2005; Bellhouse, 1972; Reul *et al.*, 1981; Wieting & Stripling, 1984; Gharib *et al.*, 2006; Dabiri & Gharib, 2005*a*), as well as in the release of spores by *Sphagnum* moss (Whitaker & Edwards, 2010) and certain fungi (Roper *et al.*, 2010).

In man-made flows, buoyant vortex rings are often observed to form after explosions (Turner, 1960) or the discharge of artillery rounds (Lugt, 1995), and in industrial chimneys (Lugt, 1995). Additionally, cavitated vortex rings are used in underwater drilling (Chahine & Genoux, 1983), and they have been used to combat fires at gushing oil and gas wells (Akhmetov (1980), see Akhmetov (2009) for a review).

Vortex rings are often found in the wakes of swimming and flying animals (Dickinson *et al.*, 2000). Jetting swimmers, such as jellyfish and squid, are known to generate nearly axisymmetric vortex rings during normal propulsion (Dabiri & Gharib, 2005*a*; Bartol *et al.*, 2008, 2009; Linden & Turner, 2004; Dabiri *et al.*, 2006, 2010). However, a wider class of animals generates non-circular vortex rings for swimming, flying, or hovering. Flying and hovering birds (Kokshaysky, 1979; Rayner, 1979) and insects (Dickinson & Götz, 1996; Ellington, 1984) are known to generate elongated, non-circular vortex rings. Similarly, chains of deformed vortex rings or loops have been observed in the wakes of swimming fish (Drucker & Lauder, 1999; Kern & Koumoutsakos, 2006). Finally, vortex rings are known to play an important part in the propulsion of animals such as water striders (Hu *et al.*, 2003) and basilisk lizards (Hsieh & Lauder, 2004), at the water surface.

Given their ubiquity in nature and technology, vortex rings have been the subject of numerous studies, beginning with Helmholtz's theory of vortex motions in the 19th century (Helmholtz, 1858). Thereafter, the work of noted fluid dynamicists such as Lord Kelvin (Kelvin, 1867), Osborne Reynolds (Reynolds, 1876), Ludwig Prandtl (Prandtl & Tietjens, 1934), Sir Horace Lamb (Lamb, 1932), and G.K. Batchelor (Batchelor, 1967), laid the mathematical foundations for the understanding of ideal inviscid vortex rings. Thus, models for ideal vortex rings were developed, and expressions for the fundamental properties of vortex rings (impulse, energy, translational velocity) were derived.

Additionally, numerous dye visualization and digital particle image velocity (DPIV) experiments have characterized the properties and behavior of real, viscous, laminar and turbulent vortex rings. In the majority of these studies, vortex rings were generated using the 'piston-cylinder' arrangement. In these experiments, a fluid column of length L is ejected through the circular aperture or nozzle at the end of a hollow cylinder of diameter

D, by a piston moving inside the cylinder with a prescribed velocity. A boundary layer of vorticity forms on the inside of the cylinder as the piston moves, and then separates at the edge of the aperture or nozzle and rolls up into a vortex ring.

A wide class of experimental studies of vortex rings using this arrangement have characterized the evolution of the vortex ring's size, position, velocity, circulation, impulse, and distribution of vorticity, throughout its formation and as it advects away from the nozzle owing to its self-induced velocity (Maxworthy, 1972, 1977; Weigand & Gharib, 1997; Didden, 1979; Glezer & Coles, 1990; Auerbach, 1987). The understanding of vortex rings that stemmed from these experiments is described in the reviews of Shariff & Leonard (1992) and Lim & Nickels (1995). In particular, a number of researchers have considered the evolution of the vortex ring and its fundamental properties during vortex formation. Their analyses relied on experimental results (Didden, 1979; Auerbach, 1987), as well as models based on slug-flow and self-similar roll-up (Saffman, 1978; Pullin, 1979). These studies found the size, circulation, and impulse of the vortex ring to increase throughout the formation process, as the vortex ring accepted vortical fluid from the separated shear layer feeding it.

However, all of the aforementioned investigations considered the formation of experimental vortex rings using only small ratios of the length L of the column of fluid ejected, to the diameter D of the circular nozzle or aperture (called the stroke ratio L/D). In a seminal paper, Gharib *et al.* (1998) showed that the growth of vortex rings during fluid ejection cannot continue indefinitely, but rather there is a physical limit to their size. Using a piston-cylinder arrangement, Gharib *et al.* (1998) considered the formation of vortex rings using stroke ratios ranging from 0.5 to 14.5 , and a variety of piston velocity programs (i.e., different functions of piston velocity in time). The authors found the size and circulation of vortex rings to increase with stroke ratio, in accordance with previous studies, until a stroke

ratio of approximately $L/D \approx 4$. Beyond this stroke ratio, Gharib *et al.* (1998) found that vortex rings stopped accepting vorticity during fluid ejection, and additional vorticity flux formed a wake of Kelvin-Helmoltz type vortices instead. They termed the disconnection of velocity and vorticity fields of the vortex ring from its feeding shear layer 'vortex pinch-off'.

Figure 1.1, shows planar laser-induced fluorescence (PLIF) visualizations of the vortex wake in three cases. In figure 1.1(a), the stroke ratio is approximately two, and the resulting vortex ring has accepted all of the vortical fluid ejected from the nozzle. The stroke ratio of the vortex ring in figure 1.1(b) is $L/D \approx 3.8$, and as a result the vortex in this figure is larger than that shown in 1.1(a). Also in this case, almost all of the discharged fluid has been entrained into the vortex ring. In figure 1.1(c), however, the stroke ratio exceeds four ($L/D \approx 14.5$), and a wake of trailing vortices is evident. Additionally, the size of the leading vortex ring in 1.1(c) is comparable to that of the vortex ring in 1.1(b), indicating that little vorticity flux was accepted by the vortex ring in 1.1(c) after the instantaneous stroke ratio exceed four.

Gharib *et al.* (1998) defined a dimensionless vortex formation time $\hat{T} = \overline{U}_p t/D$, where t is the dimensional time, U_p is the instantaneous piston velocity, and $\overline{U}_p = 1/t \int_0^t U_p(t)\mathrm{d}t$ is the running average of the piston velocity. Since $\overline{U}_p t$ represents the length of the column of fluid already ejected at time t, the formation time is equivalent to the ratio of length to diameter of the ejected fluid column. In order to determine the formation time at which pinch-off occurred, Gharib *et al.* (1998) considered the total circulation discharged by the piston-cylinder apparatus (Γ), as well as the circulation in the leading vortex ring once it had separated from the trailing shear layer (Γ_{ring}), as a function of the formation time. The authors reasoned that only the vorticity which had emanated from the cylinder before the vortex had ceased to accept vorticity (i.e., before the onset of pinch-off) could

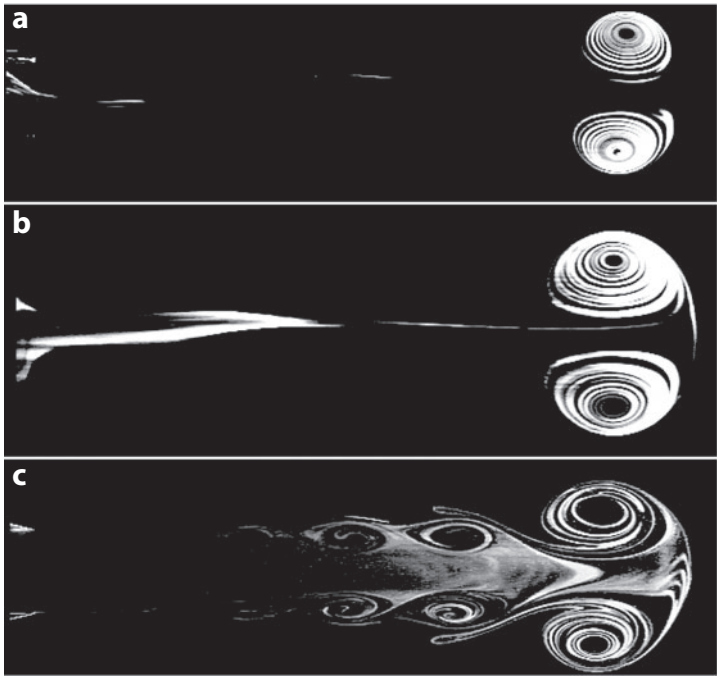

Figure 1.1: PLIF visualizations of vortex rings at $\hat{T} \approx 9$. (a) An isolated vortex ring with $L/D = 2$. (b) An isolated vortex ring with $L/D \approx 3.8$. (c) Vortex ring and wake in a case where $L/D \approx 14.5$. Figure reproduced with permission from Dabiri (2009)

accumulate in the vortex ring. In effect, the authors found the circulation in the leading vortex ring to reach a constant value which was lower than the total circulation generated by the apparatus. Therefore, they compared the time histories of the two circulations to determine the $\hat{T}$ at which the total circulation emanating from the cylinder equaled the maximum circulation of the vortex ring. They termed this $\hat{T}$ the 'formation number': the dimensionless time at which pinch-off occurred.

In all of the cases considered, Gharib *et al.* (1998) found pinch-off to occur robustly at a formation number of approximately four, suggesting that some physical process curtails vortex growth once this non-dimensional time is reached. The universality of the formation number has been verified by a number of subsequent experimental (Pawlak *et al.*, 2007; Krueger *et al.*, 2006; Dabiri & Gharib, 2004*a*) and computational studies (Rosenfeld *et al.*, 1998; Mohseni *et al.*, 2000). The concept of the universal formation number has also been

extended to more complex vortex generator setups and computational frameworks, by extending the definition of the dimensionless vortex formation time to allow for variations such as the presence of bulk co-flow (Krueger *et al.*, 2006) or bulk-counter flow (Dabiri & Gharib, 2004*a*), a time-varying exit diameter (Dabiri & Gharib, 2005*a*; Mohseni *et al.*, 2000), and differing velocity programs (Rosenfeld *et al.*, 1998; Mohseni *et al.*, 2000; Krueger & Gharib, 2003; Olcay & Krueger, 2010) and velocity profiles (Rosenfeld *et al.*, 1998). A comprehensive overview of these modifications to the original definition of Gharib *et al.* (1998) can be found in the review of Dabiri (2009), where the most general formulation for the vortex formation time is presented.

1.2 Pinch-off and the Kelvin-Benjamin principle

Gharib *et al.* (1998) attributed the apparent physical limit on vortex formation to an energy-based argument originally due to Lord Kelvin, who stated it without proof (Kelvin, 1880*b*). The proof of Kelvin's argument is due to (Benjamin, 1976), and the principle is hence referred to as the Kelvin-Benjamin principle. Benjamin (1976) showed, using a variational argument, that a steadily translating axisymmetric vortex ring, with constant density and no swirl, is a solution of the Euler equations only when it constitutes a critical point of the energy, with respect to re-arrangements of the vorticity density which preserve the same total impulse. The proof is outlined below.

Consider an axisymmetric flow in cylindrical coordinates $\mathbf{x} = (r, z, \phi)$ denoted by $\mathbf{u} = (u_r, u_z, u_\phi)$. For constant density ϱ and no swirl ($u_\phi = 0$), the fluid velocity can be expressed in terms of the vector potential $\mathbf{a}$:

$$\mathbf{u} = \nabla \times \mathbf{a} \tag{1.1}$$

where $\mathbf{a} = \psi/r\mathbf{e}_\phi$, and ψ is the Stokes streamfunction. Additionally, the vorticity equation under these conditions reduces to:

$$\frac{D}{Dt}\left(\frac{\omega}{r}\right) = 0 \tag{1.2}$$

where ω is the vorticity in the azimuthal direction, all other components being zero.

Defining the vorticity density $\xi = \omega/r$ and letting $y' = 1/2r^2$, the preceding equation can be written as:

$$\frac{D\xi}{Dt} = \frac{\partial \xi}{\partial t} + \frac{\partial \psi}{\partial y'}\frac{\partial \xi}{\partial z} - \frac{\partial \psi}{\partial z}\frac{\partial \xi}{\partial y'} = 0 \tag{1.3}$$

If ξ represents a steady solution consisting of a vortex translating with longitudinal velocity U in the z-direction, then in the frame of reference translating with constant velocity U, ξ and ψ should be independent of time. That is $\xi = \xi(y', z')$ and $\psi = \psi(y', z')$, where $z' = z - Ut$. Therefore, a steadily translating vortex ring satisfies:

$$\frac{D\xi}{Dt} = \frac{\partial}{\partial y'}(\psi - Uy')\frac{\partial \xi}{\partial z} - \frac{\partial}{\partial z}(\psi - Uy')\frac{\partial \xi}{\partial y'} = 0 \tag{1.4}$$

In the translating coordinate system, the fluid impulse I and kinetic energy E can be written as (Saffman, 1992; Batchelor, 1967):

$$I = \frac{1}{2}\varrho \int \mathbf{x} \times \boldsymbol{\omega} dV = \pi \varrho \int \int_A y' \xi \mathrm{d}y' \mathrm{d}z' \tag{1.5}$$

$$E = \frac{1}{2}\varrho \int \mathbf{u} \cdot \mathbf{u} dV = \pi \varrho \int \int_A \omega \psi \mathrm{d}r \mathrm{d}z' = \frac{1}{2}\pi \varrho \int \int_A \xi \psi \mathrm{d}y' \mathrm{d}z' \tag{1.6}$$

where A is the cross section of the vortex core (the projection of the support of ξ onto the plane $\phi = 0$). Maximizing the kinetic energy while preserving the impulse means finding

the critical points of the functional:

$$F = E - UI = \pi\varrho \int\int_A \left(\frac{1}{2}\psi - Uy'\right)\xi \mathrm{d}y'\mathrm{d}z' \tag{1.7}$$

where U acts as a Lagrange multiplier.

Taking the first variation of F:

$$\delta F = \int\int_{A'} \left(\psi - Uy'\right)\delta\xi \mathrm{d}y'\mathrm{d}z' \tag{1.8}$$

where $\delta\xi$ must be a rearrangement of ξ, and integration is now over A', which is derived from the support of $\delta\xi$. Therefore, consider some arbitrary ϵ, and let:

$$\delta\xi = \left(-\frac{\partial\epsilon}{\partial z'}\mathbf{e}_r + \frac{\partial\epsilon}{\partial y'}\mathbf{e}_z\right)\cdot\left(\frac{\partial\xi}{\partial y'}\mathbf{e}_r + \frac{\partial\xi}{\partial z'}\mathbf{e}_z\right) \tag{1.9}$$

Then, the first variation becomes:

$$\delta F = \int\int_A \left[-\left(\psi - Uy'\right)\frac{\partial\epsilon}{\partial z'}\frac{\partial\xi}{\partial y'} - \left(\psi - Uy'\right)\frac{\partial\epsilon}{\partial y'}\frac{\partial\xi}{\partial z'}\right]\mathrm{d}y'\mathrm{d}z' \tag{1.10}$$

Or, after integration by parts:

$$\delta F = \int\int_A \left[\frac{\partial}{\partial z'}\left(\psi - Uy'\right)\frac{\partial\xi}{\partial y'} - \frac{\partial}{\partial y'}\left(\psi - Uy'\right)\frac{\partial\xi}{\partial z'}\right]\epsilon \mathrm{d}y'\mathrm{d}z' \tag{1.11}$$

Therefore, for a stationary F:

$$\frac{\partial}{\partial z'}\left(\psi - Uy'\right)\frac{\partial\xi}{\partial y'} - \frac{\partial}{\partial y'}\left(\psi - Uy'\right)\frac{\partial\xi}{\partial z'} = 0 \tag{1.12}$$

That is, requiring that ξ be a steadily translating vortex ring is equivalent to requiring that ξ be a critical point of the energy (c.f. equation 1.4).

The stability of the steady solution is determined by the second variation $\delta^2\xi$: the solution is stable when the second variation is definite (i.e., ξ constitutes a maximum or a minimum), and unsteady otherwise. Kelvin (1880*b*) stated that for axisymmetric solutions, ξ must represent an absolute maximum. Benjamin (1976) did not offer proof that the second variation $\delta^2\xi$ must be negative for steadily translating vortex ring solutions, but Wan (1988) has proved that this is the case for a family of axisymmetric solutions introduced by Norbury (1973) and described in detail in chapter 4.

Therefore, Gharib *et al.* (1998) posited that vortex pinch-off occurs because, due to the Kelvin-Benjamin principle, a vortex ring can only accept additional vorticity from the shear layer and continue to grow as long as the new configuration with a larger vortex ring has greater kinetic energy than an alternative configuration with the same total impulse, consisting of a vortex ring and shear layer. However, showing that a particular vortex ring with a realistic vorticity distribution maximizes the total energy with respect to rearrangements of the vorticity density which preserve the same total impulse, is impractical. As a result, Gharib *et al.* (1998) relied on a combination of modeling and empirical results to show that, at a formation time of approximately four, the piston-cylinder vortex generator apparatus cannot meet the impulse-normalized-energy requirements necessary to generate an isolated vortex ring. To quantify the normalized energy delivered by the piston-cylinder apparatus, the authors used the slug-flow model, which assumes that the velocity external to the boundary layer at the exit plane of the cylinder is simply the piston velocity. That is, the fluid ejected from the piston-cylinder apparatus is modeled as a slug of fluid with a flat velocity profile, constant diameter D, and length $L(t)$. As a result, the circulation,

impulse, and energy delivered by the apparatus are:

$$\Gamma = \frac{1}{2}\overline{U_p^2}t \tag{1.13}$$

$$I = \frac{1}{4}\pi\varrho D^2\overline{U_p^2}t \tag{1.14}$$

$$E = \frac{1}{8}\pi\varrho D^2\overline{U_p^3}t \tag{1.15}$$

And the impulse-normalized energy defined by Gharib *et al.* (1998) is given by:

$$E^*_{piston} = \frac{E}{\sqrt{\varrho I\Gamma^3}} = \left(\frac{\pi}{2}\right)^{1/2}\left(\frac{L}{D}\right)^{-1}\frac{\overline{U_p^3}\,\overline{U_p}}{(\overline{U_p^2})^2} \tag{1.16}$$

E^*_{piston} scales with $(L/D)^{-1}$, which decreases monotonically with increased ejection time. However, the last term in 1.16 is dependent on the piston velocity program. Nonetheless, Gharib *et al.* (1998) showed that E^*_{piston} decreases monotonically for any realistic piston velocity profile. For isolated vortex rings, on the other hand, the authors generalized the results from an idealized family of vortex rings (the family of Norbury (1973), which is described in detail in chapter 4) to suggest that E^* diminishes to a limiting value E^*_{lim} as the core thickens. The value of E^*_{lim} is dependent on the vorticity distribution, and was found to be $E^*_{lim} = 0.33$ in their experimental vortex rings. Hence, they suggested that pinch-off occurs when $E^*_{piston} < E^*_{lim}$, and found that this crossover occurred at $\hat{T} \approx 4$. Thus, at $\hat{T} \approx 4$, the piston-cylinder apparatus could no longer deliver normalized energy at a rate compatible with the formation of an isolated vortex ring, leading to pinch-off.

Since the original model of Gharib *et al.* (1998) relied on empirical input, a number of models explaining and attempting to predict pinch-off were developed subsequently. The

first of these models is due to Mohseni & Gharib (1998), who constructed a model to determine the non-dimensional time at which the vortex generator could no longer deliver energy at a rate compatible with the requirement that the steady vortex ring maximize energy as outlined by the Kelvin-Benjamin principle, using a slug-flow model for the jet and modeling the steady vortex ring as a member of the Norbury family of vortex rings. This family of exact solutions to the incompressible Euler equations was developed by Norbury (1973) and Fraenkel (1972), and consists of vortex rings of increasing core size, each with a distribution of vorticity given by $\omega = \Omega r$ (where Ω is a constant). This family is described in detail in chapter 4 and has been used in several models for pinch-off, including the model of Linden & Turner (2001), which is similar to that of Mohseni & Gharib (1998). Kaplanski & Rudi (2005), on the other hand, developed a model similar to that of Mohseni & Gharib (1998) and Linden & Turner (2001), but used a more complex, viscous, family of vortex rings as a model for the growing vortex ring.

Rather than using an energy argument, Shusser & Gharib (2000) developed a criterion for pinch-off based on the kinematics of the vortex ring and trailing jet. Shusser & Gharib (2000) also used the slug-flow approximation and the Norbury family of vortex rings as models for the starting jet and vortex ring, respectively. The authors suggested that pinch-off occurs when the model vortex ring attained a translational velocity equal to that of the jet, and showed that this kinematic criterion is equivalent to the energy criterion of Mohseni & Gharib (1998). Fukumoto & Kaplanski (2008) extended this model by developing similar kinematic criteria, using a viscous model for the vortex rings. Gao & Yu (2010) also built upon this model by using kinematic criteria, but additionally considering the effects of the trailing jet on the growth of the leading vortex ring. Finally, Mohseni (2001) introduced an alternative model for pinch-off based on statistical physics.

The development of new models for pinch-off is constrained by the fact that it is impractical to apply the Kelvin-Benjamin principle directly on vorticity distributions to determine whether or not they satisfy the requirement that they maximize the energy with respect to all possible rearrangements of ξ that preserve the same total impulse. Furthermore, using the Kelvin-Benjamin variational argument to find steadily translating solutions to the incompressible Euler equations that might serve as the basis for these models, is rendered impractical by the absence of simple and accurate formulae for the kinetic energy (Saffman, 1992). In a series of recent papers, Luzzatto-Fegiz and Williamson (Luzzatto-Fegiz & Williamson, 2010*a*,*b*, 2012*b*,*a*) have been successful in using imperfect impulse-velocity diagrams to find new two-dimensional vortex equilibria, and asses the stability of families of exact solutions. Their method involves introducing small perturbations that break the symmetry of previously known vortex equilibria, in order to find hitherto unknown branches of these families of solutions. By considering plots of the translation or rotation velocity of these equilibria as a function of their impulse, they were able to identify changes in the stability of the entire family. While this method has been very successful in two-dimensional flows, it is not yet applicable to pinch-off because the only known analytical family of steadily translating vortex rings (the Norbury family) is known to be stable to the types of perturbations introduced by Luzzatto-Fegiz & Williamson (2010*a*) (Benjamin, 1976; Wan, 1988).

1.3 Optimal vortex formation

All of the models described above are concerned with understanding and predicting pinch-off. Understanding this phenomenon is of particular interest given the propulsive advantages associated with the formation of vortex rings. These benefits of vortex ring formation for

propulsion arise from two sources: the entrainment of ambient fluid by the forming vortex ring, and the added mass of the fluid surrounding the vortex that must be accelerated with the vortex ring. The propulsive force experienced by a vortex generator, be it an experimental apparatus or a biological or engineered system, is proportional to the sum of the fluid in the shear layer, the entrained fluid, and the added mass of the non-entrained fluid (Dabiri, 2009). Vortex rings are known to entrain more fluid than steady jets (Auerbach, 1991; Dabiri & Gharib, 2004*b*; Olcay & Krueger, 2007; Shadden *et al.*, 2007), thus providing an advantage in propulsive-force generation. Since steady vortex rings translate as coherent structures bounded by material lines, the added mass carried with the so-called 'vortex bubble' is mathematically equivalent to the added mass carried by a solid body in potential flow (Dabiri *et al.*, 2006). The added mass of the vortex ring is thus also advantageous in the generation of propulsive forces (Baird *et al.*, 1977; Krueger & Gharib, 2003; Weihs, 1977; Ruiz *et al.*, 2011).

Furthermore, these beneficial properties of vortex ring formation scale with increasing vortex size (Krueger, 2001). Given that the growth of vortex rings is limited by the Kelvin-Benjamin principle, this implies that a process of constrained optimization could lead to the formation of 'optimal' vortices: vortices with maximum size given the constraint imposed by the vortex formation time $\hat{T}$. This constrained optimization phenomenon is known as 'optimal vortex formation'. Krueger & Gharib (2003) showed that, for a pulsed jet, maximum time-averaged thrust per pulse is achieved at a formation time right after pinch-off, lending credence to the theory that the formation of 'optimal' vortices leads to the most advantageous harnessing of vortex ring formation for propulsive purposes.

Logically, this leads to the intriguing question of whether the formation of vortex rings in naturally occurring flows is 'optimal' as defined above. So far, researchers have uncovered

some evidence of optimality in certain biological jetting flows. For example, Gharib *et al.* (2006) found evidence of optimal vortex formation during diastolic filling of the cardiac left ventricle of healthy human patients, as well as evidence that a pathology of the left ventricle known as dilated cardiomyopathy leads to the formation of suboptimal vortices with short formation times. Similarly, Dabiri & Gharib (2005*a*) found evidence of optimal vortex formation during normal cardiac operation, and that pathologies such as cardiac ischaemia lead to the formation of vortices with formation times above the optimal.

Evidence of efficient vortex formation has also been found in the swimming behavior during cruise of several jellyfish species that are known to be 'cruising predators' (i.e., species that spend a large portion of their life cycle in constant swimming) by Dabiri *et al.* (2010). Linden & Turner (2004) also found evidence of optimal vortex formation in juvenile squid. However, one must bear in mind that propulsive efficiency is not necessarily the principal objective of natural propulsive systems. For example, adult squid are known to use primarily their lateral fins for low-speed propulsion, while using their jet-propelled mode of locomotion primarily as an escape response (Anderson & DeMont, 2000; Bartol *et al.*, 2001; O'Dor, 1988). It is therefore reasonable to assume that this jet-propelled mode need not be efficient, but rather that speed might be its principal objective. This is in agreement with the observations of Anderson & Grosenbaugh (2005), that jetting in adult squids persists for times much longer than $\hat{T} \approx 4$. Similar results were reported by Dabiri *et al.* (2010) for several jellyfish species that are known to swim primarily in short, high-speed bursts. Therefore, the existence of additional constraints such as speed and maneuverability must be taken into account when evaluating the 'optimality' of a natural system.

In addition to these constraints related to fluid mechanics and locomotion, the existence of other constraints related to physiology, feeding and reproduction, for example, must be

borne in mind before evaluating the optimality of natural behaviors. Furthermore, even in those cases where propulsive efficiency can be reasonably assumed to be the primary goal, such as the cruising behavior of animal species which are known to travel large distances regularly or the normal operation of the human heart, one cannot assume out of hand that naturally-existing solutions are necessarily optimal. It is important to note that natural selection need not always (or indeed most of the time) arrive at the optimal solution. However, a survey by Taylor *et al.* (2003) suggests the intriguing possibility that one such optimal solution might govern the cruising behavior of a wide class of swimming and flying animals.

Taylor *et al.* (2003) analyzed the cruising kinematics of a wide class of species of swimming and flying animals ranging in size from locusts to dolphins, and including insects, birds, fish, and mammals. The authors computed the non-dimensional Strouhal frequency St corresponding to cruising:

$$St = \frac{f A_{cruise}}{U_{cruise}} \tag{1.17}$$

where f is the oscillating frequency of the wing or tail, A_{cruise} is the oscillating amplitude of the propulsive appendage during cruise, and U_{cruise} is the forward velocity of the animal, also during cruise. In comparing the non-dimensional cruising frequency across species, Taylor *et al.* (2003) found the cruising Strouhal numbers of this wide class of frequencies to mostly fall in the interval $0.2 < St < 0.4$. The authors suggest that efficiency concerns constrain the range of Strouhal numbers animals cruise at, because natural selection is likely to lead to cruising strategies with high propulsive efficiency.

In their review of animal locomotion, Dickinson *et al.* (2000) suggest that the formation of vortex rings is the unifying feature linking the forms of propulsion in water and air

considered by Taylor *et al.* (2003). Given that these animals are known to generate vortex rings, that the formation of these vortex rings is constrained by the Kelvin-Benjamin principle, that maximum use of the beneficial properties of vortex rings for propulsive efficiency is made by generating 'optimal' vortex rings, and that optimal vortex formation has been shown to play a role in certain jetting natural flows; Linden & Turner (2004), Dabiri & Gharib (2005*a*), and Dabiri (2009) have suggested that the formation of optimal vortex rings might be the principle underlying the cruising behavior of swimming animals. Thus, Dabiri (2009) suggests that the constraints on the growth of individual vortex rings imposed by the Kelvin-Benjamin principle might govern the shedding of individual vortices in the wakes of cruising animals, and that the constraints on efficient vortex ring formation might manifests themselves in the narrow range of Strouhal frequencies observed by Taylor *et al.* (2003).

Moored *et al.* (2012) developed an alternative framework, based on hydrodynamic wake resonance theory, to explain the existence of optima in the flapping-fin type of propulsion exhibited by the organisms in the survey by Taylor *et al.* (2003). The authors suggested a different method for identifying maxima in the propulsive efficiency of flapping-fin propulsion, based on the hydrodynamic resonance of the wake produced by these animals. Their method involves performing a linear spatial stability analysis of the velocity profiles measured in the wakes of swimming and flying animals to find the hydrodynamic resonant frequency of the base flow (that is, the time-averaged jet). The results of Moored *et al.* (2012), as well as those of previous studies by Lewin & Haj-Hariri (2003), Dewey *et al.* (2012), and Triantafyllou *et al.* (1993), suggest that maxima in efficiency occur when the driving frequency of the flapping appendage coincides with the resonant frequency of the base flow in the wake. The framework of Moored *et al.* (2012) for predicting optima using

wake resonance theory shows remarkable agreement with experimental results. Although this method has proved very accurate, it must be remarked that the method is diagnostic and not predictive: it can be used to determine whether a particular propulsive strategy represents an efficiency optimum, but not to predict the location of these optima.

Furthermore, the framework developed by Moored *et al.* (2012) has proven difficult to extend beyond the flapping-fin-type propulsion considered by the authors. The formation of starting vortices from a piston-cylinder apparatus, or by jetting swimmers, for example, cannot be examined as a perturbation on a mean flow in the style of the analysis of flapping fins in Moored *et al.* (2012). The absence of a base flow renders linear stability analysis impossible. Attempts at performing a linear stability analysis on a starting jet flow with large stroke ratio yielded spurious eigenvalues with no physical significance (Moored, private communication), suggesting that the formation of starting vortices is a highly non-linear event which is not well captured by a linear stability analysis. Therefore, the link (if any) between the wake resonance theory of Moored *et al.* (2012) and optimal vortex formation remains unknown, and the wake resonance method cannot be applied to understand or predict pinch-off.

1.4 Aims and scope of current work

Hence, identifying pinch-off in biological flows is of great interest, as is determining whether optimal vortex formation plays a role in the optimal locomotion of swimming and flying animals . This interest is compounded by the recent surge in investigations into the development of efficient underwater vehicles, many of which employ biomimetic motions (Villanueva *et al.*, 2011; Fish *et al.*, 2011; Triantafyllou & Triantafyllou, 1995) or rely on the formation of vortex rings (Ruiz *et al.*, 2011; Whittlesey, 2013; Moslemi & Krueger, 2010). At this stage,

however, identifying and predicting pinch-off and diagnosing efficiency and performance, in both natural and engineered swimmers and flyers, is rendered difficult by the shortage of universally applicable models or criteria for identifying pinch-off and predicting the optimal formation time.

Despite the wealth of models described in section 1.2, and the widespread acceptance of the Kelvin-Benjamin principle as the driving physical mechanism behind pinch-off, no single model has emerged as the preferred means of predicting pinch-off. This is due, in part, to existing models not being easily applicable to all biological flows. Most existing models rely on quantifying the circulation, impulse, energy, or velocity of the growing vortex ring, as well as of the shear layer feeding it. Therefore, existing models prove difficult to apply when the flux of circulation and energy into the vortex ring, or the velocity of the shear layer, cannot be easily quantified. In these cases, which include most examples of swimming and flying animals, the utility of the existing models is limited. In these complex biological flows, criteria for identifying and predicting pinch-off based on the properties of the vortex rings in the wake alone would be of great use.

However, developing such methods directly from the Kelvin-Benjamin principle is impractical for the reasons discussed in §1.2. At this stage, therefore, existing models predicting and explaining pinch-off and vortex formation are not applicable to all complex flows of biological interest. Hence, current research on pinch-off in biological flows often relies on using the method of comparing circulations introduced by Gharib *et al.* (1998) as a diagnostic tool. There is need, therefore, for more general models for pinch-off that might be applicable to a wider class of biological flows, as well as for criteria to facilitate the identification of pinch-off in complex biological flows where the circulation criterion might prove difficult to apply. Hence, the aim of this thesis is to address some of these issues

by introducing an alternative criterion for pinch-off, extending the definition of the vortex formation time to non-axisymmetric starting jets, and improving our understanding of the perturbation response of model vortex rings in order to develop models for pinch-off based on the properties of the vortex rings generated by swimming and flying animals.

In chapter 2 we introduce a criterion for identifying pinch-off based on the Lagrangian coherent structures (LCS), which serve as finite-time analogues to the stable and unstable manifolds in time-independent systems, in axisymmetric jetting flows. This method has the potential to prove useful in identifying pinch-off in complex biological flows. Since most naturally occurring vortex rings are not circular, in chapter 3 we consider the formation number for non-axisymmetric vortex rings, and show that vortex rings with moderate departure from axisymmetry can be modeled as circular vortex rings of the same equivalent diameter. In chapters 4 and 5 we examine the perturbation response of model vortex rings and dipoles of increasing complexity. The results highlight a link between the perturbation response of models for isolated vortex rings, and pinch-off. This link provides the basis for the development of models for pinch-off based on the properties of the vortices generated by swimming and flying animals. Finally, concluding remarks and avenues for future work are presented in chapter 6.

Chapter 2

A Lagrangian approach to identifying vortex pinch-off

2.1 Introduction

In their paper introducing the concept of the vortex formation number, Gharib *et al.* (1998) calculated the formation number by comparing the time history of the total circulation emanating from their vortex generator, to that of the leading vortex ring. Their method is described in detail in the preceding chapter, and has been employed by Dabiri & Gharib (2004*a*), Dabiri & Gharib (2005*a*), Krueger *et al.* (2006), and others to identify the formation number for vortex rings in a variety of flow conditions, using the piston-cylinder configuration. Dabiri & Gharib (2004*a*) considered the delay of pinch-off in piston-cylinder vortex generators when a bulk counter flow was imposed. Similarly, Krueger *et al.* (2006) considered the case of vortex rings in uniform co-flow. Dabiri & Gharib (2005*a*) considered the formation of vortex rings when no background flow was imposed, but the exit diameter of the cylinder was time varying.

Also using the circulation method of Gharib *et al.* (1998), several researchers have identified pinch-off in other vortex-shedding configurations, such as starting and steadily-oscillating circular cylinders (Jeon & Gharib, 2004), oscillating flat plates (Milano & Gharib,

2005), and accelerating low-aspect-ratio flat plates (Ringuette *et al.*, 2007). Furthermore, vortex pinch-off has been observed in biological flows such as that through the mitral valve in the human heart (Gharib *et al.*, 2006) and the flow generated by jetting juvenile squid (Bartol *et al.*, 2009; Linden & Turner, 2004) and jellyfish (Dabiri *et al.*, 2006, 2010).

The method of Gharib *et al.* (1998) poses several challenges, however. First, determining the final circulation of the vortex ring requires that the ring be distinguishable from its trailing jet from vorticity contours. Since such a distinction is not possible until the vortex has advected away from the wake, it requires observation of the vortex ring's evolution after the initiation of pinch-off. In unsteady flows, vortex breakdown can obscure these long-term observations. Second, even if one has the capability to record the vortex evolution for these long times, it is essential that the vorticity field not diffuse and the vortex not distort by interaction with other structures in the flow, both of which are common processes in biological flows. Finally, as Bartol *et al.* (2009) remark, in low Reynolds number flows, it can be difficult to discern whether or not the elongated nature of some naturally occurring vortex rings represents pinch-off that has been obscured by viscous diffusion.

In this chapter, an alternate method for identifying vortex ring pinch-off using Lagrangian coherent structures (LCS) is proposed. LCS are finite-time invariant manifolds in flows with arbitrary time-dependence, akin to the invariant manifolds in time-independent flows. The manifolds are Lagrangian, in that they are derived from fluid trajectories. The concept of LCS was formalized in a series of papers by Haller and co-workers (Haller, 2000, 2001*a*,*b*, 2002; Haller & Poje, 1998; Haller & Yuan, 2000), and precise quantitative definitions and properties of LCS were given by Shadden *et al.* (2005). In addition to being nearly-invariant manifolds (at least for some finite time); LCS act as barriers to transport (Du Toit & Marsden, 2010; Shadden *et al.*, 2006; Peng & Dabiri, 2009; Beron-Vera *et al.*,

2012),they act as separatrices between regions with qualitatively different kinematics (Shadden *et al.*, 2006); and they provide a 'skeleton' of the flow by identifying regions of high attraction and repulsion (Mathur *et al.*, 2007; Olascoaga & Haller, 2012; Green *et al.*, 2007). As a result, LCS have been used to investigate turbulence (Mathur *et al.*, 2007; Green *et al.*, 2007), to study transport and mixing in atmospheric and oceanic flows (Olascoaga & Haller, 2012; Du Toit, 2010; Beron-Vera *et al.*, 2012, 2010), and to analyze blood flow in the human cardiovascular system (Hendabadi *et al.*, 2012; Arzani & Shadden, 2012; Shadden & Taylor, 2008; Vétel *et al.*, 2009; Shadden *et al.*, 2010).

LCS have been used in numerous studies as a structure identification tool, to identify and investigate vortices in a variety of flows. Green *et al.* (2007, 2010) showed that LCS can be used to identify the boundaries of Hill's spherical vortex. Shadden *et al.* (2006) used LCS to identify the boundaries of a vortex ring generated from a piston-cylinder apparatus, and Shadden *et al.* (2007) studied the evolution of the LCS during the formation of a vortex ring from this arrangement. Additionally, Green *et al.* (2007) used LCS to investigate the evolution of a single hairpin vortex, while Green *et al.* (2010) considered the shedding of vortices by a pitching trapezoidal panel using LCS. In these studies, Green and co-workers demonstrated that changes in the LCS structure correspond to changes in vortex structure.

Following the success of LCS as vortex identification tools in classical experimental setups, as well as canonical numerical and analytical flows, the technique has also been applied to the study of biological vortex flows. For example, Shadden *et al.* (2006), identified the region of fluid sampled by a free-swimming *Aurelia aurita* jellyfish during its recovery stroke. This analysis was extended by Peng & Dabiri (2009),who studied the 'capture region' of free-swimming jellyfish, and predator-prey interactions between jellyfish and their planktonic prey. In numerical simulations, Lipinski & Mohseni (2009) analyzed the vortex

wake of two types of jellyfish, while Wilson *et al.* (2009) considered the propulsion of jellyfish-like swimmers at low Reynolds numbers, and Eldredge & Chong (2010) considered the vortices shed by bio-inspired flapping wings.

In this study, we used the LCS framework to analyze a starting jet flow with a stroke ratio of approximately twelve. We considered the evolution of the LCS during fluid ejection, and searched for an indication of pinch-off in the LCS structure. Since the pinch-off process involves the separation of distinct vorticity-carrying regions of the flow (i.e., the vortex ring and trailing jet), we proposed that LCS are an effective tool for quantifying the process. Indeed, using LCS, we were able to identify the onset of pinch-off, without requiring that the circulation in the vortex ring be measured after pinch-off. Furthermore, the LCS approach provided insight into the structure and dynamics of the trailing shear layer which analysis of the vorticity alone, or other traditional metrics, overlooked.

This chapter is organized as follows. §2.2 contains an overview of the experimental methods for generating vortex rings and for data collection. The LCS framework and methods utilized in this chapter are introduced in §2.3. Results of the LCS analysis for predicting pinch-off and studying vortex dynamics in the wake of the leading vortex ring, are presented in §2.4 and §2.5, and the comparison between the LCS method and existing criteria is discussed in §2.6. Finally, concluding remarks are presented in §2.7.

2.2 Vortex ring generation

Vortex rings were generated in a water tank using a piston-cylinder arrangement similar to that described in Dabiri & Gharib (2004*b*). However, whereas Dabiri & Gharib (2004*b*) considered low stroke ratios only ($L/D = 2,\ 4$), we consider a case where $L/D \approx 12$. Figure 2.1 shows a schematic of the experimental setup. Flow from a constant-head tank

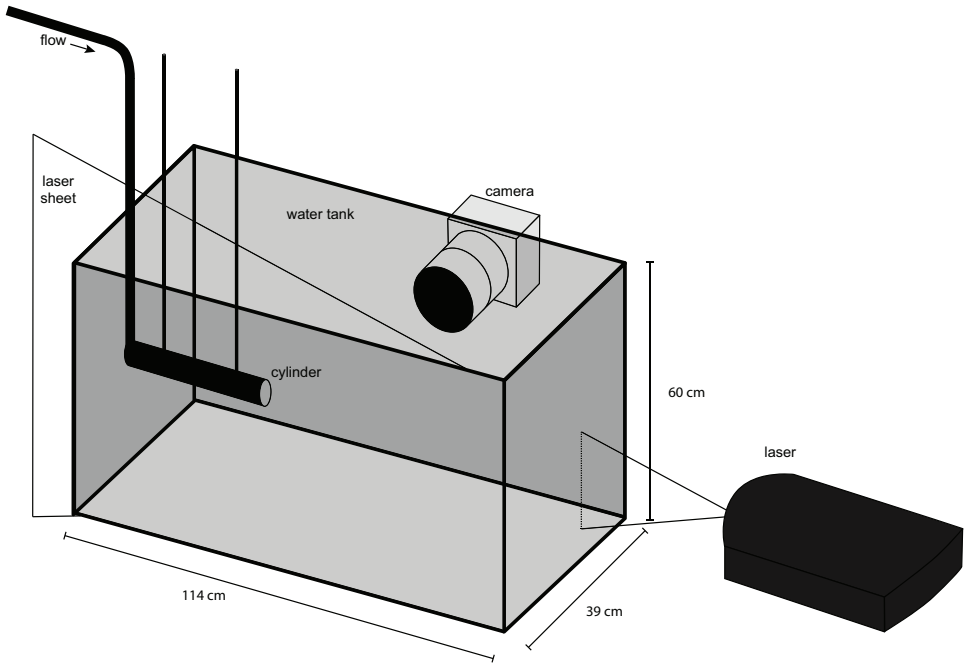

Figure 2.1: Schematic of the experimental setup for generating circular vortex rings.

was allowed to drive a piston through a hollow cylinder of internal diameter $D = 2.54$ cm submerged in the water tank. A column of fluid of length $L \approx 30.5$ cm was impulsively ejected from the sharp-edged nozzle by the motion of the piston, and rolled up into a vortex ring which propagated through the surrounding fluid owing to its self-induced velocity.

The resulting velocity field was recorded using digital particle image velocimetry (DPIV) (Willert & Gharib, 1991; Adrian, 1991). A pulsed Nd:YAG laser sheet was used to illuminate a symmetry plane of the axisymmetric flow, and the flow was seeded with nominally 13-micron, neutrally buoyant glass spheres. The spheres scattered incident light from the laser sheet onto a CCD camera whose image plane was positioned parallel to the sheet. The test section measured approximately 12 cm ($4.7D$) radially and 20 cm ($7.9D$) axially, and the resolution of the captured images was approximately 0.19×0.19 mm. The resulting images were interrogated using cross-correlation, with a separation of 18 ms between frames and an interrogation window size of 32×32 pixels with a 50% overlap. The velocity and vorticity

fields were calculated using an in-house code, and the resolution for both was approximately 3×3 mm ($0.13 \times 0.13D$) with an uncertainty of 1% and 3% respectively.

Experiments were conducted at a Reynolds number $Re = \overline{U}_p D/\nu = 1400$, based on the nozzle diameter and average piston velocity. The Reynolds number based on the circulation of the leading vortex ring was $Re_\Gamma = \Gamma_{ring}/\nu = 4000$. This data was previously reported in Dabiri & Gharib (2004*c*). However, in that study the authors considered only the time history of the total circulation emanating from the piston-cylinder vortex generator, and proposed a correction to the slug model for the flux of vorticity from these devices. The vorticity field was hence reported for the first time by O'Farrell & Dabiri (2010).

2.3 Lagrangian coherent structures

LCS are known to correspond with regions of high trajectory separation or attraction. Just as two points straddling the stable manifold of a hyperbolic fixed point in a time-independent system will diverge exponentially in forward time, points straddling a *repelling* LCS will diverge in forward time. Likewise, points straddling an *attracting* LCS will diverge in backward time, a behavior akin to the exponential divergence in backward time of points straddling the unstable manifold of a hyperbolic fixed point. These properties of LCS are exploited in developing methods for identifying their location in time-independent flows.

LCS are most often extracted from experimental, numerical, and analytical velocity fields by means of a scalar quantity known as the finite-time Lyapunov exponent, or FTLE. The FTLE is a measure of the divergence, in finite time, of trajectories starting near a point $\mathbf{x}$ in the domain. Given a flow map $\phi_{t_0}^{t_0+T} : \mathbf{x}(t_0) \mapsto \mathbf{x}(t_0 + T)$ that maps fluid particles from their initial position at t_0 to their position a time T later, the FTLE is given by:

$$\sigma_{t_0}^{T} = \frac{1}{|T|} \ln \left\| \frac{d\mathbf{x}(t_0 + T)}{d\mathbf{x}(t_0)} \right\|_2 \tag{2.1}$$

where $d\mathbf{x}(t_0 + T)/d\mathbf{x}(t_0)$ is the deformation tensor. Here $\|\cdot\|_2$ indicates the spectral norm of the tensor, which corresponds to its largest singular value. As a result, $\sigma_{t_0}^{T}$ measures the linearized divergence of trajectories starting near $\mathbf{x}(t_0)$ over a time interval T. T may be positive (indicating that the FTLE field is calculated by integrating trajectories in forward time) or negative (indicating integration in backward time). Hence, high values of the forward-time FTLE correspond to regions of large trajectory separation, while high values of the negative-time FTLE correspond to regions of large trajectory convergence.

Regions of maximum fluid particle separation (for $T > 0$) or maximum fluid particle attraction (for $T < 0$) produce locally maximizing curves known as 'ridges' in the FTLE field (Haller & Yuan, 2000; Shadden *et al.*, 2005). The integration time T is chosen according to the particular flow being analyzed, with longer integration times leading to more of the ridge being revealed, and to sharper ridges with higher spatial resolution. In practice, however, T is bounded by the numerical costs of integrating trajectories, as well as by the availability of velocity data. One of the advantageous properties of using the FTLE field for fluid structure identification is that, unlike existing Eulerian criteria, the location of the ridges remains unchanged when the integration time is varied (Green *et al.*, 2007). If the integration time is sufficiently large, the ridges in the positive-time and negative-time FTLE will intersect, providing a boundary for the flow structure of interest.

However, ridges in the FTLE field need not necessarily represent hyperbolic LCS as they may correspond to lines of high shear. In their study of the development of a single hairpin vortex into a co-moving group of like vortices (or 'hairpin packet'), Green *et al.*

(2007) demonstrated the importance of verifying the hyperbolicity of LCS in studying vortex interactions. In order to confirm that a ridge is indeed a hyperbolic LCS, the sign of the instantaneous strain rate normal to the ridge must be checked (Haller, 2002). Ridges in the forward-time ($T > 0$) FTLE field where the strain rate normal to the ridge is positive (particle stretching away from the ridge) represent a *repelling* LCS. Conversely, ridges in the backward-time ($T < 0$) FTLE field where the strain rate normal to the ridge is negative (particle attraction towards the ridge) represent an *attracting* LCS (Haller, 2002).

Shadden *et al.* (2006) were able to identify the boundaries of a vortex ring with a stroke ratio of approximately $L/D \approx 2$ using LCS. The authors found that the attracting LCS formed the forward-facing boundary of the vortex ring, while the repelling LCS formed the rear boundary of the vortex, and their intersection provided a complete boundary of the vortex. The results of Shadden *et al.* (2006) are replicated below, using the velocity data for the $L/D = 2$ vortex ring reported in Dabiri & Gharib (2004*b*). The FTLE fields were computed using Dr. Philip Du Toit's software for efficient FTLE computation: *Newman* (Du Toit, 2010). In figure 2.2, the forward-time FTLE is shown in blue, and the backward-time FTLE is shown in red. It is evident from this figure that the attracting LCS formed the forward-facing boundary of the vortex ring, while the repelling LCS formed its rear boundary. In addition, while the vortex was forming, the repelling LCS consisted of two segments attached to the nozzle of the vortex generator (figure 2.2(a)). Once fluid ejection stopped, however, the two segments merged and formed the rear boundary of the vortex. Using a setup which allowed the recording of velocity fields inside the vortex generator, Shadden *et al.* (2007) were able to observe that the two segments in figure 2.2 actually connect inside the vortex generator.

In figure 2.2, the forward- and backward-time FTLE fields are shown as contours ranging

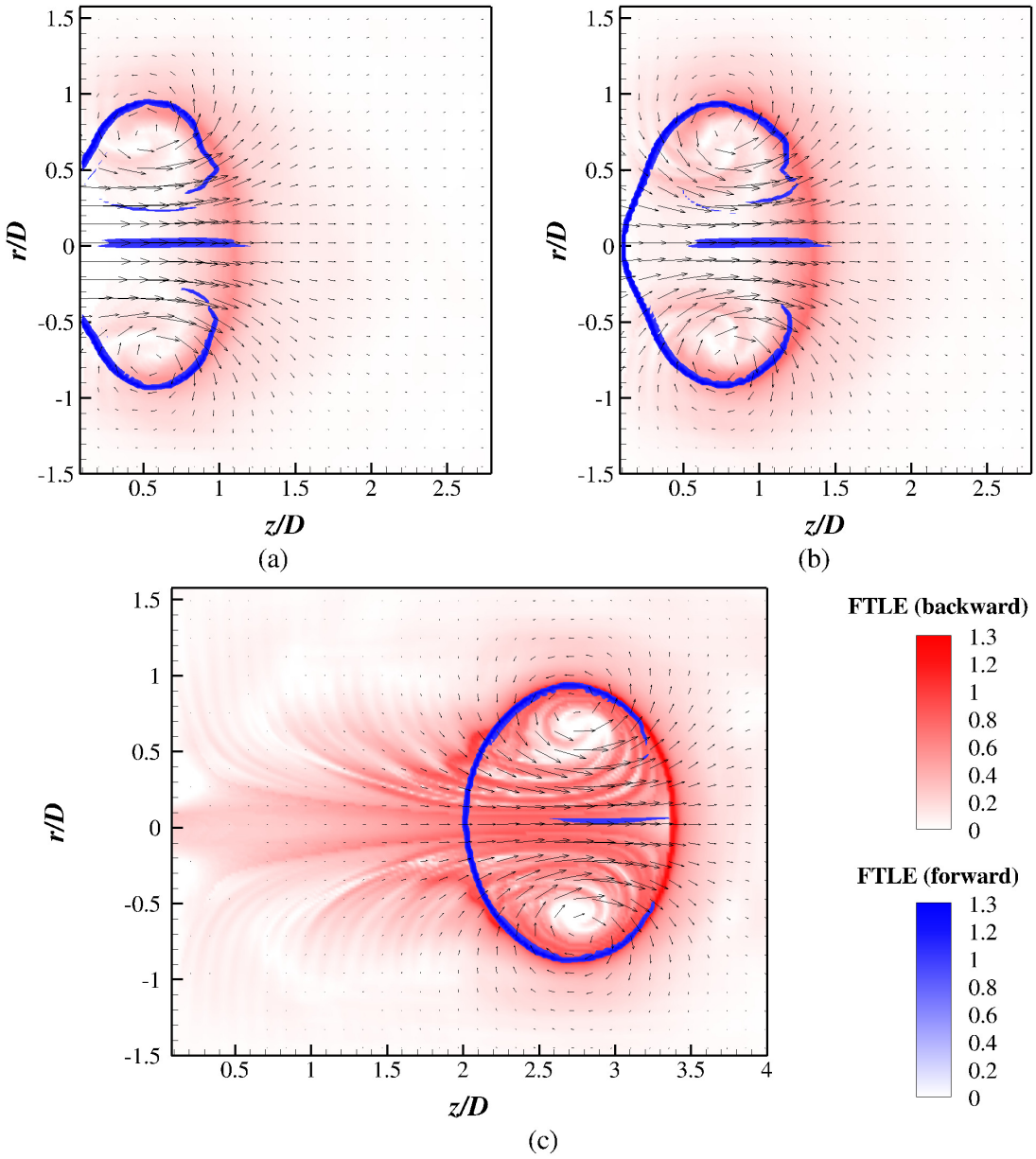

Figure 2.2: Repelling (blue) and attracting (red) LCS for the vortex ring with a stroke ration of two considered in Dabiri & Gharib (2004*b*), at: (a) $\hat{T} = 1.8$, (b) $\hat{T} = 2.3$, (c) $\hat{T} = 7.1$. Velocity vectors are shown in black for reference. Flow is from left to right, and time $\hat{T} = 0$ corresponded to the initiation of fluid ejection.

from white to blue, and white to red, respectively. Values of the forward-time FTLE below 70% of the maximum have been blanked out. No blanking was applied on the backward-time FTLE values, in order to illustrate the effect of changing integration time on the FTLE fields. In figure 2.2(a), the ridge in the backward-time FTLE is seen to be very diffuse. This occurs because, at these early stages in the formation process, scarce velocity information is available for backward integration. The integration time selected for the computation of the FTLE fields was $T = 3.3$ s ($\overline{U}_p T/D = 7.1$). In the backward-time case, when sufficient information was not available to allow the integration of trajectories backwards for a time $T = 3.3$ s (i.e., when $t_0 < 3.3$ s), the longest integration time possible was used. As a result, T for the backward-time FTLE was 0.7 s ($\overline{U}_p T/D = 1.5$) in figure 2.2(a), 1 s ($\overline{U}_p T/D = 1.5$) in figure 2.2(b), and 3.3 s in figure 2.2(c). The corresponding increase in the sharpness and length of the ridges in the backward-time FTLE is evident in figure 2.2, and it highlights the difficulty of using the backward-time FTLE for the study of the formation of new fluid structures at short times after their formation is initiated, when backward-time velocity data are scarcely available.

In the study that follows, the FTLE field was computed on a Cartesian grid with a resolution of 0.3×0.3 mm ($0.01 \times 0.01D$), using an in-house MATLAB® (The MathWorks, Inc., Natick, MA) toolkit designed by Dr. Jeff Peng, and described in Peng *et al.* (2007). This toolkit is freely available on the web at: http://www.dabiri.caltech.edu/software.html. At each time t, each point on the grid was advected by the flow by numerically integrating the velocity field data for the integration time T. A fourth-order Runge-Kutta scheme was used for the numerical integration, and bilinear interpolation was used whenever interpolation of the velocity data was required. The deformation tensor was then computed at each point on the grid using central differencing with neighboring grid points. Finally, the FTLE field

was computed by evaluating (2.1) at each point on the grid.

Ridges in the FTLE field were extracted using the method described in Mathur *et al.* (2007). We identified regions around the ridges where the gradient of the FTLE ($\nabla\sigma_{t_0}^T(\mathbf{x})$) exceeded a set threshold (50% of the maximum) and used a two-dimensional gradient climb within these regions to identify the locus of points on the ridge. A point was considered to be on the ridge when the Hessian of the FTLE ($\nabla^2\sigma_{t_0}^T(\mathbf{x})$) had at least one negative eigenvalue and no appreciable change (Mathur *et al.*, 2007) was observed in the angle between the eigenvector corresponding to the eigenvalue of $\nabla^2\sigma_{t_0}^T(\mathbf{x})$ with the smallest norm and $\nabla\sigma_{t_0}^T(\mathbf{x})$. For each point on a ridge, we approximated the unit normal to the ridge by $\mathbf{n} = \nabla\sigma_{t_0}^T(\mathbf{x})/\|\nabla\sigma_{t_0}^T(\mathbf{x})\|_2$ and computed the instantaneous rate of strain normal to ridge as $\langle\mathbf{n}, \mathbf{S}\mathbf{n}\rangle$, where the rate of strain tensor $\mathbf{S}$ is the symmetric part of the velocity gradient tensor $\nabla\mathbf{u}$.

2.4 Vortex pinch-off

In figure 2.3 we present contours of the vorticity field at three separate instants. The growing vortex ring is shown in its early stages of development in figure 2.3(a) ($\hat{T} = 1.5$). At $\hat{T} = 4.1$, a trailing shear layer carrying significant vorticity had developed (figure 2.3(b)). Figure 2.3(c) shows that at a formation time of $\hat{T} = 8.5$, the vortex ring had separated from the trailing shear layer and advected away from it by self-induction. These results are in agreement with those reported by Gharib *et al.* (1998) for large stroke ratios (see their figure 5).

To further study the pinch-off process, we computed the forward-time and backward-time FTLE fields from the PIV velocity data. The integration time was $T = 3.3$ s (or $\hat{T} = 7.3$), where time $t_0 = 0$ corresponded to the initiation of fluid ejection from the

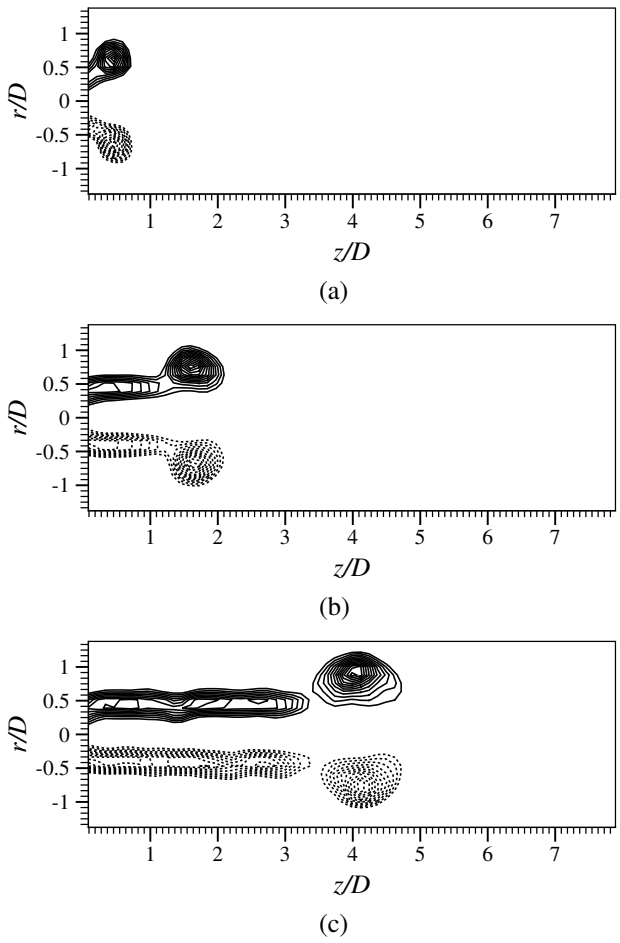

Figure 2.3: Contours of vorticity at: (a) $\hat{T} = 1.5$, (b) $\hat{T} = 4.1$ and (c) $\hat{T} = 8.5$. Contour levels, min = 25% of ω_{max}, max = 95% of ω_{max}, increment = 10%. Dashed lines indicate negative vorticity. The cylinder exit plane is located in the $z/D = 0$ plane, and the z-axis coincides with the vortex generator centerline. Flow is from left to right.

cylinder. The integration time was chosen because it yielded the complete forward-facing boundary of the vortex and excellent spatial resolution in the ridges, while remaining feasible in terms of computational expenses.

Figure 2.4 shows both the attracting and repelling LCS, in red and blue respectively, at three time instants during the vortex formation process. The forward- and backward-time FTLE fields are shown as contours ranging from white to blue, and white to red, respectively. Values of the forward-time and backward-time FTLE below 70% of the maximum have been

blanked out, in order to show the outline of the attracting and repelling LCS. Figure 2.4(a) shows the LCS at $\hat{T} = 3.0$. Since this time instant was well before expected formation number of four, the leading vortex ring was still accepting vorticity from the shear layer. As a result, the LCS structure resembled that shown in figure 2.2(a) for a stroke ratio of two. At later times (figure 2.4(b) and (c)), differences emerged between the $L/D = 2$ and $L/D = 12$ cases. Rather than close up to form the rear boundary of the vortex, the repelling LCS was found to elongate as fluid ejection continued, and new structures were observed developing in the wake of the leading vortex. In contrast, the attracting LCS resembled the LCS in the stroke-ratio-two case even up to formation times after the expected occurrence of pinch-off (figure 2.4(b)). At long formation times, however, new attracting structures appeared in the wake of the leading vortex (figure 2.4(c)).

The structure of the attracting and repelling LCS in figure 2.4 suggests that the forward-time FTLE field is most useful when studying pinch-off. The repelling LCS, extracted from the forward-time FTLE, was found to form the rear boundary of the vortex ring, which was most affected by pinch-off as evidenced by the differences between figures 2.2 and 2.4. Secondly, computing the backward-time FTLE requires backward-time data which, as mentioned previously, is not always available in sufficient quantities by the initiation of pinch-off. Furthermore, and perhaps due to one or both of the aforementioned reasons, changes in the LCS structure between the isolated vortex ring and pinched off vortex case (figures 2.2 and 2.4, respectively) were not seen until later formation times in the attracting LCS. Therefore, we focused our attention on the forward-time FTLE field and the repelling LCS.

Figure 2.5(a) shows a contour plot of the forward-time FTLE field at the arbitrary time $t_0 = 1.3$ s ($\hat{T} = 2.8$), before the vortex ring pinched off. In figure 2.5(b), the locus of

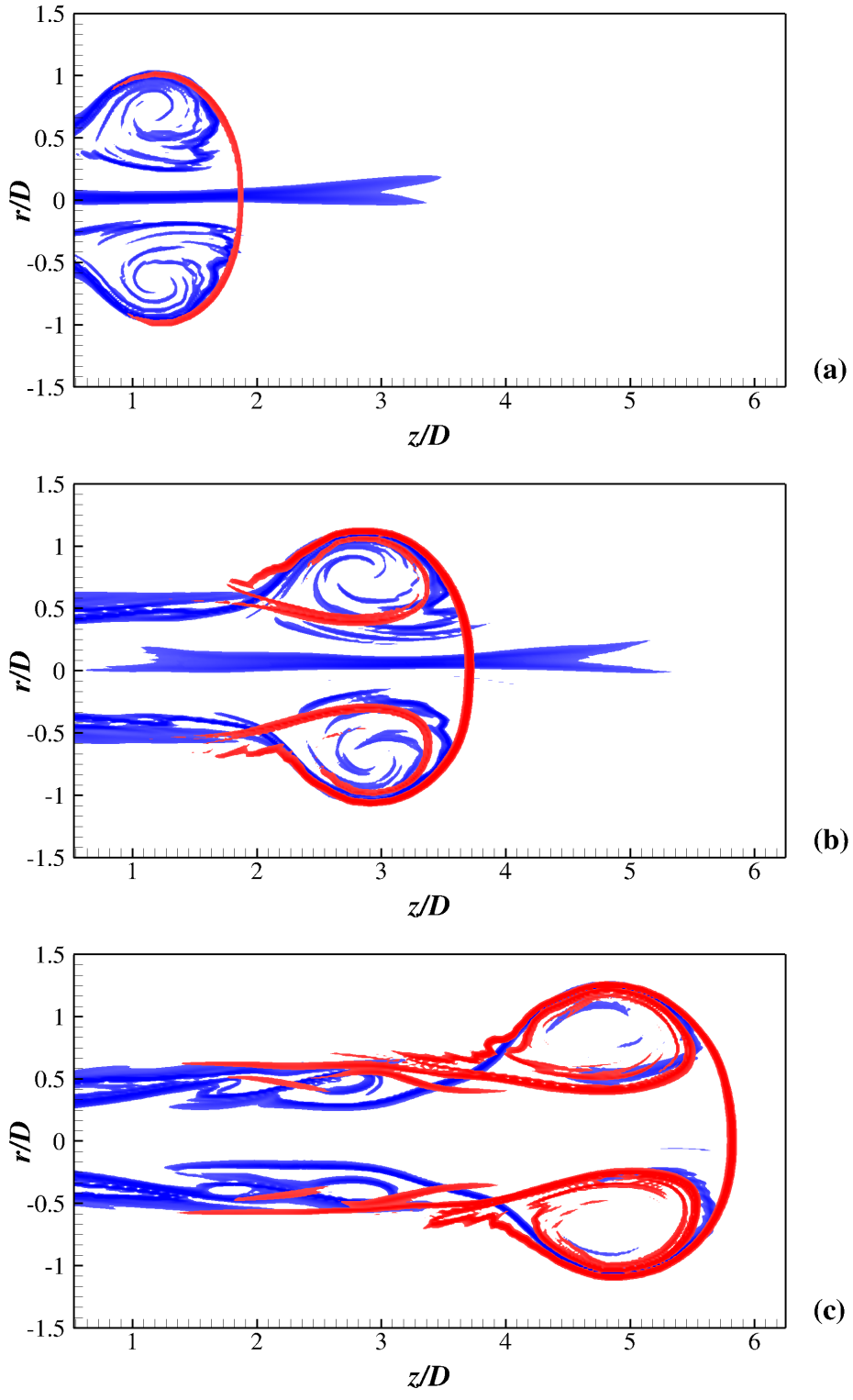

Figure 2.4: Repelling (blue) and attracting (red) LCS for the vortex ring with a stroke ratio of twelve, at: (a) $\hat{T} = 3.0$, (b) $\hat{T} = 6.2$, (c) $\hat{T} = 9.8$. Flow is from left to right.

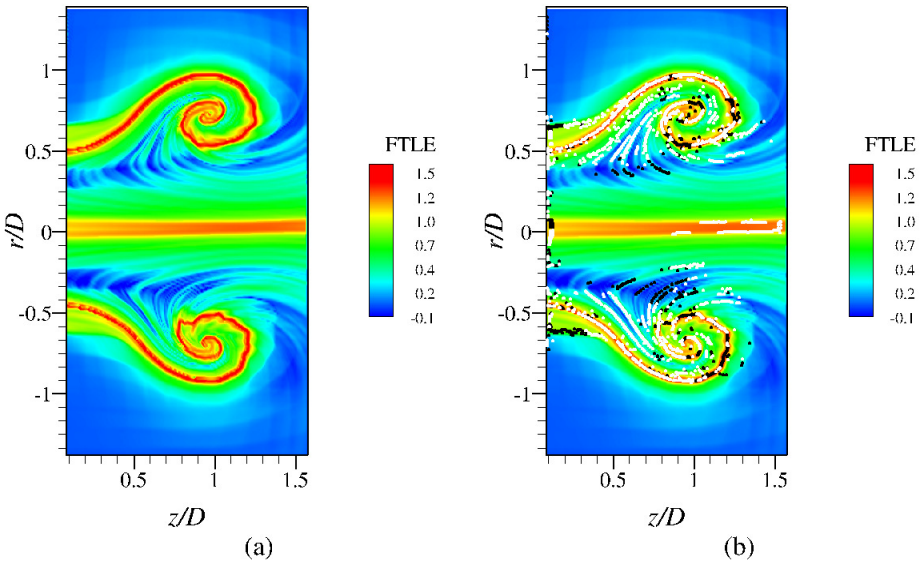

Figure 2.5: Contours of the forward-time FTLE field at $\hat{T} = 2.8$. In (b) the strain rate normal to the LCS has been superimposed. Positive strain rate is shown in white, negative in black.

points on the repelling LCS has been superimposed on the FTLE field, and points where the rate of strain was negative have been colored black, while regions of positive strain rate have been colored white. The spiral regions that corresponded to the vortex ring core showed alternating patterns of positive and negative strain rate, consistent with the shearing rotational flow within them (Green *et al.*, 2007). Upstream of the spiral regions, the strain rates normal to the LCS were positive, indicating that the ridge did indeed represent a hyperbolic repelling line. The hyperbolicity of the LCS was checked throughout the formation process, but the strain rate information was omitted from subsequent figures to avoid obscuring important details of the LCS structure.

As fluid continued to be ejected out of the cylinder, the vortex ring convected downstream by self-induction and the repelling LCS lengthened until, at a formation time of 4.1 ($t_0 = 1.9$ s), there was an abrupt change in the structure of the LCS. A new ridge, discontinuous from the original one, appeared and the first LCS ended on the upstream end

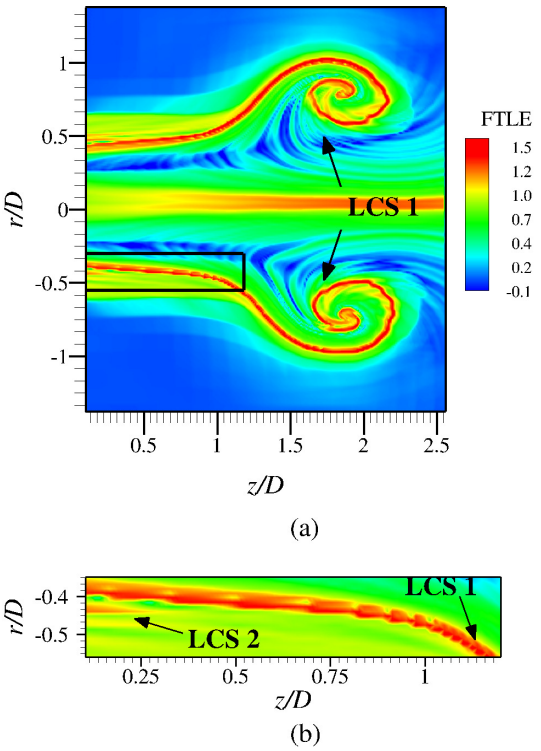

Figure 2.6: Contours of the forward-time FTLE field at $\hat{T} = 4.5$. A detail of the boxed region in (a) is shown in (b). A new repelling LCS has formed and is indicated in (b) by an arrow.

a few instants later. Figure 2.6 shows a contour plot of the FTLE field, at a formation time of 4.5 ($t_0 = 2.1$ s). The presence of a new ridge just downstream of the cylinder exit plane ($z = 0$) is evident in this figure, which corresponds to an instant 0.2 s (0.43 formation time units) after the first appearance of the new ridge. The termination of the first repelling LCS was visible a few instants later, and is evident in figure 2.7, taken at a formation time of 5.9.

At a formation time of $\hat{T} = 4.7$ ($t_0 = 2.1$ s), a third disconnected ridge appeared just downstream of the cylinder exit, and the second repelling LCS ended several time steps later. Figure 2.7 shows a contour plot of the FTLE field, at a formation time of $\hat{T} = 5.9$ ($t_0 = 2.7$ s). The presence of a new ridge just downstream of the cylinder exit plane is evident in this figure, which corresponds to an instant 0.5 s (1.1 formation time units) after

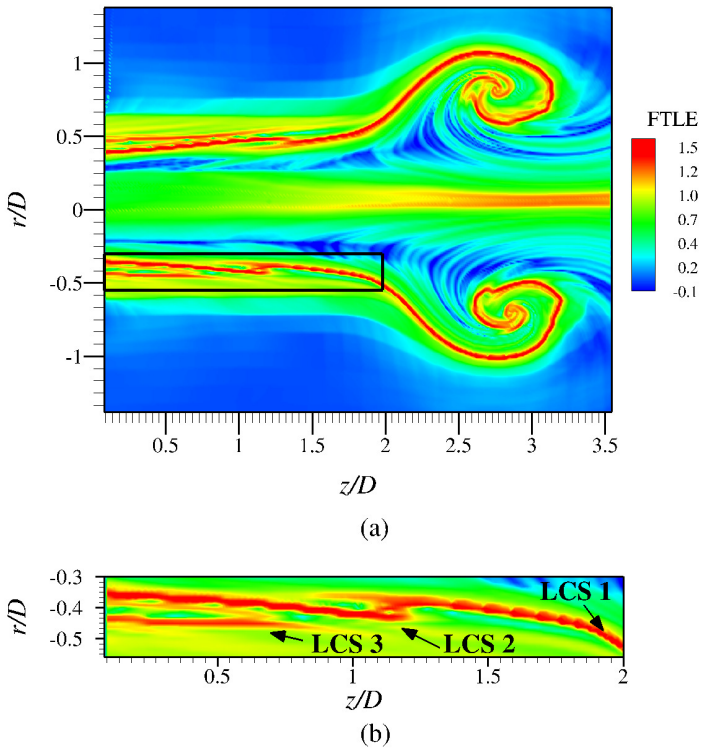

Figure 2.7: Contours of the forward-time FTLE field at $\hat{T} = 5.9$. A detail of the boxed region in (a) is shown in (b). LCS 1 through 3 are indicated by arrows in (b). A new repelling LCS (LCS 3) has just formed, and the termination of LCS 1 after the appearance of LCS 2 is also evident at this time.

the first appearance of the third ridge. The termination of the second repelling LCS was not evident until several time steps after the appearance of the third ridge, but it is clearly visible in figure 2.10.

Following Gharib *et al.* (1998), we computed the total circulation emanating from the piston-cylinder apparatus by integrating the vorticity contained within the lowest detectable contours. The circulation in the leading vortex ring was measured for large formation times, where the separation between the vorticity contours of the ring and those of the shear layer was clear. Figure 2.8 shows the total circulation and vortex ring circulation as a function of formation time. Gharib *et al.* (1998) found that for large stroke ratios the vortex ring circulation increased in a step-like fashion after long formation times (see

their figure 10). This step-like increase was caused by the leading vortex in the trailing wake (hereafter referred to as vortex 2) catching up to and coalescing with the original vortex ring (hereafter referred to as vortex 1). This phenomenon is commonly observed in configurations with two co-axial vortex rings traveling in the same direction. The leading vortex ring induces a velocity on the second vortex ring, which causes it to contract and accelerate. Simultaneously, the velocity field induced by the trailing vortex causes the first vortex to expand in diameter and decelerate. As a result, under certain conditions, the trailing vortex may catch up to the leading vortex. If the initial conditions are favorable, the second vortex ring can be drawn through the center of the leading vortex ring and pass through it, a phenomenon known as 'leapfrogging' (Yamada & Matsui, 1979; Lim, 1997). Often, however, the vortices instead coalesce into a single vortex ring (Maxworthy, 1972; Oshima *et al.*, 1975).

In figure 2.8 we observe a similar step-like behavior after formation times of $\hat{T} \approx 10$, due to the merger of vortices 1 and 2. For formation times between $\hat{T} \approx 8$ and $\hat{T} \approx 10$, the vortex ring circulation was constant at $\Gamma = 40 \pm 2$. A straight line in figure 2.8 shows that at a formation time of approximately 4.2 the total circulation equaled the circulation of vortex 1 for formation times between ≈ 8 and ≈ 10. The formation number was hence 4.2 ± 0.2, which agreed well with the appearance of the second repelling LCS. A second straight line in figure 2.8 shows that at a formation time of $\hat{T} = 4.6 \pm 0.2$ the total circulation equaled the final vortex ring circulation (i.e., the circulation of the combined vortices 1 and 2, $\Gamma = 47.7 \pm 1.5$), meaning that vortex 2 must have itself pinched off from the trailing jet at this formation time. The initiation of pinch-off of vortex 2 at a formation time of $\hat{T} = 4.6 \pm 0.2$ was found to correspond well with the appearance of a third repelling LCS at a formation time of $\hat{T} = 4.7$.

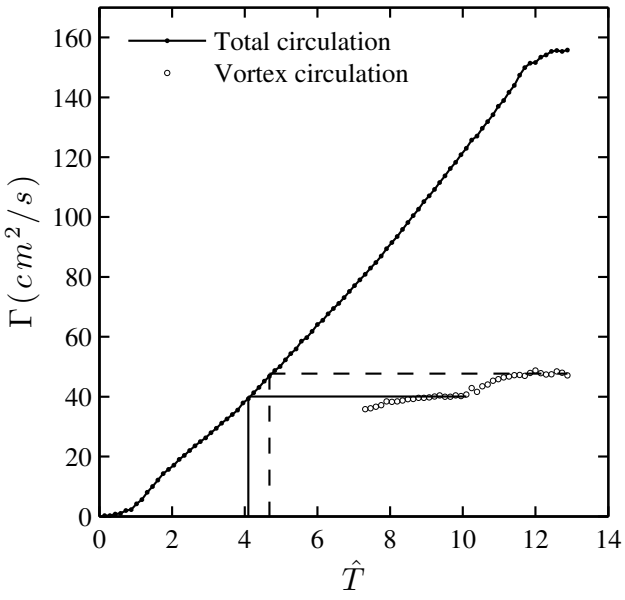

Figure 2.8: Total circulation and vortex ring circulation as a function of formation time. The solid straight line indicates the $\hat{T}$ at which vortex 1 pinched-off, and dashed line indicates the $\hat{T}$ at which vortex 2 stopped accepting circulation. The step-like increase in the vortex circulation is due to vortex 2 coalescing with vortex 1.

2.5 Vortex pairing

Observing the continued evolution of the LCS revealed the appearance of additional, disconnected, repelling LCS at later times. The location of these LCS corresponded to the location of additional vortex rings developing in the trailing shear layer, so that the development of each new repelling LCS provided insight into the evolution of vortices in the trailing wake. As new repelling LCS developed, many of them began to roll up into spirals, and their structure began to resemble that of the vortex ring core in the first LCS.

However, some of the new LCS did not develop fully into tight spirals consistent with the formation of a new vortex ring, but rather merged with the preceding LCS. Figure 2.9(a) shows the first and second repelling LCS intersecting and beginning to merge. Figure 2.9(b) shows that LCS 2 merged completely with the first repelling LCS and eventually became

indistinguishable from it. This process was indicative of the beginning of the merger of vortices 1 and 2.

The third repelling LCS (whose corresponding vortex we shall refer to as vortex 3) did, however, develop fully into a tight spiral. Figure 2.10(a) shows the third repelling LCS rolling up into a spiral. Figure 2.10(b), on the other hand, shows the fourth repelling LCS (corresponding to vortex 4) intersecting with the third LCS. This intersection persisted in time and constituted the first stage in the merger of the third and fourth repelling LCS, a process akin to the merging of the first and second LCS in figure 2.9(b). The merging of the third and fourth repelling LCS was indicative of the beginning of the merger of vortices 3 and 4.

Continued observation of the evolution of the emerging repelling LCS revealed a consistent 'pairing' of adjacent vortices in the trailing jet. This phenomenon of vortex ring pairing in circular jets is well documented in the literature of turbulent mixing layers (Grinstein, 1995; Winant & Browand, 1974; Ho & Huerre, 1984; Hussain & Zaman, 1980; Yule, 1978). This pairing process is believed to be initiated by wave instabilities in the shear layer causing small radial displacements of the vortex rings in the jet (Petersen, 1978; Ho & Huerre, 1984; Grinstein, 1995). The mutual interaction of the vortex rings then leads to their merger at nearly fixed locations (Grinstein, 1995).

Although the appearance of new, disconnected repelling LCS is a subtle feature, the new LCS were found to be persistent in time. The second repelling LCS remained apparent from the forward-time FTLE field until the merger of vortices 1 and 2 at a formation time of approximately 6.7, when it disappeared as the repelling LCS corresponding to these vortices merged into a single coherent structure. In contrast, the third repelling LCS remained separate from LCS 2 until the jet had shut off completely, since vortex 3 did not

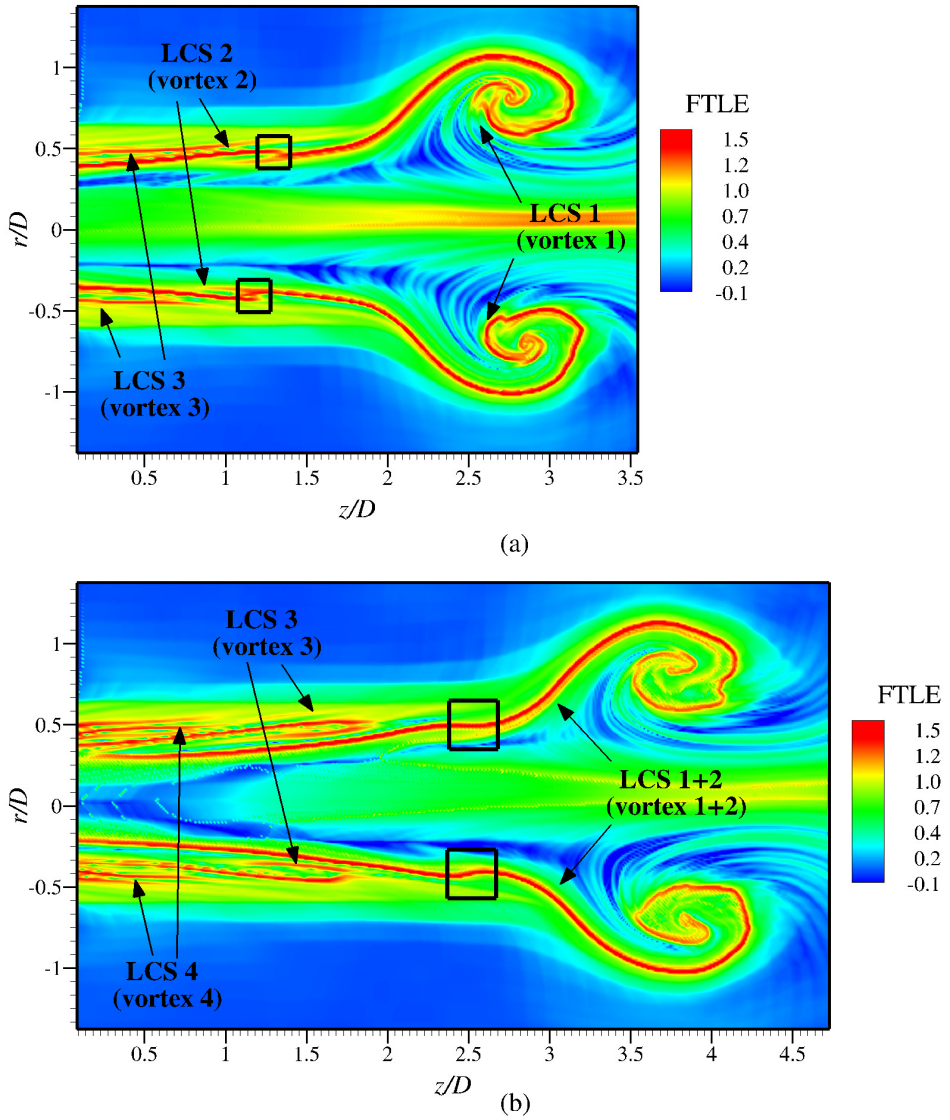

Figure 2.9: Contours of the forward-time FTLE field. (a) $\hat{T} = 6.7$. The boxed regions show the initial stages of the merger of LCS 1 and 2. (b) $\hat{T} = 8.0$. The first and second repelling LCS have merged at the regions indicated by the boxes.

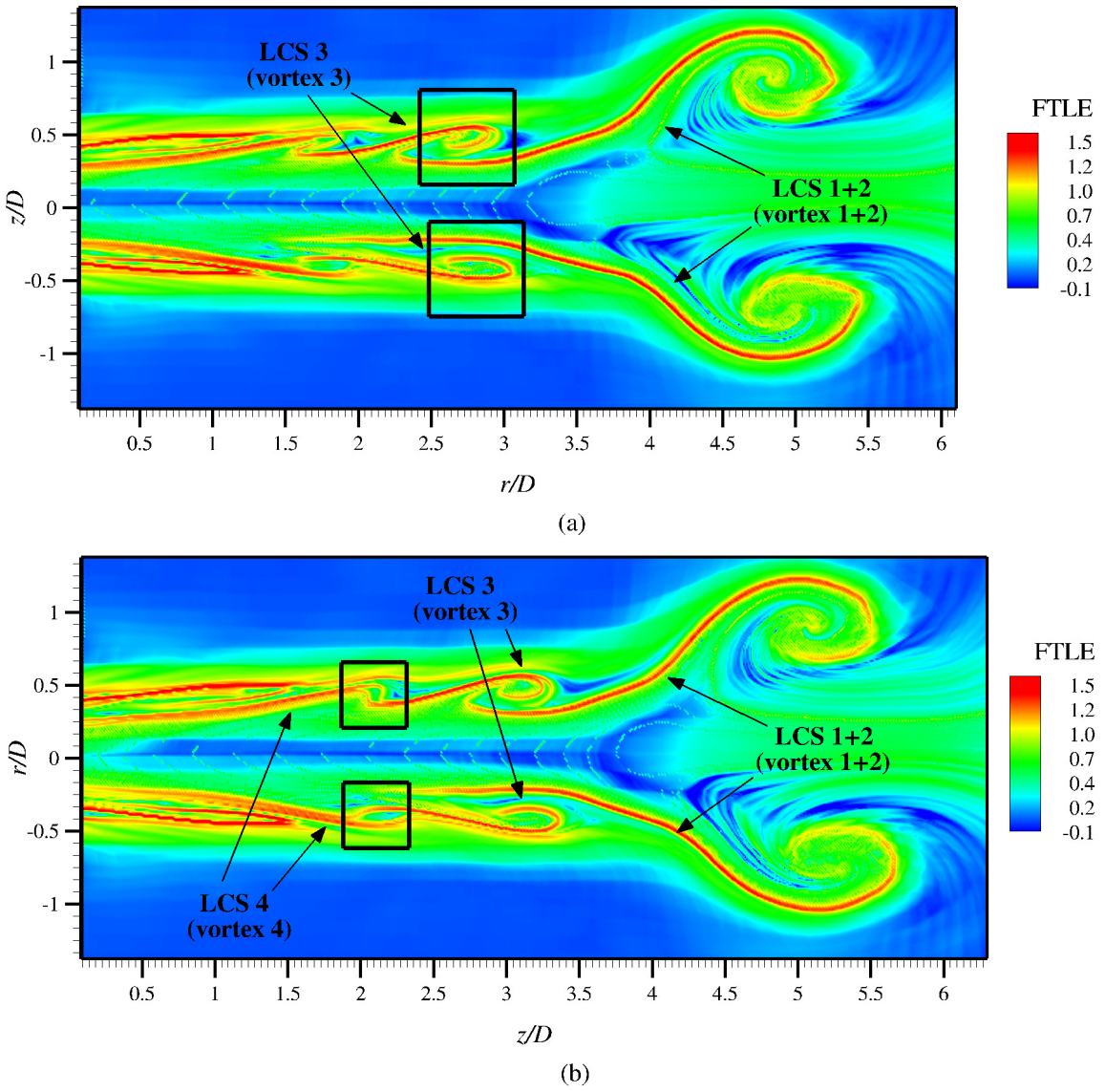

Figure 2.10: Contours of the forward-time FTLE field. (a) $\hat{T} = 9.8$. The boxed regions show the third repelling LCS beginning to curl into a spiral. (b) $\hat{T} = 10.2$. The third and fourth repelling LCS are merging at the regions indicated by the boxes. In both (a) and (b), the termination of LCS 2 (now merged with LCS 1) several time steps after the appearance of LCS 3, is evident.

merge with the vortex ahead of it. Subsequent repelling LCS remained disconnected from their neighbors either until they disappeared due to the merger of two vortices and their corresponding LCS, or until fluid had ceased to exit the nozzle.

The FTLE field is not an instantaneous measure of fluid particle separation, but rather an indication of the divergence of nearby trajectories over the integration time T. As a result, Haller (2002) has shown that LCS are robust to local anomalies in the velocity field, or short-lived features which have little or no effect on the overall flow. The observed appearances of new repelling LCS were therefore robust indicators of a physical change in the underlying vortex structures, as also found by Green *et al.* (2010). The appearance of a new repelling LCS and termination of an existing one was the result of the separation of two distinct regions of vorticity-carrying fluid, which resulted in the formation of regions with separate dynamics. The merger of two repelling LCS into a single coherent structure, on the other hand, was indicative of the merger of two regions of vorticity into a single vortex.

2.6 Comparison with other criteria

Figure 2.3(b) shows a contour plot of the vorticity field at the initiation of pinch-off ($\hat{T} = 4.1$). Although the vortex ring ceased to accept vorticity at this time, it had not yet advected away from its trailing shear layer. A clear separation between vorticity contours of ring and wake was not evident until more than 4 formation time units later (figure 2.3(c)), and hence vorticity contours alone were insufficient to identify the initiation of pinch-off.

The vorticity field, however, can be integrated to obtain the circulation and apply the criterion of Gharib *et al.* (1998). Using this criterion, Krueger *et al.* (2006), Dabiri & Gharib (2004*a*), and others (Jeon & Gharib, 2004; Milano & Gharib, 2005; Ringuette *et al.*,

2007) were able to determine the formation number for a variety of flow configurations. As discussed previously in §2.4, our results are in excellent agreement with the circulation method proposed by Gharib *et al.* (1998). Moreover, unlike the circulation criterion of Gharib *et al.* (1998), the current Lagrangian method is 'instantaneous': the initiation of pinch-off was evident from the forward FTLE field corresponding to the instant when it occurred. This does not imply, however, that the need for recording data past pinch-off is eliminated, but knowledge of only the velocity field is required. This is of particular relevance in many real flows of biological interest, where the vorticity field breaks down and diffuses due to viscous effects (Bartol *et al.*, 2009), and criteria based on circulation prove difficult to use.

Like LCS, instantaneous streamlines can be derived from the velocity fields alone and have been previously used to approximately describe vortex ring flows (Stanaway *et al.*, 1988; Dabiri & Gharib, 2004*b*). Figure 2.11 shows the instantaneous streamlines of the flow, computed in the laboratory reference frame. We do not present the streamlines in the reference frame of the leading vortex ring, unlike Dabiri & Gharib (2004*b*), since the leading ring and trailing jet are known to translate with different velocities (Shusser & Gharib, 2000). Since all of the flow structures do not translate at the same speed, a Galilean transformation to the frame of reference of the vortex ring cannot be applied.

In figure 2.11, the streamline patterns before the initiation of pinch-off (2.11(a)), as pinch-off is initiated (2.11(b)), and after the completion of the pinch-off process (2.11(a)), are at formation times of $\hat{T} = 2.2, 4.1$ and 8.7, respectively. There is no salient feature in figure 2.11(b) to indicate the initiation of pinch-off, and moreover there are no significant qualitative differences between the streamline patterns in figures 2.11(a) through (c).

A variety of Lagrangian metrics also yielded relatively little insight into the dynamics of

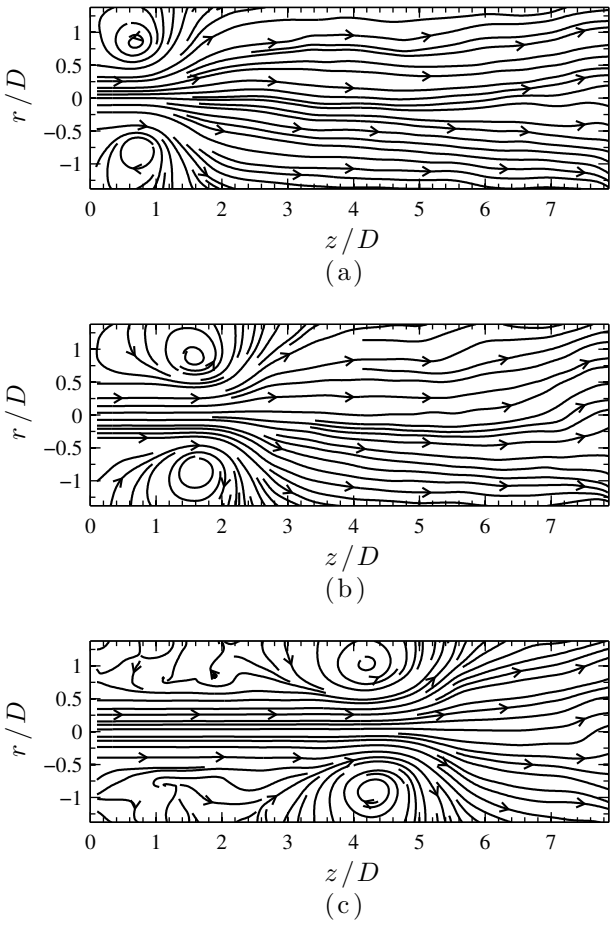

Figure 2.11: Instantaneous streamlines in the laboratory reference frame at: (a) $\hat{T} = 2.2$, (b) $\hat{T} = 4.1$ and (c) $\hat{T} = 8.7$.

pinch-off. Figure 2.12 shows the paths traced by twenty particles released at the nozzle exit plane as the jet was initiated. Figures 2.12(a) through (c) show the pathlines before pinch-off, at the onset of pinch-off, and after pinch-off, respectively. Figure 2.13 shows streaklines starting at ten different locations on the nozzle exit plane before (2.13(a)), at the onset of (2.13(b)), and after pinch-off (2.13(c)). Finally, figure 2.14 shows the timelines of the flow at points before (2.14(a)), at the initiation of (2.14(b)), and after pinch-off (2.14(c)). There are no salient features in figures 2.12(b), 2.13(b) and 2.14(b), to reveal that the pinch-off process has been initiated. Moreover, careful comparison of the three parts in each figure does not suggest that either pathlines, streaklines, or timelines give insight into the pinch-off process.

While none of these Lagrangian metrics were particularly effective at identifying pinch-off, LCS are provide effective tool because they are a quantitative indicator of *relative* Lagrangian trajectories over time. Repelling LCS identify regions of high particle separation and act as separatrices between regions of qualitatively different flow (Shadden *et al.*, 2006; Haller, 2002), and are thus suited for identifying the separation of different regions of vorticity-carrying flow that occurs during pinch-off. Furthermore, instantaneous streamlines, like streaklines and other Lagrangian metrics, are frame-dependent and thus not suited for robust identification of the vortex structure in unsteady flows (Shadden *et al.*, 2006; Mathur *et al.*, 2007). In these cases, robust vortex identification requires knowledge of the time history of the motion (Lugt, 1995), information that is built into the definition of the frame-independent FTLE.

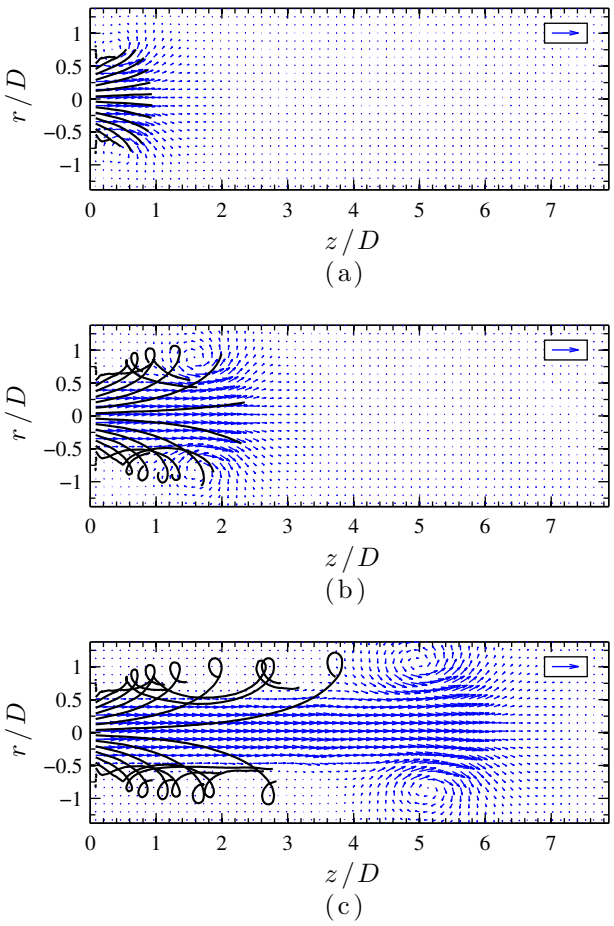

Figure 2.12: Pathlines for twenty particles released at $\hat{T} = 0$, at : (a) $\hat{T} = 1.5$, (b) $\hat{T} = 4.1$ and (c) $\hat{T} = 10.0$. The velocity vector field is shown in the background for reference. The boxed arrows represent a speed of 4 nozzle diameters per second (D/s)

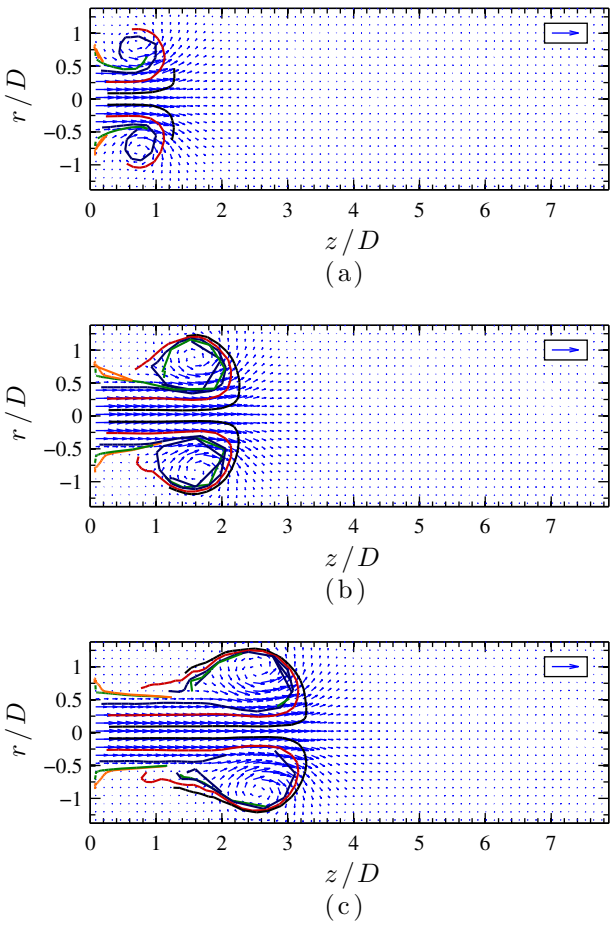

Figure 2.13: Streaklines originating a ten different points on the nozzle exit plane, at: (a) $\hat{T} = 2.2$, (b) $\hat{T} = 4.1$ and (c) $\hat{T} = 5.9$. The velocity vector field is shown in the background for reference. The boxed arrows represent a speed of 4 nozzle diameters per second (D/s)

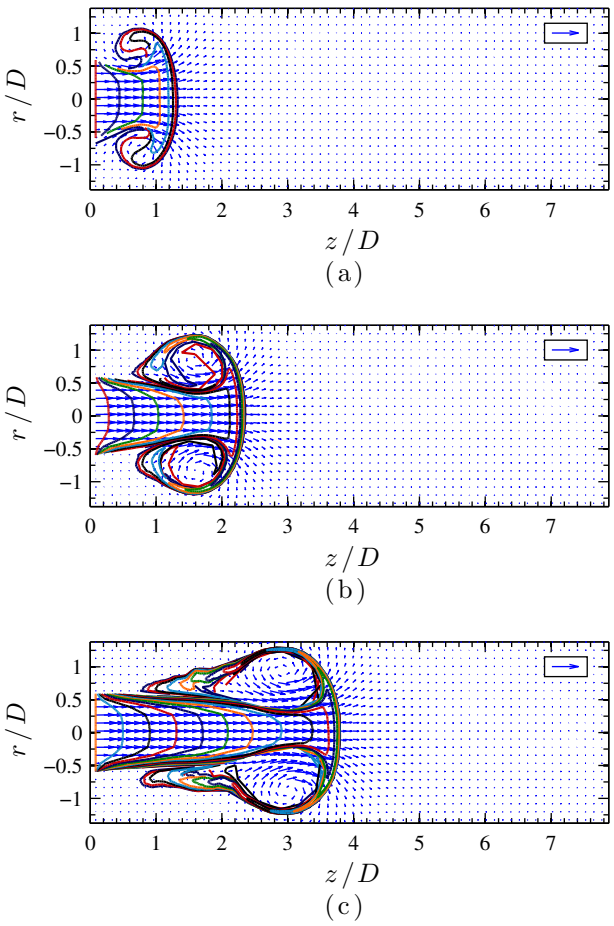

Figure 2.14: Timelines at: (a) $\hat{T} = 2.2$, (b) $\hat{T} = 4.1$ and (c) $\hat{T} = 6.6$. The velocity vector field is shown in the background for reference. The boxed arrows represent a speed of 4 nozzle diameters per second (D/s)

2.7 Conclusions

A Lagrangian criterion for identifying vortex ring pinch-off in jet flow was proposed, and demonstrated on a starting jet with a stroke ratio of twelve. The appearance of a new repelling LCS, disconnected from the original one, and the subsequent termination of the original repelling LCS, was found to coincide with the initiation of pinch-off. The new repelling LCS were found to either roll up into spirals, indicating the appearance of persistent vortices, or merge with the preceding LCS, indicating the merger of vortices in the shear layer. Hence, the appearance of a new repelling LCS was found to be indicative of the initiation of vortex pinch-off and used to determine the formation number. Results obtained using the LCS criterion were compared to those obtained using the circulation criterion of Gharib *et al.* (1998), and were found to be in good agreement.

Furthermore, whereas Gharib *et al.* (1998) and others using similar methods have recorded and identified the merging of the detached vortex ring with the first vortex in its trailing wake, the repelling LCS revealed a consistent pattern of vortex pairing that extends beyond these first and second vortices. This continuous vortex pairing pattern has been identified as a recurrent feature in turbulent circular jets by various hot wire studies (Petersen, 1978; Hussain & Zaman, 1980; Yule, 1978), yet it is difficult to observe from the velocity and vorticity fields alone. The LCS, on the other hand, allowed for clear identification of the pairing process from DPIV data.

Other pinch-off identification criteria, both Eulerian (vorticity contours, instantaneous streamline patterns) and Lagrangian (pathlines, streaklines and timelines) were considered, but found to yield little or no insight into the dynamics of pinch-off. The proposed LCS criterion therefore proved a superior identifier of pinch-off for the flow considered. Further,

because the proposed LCS criterion is frame-independent, independent of velocity derivatives, and robust to anomalies in the velocity field, it has the potential to prove a robust identifier of pinch-off in a wide variety of flows.

In particular, the proposed LCS criterion may prove to be a more suitable tool for characterizing unsteady and low Reynolds number biological flows, such as those generated by jetting swimmers (Dabiri & Gharib, 2005*b*; Bartol *et al.*, 2009) or in the human heart (Gharib *et al.*, 2006; Hendabadi *et al.*, 2012). Future work focused on applying the proposed criterion to such flows, should determine the suitability of the criterion and its robustness.

The proposed Lagrangian approach to vortex pinch-off is of particular interest in conjunction with the concept of 'optimal' vortex formation introduced in §1.3. This question has been previously addressed (Linden & Turner, 2004; Gharib *et al.*, 2006; Bartol *et al.*, 2009; Dabiri *et al.*, 2006; Dabiri & Gharib, 2005*a*), but the proposed LCS analysis has the potential to provide a more robust pinch-off identification criterion to aid in future studies of optimal vortex formation in more complex biological flows. Additionally, proposed LCS criterion could prove useful in assessing and understanding the performance of bio-inspired and biomimetic underwater vehicles which incorporate pulsed jets.

Finally, it must be noted that although the LCS criterion is 'instantaneous' in the sense that the LCS signature of the pinch-off process is evident at the initiation of pinch-off, it does not eliminate the need for recording forward-time data past pinch-off. Computing the forward-time FTLE field requires integrating particle trajectories in forward time, and thus requires recording the velocity field after pinch-off. However, the LCS criterion is dependent only on the forward-time velocity field, whereas criteria based on vortex circulation rely on the vorticity field. So although the need for forward-time data persists, the LCS metric eliminates the dependence on velocity derivatives, which become increasingly noisy during

vortex breakdown.

Although this criterion provides a useful tool for identifying pinch-off in starting and pulsed jets, the criterion is diagnostic and not predictive. While such criteria are useful in uncovering the kinematics of the flow, they provide little insight into the dynamics of the pinch-off process, and hence do not shed light on the underlying physical principles. However, understanding these dynamics is key in predicting pinch-off. Therefore, in the chapters that follow we examine the dynamics of pinch-off. Since most most naturally occurring vortex rings are not circular, and the pinch-off of these types of vortices has not been characterized in the past, we consider the formation of non-axisymmetric vortex rings in the following chapter.

The material in this chapter was published in O'Farrell C and Dabiri JO (2010) "A Lagrangian approach to identifying vortex pinch-off," *Chaos* **20**: 017513.

Chapter 3

Pinch-off of non-axisymmetric vortex rings

3.1 Introduction

The robust occurrence of pinch-off in axisymmetric jet flows has been demonstrated in a number of configurations (Gharib *et al.*, 1998; Dabiri & Gharib, 2005*b*; Krueger *et al.*, 2006). However, naturally occurring vortices are rarely circular, and axisymmetric flows, such as those generated by squid or jellyfish, are scarce in nature. In fact, most swimming and flying animals generate elongated loop-like vortices rather than circular vortex rings (Kokshaysky, 1979; Rayner, 1979; Dickinson & Götz, 1996; Kern & Koumoutsakos, 2006; Kim & Gharib, 2011). For example, nearly elliptical vortices have been observed in the wakes of flying birds (Kokshaysky, 1979), chains of elongated loop-like vortices have been found in the wakes of an anguilliform swimmer by Kern & Koumoutsakos (2006), and Dickinson & Götz (1996) found that fruit flies generate deformed vortex rings during flight. Similarly, the mitral valve in humans is not axisymmetric, so circular vortex rings do not describe the flow in the human left ventricle with complete accuracy (Domenichini *et al.*, 2005; Bellhouse, 1972; Reul *et al.*, 1981; Wieting & Stripling, 1984) .

The departure from axisymmetry of most vortex rings of biological relevance is of im-

port because the limit on vortex ring growth imposed by the Kelvin-Benjamin principle has only been shown to apply to axisymmetric jetting flows. Benjamin (1976)'s proof of Kelvin's argument relies on the the assumption of axisymmetry. In other, non-axisymmetric, vortex-shedding configurations, no limit on the growth or size of vortices is known. In the case of vortex formation from two-dimensional orifices, for example, recent experimental (Afanasyev, 2006) and computational (Pedrizzetti, 2010) results suggest that there is no limit on the growth of a vortex dipole.

In this regard, the work of Domenichini (2011) is of particular interest. Domenichini (2011) studied the formation of vortices from slender orifices whose outline consisted of two semicircular portions connected by two rectilinear segments of varying length (figure 3.1). In his computations, the author found that the roll-up of the shear layer and vortex formation process on the circular and rectilinear segments differed considerably. In particular, for nozzles with rectilinear segments of sufficient length, he found evidence of pinch-off at the center of the circular portions at a non-dimensional time consistent with the work of Gharib *et al.* (1998), but no evidence of pinch-off at the center of the rectilinear portions. The author ascribed these differences to the dependence on local curvature of the self-induced velocity of the lead vortex ring (Saffman, 1992; Leonard, 1985; Hussain & Husain, 1989), which caused the portions of the vortex closest to the circular sides of the slender orifices to move away from the shear layer faster than the portions near the rectilinear sides. Hence, Domenichini (2011) concluded that pinch-off in these non-axisymmetric vortex rings can be a local phenomenon, determined by local curvature.

In his concluding remarks, Domenichini (2011) theorized that his findings could, with small modifications, extend to other non-axisymmetric geometries in general, and elliptical vortex rings in particular. However, while the behavior of isolated non-circular vortex rings

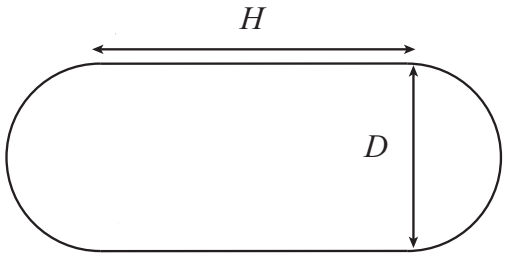

Figure 3.1: Schematic of Domenichini's slender orifices. The orifices consisted of two semi-circular segments of diameter D connected by rectilinear segments of length H. The ratio of the length of the flat segment to the diameter of the circular segment ($h = H/D$) was varied in order to consider increasingly slender orifices.

and of non-axisymmetric jets have been the subject of extensive study, the vortex formation process for non-axisymmetric rings has not been studied in detail. Hence, Domenichini's conjecture remains untested.

The evolution of isolated vortex rings of non-circular shape has been examined in a variety of computational, analytical, and experimental investigations. In particular, the behavior of elliptical vortex rings is well documented, mostly through computational studies which make use of the localized induction equation of Arms & Hama (1965) (Viets & Sforza, 1972; Kimura, 2006), the Rosenhead-Moore approximation (Dhanak & de Bernardinis, 1981), or other vortex filament methods (Fernandez *et al.*, 1995; Ryu & Lee, 1997). These simulations are complemented by a number of experiments, including smoke and dye visualizations (Viets & Sforza, 1972; Dhanak & de Bernardinis, 1981; Hussain & Husain, 1989; Hussain & Hussain, 1991), hot wire studies (Oshima *et al.*, 1988), and particle image velocimetry measurements (Adhikari, 2009). The bulk of these studies focused on the time-dependent deformation of the elliptical vortex ring due to the curvature-dependence of the vortex propagation velocity (Arms & Hama, 1965; Dhanak & de Bernardinis, 1981; Viets & Sforza, 1972). Similar experimental and numerical methods have been applied in studies

of the deformation of isolated vortex rings with other non-circular geometries, including those with initially rectangular (Viets & Sforza, 1972; Grinstein, 1995; Kambe & Takao, 1971) and lenticular (Kambe & Takao, 1971; Oshima, 1972) shapes. Viets & Sforza (1972) considered the evolution of a vortex ring whose initial shape was described by a superellipse or Lamé curve. It is interesting to note that Kiya & Ishii (1991) and Kiya *et al.* (1992) characterized the deformation of isolated 'pseudo-elliptic' vortex rings of a shape identical to those considered by Domenichini (2011).

Considerable attention has also been devoted to the study of non-circular free jets, much of it motivated by their favorable mixing properties and reduced jet noise when compared to circular jets (Gutmark & Grinstein, 1999; Ho & Gutmark, 1987; Ahuja *et al.*, 1990). Since the dynamics of the non-circular vortex rings in these jets are thought to be the driving force behind these beneficial properties, numerous studies on non-circular jets have focused on the dynamics of the vortex rings in the jet. In particular, Husain and Hussain (Hussain & Husain, 1989; Hussain & Hussain, 1991; Husain & Hussain, 1993) conducted a comprehensive study of the dynamics of vortex rings in elliptic jets. A similarly detailed treatment of the dynamics of vortex rings in rectangular jets is found in the works of Grinstein, Gutmark and others (Grinstein, 2001; Grinstein *et al.*, 1995; Gutmark & Grinstein, 1999).

Except for the work of Adhikari (2009), however, all of the above studies focused on either isolated vortex rings at low stroke ratios, or on the dynamics of vortices in a steady jet. Adhikari (2009) considered the effect of increasing stroke length on the formation of elliptical vortex rings, and compared the interaction of the growing vortex ring with its trailing shear layer to the dynamics and pairing of vortex rings in elliptic jets as described in Husain and Hussain's work (Hussain & Husain, 1989; Hussain & Hussain, 1991; Husain

& Hussain, 1993). In addition to many excellent dye visualizations of elliptical vortex rings at different stroke ratios, Adhikari (2009) conducted the only experimental study of non-circular vortex rings using DPIV to date. However, the author did not address the existence of any limits on the size of the vortex ring, nor did he compute a formation number analogous to that of Gharib *et al.* (1998) or consider the dependence of the vortex formation on curvature. As a result, the relationship of Adhikari (2009)'s vortex rings to Domenichini's conjecture remains unknown.

This chapter describes investigations into the formation of non-axisymmetric vortex rings at long stroke ratios, and into the effect of curvature on the vortex formation process and on the maximum size of the vortex ring. This study bridges the gap in our current understanding of non-circular vortex rings, by considering the intermediate states lying between isolated non-axisymmetric vortex rings, and steady non-circular jets. In particular, we tested Domenichini's hypothesis in a wider class of non-circular vortex rings, in order to determine what role local and global parameters play in the onset of pinch-off in non-circular starting jets. Ultimately, the goal of this study was to define an analogue to the formation number of Gharib *et al.* (1998), for the development of vortex rings with moderate departure from axisymmetry of relevance to biological flows. To this end, we conducted an experimental study of the formation of vortex rings from three non-circular nozzles: two elliptical nozzles with aspect ratios of two and four, respectively, and an oval nozzle constructed from two pairs of tangent circular arcs.

In addition to classical Eulerian techniques, we visualized the non-circular vortices by means of the Lagrangian coherent structures (LCS) in the flow. LCS were introduced in the preceding chapter, and are finite-time analogues to the stable and unstable manifolds, for systems with arbitrary time dependence. These structures have been employed for structure

identification and for investigating vortex dynamics in the preceding chapter, as well as by Shadden *et al.* (2006, 2007), Green *et al.* (2007, 2010), and others.

The results of the Eulerian and Lagrangian analyses suggested that, for vortex rings with a moderate deviation from axisymmetry such as those found in biological flows, global parameters dominate the formation process. Hence, a non-dimensional critical formation time, or formation number, for this class of vortex rings was defined based on the equivalent diameter of the nozzle (the diameter of a circular nozzle with equivalent cross-sectional area).

This chapter is organized as follows. In §3.2 we describe the experimental setup and methods utilized to collect planar velocity data on the non-circular nozzles, as well as the numerical methods used to compute the LCS. The formation and later deformation of the vortex rings are described in §3.3 and §3.4, from the Eulerian and Lagrangian perspectives, respectively. The effect of curvature on the growth and limiting formation number of non-axisymmetric rings is examined in §3.5. Finally, a comparison of our results with those of Domenichini (2011), and their implications to the study of biologically relevant vortex flows are considered in §3.6.

3.2 Methods

3.2.1 Experimental methods

We considered the formation of non-axisymmetric vortex rings from three nozzles of different cross sectional shape: an elliptical nozzle with an aspect-ratio of two, an elliptical nozzle with an aspect-ratio of four, and an oval nozzle constructed from four connected segments with constant, non-zero curvature. These nozzles will henceforth be referred to as the AR2 nozzle, the AR4 nozzle, and the oval nozzle, respectively. The three vortex generator devices

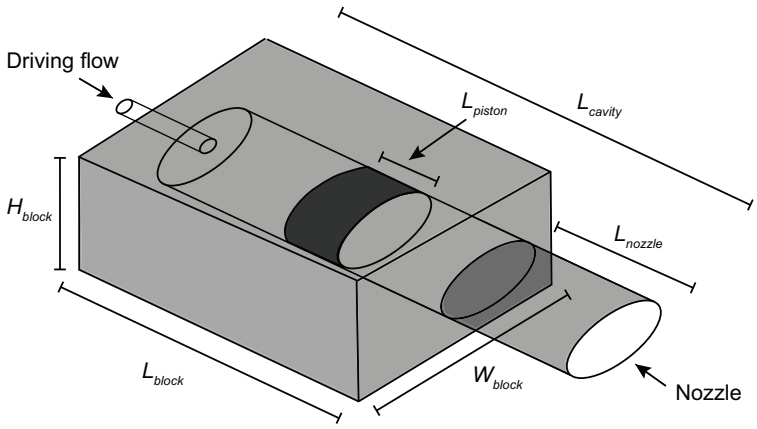

Figure 3.2: Vortex ring generator geometry. The vortex generator consisted of an acrylic block attached to a non-circular nozzle with one of three cross sectional shapes: an ellipse with an aspect-ratio of two, an ellipse with an aspect-ratio of four, and an oval constructed from tangent circular segments of constant curvature.

Dimension	AR2 ellipse	AR4 ellipse	Oval nozzle
L_{block}	19.05	19.05	24.13
W_{block}	12.7	12.7	12.7
H_{block}	5.1	5.1	5.1
L_{nozzle}	8.89	8.89	8.89
L_{piston}	2.54	2.54	2.54
L_{cavity}	25.4	25.4	30.48

Table 3.1: Key dimensions (in cm) of the vortex generators with different nozzle geometries.

consisted of an acrylic block culminating in a sharp-edged nozzle with a cross section in one of the three aforementioned shapes (figure 3.2). A hollow cavity with the same cross sectional shape as the nozzle ran the length of the device, and an identically-shaped piston was allowed to slide freely along the cavity. Table 3.1 shows the key dimensions of the three vortex generators with different nozzle geometry.

A summary of the geometrical properties of the three nozzle shapes considered is given

Nozzle shape	D_{eq} (cm)	κ_{min} (cm^{-1})	κ_{max} (cm^{-1})	Max. piston stroke (cm)
AR2 ellipse	4.45	0.16	1.26	21.6
AR4 ellipse	4.45	0.06	3.6	21.6
Oval	3.62	0.33	1.31	26.4

Table 3.2: Shape and dimensions of the three non-axisymmetric nozzle shapes considered.

in table 3.2. The three nozzle shapes were selected to encompass a wide class of those non-circular nozzles not considered by Domenichini (2011). In the two elliptical nozzles, the curvature varied continuously from it minimum value at the minor axis of the ellipse, to its maximum value at the major axis. However, the range of curvatures was much larger in the AR4 nozzle, than in the AR2 nozzle ($\kappa_{max}/\kappa_{min} \approx 60$ and ≈ 8, respectively). This allowed us to asses the relative importance of local curvature and global parameters to pinch-off, and to ascertain whether large variations in curvature were required to produce the spatially varying results reported by Domenichini (2011).

However, the nozzles considered by Domenichini (2011) did not exhibit a smooth variation in the curvature, but rather they contained discontinuities in their curvature where the straight segments met the circular segments. Furthermore, the curvature on the rectilinear segments of Domenichini's nozzles was zero, while the elliptical nozzles described above did not include regions of zero curvature. In order to ascertain whether discontinuities in curvature are required to produce the spatially varying pinch-off observed by Domenichini (2011), we constructed an oval nozzle from the intersection of two pairs of circular segments with distinct curvature, which resulted in discontinuities in the curvature at the intersections of the segments.

The vortex generators were submerged in a water tank, and vortex rings were generated using an arrangement similar to that described by Dabiri & Gharib (2004*b*). Figure 3.3 shows a schematic of the experimental setup. Flow from a constant-head tank, delivered by a computer-controlled solenoid valve, was allowed to drive the piston forward in its cavity. A column of fluid of was impulsively ejected from the sharp-edged nozzle by the motion of the piston, and rolled up into a vortex ring which propagated through the surrounding fluid owing to its self-induced velocity.

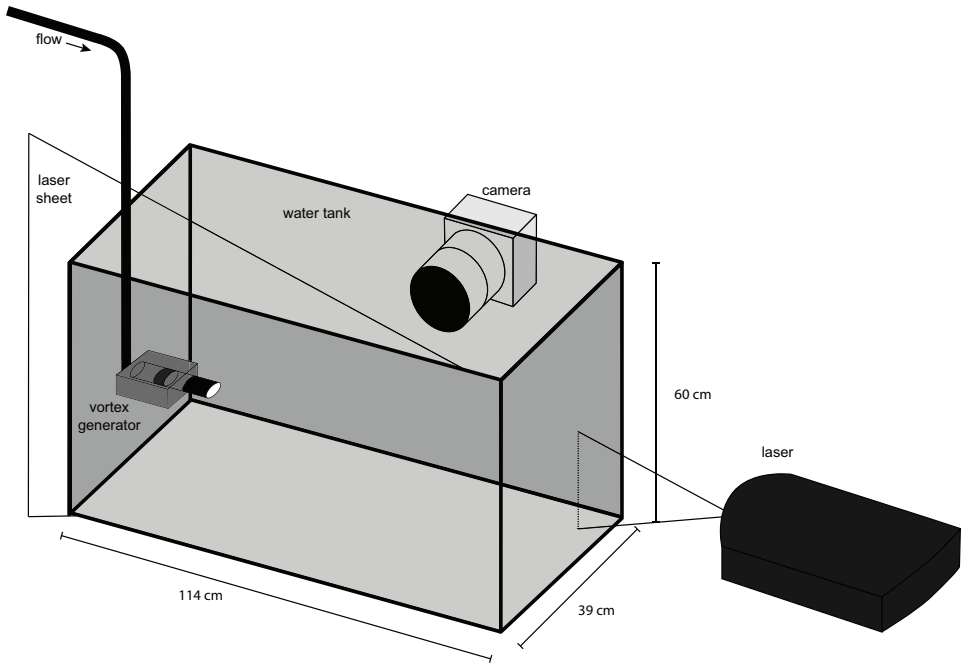

Figure 3.3: Schematic of the vortex ring generator setup.

The resulting velocity field was mapped using two-component, planar digital particle image velocimetry (DPIV) (Willert & Gharib, 1991; Adrian, 1991). A pulsed Nd:YAG laser sheet was used to illuminate a plane through the non-axisymmetric nozzle, and the flow was seeded with $13\mu m$ neutrally-buoyant glass spheres. Light from the incident laser sheet was scattered by the glass spheres onto a CCD camera whose image plane was positioned parallel to the laser sheet. The test section measured approximately 18 cm $\times$ 18 cm, and the resolution of the captured images was approximately 0.18×0.18 mm^2. The resulting images were interrogated using cross-correlation, with a separation between images of 33 ms, and an interrogation window size of 32×32 pixels with a 50% overlap. The velocity and vorticity fields were calculated using an in-house code, and the resolution for both was approximately 3×3 mm^2 with an uncertainty of 1% and 3%, respectively.

The first of the non-axisymmetric nozzles considered had a cross section in the shape of an ellipse with an aspect-ratio of two. The nozzle measured 6.35 cm at the major axis,

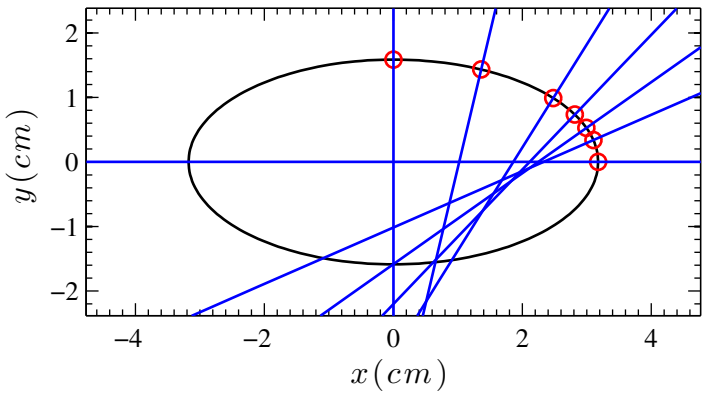

Figure 3.4: Data-collection points along the edge of the AR2 nozzle. The nozzle outline is shown in black, and seven data-collection points spanning the range of available curvatures are shown in red. The corresponding DPIV planes are denoted by the blue lines.

and 3.17 cm at the minor axis, and its equivalent diameter ($D_{eq} = \sqrt{\frac{4\times\text{Area}}{\pi}}$) was 4.45 cm. The local curvature along the nozzle contour varied from a minimum of $\kappa = 0.16$ cm^{-1} at the minor axis, through a maximum of $\kappa = 1.26$ cm^{-1} at the major axis. To determine the effect of local curvature on vortex formation, we recorded the velocity field at seven locations between the major and minor axes. Figure 3.4 shows the outline of the nozzle with the AR2 elliptical cross section, as well as the location of the seven data-collection points along the nozzle edge, which spanned the entire range of available curvature values.

At each curvature point, the vortex generator was oriented such that the laser sheet was locally normal to the nozzle edge, so as to minimize out-of-plane motions. The precise alignment of the laser sheet and nozzle at each curvature point was achieved by constructing a device that secured the vortex generator at a set of pre-defined angles. The mounting device consisted of a three-sided box, with slots etched into the inside of the two opposing faces of the box (the side-walls). The box sat on the bottom of the tank on its bottom plate, and acrylic plates could be fitted into the two sets of slots to complete the front and back walls of the open-top box (see figure 3.5). The acrylic plates were laser-cut to hold the

rectangular portion of the vortex generator at a specific angle, and could be interchanged to achieve each of the pre-set angles precisely. The laser sheet and camera were aligned with the mounting box at the start of the experiment, and remained stationary throughout data collection. Since the main body of all three vortex generators consisted of a rectangular block with the same dimensions, the design of the mounting box allowed us to conduct experiments on the second and third nozzles using the same setup.

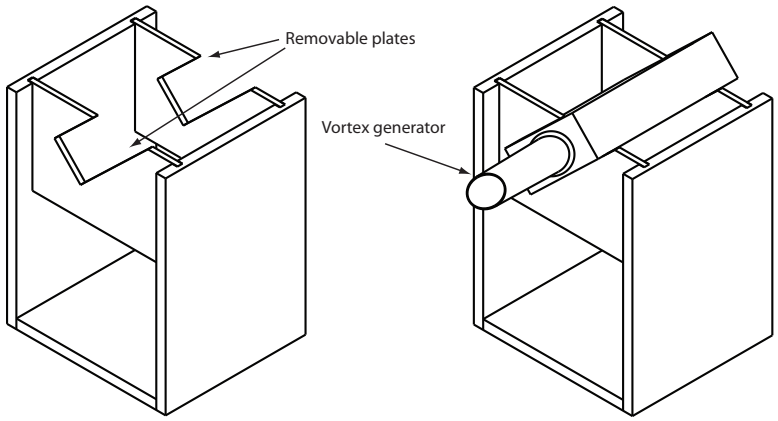

Figure 3.5: Vortex generator mounting box. Pairs of acrylic plates slid into slots on the sides of the mounting box. The plates were designed to hold the vortex generator at several pre-defined angles, to collect data at different curvature values and ensure proper alignment of the laser sheet and camera.

The second nozzle had an elliptical cross section of the same equivalent diameter as the AR2 nozzle, but with an aspect-ratio of four. This nozzle, which is referred to as the AR4 nozzle, measured 8.89 cm at the major axis, and 2.22 cm at the minor axis. In this case, the curvature ranged from $\kappa = 0.06$ cm^{-1} on the minor axis, to $\kappa = 3.6$ cm^{-1} on the major axis. Since this nozzle spanned a much larger range of curvatures than the AR2 nozzle, the deformation of the elliptical vortex ring was more pronounced in this case. As a result, we were only able to collect data on planes aligned with the major and minor axes of the ellipse, since the deformation was symmetric about these two planes. The increased range of curvatures is evident in figure 3.6, which shows the outline of the AR4 nozzle.

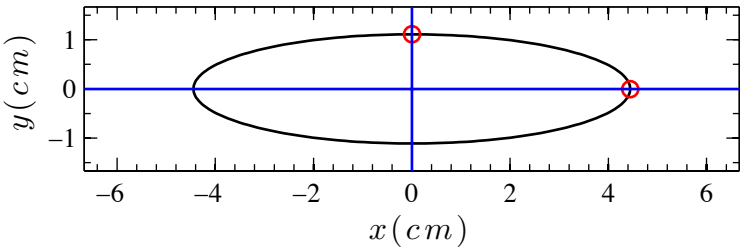

Figure 3.6: Data-collection points along the edge of the AR4 nozzle. The nozzle outline is shown in black, and the two data-collection points on the major and minor axes are shown in red. The corresponding DPIV planes are denoted by the blue lines.

Finally, we considered a third nozzle with a non-circular cross section. However, rather than having an elliptical cross section where the curvature varied smoothly, the third nozzle nozzle was constructed from segments with one of two distinct, non-zero, curvature values. Figure 3.7 shows the outline of this oval nozzle, which was constructed from two pairs of tangent circular arcs. On the two segments nearest the x-axis, the curvature of the nozzle was $\kappa = 1.31$ cm^{-1}, whereas the curvature on the remaining two segments was $\kappa = 0.33$ cm^{-1}. The four circular segments were tangent at their intersection, but there was a discontinuity in the local curvature at the four intersection points. This oval nozzle had an equivalent diameter of $D_{eq} = 3.62$ cm. DPIV measurements were only conducted at the two symmetry axes of the nozzle, which corresponded to the midpoints of the constant curvature segments (the x- and y- axes).

The coordinate system for all experiments was defined relative to the nozzles as follows: the z-axis was parallel to the direction of fluid ejection, and set to coincide with the nozzle centerline, with the nozzle exit plane located at the plane $z = 0$. The x-axis was aligned with the major axis of the nozzle, and the y-axis coincided with the minor axis of the nozzle. In all three cases, experiments were conducted at a Reynolds number based on the piston speed and equivalent diameter of the nozzle ($Re = \overline{U}_p D_{eq}/\nu$) of approximately 2000, and a

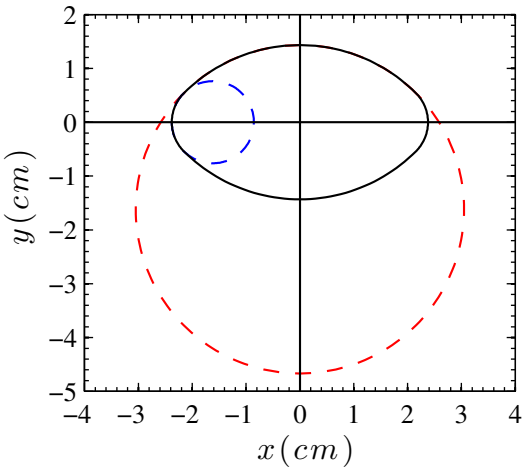

Figure 3.7: Cross section of the oval nozzle. The two sections closest to the x-axis are tangent to a circle of radius $R = 0.8$ cm (– –), and the two sections nearest to the y-axis are tangent to a circle of radius $R = 3.1$ cm (– –)

Reynolds number based on vortex ring circulation (Γ_{ring}/ν) between 3000 and 4000.

3.2.2 Lagrangian coherent structures

We identified the LCS on each data-plane, from the recorded planar velocity data, using the method described in §2.3. The FTLE field was computed on a Cartesian grid with a resolution of 0.6×0.6 mm, using *Newman* (Du Toit, 2010). At each time t, each point on the grid was advected by the flow by numerically integrating the velocity field data for the integration time T. A fourth-order Runge-Kutta scheme was used for the numerical integration, and bilinear interpolation was used whenever interpolation of the velocity data was required. T was chosen to be ± 3.3 s ($\overline{U}_p T/D_{eq} = \pm 4$ for the elliptical nozzles, and ± 5 for the oval nozzle), since this integration time was found to yield the complete boundary of the vortex, while remaining practical in terms of computational expense.

3.3 Eulerian analysis

3.3.1 AR2 elliptical nozzle

We recorded the velocity field at seven locations along the edge of the AR2 nozzle, where the local curvature was $\kappa = 1.26$ cm^{-1} (major axis), 1.04 cm^{-1}, 0.82 cm^{-1}, 0.60 cm^{-1}, 0.39 cm^{-1}, 0.20 cm^{-1}, and 0.16 cm^{-1} (minor axis). In order to investigate the separation of the leading vortex ring from its trailing shear layer, experiments were conducted at the longest piston stroke length possible (21.6 cm). In accordance with Hussain and Husain's finding that the equivalent diameter is a proper choice of length scale in elliptic jets with moderate aspect-ratio (Hussain & Husain, 1989), distances were normalized by D_{eq}, and time by $D_{eq}/\overline{U}_p$. The resulting stroke ratio in experiments conducted on this nozzle was $L/D_{eq} = 4.8$.

Figures 3.9 through 3.15 show contours of the out-of-plane vorticity ω at two time instants, for all seven curvature planes. Since the flow is symmetric about the major and minor planes of the nozzle, on these two planes we recorded nearly symmetric data corresponding to the two locations where the DPIV plane intersected the nozzle contour at right angles. The major axis symmetry plane is aligned with the x-z plane (figure 3.9) in our coordinate system, and the minor axis symmetry plane is aligned with the y-z plane (figure 3.15).

On the remaining planes, the flow was not symmetric, and the DPIV plane only intersected the nozzle contour at right angles at one location. In figures 3.10 through 3.14, results have been plotted in s-z coordinates, where s is the coordinate along the DPIV plane, in the direction normal to the direction of flow (the z-axis). The origin of the s-axis is located at the intersection of the DPIV plane and the major axis (see figure 3.8). Only

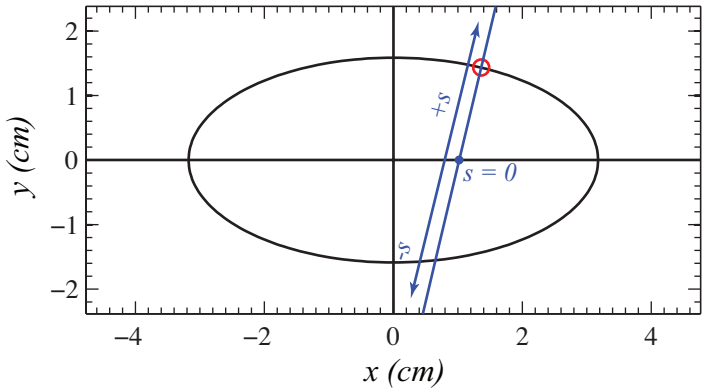

Figure 3.8: Coordinates in the oblique data planes.

the vorticity fields in the region where $s > 0$ where analyzed, since it is in these regions that the DPIV plane is correctly aligned with the nozzle.

Part (a) of figures 3.9 through 3.15 depict the growing elliptical vortex ring in its early stages of development, at $\hat{T} = \overline{U}_p t/D_{eq} = 1.6$. At this stage, the roll-up the shear layer was locally two-dimensional, on a plane normal to the nozzle edge (Domenichini, 2011). As a result, the vortex core cross section was roughly the same shape and size on all data planes, and had advected approximately $0.3D_{eq}$ downstream in all cases.

At later stages in the development of the elliptical vortex (part (b) of figures 3.9 through 3.15) however, significant differences were evident in the major and minor axes cross sections. Since the velocity induced by a vortex ring is a function of the local curvature (Saffman, 1992; Leonard, 1985; Hussain & Husain, 1989), the self-induced velocity of the elliptical vortex ring was greater at the major axis than at the minor axis. As a result, the vortex ring deformed. On the major axis, the vortex cores advected downstream faster than anywhere else on the nozzle contour, and the resulting deformation caused the cores to move towards each other along the direction parallel to the major axis of the elliptical nozzle (the x-axis, see figure 3.9(b)). In contrast, on the minor axis, the downstream velocity of

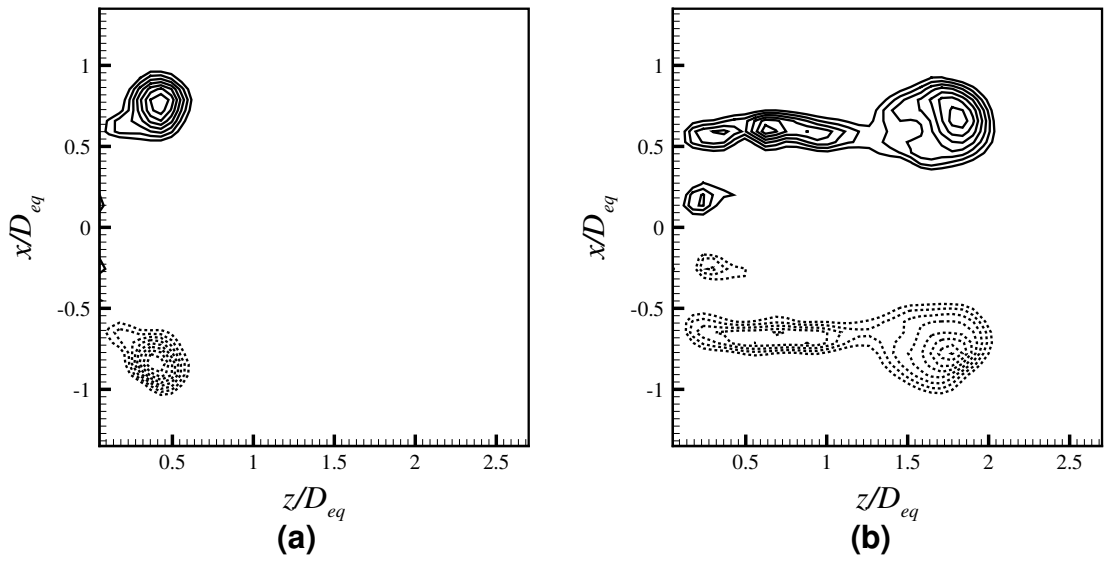

Figure 3.9: Contours of vorticity on the major axis of the AR2 nozzle at (a) $\hat{T} = 1.6$, and (b) $\hat{T} = 4.8$. Contour levels: min= 25% of ω_{max}, max= 95% of ω_{max}, increment= 10%. Flow is from left to right.

the vortex cores reached a minimum value which was lower than the jet velocity, causing the shear layer to curve around the front of the ring in order to feed into the vortex cores (figure 3.15(b)). On this plane, the deformation caused the cores to move away from each other along the y-axis. As a result, what was originally the minor axis became the major axis of the deformed vortex ring, the curvature trend was reversed, and the deformation process continued.

On the major and minor planes, the vorticity fields were qualitatively in good agreement with those reported by Adhikari (2009). Adhikari (2009) showed the evolution of the vorticity field only for stroke ratios of two and six. A stroke ratio of two resulted in the formation of only an isolated vortex ring, but at a stroke ratio of six, the geometry of the vortex ring and shear layer reported by Adhikari (2009) is qualitatively very similar to that shown in figures 3.9 and 3.15. On the remaining five planes, we can observe the gradual transition between the geometry at the major axis, and that at the minor axis.

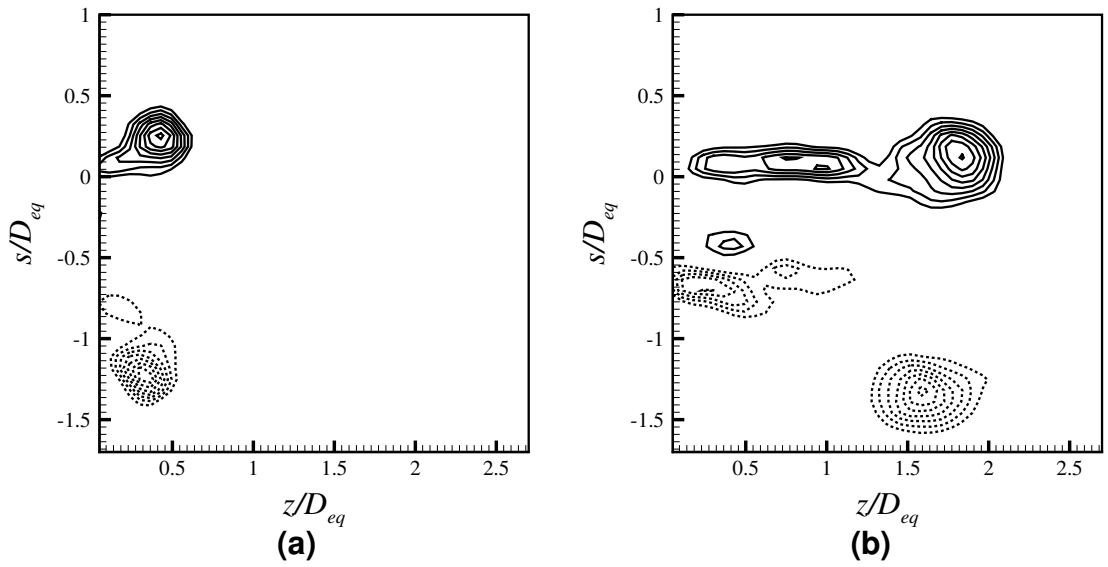

Figure 3.10: Contours of vorticity on the plane of the AR2 nozzle where $\kappa = 1.04$ cm^{-1} at (a) $\hat{T} = 1.6$, and (b) $\hat{T} = 4.8$. Contour levels: min= 25% of ω_{max}, max= 95% of ω_{max}, increment= 10%. Flow is from left to right.

The shape of the entire vortex ring can be appreciated by reconstructing the three-dimensional vorticity field from the planar vorticity data. In each of the seven data planes, the out-of-plane vorticity was assumed to dominate and was taken as an approximate measure of the total vorticity magnitude. Because the deformation of the vortex ring was symmetric about the x- and y-axes, we were able to reconstruct the deformed vortex ring from the approximate vorticity magnitude on the seven planes of available data. At each z-location, we interpolated the vorticity field onto a rectangular x-y grid from the data available along the seven data-planes. This was achieved by using MATLAB® (The MathWorks, Inc., Natick, MA) built-in functions to find the Delaunay triangulation of the available data points, using it to construct a surface of the form $\omega = f(x, y)$, and finally interpolating this surface at the points specified by our rectangular grid. By compiling the planar data at each z-location into a volume, we then obtained an approximate three-dimensional field of the magnitude of the vorticity.

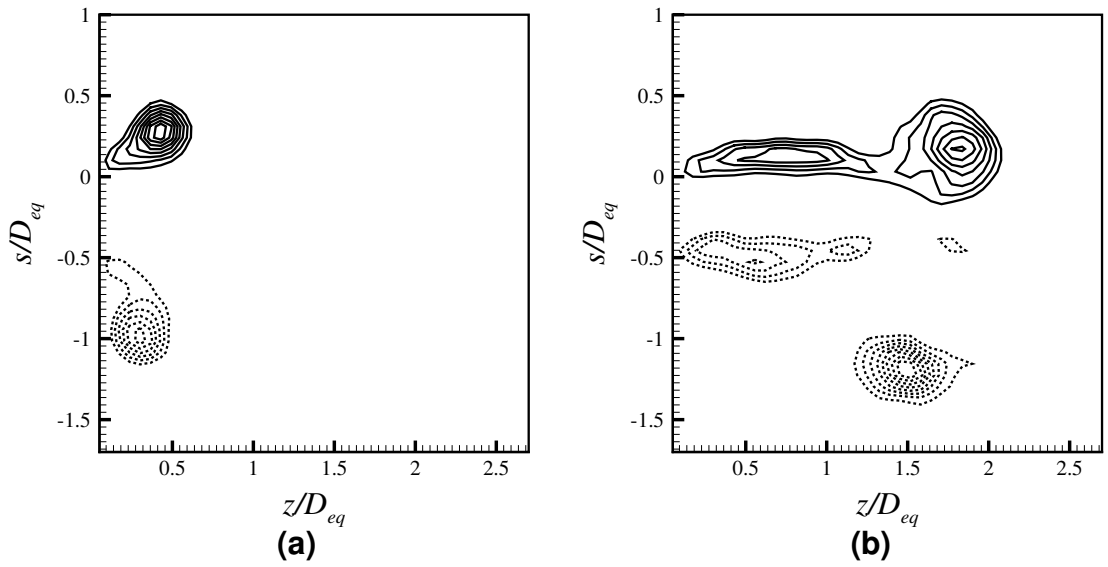

Figure 3.11: Contours of vorticity on the plane of the AR2 nozzle where $\kappa = 0.82$ cm^{-1} at (a) $\hat{T} = 1.6$, and (b) $\hat{T} = 4.8$. Contour levels: min= 25% of ω_{max}, max= 95% of ω_{max}, increment= 10%. Flow is from left to right.

Figure 3.16 shows iso-surfaces of constant vorticity magnitude for the reconstructed vorticity field at four separate time instants. Initially, the vortex shape closely resembled the nozzle shape, and the plane of the vortex ring was parallel to the nozzle exit plane, as shown in figure 3.16(a). However, at later stages (figures 3.16(c) and (d)) the vortex had deformed significantly, and the deformed vortex resembled the seam on a tennis ball (Hussain & Husain, 1989). The shape of the vortex ring obtained from iso-surfaces of the reconstructed vorticity was in excellent agreement with the dye visualizations of Adhikari (2009) for similar stroke ratios.

In addition to deformation of the vortex ring, the development of a trailing shear layer of significant length was observed on all planes by the termination of fluid ejection at $\hat{T} = 4.8$. The geometry of the vortex ring and shear layer bore qualitative resemblance to the geometry observed by Domenichini (2011).

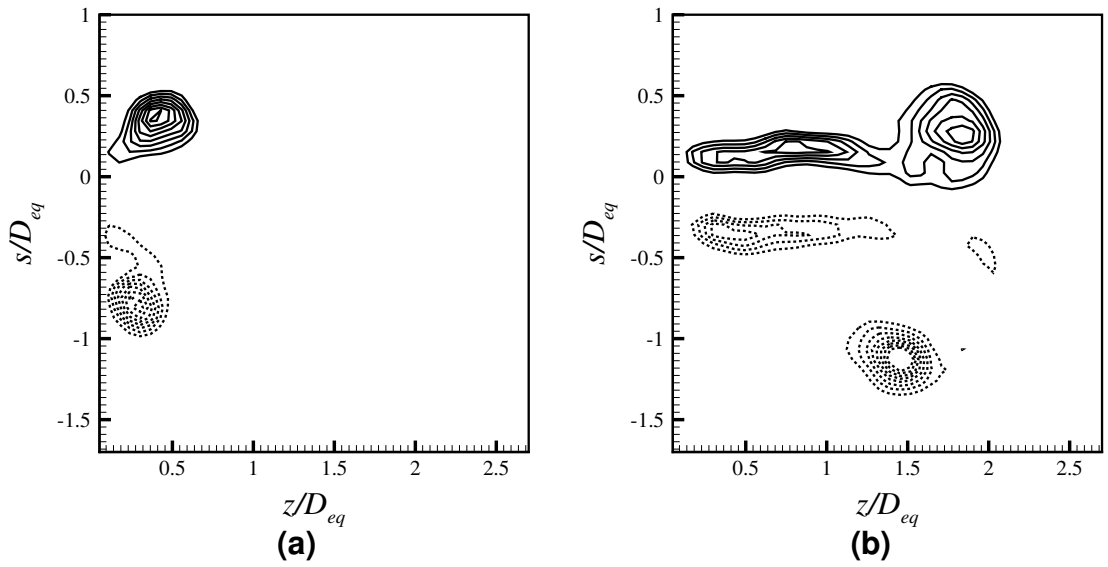

Figure 3.12: Contours of vorticity on the plane of the AR2 nozzle where $\kappa = 0.60$ cm^{-1} at (a) $\hat{T} = 1.6$, and (b) $\hat{T} = 4.8$. Contour levels: min= 25% of ω_{max}, max= 95% of ω_{max}, increment= 10%. Flow is from left to right.

3.3.2 AR4 elliptical nozzle

A second set of experiments was conducted on the AR4 elliptical nozzle, at the largest possible stroke ratio of $L/D_{eq} = 4.8$. The AR4 nozzle spanned a much larger range of curvatures than the AR2 nozzle: the curvature on the major axis was sixty times that on the minor axis. Figures 3.17 and 3.18 show contours of vorticity on the major and minor axes of the aspect-ratio four nozzle. Vorticity data is not available on curvature planes other than the two symmetry planes because the deformation of the elliptical vortex ring was more pronounced in this case, owing to the wide range of curvatures. As a result, we were only able to collect data on planes aligned with the major and minor axes of the ellipse, since the deformation was symmetric about these two planes. On other curvature data planes along the nozzle contour, we found that the vortex deformed so rapidly as to exit the DPIV plane before the lead vortex had pinched off. The severity of the deformation is in qualitative agreement with the results of Hussain & Husain (1989), who encountered

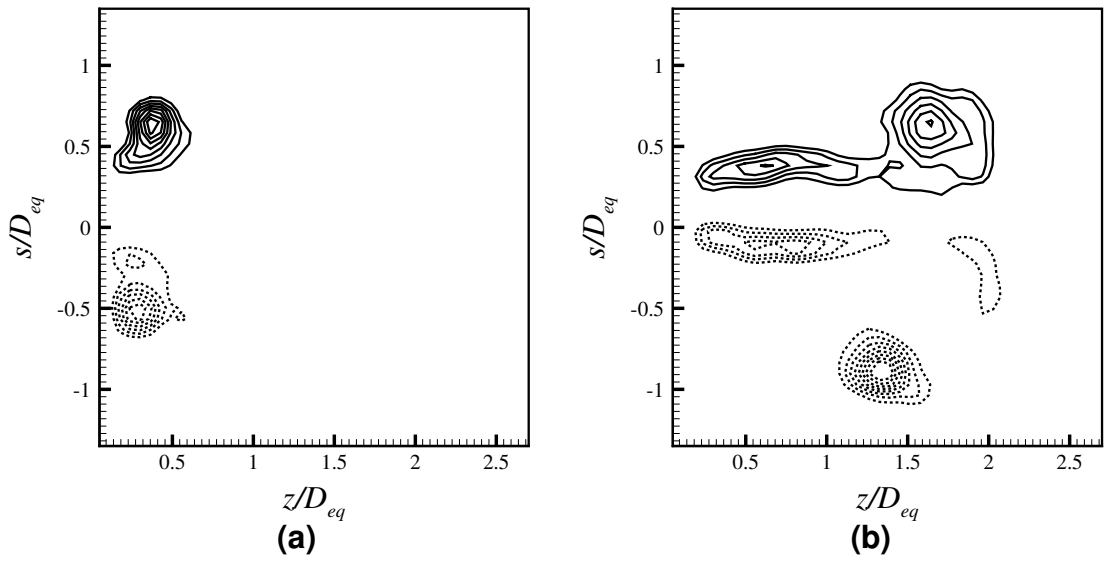

Figure 3.13: Contours of vorticity on the plane of the AR2 nozzle where $\kappa = 0.39$ cm^{-1} at (a) $\hat{T} = 1.6$, and (b) $\hat{T} = 4.8$. Contour levels: min= 25% of ω_{max}, max= 95% of ω_{max}, increment= 10%. Flow is from left to right.

similar effects when studying elliptic jets with aspect-ratios greater than approximately 3.5.

On the symmetry planes, however, the development of the vortex ring was qualitatively similar to that of the AR2 vortex ring shown in figures 3.9 and 3.15, although the deformation was much more pronounced in the AR4 ring. Figures 3.17(a) and 3.18(a) show the growing AR4 vortex ring in its early stages of development, at $\hat{T} = 1.6$. Even at this early stage, the deformation of the vortex ring was already evident, since the cores had translated approximately $0.5D_{eq}$ on the major axis, but only $0.25D_{eq}$ on the minor axis. At $\hat{T} = 4.8$, the displacement of the vortex cores towards the centerline of the nozzle along the major axis (figure 3.17(b)), and away from the centerline on the minor axis (figure 3.18(b)) was apparent. Once again, a significant trailing jet was observed on both planes at $\hat{T} = 4.8$, in a configuration that is qualitatively similar to that observed by Domenichini (2011).

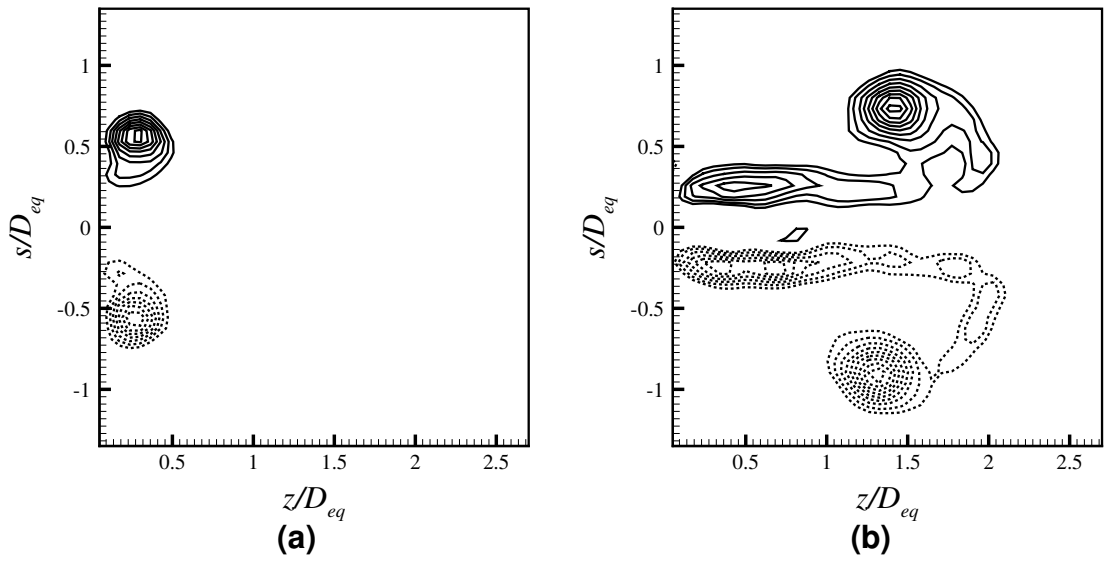

Figure 3.14: Contours of vorticity on the plane of the AR2 nozzle where $\kappa = 0.20$ cm^{-1} at (a) $\hat{T} = 1.6$, and (b) $\hat{T} = 4.8$. Contour levels: min= 25% of ω_{max}, max= 95% of ω_{max}, increment= 10%. Flow is from left to right.

3.3.3 Oval nozzle

The final set of experiments was conducted on the oval nozzle. Along the contour of this nozzle, there were four points of discontinuity in the curvature, located at the points of tangency of the circular segments. These discontinuities in curvature engendered highly three-dimensional motions in their vicinity, which we were unable to capture using planar DPIV. As a result, we once again recorded velocity data only on the two symmetry planes of the nozzle. The oval nozzle had a smaller cross sectional area than the elliptical nozzles ($D_{eq} = 3.62$ cm for the former, and $D_{eq} = 4.45$ cm for the latter), which allowed us to consider stroke ratios up to $L/D_{eq} = 7.3$.

Figures 3.19 and 3.20 show contours of vorticity on the major and minor axes of the two-contour nozzle, for a stroke ratio of $L/D_{eq} = 6.3$. It is evident from these figures that the development of the vortex ring ejected from the oval nozzle was qualitatively similar to that of the two elliptical vortex rings considered in this study. The deformation of the

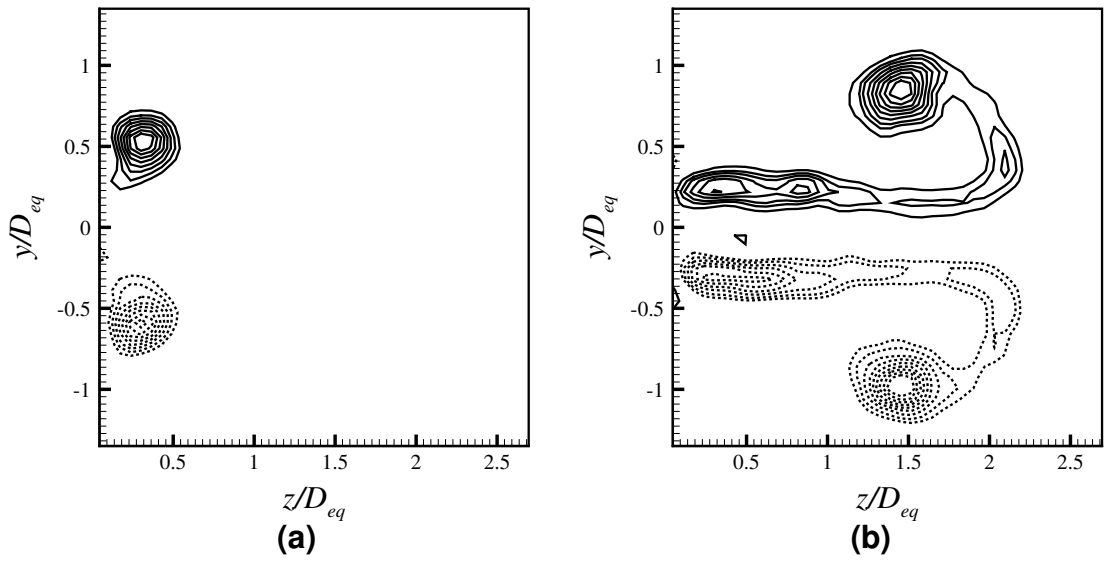

Figure 3.15: Contours of vorticity on the minor axis of the AR2 nozzle at (a) $\hat{T} = 1.6$, and (b) $\hat{T} = 4.8$. Contour levels: min= 25% of ω_{max}, max= 95% of ω_{max}, increment= 10%. Flow is from left to right.

vortex ring due to the curvature-dependence of the ring's propagation velocity is once again evident in figures 3.19(b) and 3.20(b), as is the development of a trailing jet similar to that observed by Domenichini (2011).

3.4 Lagrangian analysis

The length of the trailing jet observed from vorticity contours in all three nozzles (e.g. figures 3.19(b) and 3.20(b)) suggested that pinch-off was likely to have occurred on at least some portions of the nozzles. Hence, we sought to determine the formation time at which pinch-off occurred. This required applying the method of Gharib *et al.* (1998), i.e. comparing the total circulation ejected by the vortex generator, to the lead vortex circulation. However, in some of the vorticity distributions presented in the previous section, the boundaries of the leading vortex ring were ambiguous. On the major axis (and the data planes adjacent to it, in the AR2 case), the boundaries of the leading vortex were easily identifiable, as

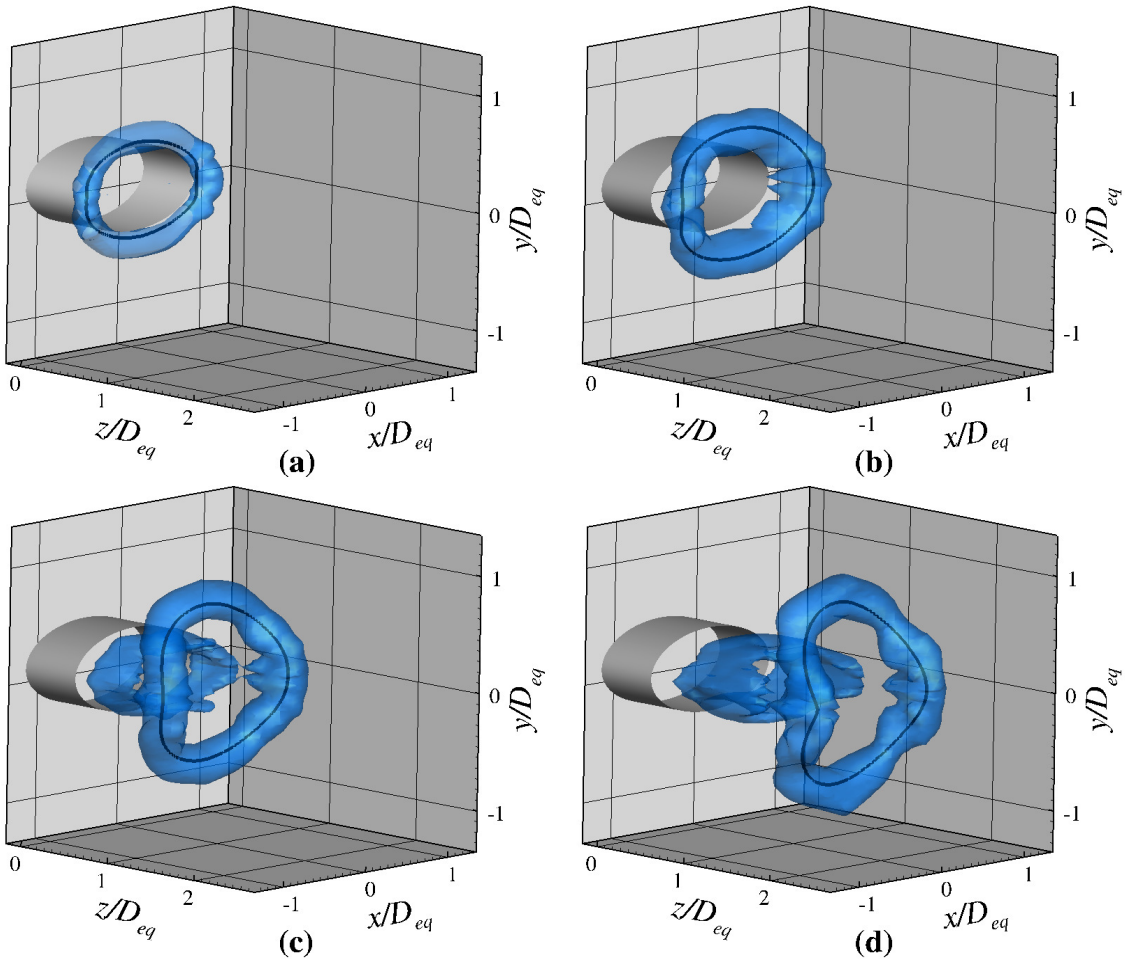

Figure 3.16: Iso-surfaces of 33% of the maximum vorticity at (a) $\hat{T} = 0.5$, (b) $\hat{T} = 1.6$, (c) $\hat{T} = 3.2$, and (d) $\hat{T} = 4.8$. The elliptical nozzle is shown in grey, and the black line is a spline fit through the core center at each plane.

the vorticity field consisted solely of a shear layer and circular lead vortex core (e.g. figure 3.19(b)). On the data planes closer to the minor axis, however, the vorticity field consisted of a shear layer, circular lead vortex core, and a crescent-shaped vortex segment connecting the two (e.g. figure 3.20(b)).

Adhikari (2009) also identified this crescent-shaped vortex structure, which he termed "flow structure 1" in his visualizations of elliptic vortex rings generated with a stroke ratio of $L/D_{eq} = 2$. At these small stroke ratios, Adhikari (2009) found the crescent vortex to merge with the vortex ring completely at later times. In contrast, for larger stroke ratios (e.g.

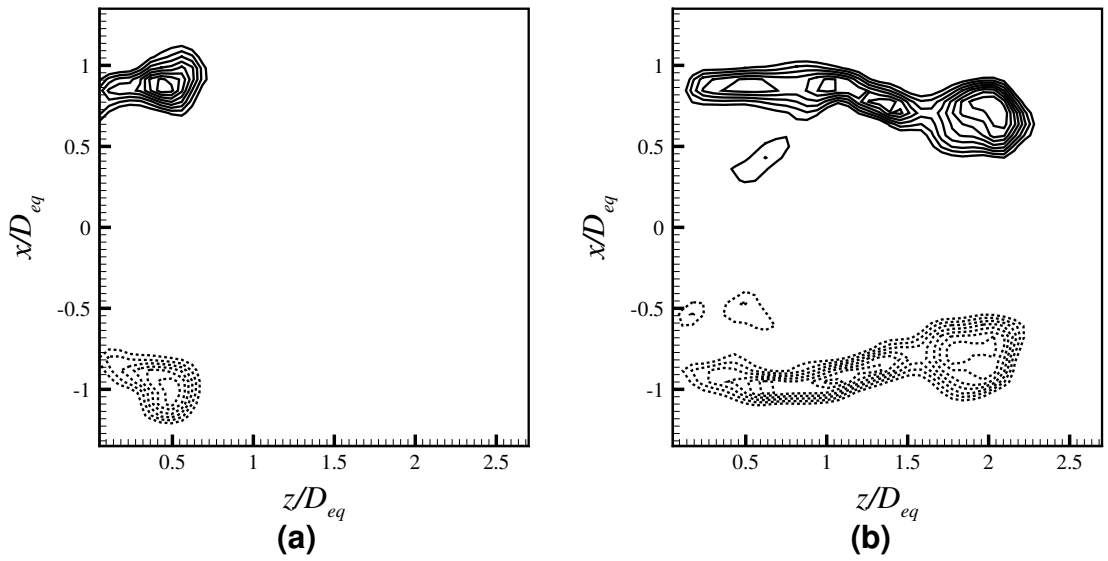

Figure 3.17: Contours of vorticity on the major axis of the AR4 nozzle at (a) $\hat{T} = 1.6$, and (b) $\hat{T} = 4.8$. Contour levels: min= 25% of ω_{max}, max= 95% of ω_{max}, increment= 10%. Flow is from left to right.

$L/D_{eq} = 6$), he found that this structure overtook and separated from the circular vortex cores on the minor axis plane, and developed into what he termed an "arc-like structure." However, this arc-like structure was observed from dye visualizations to connect to the outer regions of the core on the major axis (c.f. figures 4-41 and 4-42 in Adhikari (2009)). As a result, it was unclear whether the crescent vortex observed in contours of vorticity on the minor axis of all three nozzles constituted a part of the leading vortex ring, or a separate flow entity.

In these situations, where the vortex structure consists of several component vortices moving at different velocities, Eulerian quantities such as vorticity can prove difficult to interpret. This is especially true when the perceived size and shape of the vortices varies depending on the thresholds or contour levels in use. In contrast, LCS often prove useful in these cases because they are frame-invariant, their location is independent of threshold selection, and they identify kinematically distinct regions even in complex vortex flows

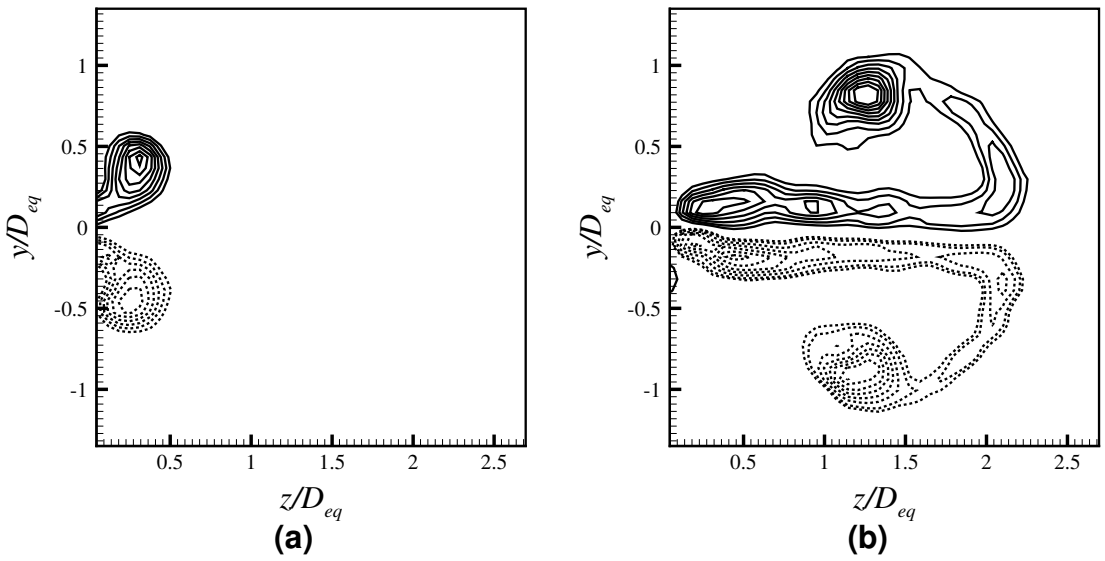

Figure 3.18: Contours of vorticity on the minor axis of the AR4 nozzle at (a) $\hat{T} = 1.6$, and (b) $\hat{T} = 4.8$. Contour levels: min= 25% of ω_{max}, max= 95% of ω_{max}, increment= 10%. Flow is from left to right.

(Shadden *et al.*, 2006; Green *et al.*, 2007; O'Farrell & Dabiri, 2010). Therefore, to resolve the ambiguity in defining the boundary of the leading vortex ring, we considered the LCS in the flow.

Since the oval nozzle had a smaller cross-sectional area and a longer cavity, it allowed us to consider a greater range of stroke ratios than the elliptical nozzles. As a result, we conducted a set of experiments on the oval nozzle, at four stroke ratios ranging from 1.8 to 7.8, and we observed the evolution of the crescent vortex. For each of these cases, we recorded the velocity and vorticity fields, and computed the FTLE field at several time steps using the methods outlined in §3.2.2. In figures 3.21 through 3.24 we present the forward-time and backward-time FTLE fields at four separate time instants, for experiments conducted using stroke ratios of $L/D_{eq} = 1.8, 3.3, 6.3,$ and 7.8. The forward-time and backward-time FTLE fields are represented in the form of contours ranging from white to blue and white to red respectively, and contours of vorticity are superimposed on the FTLE

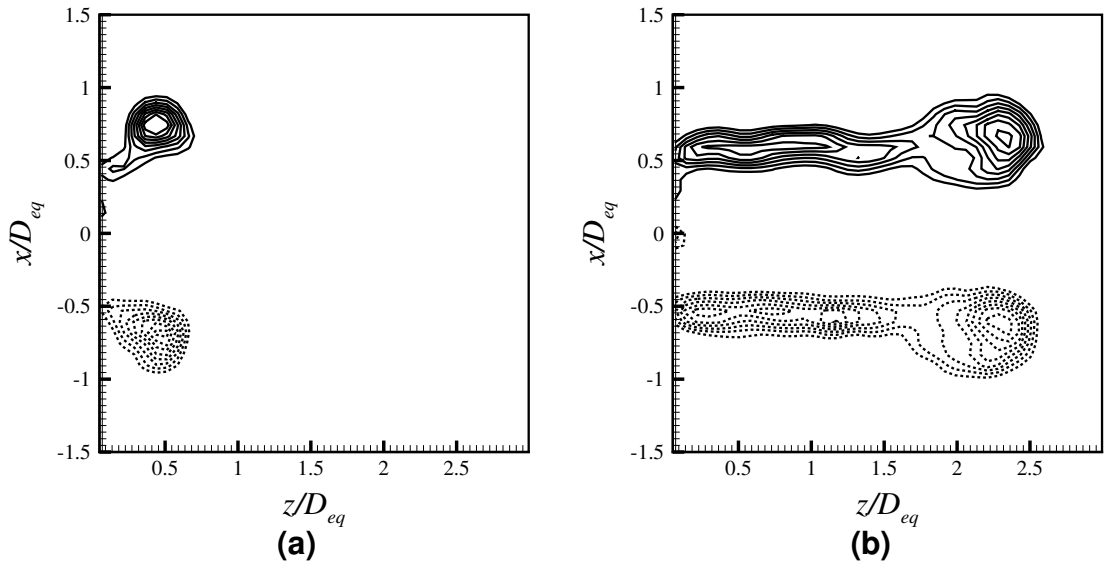

Figure 3.19: Contours of vorticity on the major axis of the oval nozzle at (a) $\hat{T} = 1.6$, and (b) $\hat{T} = 5.8$. Contour levels: min= 25% of ω_{max}, max= 95% of ω_{max}, increment= 10%. Flow is from left to right.

fields for reference.

Figure 3.21 shows contours of vorticity and FTLE for an experiment conducted using a stroke ratio of 1.8. In this case, the stroke ratio was sufficiently small as to result in the formation of an isolated circular vortex core on both the major and minor axis planes of the oval nozzle. Figures 3.21(a) and (e), depict the vortex ring at $\hat{T} = 1.2$, on the major and minor axes of the nozzle, respectively. At this stage, fluid ejection had not yet stopped, so the rear boundary of the vortex (formed by the repelling LCS) was not complete. By $\hat{T} = 4.1$, fluid ejection had stopped and the attracting and repelling LCS formed the boundaries of the vortex ring on both planes (figures 3.21 (b) and (f)). In this case, the LCS structure on both planes qualitatively resembled that observed by Shadden *et al.* (2006) for isolated circular vortex rings formed at similar stroke ratios. In addition, the time-varying deformation of the isolated vortex ring was evident from the oscillations in the diameter of the vortex ring on both the major and minor planes (figures 3.21 (b)-(d)

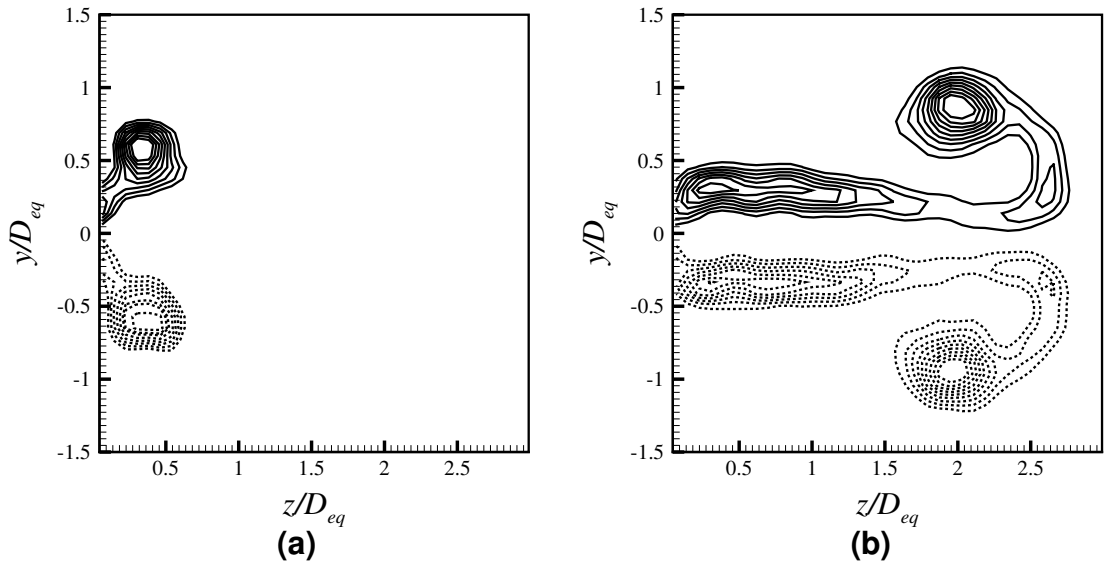

Figure 3.20: Contours of vorticity on the minor axis of the oval nozzle at (a) $\hat{T} = 1.6$, and (b) $\hat{T} = 5.8$. Contour levels: min= 25% of ω_{max}, max= 95% of ω_{max}, increment= 10%. Flow is from left to right.

and (f)-(h)).

When the stroke ratio was increased to 3.3, a small crescent vortex was evident on the minor plane during formation (figure 3.22(f) and (g)). Pinch-off was not observed in this case, so nearly all of the vorticity ejected from the nozzle was entrained into the vortex ring and the remainder dissipated due to viscous diffusion. Once the vorticity in the short shear layer had been entrained into the leading vortex core, the LCS structure largely resembled that observed in the case where $L/D_{eq} = 1.8$ (c.f. figures 3.22(c) and (g), and figures 3.21(b)-(d) and (f)-(h)). However, two new branches were observed to form in the repelling LCS, and they are shown to intersect the crescent vortices on the minor plane at $\hat{T} = 5.9$ in figure 3.22(g). The small amounts of vorticity which were separated from the main vortex core by these new branches in the repelling LCS (e.g. "Region 1" in figure 3.21), were found to overtake the leading vortex core and form the flow structure observed by Adhikari (2009) (figure 3.22(h)). At $\hat{T} = 8.6$, the core was also observed to become more diffuse on the major

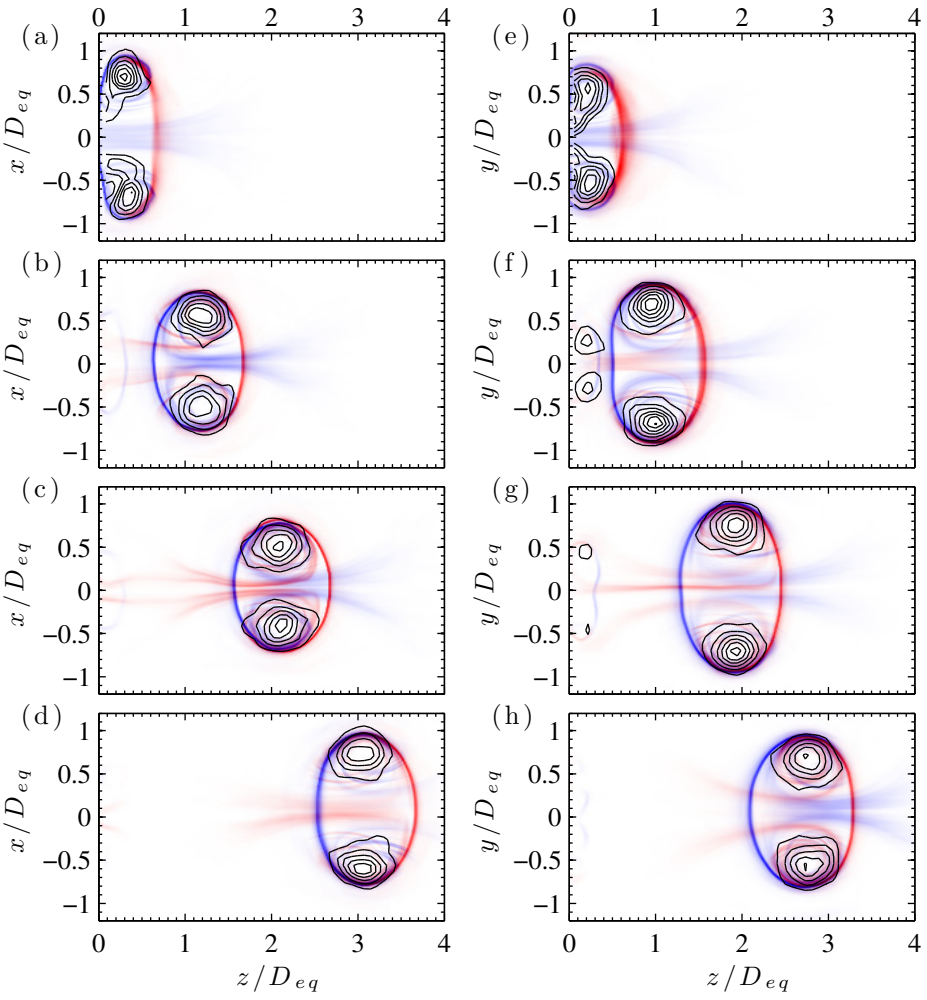

Figure 3.21: Contours of the forward-time (white to blue) and backward-time FTLE for an oval vortex ring with a stroke ratio of 1.8. (a)-(d) Major axis. (e)-(h) Minor axis. Contours of vorticity are superimposed: min = 10% of the maximum ω, max = 95% of the maximum ω, increment = 15%. Formation time increases down each column: $\hat{T} = 1.2, 4.1, 7, 10$.

axis, leading to the appearance of a gap between the attracting and repelling LCS on this plane (figure 3.22(d)). This structural change in the LCS was indicative of the connection of the flow structure identified on the minor axis, to the outer regions of the core on the major axis as observed in Adhikari's dye visualizations at larger stroke ratios. Throughout the formation process, the crescent vortex was found to remain within the bounds of the leading vortex formed by the LCS, thus indicating that the crescent vortex was part of the leading vortex ring.

The LCS structure observed in figure 3.22 for a stroke ratio of 3.3 persisted for higher stroke ratios, including those exceeding 4, in which the formation of a persistent trailing jet was observed. Figure 3.23 shows the LCS structure and contours of vorticity for the experiment conducted with a stroke ratio of 6.3, and previously analyzed in §3.3.3. In this case, a clear crescent vortex was observed in the minor plane (figure 3.23(g)), and the portions of this crescent vortex delimited by the branching repelling LCS were observed to form a much stronger vortex pair which overtook the leading vortex core at large formation times (figure 3.23(h)). The deformation of the core on the major axis at large formation times, due to the connection of the vortex pair on the minor axis to the outer regions of the core on the major axis, was found to be more pronounced in this case as well (figure 3.23(d)). In addition, a significant amount of vorticity was found to trail in the regions behind the boundaries of the leading vortex core, and a secondary vortex ring was even observed to form in the minor plane by $\hat{T} = 9.1$ (figure 3.23(h)). However, unlike the secondary vortex in the wake, the crescent vortex was found to remain within the bounds formed by the LCS for the duration of the vortex formation process.

A similar structure was observed in the experiments conducted on the oval nozzle at the maximum achievable stroke ratio of 7.8. Figure 3.24 shows the LCS structure and contours

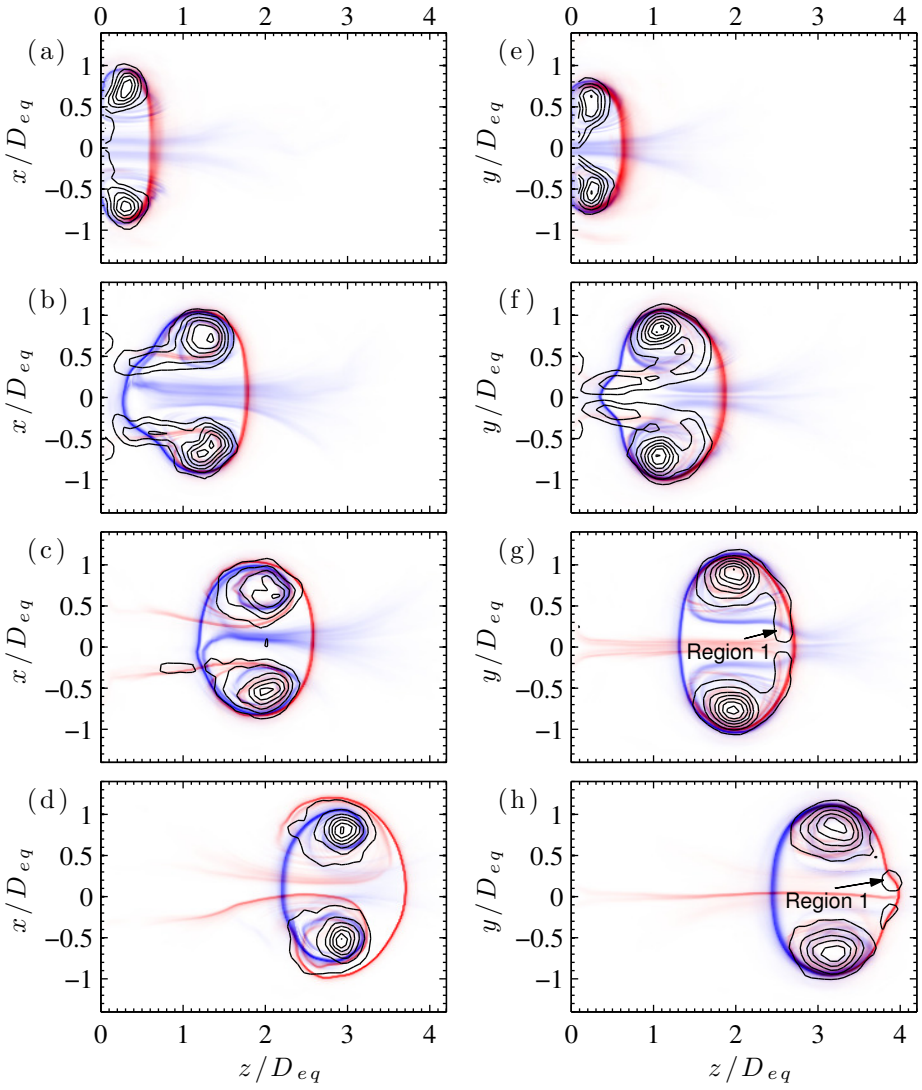

Figure 3.22: Contours of the forward-time (white to blue) and backward-time (white to red) FTLE for an oval vortex ring with a stroke ratio of 3.3. (a)-(d) Major axis. (e)-(h) Minor axis. Contours of vorticity are superimposed: min = 10% of the maximum ω, max = 95% of the maximum ω, increment = 15%. Formation time increases down each column: $\hat{T} = 1.2, 4.0, 5.9, 8.6$.

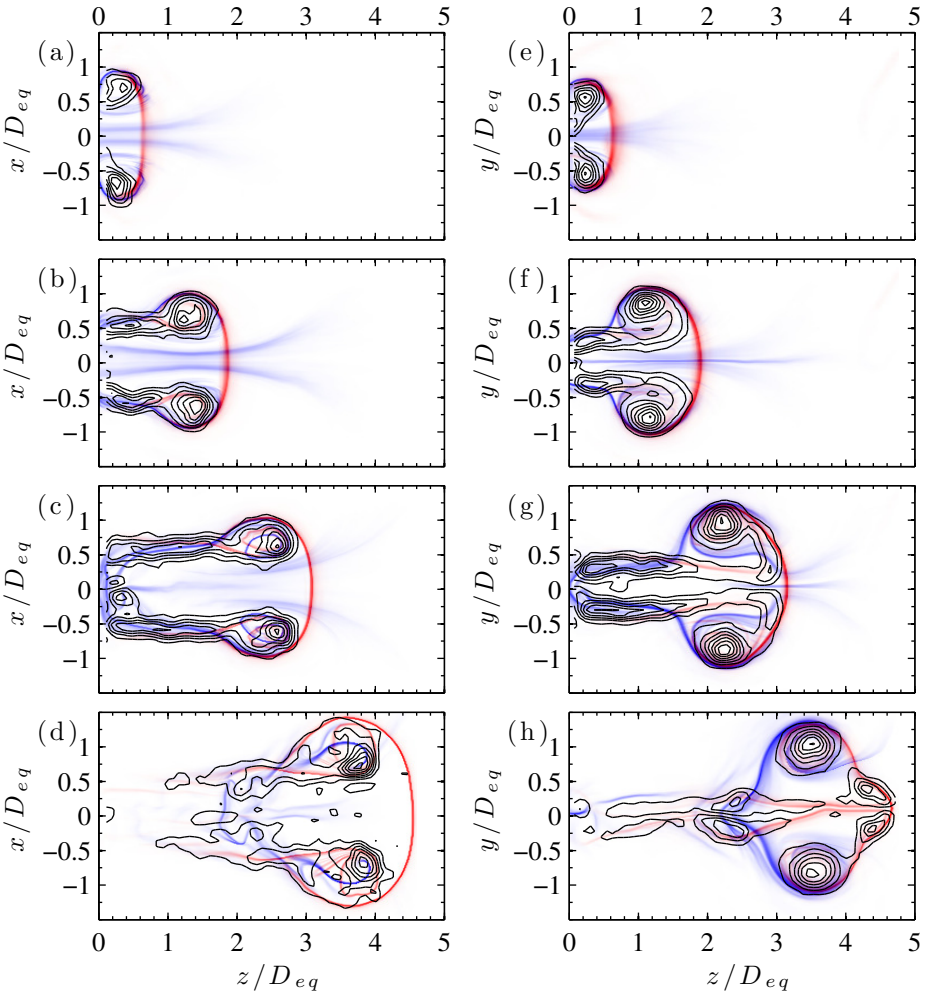

Figure 3.23: Contours of the forward-time (white to blue) and backward-time (white to red) FTLE for an oval vortex ring with a stroke ratio of 6.3. (a)-(d) Major axis. (e)-(h) Minor axis. Contours of vorticity are superimposed: min = 10% of the maximum ω, max = 95% of the maximum ω, increment = 15%. Formation time increases down each column: $\hat{T} = 1.2, 4.0, 6.4, 9.1$.

of vorticity for this stroke ratio. In this case, several Kelvin-Helmholtz-type vortices were seen to develop in the wake of the leading vortex at long formation times (figure 3.24(h)), and new repelling LCS similar to those observed in a circular starting jet in chapter 2, are visible in the wake in figures 3.24(e) and (h). However, the kinematics of the crescent vortex remained unchanged.

The main features of the LCS structure observed in figures 3.23 and 3.24 can also be identified in figures 3.25 and 3.26, which depict contours of vorticity superimposed on the contours of the forward-time and backward-time FTLE fields for the AR2 and AR4 nozzles, respectively. Once again, the crescent vortex was found to remain within the boundaries of the vortex ring during formation, and branches of the repelling LCS were found to delimit the portions of the crescent vortex which would later form the arc-like structure observed by Adhikari (2009). Therefore, the LCS analysis revealed that the crescent vortex observed in the minor planes of all three nozzles was part of the leading vortex ring. In addition, the LCS predicted the development of the arc-like structure, which was found to connect portions of the crescent vortex to the outer boundaries of the core on the major axis. The deformation and eventual break-up (Adhikari, 2009) that results from the formation of this arc-like structure, while interesting, is not relevant to the study of vortex pinch-off, since it occurs after the vortex has separated from the nozzle. Thus, it has no impact on the properties of the vortex ring during formation.

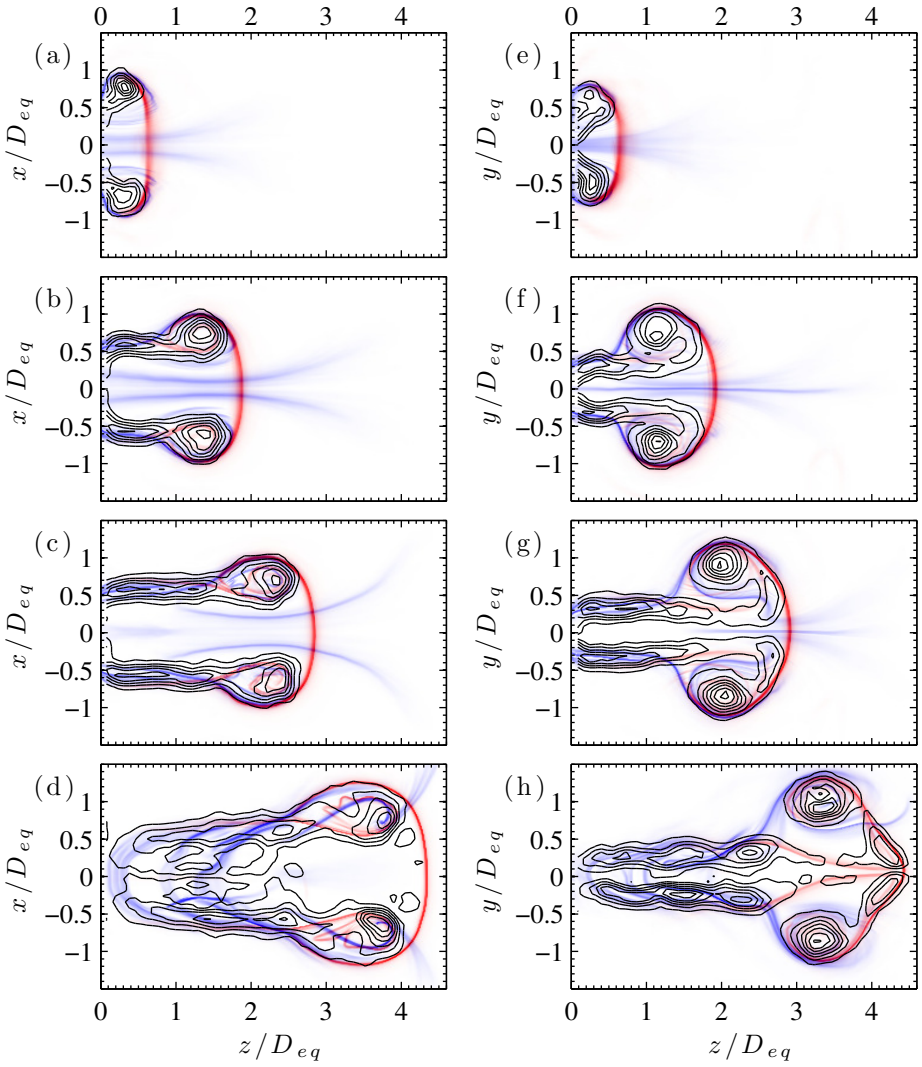

Figure 3.24: Contours of the forward-time (white to blue) and backward-time (white to red) FTLE for an oval vortex ring with a stroke ratio of 7.8. (a)-(d) Major axis. (e)-(h) Minor axis. Contours of vorticity are superimposed: min = 10% of the maximum ω, max = 95% of the maximum ω, increment = 15%. Formation time increases down each column: $\hat{T} = 1.2, 4.0, 5.9, 8.6$.

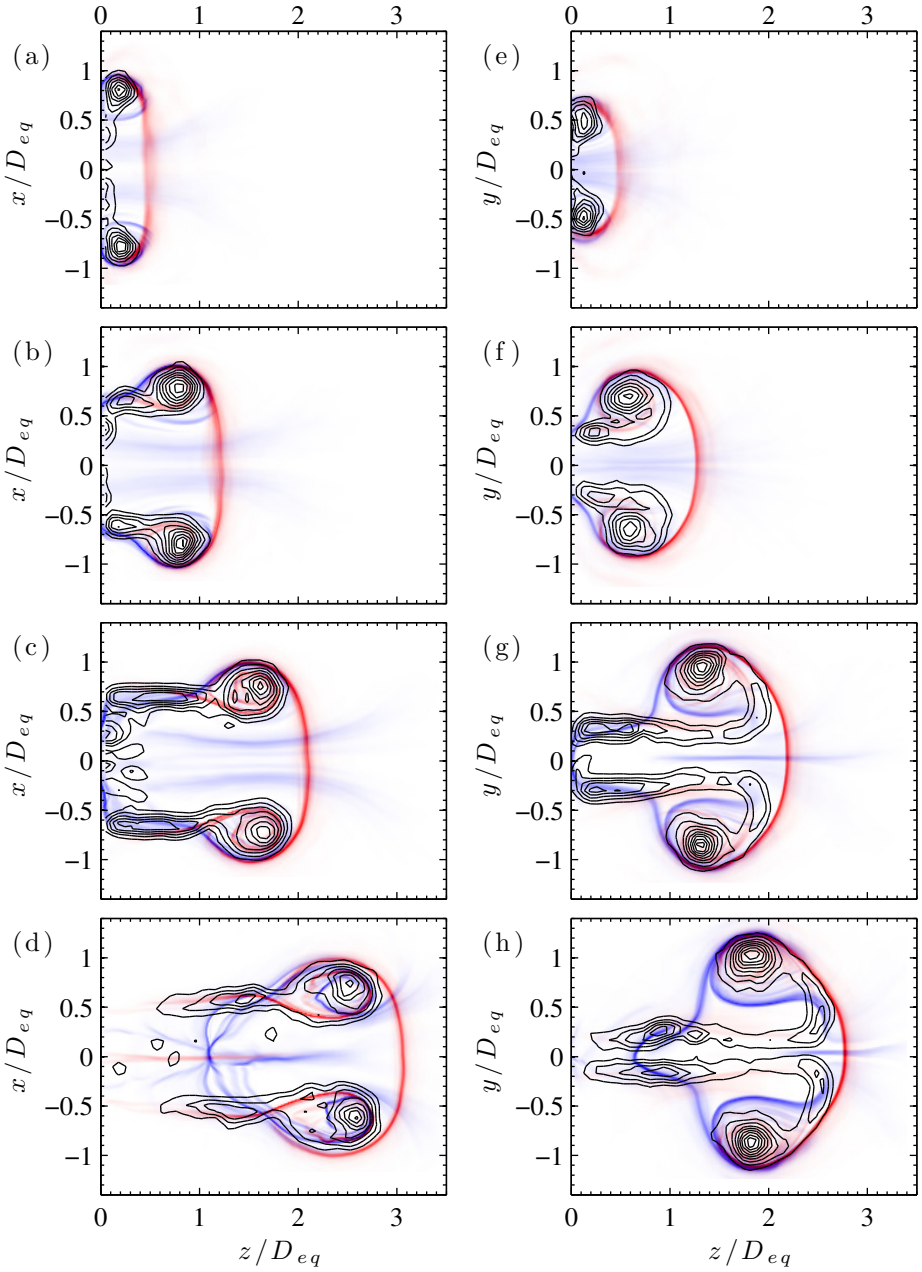

Figure 3.25: Contours of the forward-time (white to blue) and backward-time (white to red) FTLE for a vortex ring formed from the AR2 nozzle with a stroke ratio of 5.8. (a)-(d) Major axis. (e)-(h) Minor axis. Contours of vorticity are superimposed: min = 10% of the maximum ω, max = 95% of the maximum ω, increment = 15%. Formation time increases down each column: $\hat{T} = 0.8, 2.7, 4.7, 6.7$.

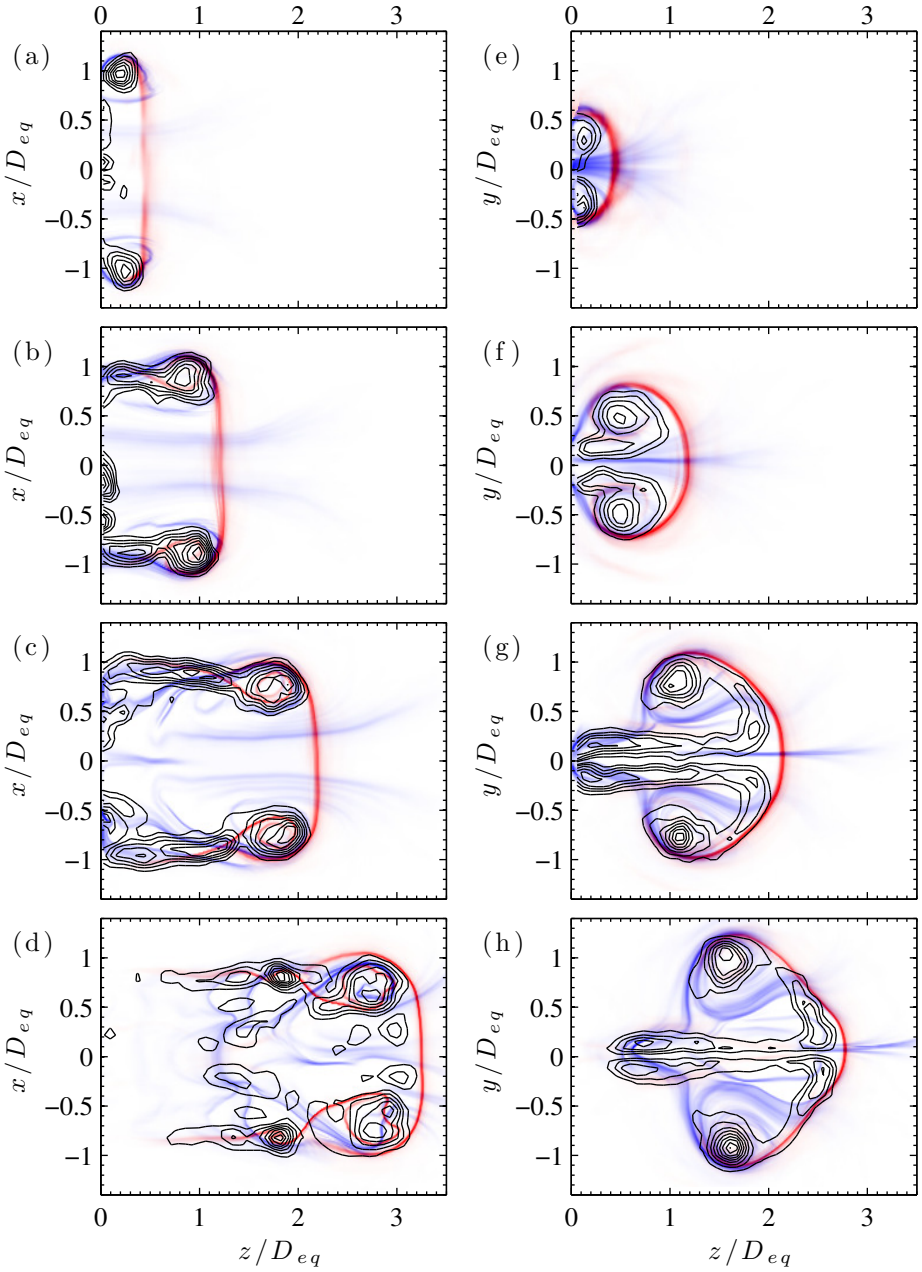

Figure 3.26: Contours of the forward-time (white to blue) and backward-time (white to red) FTLE for a vortex ring formed from the AR4 nozzle with a stroke ratio of 5.8. (a)-(d) Major axis. (e)-(h) Minor axis. Contours of vorticity are superimposed: min = 10% of the maximum ω, max = 95% of the maximum ω, increment = 15%. Formation time increases down each column: $\hat{T} = 0.9, 2.8, 4.8, 6.8$.

3.5 Vortex formation number

3.5.1 AR2 elliptical nozzle

Following Gharib *et al.* (1998), we computed the total circulation emanating from the piston-cylinder apparatus, as well as the circulation in the leading vortex ring, by integrating the vorticity contained within the lowest detectable contours. Figure 3.27(a) shows the total circulation as a function of non-dimensional formation time based on the nozzle equivalent diameter, for the seven values of curvature considered. In all the planes considered, the total circulation increased at an almost constant rate until fluid ejection stopped at approximately $\hat{T} = 4.8$, when it leveled off at final value ranging between $\Gamma = 48$ cm^2/s and $\Gamma = 54$ cm^2/s. In figure 3.27(b), we present the time history of the circulation in the leading vortex ring for the seven curvature points. Once again, the seven cases considered exhibited similar trends, with the lead vortex circulation achieving a final value ranging from $\Gamma_{ring} = 31$ cm^2/s to $\Gamma_{ring} = 36$ cm^2/s, at a approximately $\hat{T} = 6$.

When computing the lead vortex circulation, we defined the lead vortex core as outlined in §2.3. Figure 3.28 shows the outline of the lead vortex core on the major and minor planes of the AR2 nozzle. The fact that the circulation within the core as defined above was found to be constant at long formation times confirms our definition of the lead vortex on planes near the minor axis. In contrast, the circulation of the circular portion of the leading vortex on the minor plane continuously increased by drawing circulation from the crescent-shaped vortex. Hence, although the final circulation in the lead vortex was found to be approximately constant across the different curvature planes (figure 3.27(b)), the shape of the lead vortex varied significantly between the major axis and the minor axis.

By comparing the time history of the total circulation and the final circulation in the

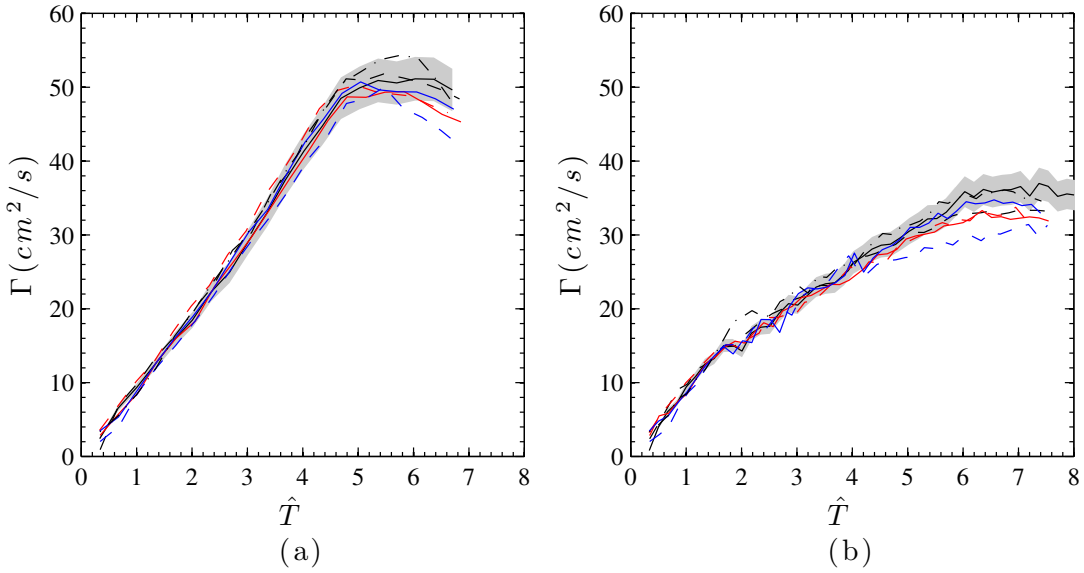

Figure 3.27: Time history of (a) the total circulation emanating from the nozzle, and (b) the circulation in the lead vortex, at seven different curvature points. The error in the measurements was $\approx 6\%$, and it is shown in grey for the curve on the major axis, for reference. $\kappa = 1.26$ cm^{-1} (—); 1.04 cm^{-1} (– –); 0.82 cm^{-1} (—); 0.60 cm^{-1} (– –); 0.39 cm^{-1} (—); 0.20 cm^{-1} (– –); 0.16 cm^{-1} (–.–).

lead vortex, one can determine the non-dimensional time at which the lead vortex ceased to accept additional circulation. We performed this comparison at each data plane, in order to determine whether the formation time at pinch-off varied with the local curvature. Figure 3.29 illustrates this comparison for two of the seven curvature planes considered: the major and minor axes. On the major axis (figure 3.29(a)), the formation time at pinch-off was found to be $\hat{T} = 3.6 \pm 0.4$, whereas on the minor axis (figure 3.29(b)) it was found to be $\hat{T} = 3.4 \pm 0.4$.

Figure 3.30 shows the formation time at pinch-off as a function of curvature, for the seven curvature points along the elliptical nozzle. The symbols show the formation time at pinch-off at each data plane, and the black line shows the average formation time at pinch-off ($\hat{T} = 3.3 \pm 0.4$), over the seven curvature points. These results suggest that there is no dependence of the formation time at pinch-off on the local curvature, but rather pinch-off

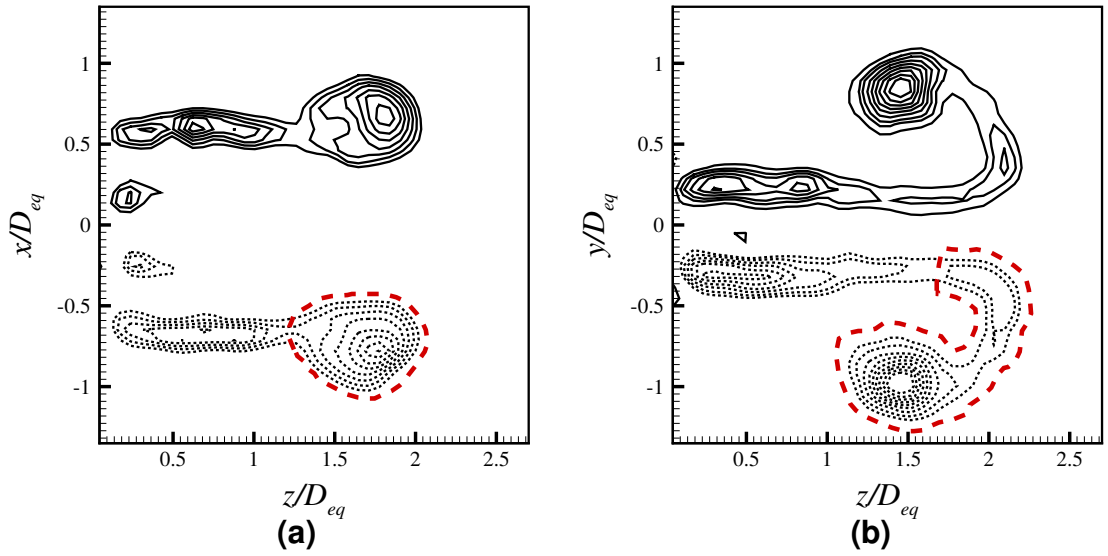

Figure 3.28: Contours of vorticity on (a) the major axis and (b) the minor axis at $\hat{T} = 4.8$. The region considered to correspond to the lead vortex in each plane is outlined in red. Contour levels: min= 25% of ω_{max}, max= 95% of ω_{max}, increment= 10%. Flow is from left to right.

occurs simultaneously throughout the nozzle contour, at a formation number based on the equivalent diameter of the nozzle of $\hat{T} = 3.3 \pm 0.4$.

3.5.2 AR4 elliptical nozzle

The results of the experiments on the formation of vortex rings from an elliptical nozzle with an aspect-ratio of two suggest that, in this kind of moderate aspect-ratio elliptical vortex rings, pinch-off is a global process governed by the equivalent diameter of the nozzle. In contrast, local curvature affects only the shape of the forming vortex. However, these results would appear to contradict those of Domenichini (2011), which suggest that local curvature is a key factor governing the local vortex formation process. Therefore, we compared the vortex formation process on the AR2 nozzle to the formation of vortices from the remaining two nozzles: the elliptical nozzle with an aspect-ratio of four, and the oval nozzle. Since the AR4 nozzle spanned a much larger range of curvatures, it allowed us to determine whether

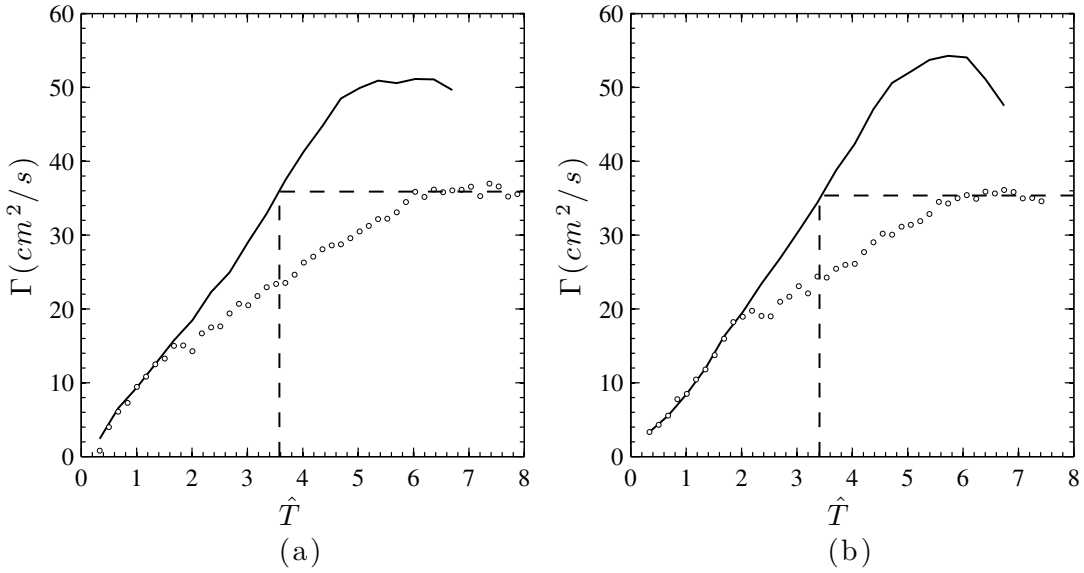

Figure 3.29: Time history of the total circulation (—) and lead vortex circulation (∘) on: (a) the major axis, and (b) the minor axis of the AR2 elliptical nozzle. Comparing the final circulation in the lead vortex with the time history of the total circulation yields the non-dimensional time at which the vortex stopped accepting vorticity (– –).

the independence of the formation number on local curvature extends to the formation of elliptical vortex rings of larger aspect-ratios, where the curvature on the minor axis is close to zero ($\kappa_{min} = 0.06$ cm^{-1} in this case).

Figure 3.31 shows the time history of the total circulation emanating from the nozzle, as well as the circulation in the lead vortex ring, on the major and minor axes of the AR4 nozzle. Comparing the final circulation in the lead vortex ring to the time history of the total circulation yielded a formation time at pinch-off of $\hat{T} = 3.1 \pm 0.4$ on the major axis, and $\hat{T} = 3.5 \pm 0.4$ on the minor axis. Therefore, the formation number based on equivalent diameter for the AR4 nozzle was found to be identical to the formation number for the AR2 nozzle, within experimental error.

The results in figure 3.31 are similar to those for the symmetry planes of the AR2 nozzle, with the exception of a step-like increase in the circulation of the lead vortex ring at $\hat{T} = 5.5$

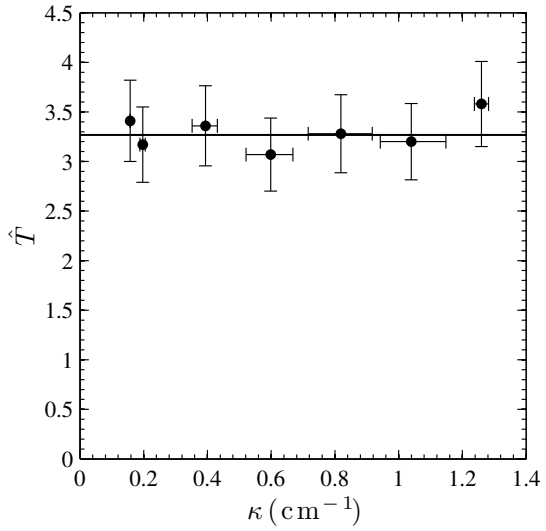

Figure 3.30: Non-dimensional pinch-off time ($\hat{T} = \overline{U}_p t/D_{eq}$) as a function of curvature. The average over all curvature points ($\hat{T} = 3.3 \pm 0.4$) is denoted by the solid black line.

in figure 3.31(a), which is absent in figure 3.29(a). In their study of circular vortex rings, Gharib *et al.* (1998), found that for large stroke ratios, the vortex ring circulation increased in a step-like fashion after long formation times. This step-like increase was caused by the first vortex in the trailing wake catching up to, and coalescing with, the leading vortex ring (see §2.4). This same phenomenon was responsible for the jump in the lead vortex circulation in figure 3.31(a), as illustrated by the vorticity contours in figure 3.32. However, unlike in the circular case, the jump occurred before the lead vortex circulation has leveled off (*i.e.* before the vortex ring had pinched off).

3.5.3 Oval nozzle

Although in the AR4 nozzle the portions of the nozzle contour adjacent to the minor axis had a curvature close to zero, the curvature varied smoothly between its maximum value at the major axis and its minimum value at the minor axis. In contrast, the slender orifices of Domenichini (2011) consisted of connected segments with constant, distinct curvatures, with

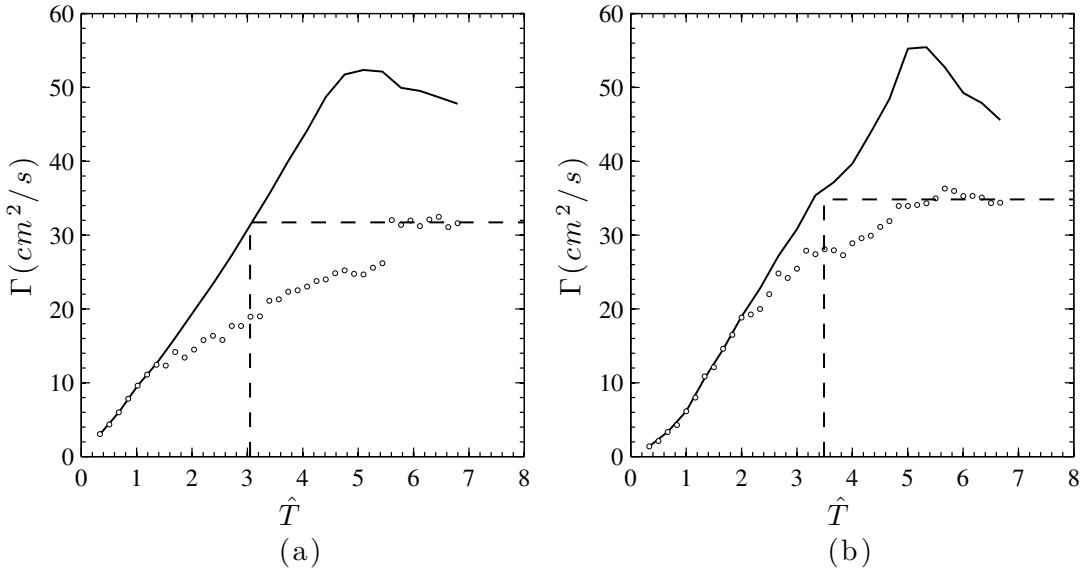

Figure 3.31: Time history of the total circulation (—) and lead vortex circulation (∘) on: (a) the major axis, and (b) the minor axis of the AR4 elliptical nozzle. Comparing the final circulation in the lead vortex with the time history of the total circulation yields the non-dimensional time at which the vortex stopped accepting vorticity (– –).

discontinuities in the curvature at their points of tangency. Given that Domenichini (2011) found stark differences in the vortex formation process between the curved segments and the straight segments of his slender orifices, and that these differences were not replicated in our results for elliptical nozzles, the question of whether discontinuities in the curvature are required to produce a spatially varying formation number was of interest. Therefore, we studied the occurrence of pinch-off on two planes of the oval nozzle, which also contained points of discontinuity in the curvature along its contour.

Figure 3.33 shows the time history of the total circulation emanating from the nozzle, as well as the circulation in the lead vortex ring, on the major and minor axes of the oval nozzle. In this nozzle, pinch-off was found to occur at a formation time of $\hat{T} = 3.9 \pm 0.4$ and $\hat{T} = 3.6 \pm 0.4$, on the major and minor axes respectively. Our results are summarized in figure 3.34 , which shows the formation time at pinch-off as a function of curvature,

for all three nozzles. These results suggest that there is no dependence of the formation time at pinch-off on the local curvature. Moreover, it appears that, for the nozzle shapes considered, the critical formation time, or formation number, is a function of the equivalent diameter of the nozzle.

3.6 Conclusions

In this chapter, we investigated, the formation of vortex rings from three different non-circular nozzles: an elliptical nozzle with an aspect-ratio of two, an elliptical nozzle with an aspect-ratio of four, and an oval nozzle constructed from tangent circular arcs. The nozzles selected encompass a wide class of those non-circular nozzles not considered by Domenichini (2011), since they include nozzles with both smooth and discontinuous variation in the curvature, and span from nozzles with a moderate range of curvatures to those with extreme variations in curvature ($\kappa_{max}/\kappa_{min} = 4$ in the oval nozzle, and ≈ 60 in the AR4 nozzle.)

On all three nozzles, we found that the limiting size and circulation at saturation of the vortex ring were not spatially varying along the nozzle contour, and thus not a function of the local curvature. Therefore, pinch-off was not found to be a local phenomenon in either of the three nozzle shapes considered. The shape of the leading vortex ring was found to vary along the contour of the nozzle in all three cases, and to be strongly dependent on the local curvature. However, the LCS analysis revealed the leading vortices of various shapes to belong to a single coherent leading vortex core during the formation process, thus leading to the observed invariance of the circulation. In addition to the spatial variation in the vortex ring shape, we observed the time-dependent deformation of the vortex, which, in the case of elliptical nozzles, was in agreement with previous studies (Viets & Sforza, 1972; Dhanak & de Bernardinis, 1981; Hussain & Husain, 1989; Adhikari, 2009). The deformation

of vortex rings from oval nozzles is reported here for the first time, and was found to be qualitatively similar to the deformation of elliptical vortex rings.

In agreement with Hussain & Husain (1989), we found that the equivalent diameter of a non-circular nozzle is a proper length scale in quantifying the formation of vortex rings with moderate departure from axisymmetry. As a result, we extended the definition of the formation number introduced by Gharib *et al.* (1998), to vortex rings of this class, using the equivalent diameter of the nozzle as the relevant length scale ($\hat{T} = \overline{U}_p t/D_{eq}$). In all three nozzles considered, we found the formation number thus defined to be constant along the contour of each nozzle, and to lie in the range between 3 and 4. This range falls slightly below that observed in circular vortex rings by Gharib *et al.* (1998) (approximately 3.6 to 4.5), yet is in remarkably good agreement given the wide class of nozzles considered, and their departure from axisymmetry.

The present results for the shape and deformation of elliptical vortex rings are in good agreement with those of Adhikari (2009). However, our results for the formation number of vortex rings of the three shapes considered contradict Domenichini's conjecture that pinch-off in these geometries should be a local phenomenon governed by the curvature. Given the stark differences between our conclusions about the role of curvature in vortex formation, and those of Domenichini (2011), a comparison of the results of the two studies is illuminating.

At the early stages of vortex development, our findings regarding the shape and deformation of the vortex agreed qualitatively with those of Domenichini (2011). Moreover, our results appear compatible with Domenichini's results for the formation of small-aspect-ratio vortex rings ($h = 0.05, 0.5$ in Domenichini's formulation). In these cases, Domenichini (2011) found the evolution of the non-circular vortices to be similar to that of circular vor-

tex rings, albeit with some deformation. Furthermore, in these cases, pinch-off appeared to occur simultaneously on the straight and circular sections of the vortex ring.

For larger aspect-ratios ($h = 1.5, 2$ in Domenichini's formulation), the geometry of the vortex ring and shear layer on the symmetry planes was similar in Domenichini's computations and our experimental results. In both studies, a leading vortex ring and trailing shear layer were observed on the major axis plane, while a geometry consisting of a leading vortex ring, crescent vortex, and circular vortex core was observed in the minor plane. However, Domenichini (2011) concluded that the circulation in the leading vortex was higher in the flat portions of the vortex than in the circular portions, and that pinch-off occurred exclusively on the circular portions of the orifice at a formation time $T^* = Ut/D = 3.6$ based on the diameter of the circular portion of the orifice (D).

The discrepancy between our results and those of Domenichini's computations for more slender orifices can be attributed, in part at least, to a difference in the definition of the boundaries of the leading vortex on the minor axis between the two studies. Domenichini (2011) presented only results for the circulation on the major plane for one of his pseudo-elliptic orifices ($h = 2$). However, the author kindly granted us access to time-resolved vorticity fields on the two symmetry planes for two of his orifices: one where $h = 2$, and one where $h = 4$. When computing the circulation of the vortex in both symmetry planes of the $h = 2$ orifice using the definition of the vortex boundaries outlined in §3.5, we found the circulation in both planes to be similar, indicating that pinch-off occurred simultaneously on both sections of the orifice.

On both axes of the $h = 2$ orifice, however, pinch-off appeared to take place at a formation time of 3.6 based on the diameter of the circular portion of the orifice ($T^* = Ut/D$), which corresponds to a formation time of $\hat{T} = 1.9$ based on the equivalent diameter

of the orifice. Since Domenichini (2011) did not present the time history of the total circulation and vortex ring circulation for orifices other than the $h = 2$ case, the relevance of the diameter of the circular segments (D) or the equivalent diameter of the orifice (D_{eq}) as length scales for Domenichini's flows cannot be ascertained.

Additionally, the crescent-shaped vortex observed in the minor plane in both our experiments and those of Adhikari (2009) was not found in the vorticity data for Domenichini's most slender orifices ($h = 4$). In this case, the shear layer was found to curve around the leading vortex, but no separation of the crescent-shaped portion of the shear layer from its main section was observed. The absence of the crescent vortex might be indicative of a change in the vortex formation process for very high aspect-ratio orifices which resemble thin slits. Such a change is consistent with the two-dimensional roll-up observed in the limiting case of extremely thin slits (Afanasyev, 2006; Pedrizzetti, 2010).

The present results have potentially far-reaching implications for the study and modeling of vortex ring flows of biological relevance. Elliptical, elongated, and otherwise non-circular vortex rings such as those investigated in this chapter are known to be a distinguishing feature in many biological flows (Kokshaysky, 1979; Dickinson & Götz, 1996; Kern & Koumoutsakos, 2006; Bellhouse, 1972; Domenichini *et al.*, 2005). Our results on the formation number of vortex rings of this class therefore allows for a more accurate understanding of the parameters governing the formation of vortex rings in the human left ventricle, for example.

Furthermore, the concepts of the vortex formation number and optimal vortex formation have been applied successfully to evaluating the efficiency or optimality of propulsive flows (Krueger & Gharib, 2003; Dabiri *et al.*, 2010; Linden & Turner, 2004) which feature vortex rings of almost circular shape. However, in other locomotory flows where non-axisymmetric

vortex rings are the norm, the absence of known limits on vortex ring size previously precluded this sort of analysis. The present results, however, suggest that we can reduce vortex rings with moderate departure from axisymmetry to circular vortex rings with the same equivalent diameter. Such a reduction allows for greater ease of modeling, and a decrease in computational complexity in numerical studies, through the exploitation of axisymmetry. Such a reduction has been perfumed in the past by researchers studying both cardiac (Steen & Steen, 1994; Gharib *et al.*, 2006; Kheradvar & Gharib, 2007) and locomotory flows (Drucker & Lauder, 1999; Dickinson *et al.*, 2000; Hsieh & Lauder, 2004).

Once reduced to a circular shape, these vortex rings can be studied using a variety of numerical and analytical tools. In the two chapters that follow, we introduce a method for studying pinch-off by analyzing the perturbation response of model axisymmetric vortex rings. The results presented in this chapter allow us to extend these types of methods to non-circular vortex rings by reducing them to circular vortex rings.

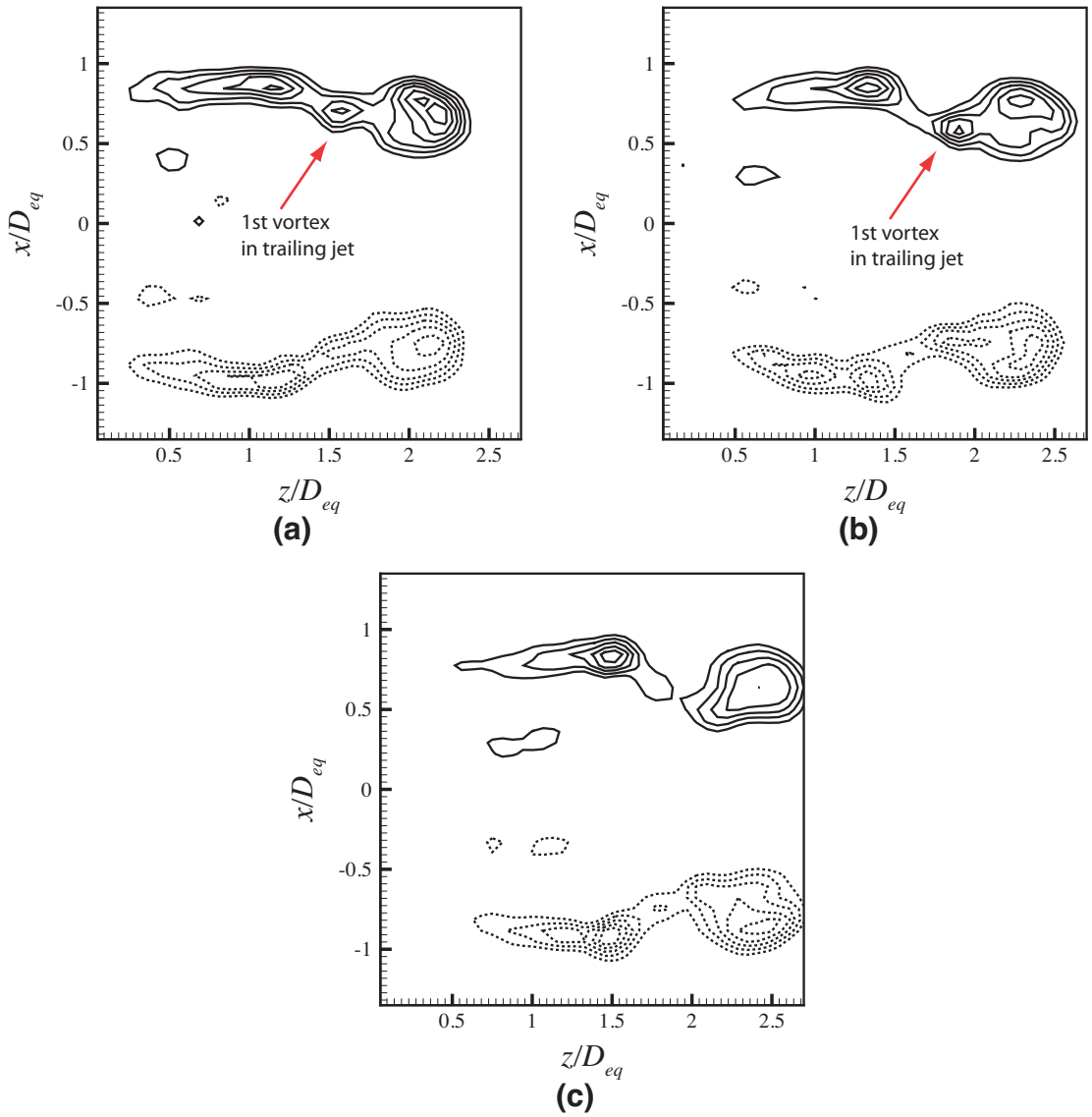

Figure 3.32: Contours of vorticity on the major axis of the AR4 nozzle at (a) $\hat{T} = 5.4$, (b) $\hat{T} = 5.8$, and (c) $\hat{T} = 6.1$. In (a), the first vortex in the trailing jet is identifiable just before merging with the lead vortex. (b) shows the early stages of the merger of the lead vortex and the first vortex in the trailing jet. In (c), the two vortices have coalesced and are indistinguishable. Contour levels: min= 25% of ω_{max}, max= 95% of ω_{max}, increment= 10%. Flow is from left to right.

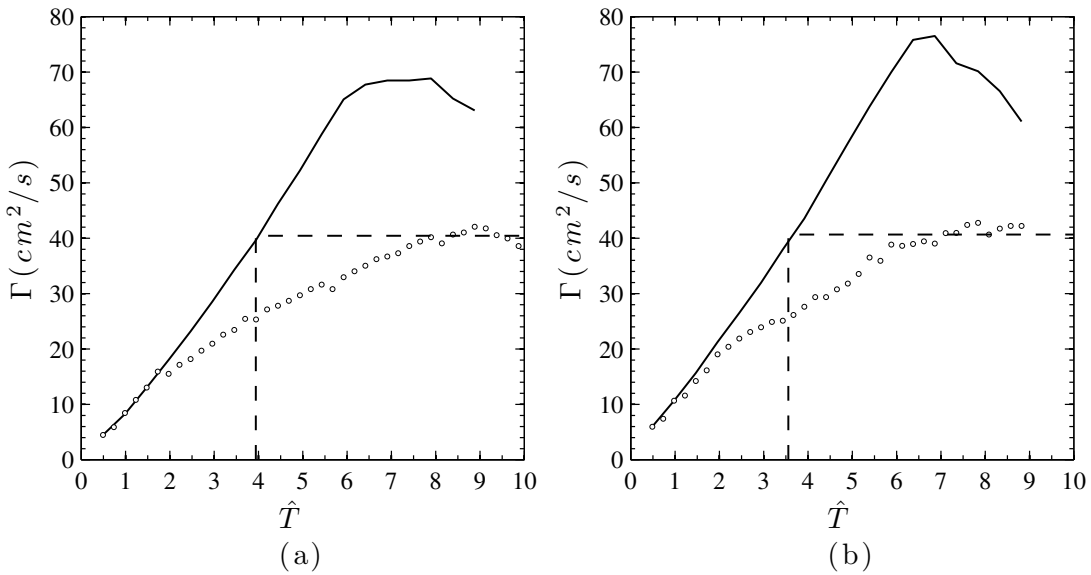

Figure 3.33: Time history of the total circulation (—) and lead vortex circulation (○) on: (a) the major axis, and (b) the minor axis of the oval nozzle. Comparing the final circulation in the lead vortex with the time history of the total circulation yields the non-dimensional time at which the vortex stopped accepting vorticity (– –).

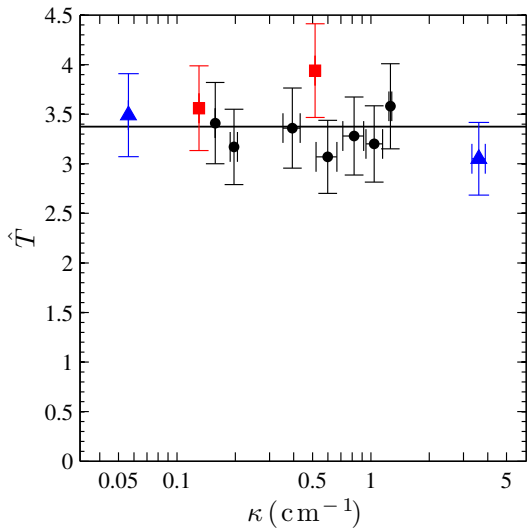

Figure 3.34: Non-dimensional pinch-off time ($\hat{T} = \overline{U}_p t/D_{eq}$) as a function of curvature for the three nozzle shapes: ●, AR2 nozzle; ▲, AR4 nozzle; ■, oval nozzle. The average over all curvature points in the three nozzles ($\hat{T} = 3.4 \pm 0.4$) is denoted by the solid black line.

Chapter 4

Perturbation response and pinch-off of vortex rings and dipoles

4.1 Introduction

Several arguments and models predicting or explaining pinch-off have been put forth, beginning with the original study of Gharib *et al.* (1998). These include the models of Mohseni & Gharib (1998), Shusser & Gharib (2000), Linden & Turner (2001) and Gao & Yu (2010), which are described in the introductory chapter to this thesis. However, no definitive model for pinch-off in every configuration has been presented yet. The principal shortfall of these methods is that they require modeling of the shear layer feeding the vortex, as well as the vortex rings themselves. As a result, these models are application-specific, as well as difficult to apply to flows of biological interest beyond jetting flows. Our objective, therefore, is to determine a physically rooted criterion for pinch-off that can be applied to all vortex loops. We desire such a criterion to be tractable for wake-only measurements. However, since direct application of the Kelvin-Benjamin to vortex wakes is impractical, we resort to a modeling and perturbation-response approach.

Notably, both the argument of Gharib *et al.* (1998) and the aforementioned models make

use of a family of vortex rings introduced by Norbury (1973), as a model for axisymmetric vortex rings. The Norbury family consists of steadily translating axisymmetric vortex rings with finite core size, ranging from classical thin-cored vortices to Hill's spherical vortex. In all members of the family, the vorticity density (ω/r, where r is the radial coordinate) is constant inside the core. These vortex rings serve as a low-order model of experimentally generated vortex rings of different core sizes. Despite its simplicity, the Norbury family of vortex rings has been successfully employed as a model for axisymmetric vortex rings at different stages in their development (Gharib *et al.*, 1998; Mohseni & Gharib, 1998; Shusser & Gharib, 2000; Linden & Turner, 2001; Kaplanski & Rudi, 2005; Gao & Yu, 2010).

That Hill's spherical vortex and nearly spherical members of the Norbury family are the solution to a maximization problem on the energy function as outlined by Benjamin (1976) was shown by Wan (1988). Moffatt & Moore (1978) considered the linear stability of Hill's spherical vortex subjected to axisymmetric perturbations, and found that these decay everywhere except in a region near the rear stagnation point, where a tail of growing length develops. Building on this analysis, Pozrikidis (1986) studied the nonlinear instability of Hill's spherical vortex to axisymmetric shape perturbations of finite size. When subjected to an axisymmetric prolate perturbation, Pozrikidis (1986) found that Hill's vortex returned to a smaller spherical vortex by detraining rotational fluid into a tail. Gharib *et al.* (1998) noted that this circulation shedding is analogous to pinch-off, thus suggesting such perturbations might be a promising avenue of research for improving our understanding of pinch-off. In contrast, Ye & Chu (1995) investigated the response of a member of the Norbury family of moderate core thickness to similar shape perturbations, and found no evidence of tail shedding. However, the nonlinear response of the remainder of the Norbury family to prolate shape perturbations is unknown, and the transition from the observations of Ye &

Chu (1995) to those of Pozrikidis (1986) has not been previously characterized.

In two dimensional flows, a coherent structure similar to the axisymmetric vortex ring is often observed: the symmetric vortex dipole. Dipolar vortices have been observed experimentally in flows in which three-dimensional motions have been suppressed by stratification (van Heijst & Flór, 1989), by utilizing a thin soap film (Couder & Basdevant, 1986) or two-fluid interface (Afanasyev, 2006), by rotation of the ambient fluid (Velasco Fuentes & van Heijst, 1994; Trieling *et al.*, 2010), or by the imposition of a magnetic field on a layer of mercury (Nguyen Duc & Sommeria, 1998). In these experiments and in computational studies (van Geffen & van Heijst, 1998; Duran-Matute *et al.*, 2010; Pedrizzetti, 2010), thick-cored, nearly symmetry-axis-touching dipoles were often observed, leading to speculation that the physical constraint on vortex growth identified by Gharib *et al.* (1998) for axisymmetric vortex rings does not extend to two dimensional vortex pairs. Nitsche (2001) also found a difference in the behavior of axisymmetric vortex rings and vortex dipoles using vortex sheet methods. The author observed self-similar shedding of circulation into a tail in the roll-up of a spherical vortex sheet into a vortex ring, but no shedding of circulation in the in the roll-up of a cylindrical vortex sheet into a vortex pair.

Recently, Afanasyev (2006) and Pedrizzetti (2010) have considered the formation of two dimensional dipoles by the ejection of fluid from thin slits. Unlike in the axisymmetric case, both studies found that vortex pairs continue to accept vorticity after ejection times well beyond those observed in circular vortex rings. Afanasyev (2006) also observed that, throughout their formation, vortex dipoles formed by the ejection of fluid from thin slits could be modeled by different members of a family of steadily translating vortex pairs described by Pierrehumbert (1980). These vortices form a family of constant-vorticity vortex pairs of finite core size, ranging from point vortex dipoles to the symmetry-axis-

touching limit. Although the dipoles could be more realistically modeled by the more complex vorticity distributions proposed by Kizner & Khvoles (2004) and Khvoles *et al.* (2005), the Pierrehumbert family is of interest because of its simplicity, and because it serves as a two dimensional analogue to the Norbury family of vortex rings.

In the study presented in this chapter, we investigated the nonlinear perturbation response of the members of the families of vortices introduced by Norbury (1973) and Pierrehumbert (1980) to prolate shape perturbations similar to those considered by Pozrikidis (1986). The class of prolate perturbations considered was similar to that described in Pozrikidis (1986), yet differed slightly in its mathematical formulation due to geometrical constraints outlined in §4.2.2. These perturbations are not of the circulation- and impulse-preserving type described by Benjamin (1976). However, they are of interest because the perturbations experienced by forming vortex rings and dipoles in an experimental setting are also not of the type described by Benjamin (1976). The response of the entire Norbury family to this type of perturbations was considered, in order to bridge the gap between the observations of Ye & Chu (1995) for thin-cored rings and those of Pozrikidis (1986) for Hill's spherical vortex. In particular, we searched for a change in the perturbation response as we considered vortex rings of increasing core thickness. Finally, we considered the difference in the responses of the Norbury and Pierrehumbert families, to ascertain whether they reflect the differences observed in the formation of vortices in axisymmetric and two dimensional experiments.

Contour dynamics methods (Zabusky *et al.*, 1979; Shariff *et al.*, 2008) were employed to compute the nonlinear evolution of members of the Norbury and Pierrehumbert families subject to prolate shape perturbations. We identified a change in the perturbation response of vortex rings as we considered members of the Norbury family with progressively thicker

cores, and this change was found to be analogous to the onset of pinch-off in experimentally generated vortex rings. Furthermore, we found no such change in response when considering members of the Pierrehumbert family of increasing core size. This difference in behavior between the two families is akin to the absence of a critical time scale, or formation number, in two dimensional vortex dipole formation. Hence, we hypothesized that these findings on the perturbation response of low-order vortex models can be used to study and possibly predict pinch-off in real flows with more complex vorticity distributions.

The chapter is organized as follows. In §4.2 we introduce the mathematical formulation of the two vortex families, as well as the perturbation method and the contour dynamics procedures employed. This numerical method is employed in §4.3 and §4.4 to examine the nonlinear evolution of perturbed members of the Norbury and Pierrehumbert families, respectively. Finally, concluding remarks are presented in §4.5.

4.2 Mathematical formulation and numerical method

4.2.1 The Norbury and Pierrehumbert families of solutions

In two dimensions, the vorticity equation for inviscid, constant-density flow reduces to the following simple form:

$$\frac{D\omega}{Dt} = 0 \tag{4.1}$$

Evidently, this equation is satisfied for all time by any region of constant vorticity $\omega = \Omega$, where Ω is a constant. Therefore, one can find exact solutions to the Euler equation in two dimensions, which consist of one or more such patches of constant vorticity. These patches might translate and undergo deformations, but their area, impulse, and kinetic energy remain constant.

Similarly, in cylindrical coordinates (r,z,ϕ), the vorticity equation for inviscid, constant-density, axisymmetric flow without swirl ($u_\phi = 0$) is reduced to:

$$\frac{D}{Dt}\left(\frac{\omega}{r}\right) = 0 \tag{4.2}$$

In this case, the vorticity equation is satisfied for all time by any region containing a distribution of vorticity which is linear in r: $\omega = \Omega r$. Therefore, one can find exact solutions to the axisymmetric Euler equations, which consist of one or more toroidal or spherical regions with a linear distribution of vorticity. The position, cross-sectional area, or shape of these regions may vary, but their volume (of which the circulation is a constant multiple), impulse, and kinetic energy remain constant.

Norbury (1973) introduced a family of steadily translating solutions of the axisymmetric Euler equations, in the form of vortex rings with core boundary ∂A that satisfy:

$$\omega = \begin{cases} \Omega r & \text{inside } \partial A \\ 0 & \text{outside } \partial A \end{cases} \tag{4.3}$$

He classified these rings by the parameter $\alpha = \sqrt{\frac{A}{\pi R^2}}$, where A is the core cross-sectional area and R is the ring radius (defined as the radial distance to the center of the core). The parameter α is the ratio of the mean core radius to the ring radius, and it describes a family ranging from thin-cored vortex rings as α tends to zero, to Hill's spherical vortex for $\alpha = \sqrt{2}$. In figure 4.1(a), we present the calculated core boundary for Norbury vortices with various values of α, ranging from 0.2 to $\sqrt{2}$.

Similarly, Pierrehumbert (1980) found a family of steadily translating solutions to the two dimensional Euler equations, in the form of symmetric vortex pairs with boundary

$\partial A_{1,2}$ that satisfy:

$$\omega = \begin{cases} \Omega & \text{inside } \partial A_1 \\ -\Omega & \text{inside } \partial A_2 \\ 0 & \text{elsewhere} \end{cases} \tag{4.4}$$

Following Norbury (1973), the resulting family can also be parametrized by $\alpha = \sqrt{\frac{A_1}{\pi R^2}}$, where in this case R is defined as the distance from the symmetry axis to the center of one of the symmetric vortices. The Pierrehumbert family spans the range from point-like vortices as $\alpha \to 0$, to symmetry-axis-touching vortex pairs. Figure 4.1(b) shows the calculated core boundaries $\partial A_{1,2}$ of Pierrehumbert pairs for values of α ranging from 0.1 to 1.7.

The shapes of the members of the Norbury family were determined using the numerical method outlined in Norbury (1973), which required solving the integral equation for the streamfunction using a modified Newton-Raphson method. Similarly, the shapes of the members of the Pierrehumbert family were determined by solving the corresponding integral equation for the streamfunction using the relaxation method described in Pierrehumbert (1980). Note that the symmetry-axis-touching solution is not depicted in figure 4.1(b). Pierrehumbert (1980) found an axis-touching solution which included a cusp at the symmetry axis. Shortly thereafter, Saffman & Tanveer (1982) demonstrated that the axis-touching solution is not unique, and presented an alternative solution with no cusp. However, whether this solution is the limiting case for the Pierrehumbert family remains an open question (Saffman & Szeto, 1980). In this study, we have excluded the axis-touching case from the analysis for simplicity.

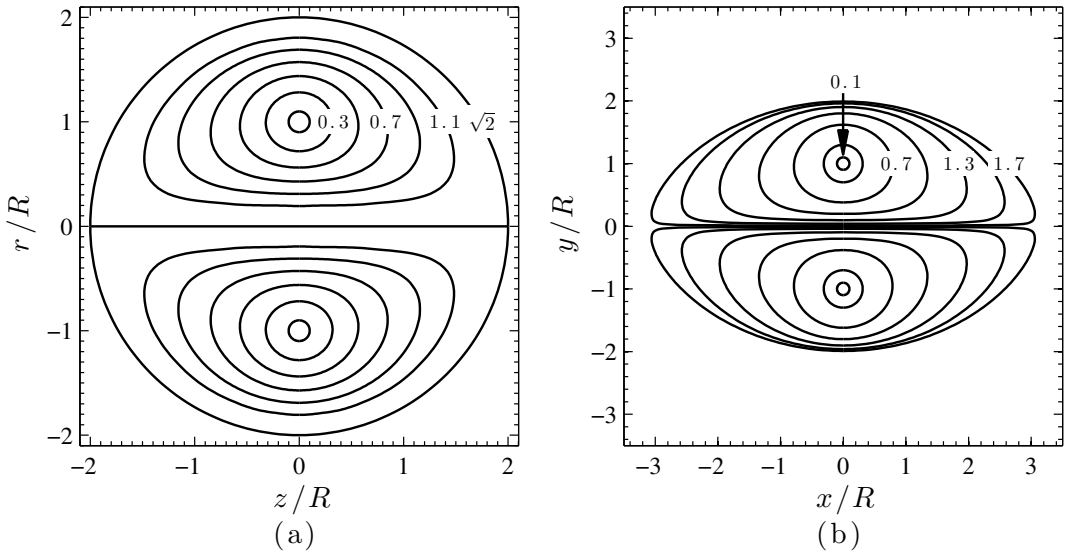

Figure 4.1: The Norbury (a) and Pierrehumbert (b) families of vortices. Core shapes for various values of α ranging from 0.2 to $\sqrt{2}$ (Norbury) and 0.1 to 1.7 (Pierrehumbert)

4.2.2 Shape perturbations

Pozrikidis (1986) studied the response of a limiting member of the Norbury family, namely a Hill's spherical vortex of radius $2R$, to prolate and oblate shape perturbations. He introduced the spheroidal perturbations by expressing the boundary of the vortex in the form:

$$\rho = 2R\gamma\left(1 + \frac{\epsilon}{4}(1 + 3\cos 2\zeta)\right) \tag{4.5}$$

where ρ and ζ are, respectively, the vortex radius and polar angle defined in figure 4.2. The spheroidal perturbations were achieved by introducing a perturbed second order Fourier mode which was scaled by a fraction of the unperturbed vortex radius ($\frac{3\epsilon}{2}R$), to the expression for the vortex core boundary. The sign of the parameter ϵ indicates the direction of the deviation from the spherical shape, with a positive value corresponding to an oblate perturbation and a negative value corresponding to a prolate perturbation. The factor $\gamma(\epsilon)$ was

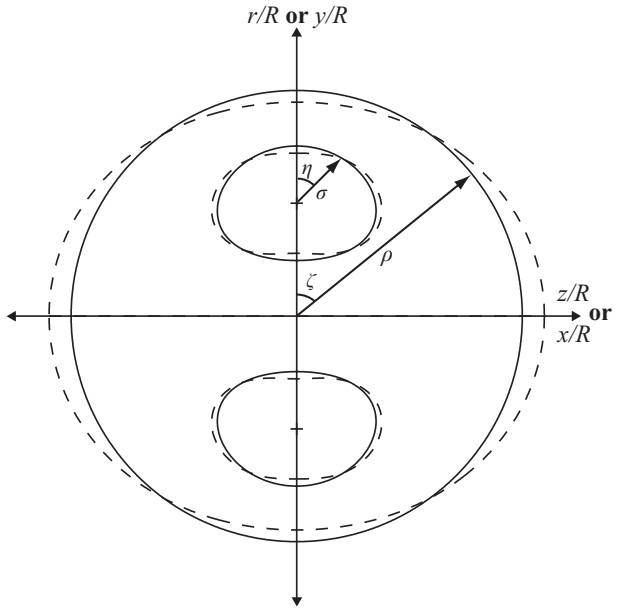

Figure 4.2: Perturbations and coordinates defined in the text. Hill's spherical vortex and a Norbury vortex with $\alpha = 0.6$ are depicted by the solid lines. The dashed lines represent a perturbation of $\epsilon = -0.1$ to Hill's spherical vortex, of the type studied by Pozrikidis (1986), as well as a perturbation to the Norbury vortex of $\delta = -0.1$ as defined in equation 4.7. The vortices propagate from left to right.

introduced to preserve the original vortex core circulation, implying that the perturbations constitute re-arrangements of the vorticity density ($\xi = \omega/r$).

In the formulation of Pozrikidis (1986), the vortex radius and polar angle were measured from the center of the spherical vortex, which is on the symmetry axis of the flow. In the more general case of the Norbury and Pierrehumbert families, however, such a formulation is not possible, as the vortex cores are not symmetry-axis-touching in general. As a result, the core boundary for each member of the Norbury and Pierrehumbert families was defined here in polar coordinates measured from the center of the core. In this coordinate system, the core boundary ∂A can be expressed in the form of a Fourier cosine polynomial:

$$\sigma = f(\eta, \alpha) = \sum_{j=0}^{N} a_j(\alpha) \cos j\eta \tag{4.6}$$

where N was chosen to be 30, and the quantities σ and η (defined in figure 4.2) are the local core radius and the polar angle measured from the center of the core, respectively. In this formulation, perturbations to the core boundary similar to those first introduced to circular vortex patches by Kelvin ($1880a$) can be readily introduced. Following Pozrikidis (1986), we introduced shape perturbations to ∂A by adding a fraction of the mean core radius ($\delta\alpha R$) to the second-order mode:

$$\sigma = f(\eta,\alpha) = \gamma \sum_{j=0}^{N} a'_j(\alpha)\cos j\eta \tag{4.7}$$

$$a'_2 = a_2 + \delta\alpha R \tag{4.8}$$

$$a'_j = a_j \quad \text{for} \quad j \neq 2 \tag{4.9}$$

δ expressed the deviation from the unperturbed shape, and it took on positive values for oblate perturbations and negative values for prolate perturbations. For consistency with the previous studies by Pozrikidis (1986) and Ye & Chu (1995), the factor $\gamma(\alpha,\delta)$ was introduced in order to preserve the unperturbed core circulation. For each member of the family and perturbation size δ, analytical expressions for the circulation of the perturbed and unperturbed vortices were obtained by integrating the vorticity over the regions described by equations 4.6 and 4.7—4.9. To meet the requirement that the circulation remain unchanged, these two expressions were equated and the value of the multiplicative constant $\gamma(\alpha,\delta)$ was determined by solving the resultant cubic equation.

Like the perturbations introduced by Pozrikidis (1986), these perturbations constitute re-arrangements of the unperturbed vorticity (in the two dimensional case) or the vorticity density (in the axisymmetric case). However, both types of perturbations differ from those described by Benjamin (1976) in that the perturbed vortices do not preserve the un-

perturbed vortex impulse. These perturbations are of interest because the perturbations encountered by vortex rings and dipoles in an experimental setting are also not of the impulse- and circulation-preserving type described by Benjamin (1976). Furthermore, the fact that, in his study of Hill's vortex, Pozrikidis (1986) reported a detrainment of circulation analogous to pinch-off utilizing these types of perturbations, suggests that they are suited for the study of an analogue to pinch-off in the Norbury and Pierrehumbert families.

The perturbations described in equations 4.7—4.9 differ from those described in equation 4.5, in that Pozrikidis perturbed only the shape of the outer boundary of the vortex core (a semi-circle of radius $2R$) while scaling the portion of the boundary nearest the symmetry axis (for Hill's spherical vortex, a straight line at the symmetry axis), in order to preserve the continuity of the core boundary. In contrast, our formulation results in a perturbation being introduced to the entire core boundary. As a result, for Hill's spherical vortex, our perturbation is not equivalent to the type of perturbations considered by Pozrikidis (1986). Hence, the perturbation scheme described in equation 4.5 was employed in validating our implementation of the numerical method described in the following section against the results of Pozrikidis (1986) (§4.2.5). Subsequently, however, the perturbations described in equations 4.7—4.9 were applied in order to investigate the nonlinear perturbation response of the Norbury and Pierrehumbert families.

4.2.3 Contour dynamics formulation

The evolution of the perturbed vortex cores was computed using contour dynamics methods. The original two dimensional contour dynamics solution is due to Zabusky *et al.* (1979); however, we employed an alternative formulation from Pullin (1981). The velocity induced by one of the symmetric vortex patches in a Pierrehumbert pair at a point $z = x + iy$ in

the complex plane was computed using:

$$u_x + iu_y = -\frac{\Omega}{4\pi}\oint_{\partial A}\frac{\mathrm{z}-\mathrm{z}'}{\bar{\mathrm{z}}-\bar{\mathrm{z}}'}\mathrm{dz}' \tag{4.10}$$

Shariff *et al.* (2008) extended the contour dynamics method to the case of axisymmetric vortex rings with a linear vorticity distribution in the radial direction, such as the Norbury family. In this case, the velocity induced by a compact region of vorticity A at a point $\mathbf{x}$ is given by:

$$\begin{aligned}
\mathbf{u}(\mathbf{x}) &= \Omega\oint_{\partial A}[(z-z')G(s')\cos\theta' - rH(s')\sin\theta']\hat{z} + r'H(s')\cos\theta'\hat{r}\,\mathrm{d}s' && (4.11)\\
G(s') &= \frac{r'}{\pi\sqrt{C+B}}K(k) && (4.12)\\
H(s') &= \frac{1}{2\pi r}\left(\frac{C}{\sqrt{C+B}}K(k) - E(k)\sqrt{C+B}\right) && (4.13)\\
k &= \sqrt{\frac{2B}{C+B}} && (4.14)\\
C &= (z-z')^2 + r^2 + r'^2, \quad B = 2rr' && (4.15)
\end{aligned}$$

where $\theta(s',\alpha)$ is the angle of the outward-pointing normal relative to the symmetry axis, and $K(k)$ and $E(k)$ are the complete elliptic integrals of the first and second kind, respectively.

4.2.4 Numerical method

The contour dynamics formulation reduces the evolution problem to tracking the motion of a collection of marker points on the core boundary by numerical integration of equation 4.10 or equation 4.11. Contour integration was performed by discretizing the boundary using linear segments, and evaluating the contribution from segments not adjacent to the field

point using Gaussian quadrature. The singularities in the evolution equations were dealt with by explicit evaluation in the two dimensional case, and using the method outlined by Shariff *et al.* (2008) in the axisymmetric case.

The solution was marched forward in time using a fourth-order Runge-Kutta scheme. At each time step, additional marker points were inserted where the linear segments stretched beyond $0.016R$, and removed where segments shrunk below $0.004R$ (Shariff *et al.*, 2008). Following Shariff *et al.* (2008), the time step was chosen to satisfy $\Delta t = \frac{0.05}{\Omega_0}$, where Ω_0 is the vorticity at the center of the vortex ring core in the axisymmetric case ($\Omega_0 = \Omega R$), or the strength of the positively signed vortex patch in the two dimensional case. The flow invariants (circulation, impulse, and energy) were monitored and their change was kept below 0.01% over one eddy turnover period for the impulse and circulation, and 0.02% over the same period for the energy.

4.2.5 Verification

In order to validate our implementation of the numerical algorithms described in the preceding section, we began by considering the response of Hill's spherical vortex to spheroidal shape perturbations of the type investigated by Pozrikidis (1986) and described in equation 4.5. Figure 4.3 illustrates the response of Hill's spherical vortex to a small amplitude prolate perturbation with $\epsilon = -0.05$. The perturbed vortex is seen to detrain rotational fluid into a vortex tail (figure4.3(c)), which experiences continual elongation (figure 4.3(d)) and tends to form an independent low-circulation entity which trails behind the ring (figure 4.3(e)). As noted by Gharib *et al.* (1998), the shedding of rotational fluid into a vortex tail is akin to the pinch-off phenomenon observed in experimentally generated vortex rings.

The results presented in figure 4.3 agree qualitatively with the results of Pozrikidis

(1986) for a spherical vortex subjected to the same perturbation, and computed using a different contour dynamics formulation and numerical scheme (cf. figure 2 in Pozrikidis (1986)). In figure 4.4(a) we present the deviation of the non-dimensional vorticity centroid location from its unperturbed equivalent ($z_c^* = (Ut - z_c)/R$, defined in Pozrikidis (1986)) as a function of non-dimensional time $t^* = Ut/R$, where U is the translational speed of the unperturbed spherical vortex. The lines indicate the present results for vortices subjected to perturbations of $\epsilon = -0.05$, $\epsilon = -0.15$, and $\epsilon = -0.3$, and the symbols indicate the results of Pozrikidis (1986) for the same perturbations. Similarly, figure 4.4(b) shows the present measurements of the time evolution of the vortex speed ($U_c = \mathrm{d}z_c^*/\mathrm{d}t^*$) for the same three perturbation sizes, as well as those of Pozrikidis (1986). In both figures 4.4(a) and 4.4(b), the agreement with Pozrikidis (1986) was found to be excellent.

4.3 Response of the Norbury family of vortex rings

Having validated our implementation of the numerical method described in §4.2.4, we considered the response of the remaining members of the Norbury family to shape perturbations of the type described in equations 4.7—4.9. Pozrikidis (1986) reported detrainment of circulation into a vortex tail only for prolate shape perturbations, a phenomenon of interest because it is analogous to pinch-off. Therefore, we limited our study to the response of the remainder of the family to prolate perturbations, with the goal of characterizing the response of the entire Norbury family and investigating the extent of the shedding behavior. We simulated the evolution of members of the Norbury family with α ranging from 0.2 to 1.2, subject to prolate perturbations with $\delta = -0.01$, $\delta = -0.02$, and $\delta = -0.05$.

Figures 4.5 through 4.7 show the evolution of different Norbury vortices subjected to a perturbation of 5% of the mean core radius ($\delta = -0.05$). Thin cored-members of the

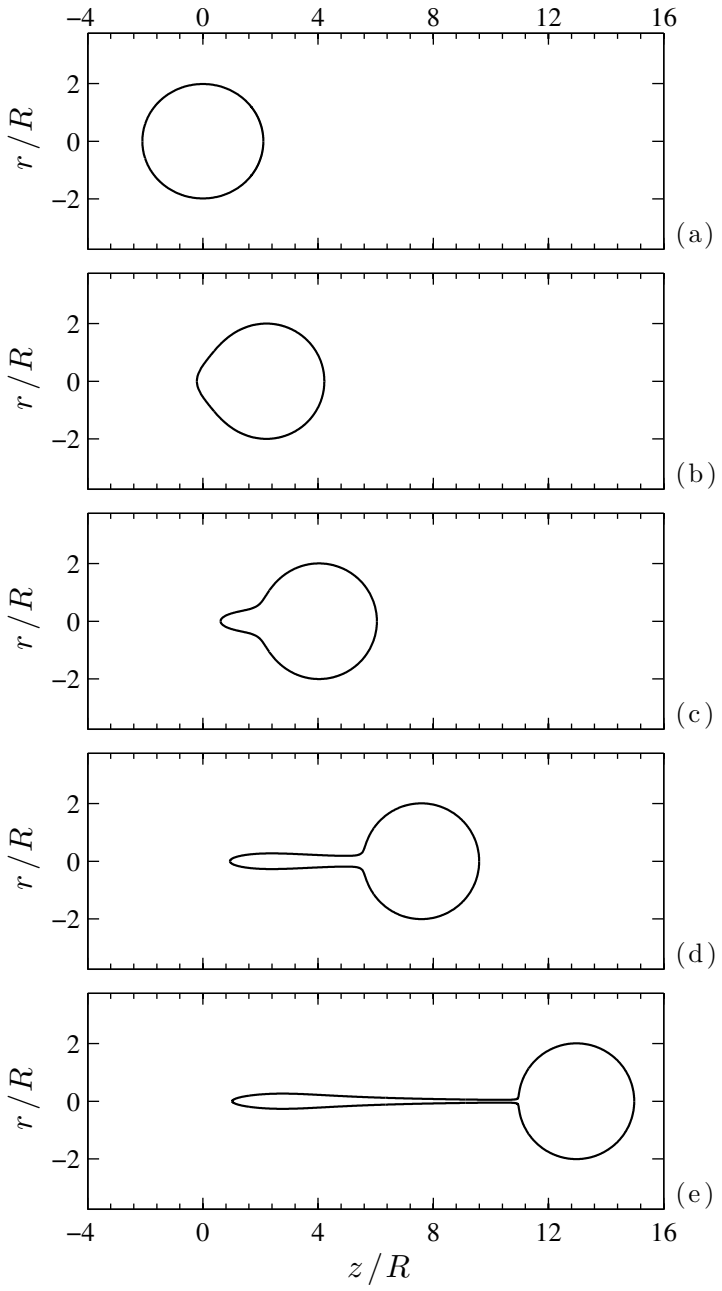

Figure 4.3: Evolution of Hill's spherical vortex subject to a Pozrikidis perturbation with $\epsilon = -0.05$ at: (a) $t^* = 0$; (b) $t^* = 2.1$; (c) $t^* = 4.0$; (d) $t^* = 7.4$; (e) $t^* = 12.8$

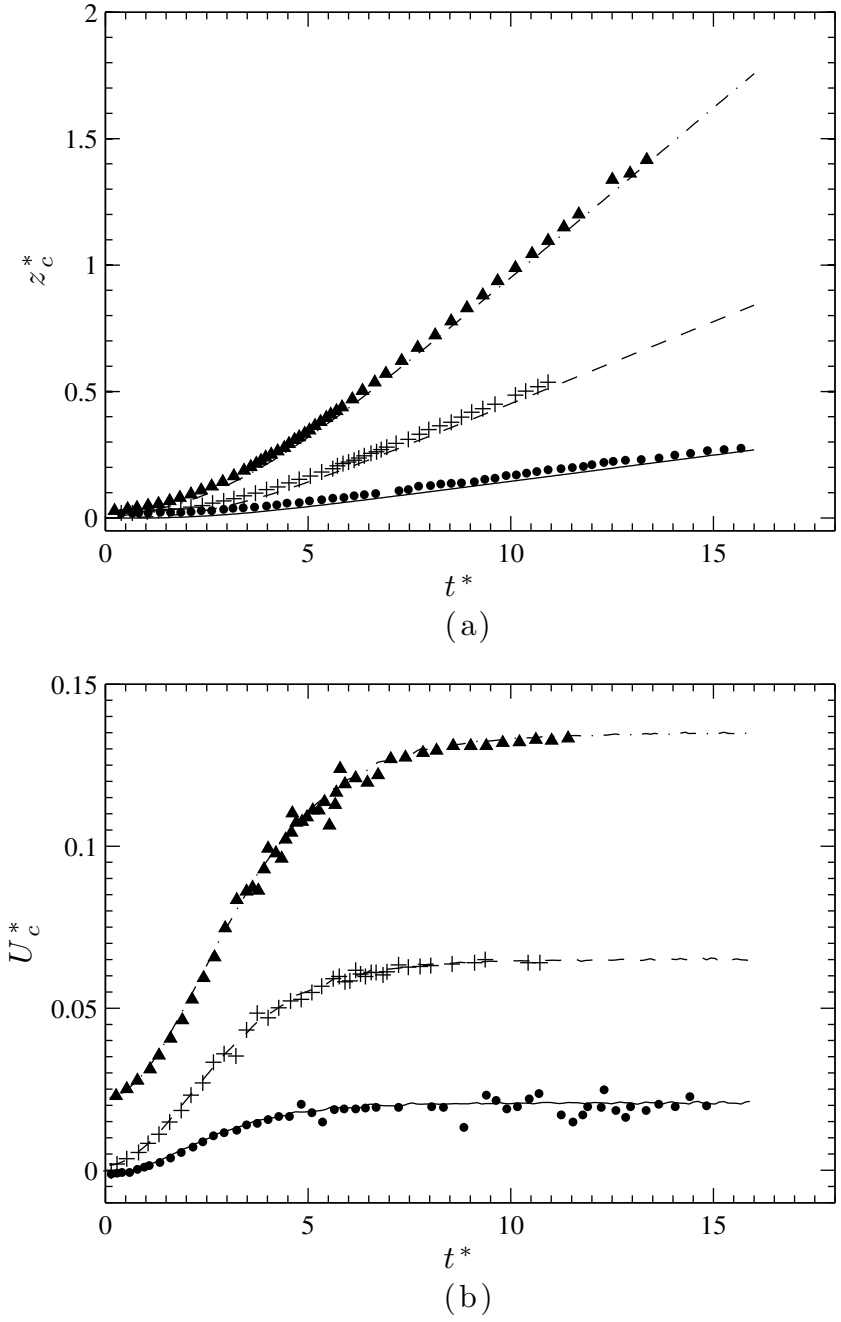

Figure 4.4: Evolution of (a) the deviation of the vorticity centroid from the unperturbed centroid ($z_c^* = (Ut - z_c)/R$) and (b) the vortex speed $U_c^* = dz_c^*/dt^*$ for prolate Pozrikidis perturbations. The symbols show the results of Pozrikidis (1986) for: •, $\delta = -0.05$; +, $\delta = -0.15$; ▲, $\delta = -0.3$. The lines show our results for these same perturbations: (—), $\delta = -0.05$; (– –), $\delta = -0.15$; (–·–); $\delta = -0.3$.

family ($\alpha < 0.7$) were found to propagate along the axial direction whilst their vortex cores underwent a quasi-periodic deformation. Eventually, the formation of small mounds on the core boundary led to the development of thin filaments, which wrapped around the vortex core. The filamentation of the vortex is a common feature in vortex dynamics, and it is observed even in linearly stable configurations (Saffman, 1992; Dritschel, 1988*b*,*a*; Deem & Zabusky, 1978; Crowdy & Surana, 2007). Thus, Pozrikidis (1986) and Ye & Chu (1995) remark that the appearance of thin filaments is of negligible importance to the dynamics of the perturbed vortex. Figure 4.5 depicts the evolution of a Norbury vortex with $\alpha = 0.5$ subject to a perturbation of $\delta = -0.05$. Initially, the vortex core was found to undergo a quasi-periodic shape deformation (figures 4.5(a)-(c)). The small deformation which was initially seen to propagate along the contour (figures 4.5(b) and (c)), eventually sharpened into a corner (figure 4.5(d)) and developed into a thin filament by $t^* = Ut/R = 6.75$ (Figure 4.5(e)).

For members of the Norbury family with increasing core thickness, the core cross-section increasingly resembled a semi-circle, and the curvature of the portion of the boundary closest to the symmetry axis approached zero. The perturbation scheme outlined in equations 4.7—4.9 therefore resulted in a perturbed vortex shape that was locally concave (see figure 4.2). As these vortices evolved, the region of concavity propagated along the contour, due to the motion of the rotational fluid within. Once the region of concavity reached the corner near the front of the vortex, it led to the formation of a small mound on the contour, which rapidly developed into a vortex filament. The filamentation of a sufficiently perturbed vortex has been observed consistently in previous studies (Saffman, 1992; Dritschel, 1988*b*,*a*; Deem & Zabusky, 1978; Crowdy & Surana, 2007), and as such the emission of a filament by these perturbed Norbury vortices is to be expected. What is particular to these vortices is the

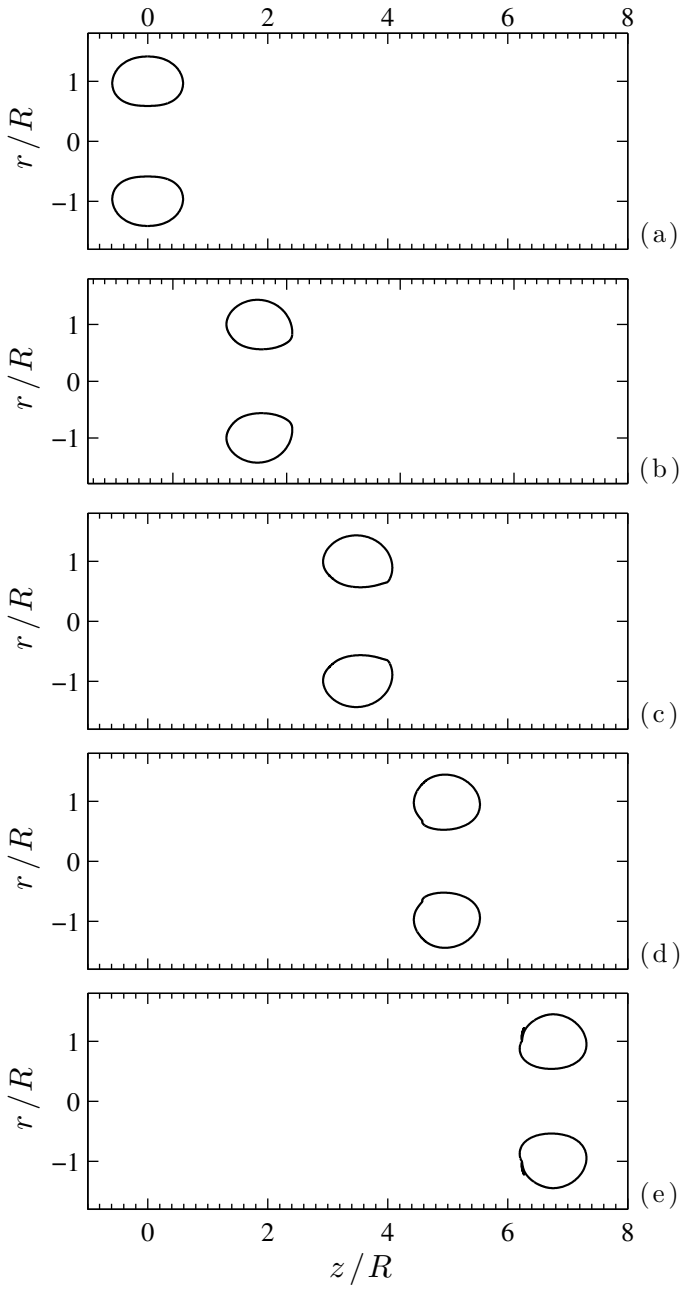

Figure 4.5: Evolution of a Norbury vortex with $\alpha = 0.5$ subject to a prolate perturbation of $\delta = -0.05$ at: (a) $t^* = 0$; (b) $t^* = 1.5$; (c) $t^* = 3.5$; (d) $t^* = 5$; (e) $t^* = 6.75$

development of the filament consistently at the location of the region of initial concavity, by the mechanism described above.

Figure 4.6 depicts the behavior typical of Norbury vortices with $0.7 < \alpha < 0.95$, when subjected to a perturbation of $\delta = -0.05$. In figure 4.6(a), a perturbed Norbury vortex with $\alpha = 0.9$ exhibits a region of local concavity on the portion of its boundary nearest the symmetry axis of the ring. A small mound was seen to develop as the region of concavity reached the front of the vortex, which by $t^* = 2.5$ had developed into a sharp spike (figure 4.6(b)). At later times, this spike was seen to develop into a thin filament which wrapped around the vortex core (figures 4.6(c)-(e)). The filament increased in length as the simulation progressed, however no detrainment of circulation into a trailing vortex tail was observed. These results are in good qualitative agreement with those of Ye & Chu (1995), who considered the unsteady evolution of a Norbury vortex with $\alpha = 0.8$, subject to a perturbation of $\delta = -0.15$.

However, for thicker-cored members of the family subject to perturbations of the same size, a change in response was observed. For Norbury vortices with $\alpha > 0.95$, the introduction of a prolate perturbation with $\delta = -0.05$ resulted in the detrainment of rotational fluid into a vortex tail which lingered behind the vortex ring. Figure 4.7 shows the evolution of a Norbury vortex with $\alpha = 1.2$, subject to a perturbation of this magnitude. Initially, excess rotational fluid from the outer regions of the core was convected towards the rear of the vortex (figure 4.7(b)). Figures 4.7(c)-(e) depict the elongation of this region of accumulated vorticity, under the influence of the high-strain region near the rear stagnation point, into a long tail which lingered behind the vortex ring and formed an independent low-circulation entity. These observations are consistent with the results of Pozrikidis (1986) for the evolution of Hill's spherical vortex under similar shape perturbations, as well as with

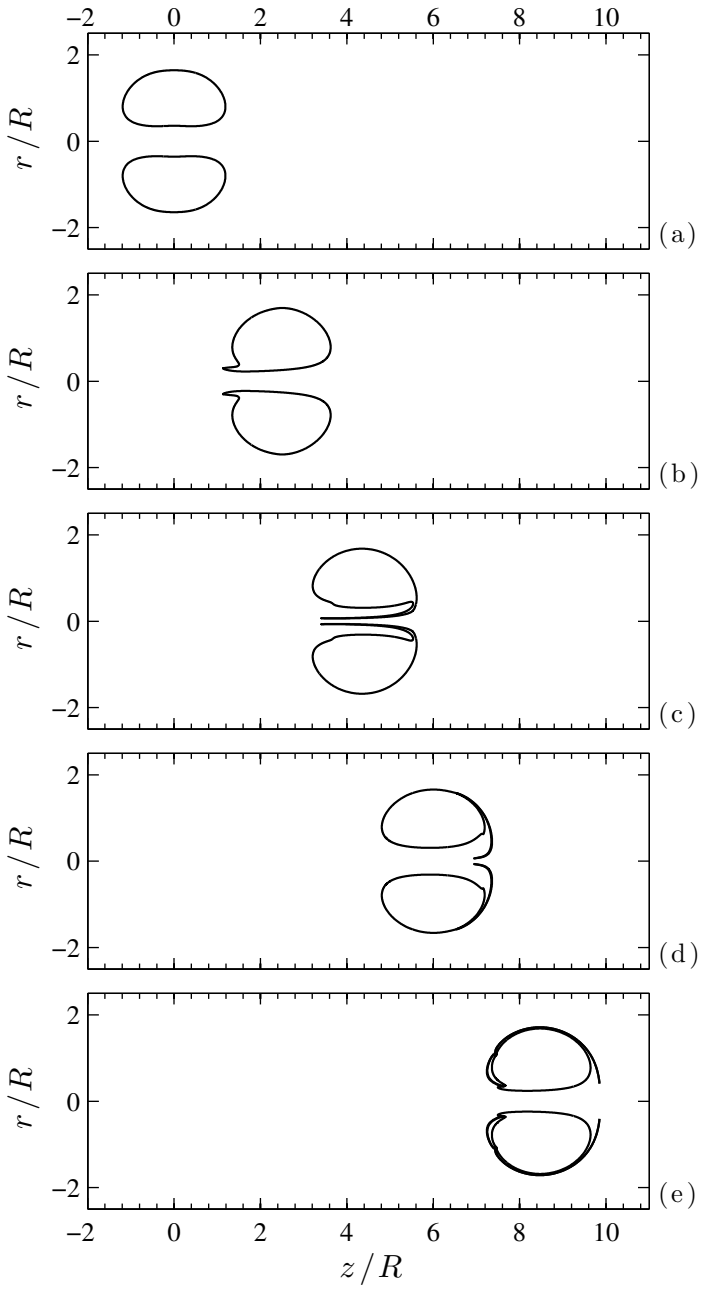

Figure 4.6: Evolution of a Norbury vortex with $\alpha = 0.9$ subject to a prolate perturbation of $\delta = -0.05$ at: (a) $t^* = 0$; (b) $t^* = 2.5$; (c) $t^* = 4.5$; (d) $t^* = 6$; (e) $t^* = 8.5$

the observations of Gharib *et al.* (1998) for experimentally generated vortex rings above a formation time of $\hat{T} = \overline{U}_p t/D = 4$.

In comparing the shedding of a vortex tail by a perturbed Hill's vortex and the phenomenon of pinch-off, Gharib *et al.* (1998) found that the processes are analogous, since both occur when patches of rotational fluid at the outer regions of the core are no longer contained within the region of fluid translating with the vortex ring, and are hence convected to the rear of the vortex. In doing so, the excess rotational fluid enters the high-strain region near the rear stagnation point and is elongated, under the influence of the stagnation-point flow, to form a vortex tail. In nearly spherical members of the Norbury family, the boundary of the vortex core lies close to the stagnation streamline. Consequently, a large enough shape perturbation was found to lead to the presence of excess rotational fluid in the region were fluid particles were being swept past the ring. The excess vorticity was hence convected to the rear of the vortex, were the proximity of the rear stagnation point resulted in its detrainment into a tail. In contrast, for thin-cored members of the Norbury family, the excess vorticity was found to revolve around the vortex core and eventually cause filamentation, but it was not detrained due to the remoteness of the rear stagnation point.

A simple metric for comparing the response of the different members of the family is the contour length of the vortex tail or filament after one eddy turnover ($\Delta\ell$), expressed as a percentage of the initial contour length. In figure 4.8 we present the contour length ($\Delta\ell$) as a function of the parameter α for three different perturbation sizes: $\delta = -0.05$, $\delta = -0.02$, and $\delta = -0.01$. The results for $\delta = -0.05$ form a curve with three distinct sections, labeled I, II, and III in figure 4.8. For small values of α, the change in the contour length is negligible, since these thin-cored rings were found to undergo quasi-periodic deformations for several eddy turnovers before thin filaments began to develop (region I). For values of α in the 0.7-

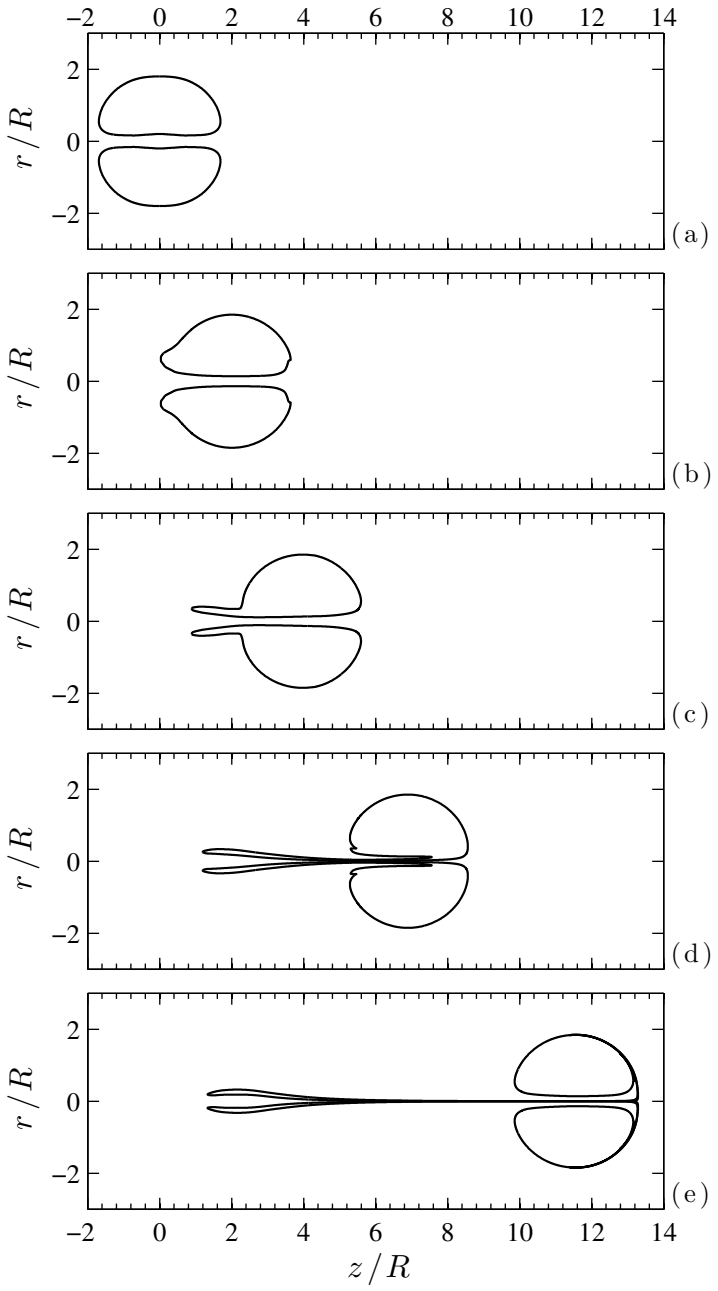

Figure 4.7: Evolution of a Norbury vortex with $\alpha = 1.2$ subject to a prolate perturbation of $\delta = -0.05$ at: (a) $t^* = 0$; (b) $t^* = 2$; (c) $t^* = 4$; (d) $t^* = 7$; (e) $t^* = 11.7$

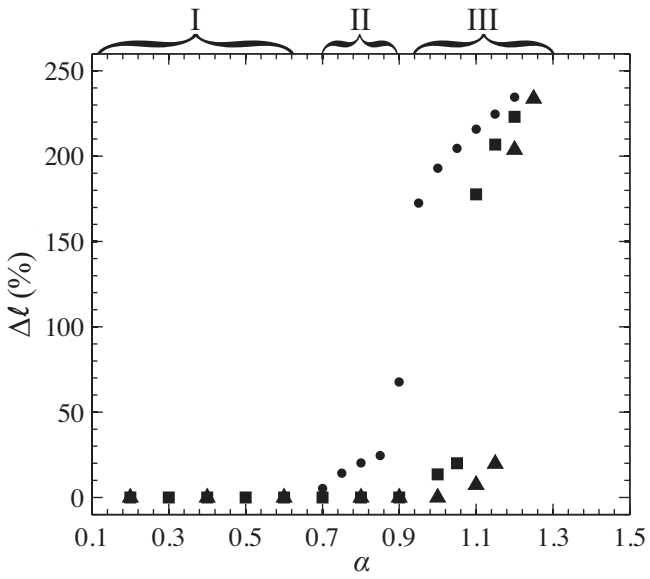

Figure 4.8: Contour length of the tail or filament after one eddy turnover (expressed as a percentage of the initial contour length) for members of the Norbury family subject to perturbations of different magnitudes: ▲, $\delta = -0.01$; ■, $\delta = -0.02$; •, $\delta = -0.05$.

0.95 range, $\Delta\ell$ increases with increasing core thickness (region II). This region corresponded to the members of the family for which a perturbation of this magnitude resulted in an initial core shape which exhibits regions of local concavity. For these vortices, thin filaments were found to develop immediately, and result in a finite $\Delta\ell$ after one eddy turnover.

The most salient feature of the curve, however, is the sharp increase in contour length when the core thickness parameter is increased past $\alpha = 0.95$ (region III). This discontinuity coincides with the first instance of tail shedding in the family, and is indicative of a change in the response of the Norbury family to perturbations of this size. The sharp increase in $\Delta\ell$ is also evident in the results for $\delta = -0.02$ and $\delta = -0.01$, shown in figure 4.8, and it was also found to coincide with the onset of trailing vortex tail formation for perturbations of these sizes. Notably, the value of α at which the detrainment of circulation into a tail was first observed appeared to be dependent on the perturbation size.

When simulating the evolution of vortex configurations which tend to form thin fila-

ments, a technique known as contour surgery, developed by Dritschel (1988*b*), is sometimes employed. This technique allows for the simulation of vortices, whose computational costs would otherwise be prohibitive due to the large numbers of segments necessary for discretization of the filaments, for long times after the formation of filaments. In the preceding figures, on the other hand, contour surgery was not applied. Instead, the filaments and vortex tails were allowed to grow, in order to observe the initial development of the instability. In his study of perturbations to Hill's spherical vortex, however, Pozrikidis (1986) was able to continue simulating the evolution of vortex rings after the formation of long filaments and tails, by excising the filaments and continuing the simulation of the vortex without the tail or filament. Furthermore, Pozrikidis (1986) found this simplification to have a negligible effect on the accuracy of the simulations of the evolution of the remaining vorticity. Therefore, following Pozrikidis (1986), we excised the filaments or tail after one eddy turnover, and continued the evolution of the vortices in the Norbury family without them.

By excising the vortex filaments, we observed the development of the perturbed vortices into nearly steady vortex rings whose asymptotic shape was another member of the Norbury family. Figure 4.9 shows the non-dimensional kinetic energy ($\bar{E} = E/(\varrho\Omega^2 R^7)$) as a function of the non-dimensional circulation ($\bar{\Gamma} = \Gamma/(\Omega R^3)$), for steadily translating and perturbed members of the Norbury family. The solid line depicts the $\bar{\Gamma}$-$\bar{E}$ curve for the unperturbed members of the Norbury family, while the black dots represent the initial circulation and energy of the perturbed vortices ($\delta = -0.05$), and the crosses represent the asymptotic states. Since the perturbations are circulation-preserving, the perturbed vortices are shifted downwards from the unperturbed curve by an amount $\Delta\bar{E}(\alpha)$, which is greater for thicker-cored members of the family. The perturbed vortices in regions I and II were found to

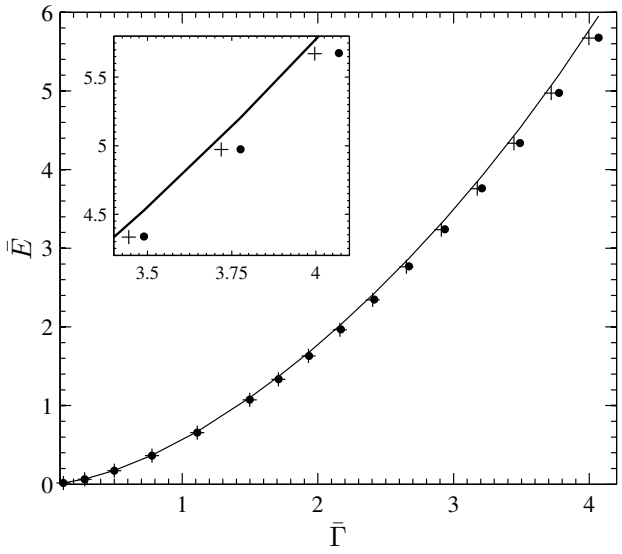

Figure 4.9: Kinetic energy ($\bar{E}$) vs. circulation ($\bar{\Gamma}$) for Norbury vortices subject to a perturbation of $\delta = -0.05$. The solid line shows the $\bar{\Gamma}$-$\bar{E}$ curve for the unperturbed Norbury family. The filled dots represent the initial circulation and energy of the perturbed vortices. The crosses represent the values that the perturbed vortices asymptote to after contour surgery. These same quantities are shown on the inset, which focuses on the thick-cored members of the family.

lose small amounts of both energy and circulation through filamentation, as their shape slowly approached a nearly steady state with a slightly smaller mean core radius than they originally possessed. In contrast, in detraining circulation into a vortex tail, the vortices in region III rapidly shed circulation and a comparatively small amount of kinetic energy. This resulted in a near-horizontal shift in the $\bar{\Gamma}$-$\bar{E}$ curve, as shown in figure 4.9. After the initial detrainment, these vortices continued to approach a steady state by successively losing small amounts of circulation and energy by filamentation, much like the vortices in regions I and II.

The nonlinear response of the Norbury family to arbitrary shape perturbations intended to resemble those encountered by experimentally generated vortex rings (such as adding a 'tail' of vorticity to the rear of a Norbury vortex) was also considered. For these perturba-

tions, the results were qualitatively similar to those reported above for prolate shape perturbations, with thick-cored members of the family exhibiting detrainment of circulation, and thinner-cored members displaying only filamentation. However, these perturbations were found to be of use when considering more complex models for vortex rings, and are described in §5.6.

4.4 Response of the Pierrehumbert family of vortex pairs

Unlike that of the Norbury family, the stability of the Pierrehumbert family has been the subject of numerous contour dynamics studies. Dritschel (1995) examined the linear stability of the family of dipoles, and used contour dynamics to find the nonlinear stability bounds for asymmetric perturbations. Recently, Makarov & Kizner (2011) used contour dynamics methods to show that all members of the Pierrehumbert family are stable with respect to symmetric perturbations. However, the nonlinear response of this family to prolate perturbations of the type described in §4.2 has not been previously reported. Since a comparison between the perturbation responses of the two families is instructive, we considered the response of several members of the Pierrehumbert family to perturbations of the same kind and size as those introduced to the Norbury family.

Given the recent results of Makarov & Kizner (2011) it is unsurprising that, in the case of the Pierrehumbert family, we found no evidence of detrainment of rotational fluid into a trailing vortex tail, even when thick-cored members of the family were subjected to the largest of the perturbations considered ($\delta = -0.05$). Figure 4.10 depicts the evolution of a Pierrehumbert vortex pair with $\alpha = 1.2$ under a perturbation of $\delta = -0.05$. The cores of the vortices in this pair are quite thick, yet the pair's behavior resembled that of the thin-cored Norbury vortex depicted in figure 4.5. The vortex cores were observed to undergo

quasi-periodic shape deformations, and thin filaments eventually began to form where the perturbed cores were locally concave, much like in the thin-cored members of the Norbury family.

Figure 4.11 shows a plot of the excess energy ($\bar{E} = E/(\varrho\Omega^2 R^4)$) as a function of circulation ($\bar{\Gamma} = \Gamma/(\Omega R^2)$) for the unperturbed Pierrehumbert family (solid line), and for the initial and asymptotic states of the members of this family subject to shape perturbations with $\delta = -0.05$ (filled circles and crosses, respectively) . It is interesting to note that, in the case of the Pierrehumbert family, symmetric perturbations of the same type and size as those introduced to the Norbury family result in very small changes in the excess energy of the dipoles. Whereas for the Norbury family, perturbations with $\delta = -0.05$ resulted in decreases in the kinetic energy of the perturbed vortex of up to 4.5%, in this case the change was found to be less than 0.3%. Furthermore, it was found that producing percentage decreases in the energy on the order of those observed for the Norbury family required introducing perturbations so extreme that the perturbed vortices resembled figure-eights (figure 4.12). This robustness of the of the energy to shape perturbations leads to the observed absence of tail shedding.

4.5 Conclusions

The nonlinear response of the Norbury family of axisymmetric vortex rings to prolate shape perturbations was considered in this chapter. Our contour dynamics computations suggest that, for prolate shape perturbations, there is a dynamical change in the perturbation response as we traverse the Norbury family from thin-cored members to thicker-cored vortex rings, which is analogous to the onset of pinch-off in experimentally generated vortex rings. Thin-cored vortex rings were found to undergo quasi-periodic shape deformations, and to

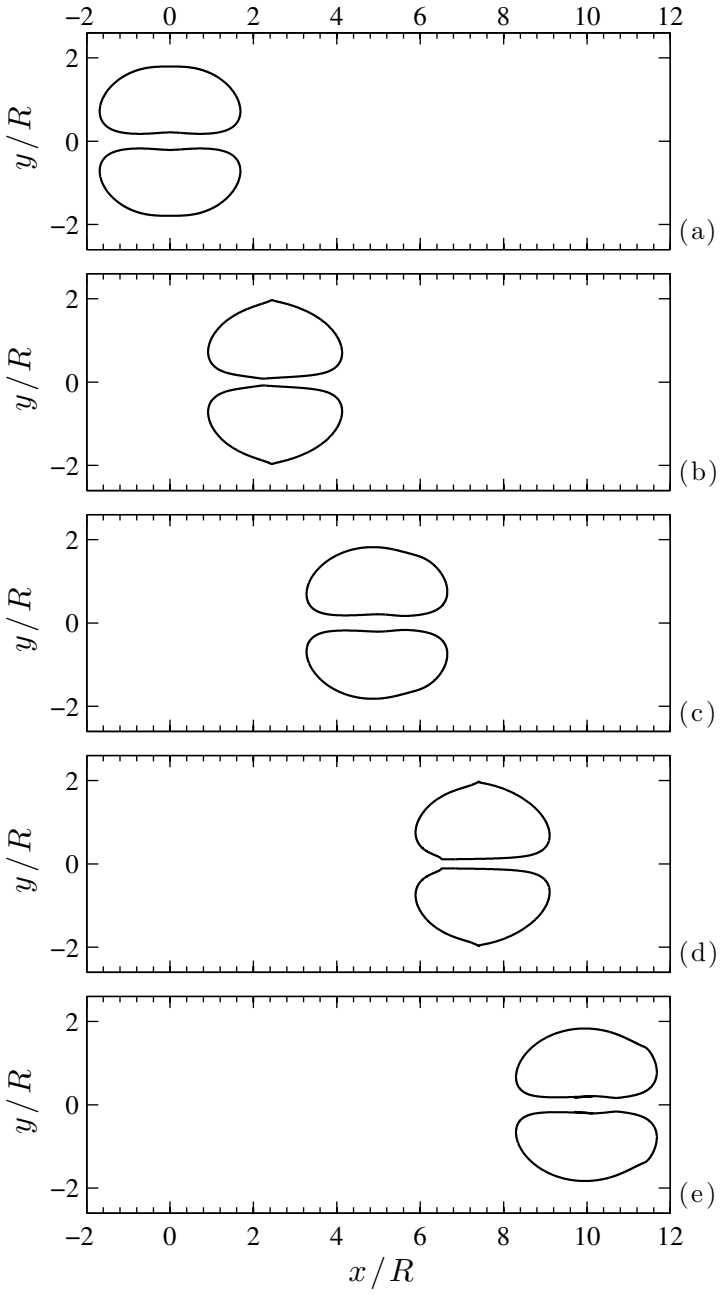

Figure 4.10: Evolution of a Pierrehumbert vortex with $\alpha = 1.2$ subject to a prolate perturbation of $\delta = -0.05$ at: (a) $t^* = 0$; (b) $t^* = 2.5$; (c) $t^* = 5$; (d) $t^* = 7.5$; (e) $t^* = 10$

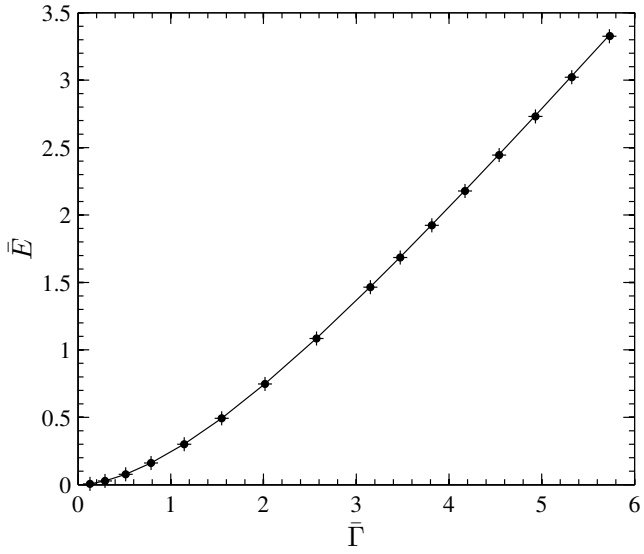

Figure 4.11: Excess kinetic energy ($\bar{E} = E/(\varrho\Omega^2 R^4)$) vs. circulation ($\bar{\Gamma} = \Gamma/(\Omega R^2)$) for Pierrehumbert vortices subject to a perturbation of $\delta = -0.05$. The solid line shows the $\bar{\Gamma}$-$\bar{E}$ curve for the unperturbed Pierrehumbert family. The filled dots represent the initial circulation and energy of the perturbed vortices. The crosses represent the values that the perturbed vortices asymptote to after contour surgery.

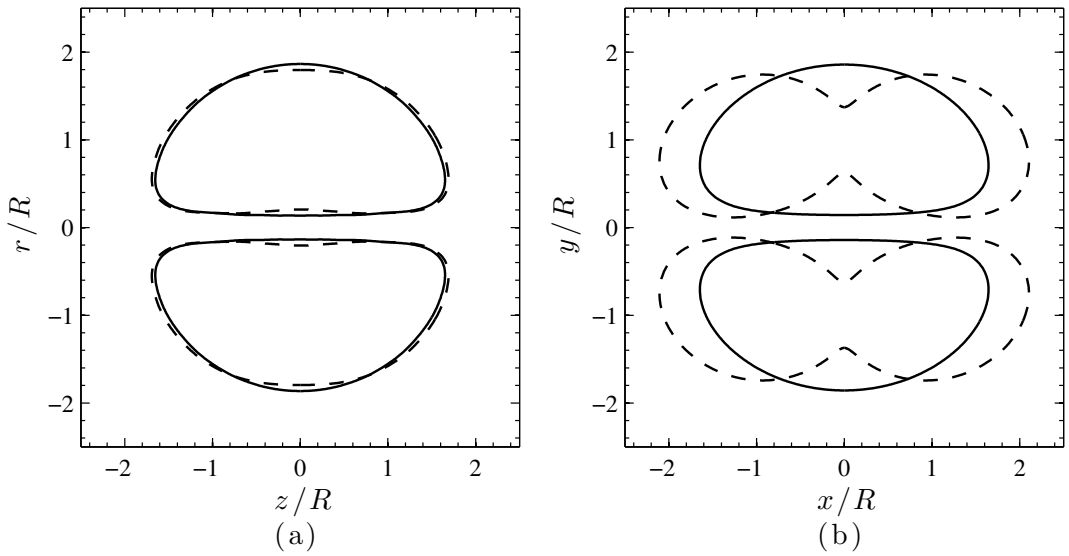

Figure 4.12: Insensitivity of the kinetic energy in the Pierrehumbert family, relative to the Norbury family. (a) Norbury vortex with $\alpha = 1.2$ (—), along with the prolate perturbation which leads to a 5% change in $\bar{E}$ (– –). (b) Pierrehumbert vortex with $\alpha = 1.2$ (—), along with the prolate perturbation which leads to a 5% change in $\bar{E}$ (– –).

eventually develop thin filaments which were largely dynamically unimportant. In contrast, in thick-cored vortex rings we observed the transport of excess rotational fluid from the outer boundaries of the core to the rear of the vortex, which led to the development of a trailing vortex tail and the detrainment of circulation into a separate trailing entity.

While the behaviors of Hill's spherical vortex and of one thin-cored member of the family under similar conditions have been previously reported, the present results illustrate the behavior of the entire family in a manner consistent with the results of Pozrikidis (1986) and Ye & Chu (1995) for these two special cases. Furthermore, the change in response observed as we traversed the Norbury family is consistent with experimental observations of the formation of circular vortex rings. Thick-cored vortex rings have been shown to detrain excess vorticity into a trailing jet in numerous experiments (Gharib *et al.*, 1998; Dabiri & Gharib, 2004*a*; Krueger *et al.*, 2006; Pawlak *et al.*, 2007). As Gharib *et al.* (1998) remark, this process is analogous to the detrainment of circulation into a tail by thick-cored members of the Norbury family observed in this study.

In contrast, we found no evidence of detrainment of circulation or tail shedding for members of the Pierrehumbert family of all core sizes subject to equivalent perturbations. This suggests a difference in the perturbation response of the two dimensional family compared to the axisymmetric Norbury family, which is attributed to the insensitivity of the kinetic energy of the Pierrehumbert dipoles to shape perturbations of the type considered (figure 4.11). This difference in response is of interest because it mirrors the observed differences in the vortex formation processes in the two dimensional and axisymmetric configurations. Recent studies by Nitsche (2001), Afanasyev (2006) and Pedrizzetti (2010) suggest that the limiting time scale for axisymmetric vortex ring formation does not apply to the formation of two dimensional vortex dipoles. In light of our findings for the Norbury family, the ab-

sence of tail shedding for any members of the Pierrehumbert family is in good agreement with these studies.

The present results show that only instantaneous shape perturbations to low-order vortex patch models are required to produce a change in response between thin-cored vortex rings and thicker-cored rings which is consistent with experimental results, whereas no such transition is evident in vortex dipoles of any size. This is of particular interest given that the Norbury family has been successfully employed to model the growth of experimental vortex rings (Gharib *et al.*, 1998; Mohseni & Gharib, 1998; Shusser & Gharib, 2000; Linden & Turner, 2001), and that Afanasyev (2006) has noted that vortex dipoles closely resemble members of the Pierrehumbert family during their development.

The results of this study suggest the existence of a relationship between vortex formation and the perturbation response of the leading vortex in a starting jet, which allows for the possibility of predicting pinch-off based on simple models for the developing vortex ring. As was mentioned in the preceding chapter, such a perturbation-response-based criterion has the advantage that it could potentially be extended even to non-axisymmetric vortex rings, and could thus prove useful in a variety of biological applications where asymmetric vortex rings are the norm, and the feeding shear layer is difficult to model. Examples include the wakes of swimming and flying animals (Dickinson & Götz, 1996; Kern & Koumoutsakos, 2006; Kim & Gharib, 2011) and the flow through the mitral valve in the human heart (Domenichini *et al.*, 2005; Bellhouse, 1972; Reul *et al.*, 1981; Wieting & Stripling, 1984).

In reality, however, vortex rings and dipoles formed from roll-up of a shear layer exhibit a smooth vorticity distribution and are subject to a continuous injection of vorticity from the shear layer. A more realistic vorticity distribution within the vortex cores could be achieved by employing nested contours. Although more computationally expensive, further

work employing more realistic vorticity distributions, and analyzing the response to perturbations where vorticity is continuously injected at the rear of the vortex, could yield further insight into the dynamics of the pinch-off of vortex rings from their feeding shear layer. In the following chapter, we consider more complex models for vortex rings and dipoles, constructed using nested patches of vorticity such as the ones employed in the current chapter. In addition, we consider a more physically pertinent class of perturbations, which simulates the injection of fluid at the rear of the vortices by a feeding shear layer.

The material in this chapter was published in O'Farrell C and Dabiri JO (2012)"Perturbation response and pinch-off of vortex rings and dipoles," *Journal of Fluid Mechanics* **704**: 280-300.

Chapter 5

Nested-contour models for vortex rings and dipoles

5.1 Introduction

In chapter 4 we discussed the existence of a process analogous to pinch-off in the perturbation response of a family of vortex rings introduced by Norbury (1973). Given that these vortices have been used to model vortex rings at different stages in their growth (Gharib *et al.*, 1998; Mohseni & Gharib, 1998; Shusser & Gharib, 2000; Linden & Turner, 2001; Gao & Yu, 2010), the existence of a change in perturbation response, when considering Norbury vortices of increasing core size, suggests that the perturbation response of models for isolated vortex rings could be a useful tool in understanding the pinch-off of vortex rings in real flows. This conjecture is supported further by the fact that no such change in response was observed in the two-dimensional Pierrehumbert family of vortex dipoles (Pierrehumbert, 1980), where pinch-off was not expected to occur (Afanasyev, 2006; Pedrizzetti, 2010; Domenichini, 2011).

The vortex rings and dipoles considered in the previous chapter, however, consisted of patches where the vorticity was constant (in the two-dimensional case), or a linear function of the distance from the axis of symmetry (in the axisymmetric case). In contrast, exper-

imentally generated vortex rings are characterized by a Gaussian distribution of vorticity (Weigand & Gharib, 1997), and the vorticity in experimentally generated dipoles is well-approximated by Bessel functions (Flór & van Heijst, 1994; Trieling *et al.*, 2010) . Therefore, there is room for improving our understanding of the relationship between the perturbation response of models for isolated vortex rings and dipoles and the pinch-off phenomenon observed in laboratory flows and in the field, by considering more realistic models for the vortices. In two dimensions, more realistic vortex models with continuous distributions of vorticity have been previously studied by Boyd & Ma (1990); Kizner & Khvoles (2004); Khvoles *et al.* (2005); Albrecht (2011), and others; whereas Kaplanski & Rudi (2005) and Fukumoto & Kaplanski (2008) have considered viscous models for vortex rings. Unlike the inviscid solutions of Pierrehumbert (1980) and Norbury (1973), these models were viscous, and studying their perturbation response required the use of viscous flow solvers.

However, more realistic models for both vortex rings and dipoles can be constructed by extending the methods described in the previous chapter to allow for multiple nested patches of vorticity. This arrangement enables the approximation of more realistic, continuous distributions of vorticity, by piecewise-constant or piecewise-linear distributions, in two-dimensional and axisymmetric flows, respectively. Thus constructed, the models remain inviscid, and their evolution can be computed by simple modifications to the contour dynamics algorithms discussed in the preceding chapter.

In two dimensions, vorticity distributions of arbitrary complexity can be approximated in a piecewise-constant fashion by using multiple nested patches of constant vorticity. This idea was first introduced by Zabusky *et al.* (1979), and its value lies in that the contributions from individual patches to the contour dynamics velocity equation can be added together by simple linear superposition. However, most past studies in contour dynamics employing

multiple contours have focused on groups or arrays of vortices consisting single patches of vorticity. Examples include those of Dritschel (1985); Overman & Zabusky (1983); Saffman & Szeto (1981) and Makarov & Kizner (2011). A comprehensive review of these studies of arrays of vortex patches is found in Pullin (1992). Nested patches have also been useful in the study of annular vortices: two-dimensional vortices with a patch of zero vorticity at their center. Dritschel (1986), for instance, considered the perturbation response of a class of these vortices.

However, a handful of studies have employed nested patches to simulate the evolution of vortices with smooth vorticity distributions. Dritschel (1989) simulated the evolution of an elliptic vortex modeled after the elliptic vortices with smooth vorticity distributions considered by Mellander *et al.* (1987), using eight nested regions of constant vorticity. Similarly, Pullin & Jacobs (1986) conducted four-contour simulations of Corcos-Lin vortex arrays (Corcos *et al.*, 1984; Corcos & Lin, 1984; Lin & Corcos, 1984), and Jacobs & Pullin (1989) utilized eight- and sixteen-contour approximations to study the evolution of a shear layer with a Gaussian vorticity distribution.

None of these studies, however, considered dipolar vortices such as those studied by Pierrehumbert (1980) and investigated in chapter 4. Along with monopolar vortices, dipolar vortices are commonly found in two-dimensional turbulence (van Geffen & van Heijst, 1998; McWilliams, 1984). As a result, vortex dipoles have been the subject of numerous studies, a subset of which are listed in §4.1. In these studies, the most commonly used model for the dipolar vortices is an analytical solution to the incompressible Euler equations known as the Lamb dipole (Lamb, 1906). van Geffen & van Heijst (1998), Kizner *et al.* (2010), Delbende & Rossi (2009), for instance, conducted numerical studies of vortex pairs which closely resembled the Lamb dipole. However, these studies made use of a combination

of theoretical analysis and direct numerical simulation. Given the ubiquity of Lamb-like vortices in studies of two-dimensional turbulence, the feasibility of modeling such vortices using nested contours is of interest.

In the case of axisymmetric flows, the contributions from multiple regions of linear vorticity distribution may be combined by linear superposition to allow the simulation of systems with multiple patches, using the axisymmetric contour dynamics algorithm of Shariff *et al.* (2008). In fact, Shariff *et al.* (2008) mentioned the the possibility of using nested contours to approximate arbitrary vorticity distributions by piecewise-linear ones. However, the authors considered only the case of a 'hollow' spherical vortex, which consisted of a region of zero vorticity nested within a spherical region with a linear distribution of vorticity (i.e., Hill's spherical vortex). To date, no studies are available which make use of nested contours to construct approximations to experimental vortex rings that are more realistic than the Norbury family employed by most existing models for pinch-off.

The goal of the current chapter was to construct more realistic models for the dipolar vortices found in two-dimensional turbulence and the vortex rings found in starting jets, than those considered in the preceding chapter. In the two-dimensional case, a model for the analytical Lamb dipole was constructed using several nested contours. In the axisymmetric case, model vortex rings were constructed from experimental data from a starting jet, and consisted of several nested contours. Since the model vortices where described by several contours, perturbations to the vortices could be easily introduced in the form of deformations to the shape of the contours. Hence, we analyzed the response of the model vortex rings to shape perturbations in a manner similar to our analysis of the Norbury family in the preceding chapter.

In order to obtain a more realistic model for the perturbations that vortex rings ex-

perience during formation, we devised a perturbation scheme that consisted of deforming the rear boundary of the vortex by introducing a small protuberance. This perturbation mimicked the introduction of a small amount of vorticity at the rear of a forming vortex ring by interaction with its feeding shear layer. Using this perturbation scheme, we were able to identify a change in the behavior of our model vortex rings which was consistent with pinch-off. Similar methods can be applied to the construction of models for vortex rings in biological flows and, by studying their perturbation response, enable prediction of the pinch-off phenomenon in more complex biological flows.

This chapter is organized as follows. In §5.2 we outline the mathematical and numerical framework for computing the evolution of multiple regions of vorticity using contour dynamics algorithms. The methods described in this section are used in §5.3 to model the Lamb dipole. In §5.4 and §5.5, we discuss the construction of model vortex rings from experimental data for a starting jet, and we consider the perturbation response of these in §5.6. Finally, concluding remarks are presented in §5.7

5.2 Mathematical formulation and numerical method

5.2.1 Contour dynamics formulation for multiple contours

The vorticity equation for inviscid, incompressible flow in two dimensions introduced in chapter 4 (equation 4.1) is satisfied by any number of patches of constant vorticity, which may or be not be nested within each other. Similarly, the vorticity equation for inviscid, incompressible axisymmetric flow without swirl (equation 4.2) is satisfied by any number of regions with a distribution of vorticity which is linear in the radial coordinate. As a result, nested patches of vorticity can be utilized to construct piecewise-constant and piecewise-

linear approximations to more complex distributions of vorticity, in the two-dimensional and axisymmetric cases, respectively. Furthermore, the contour dynamics equations describing the motion of single patches of vorticity introduced in §4.2.3, can be extended to these piecewise-constant and piecewise-linear distributions by linear superposition.

In two dimensions, the velocity at a point $\mathrm{z} = x + iy$ in the complex plane due to n patches A_j $(j = 1, \ldots, n)$ of constant vorticity (nested or otherwise) is given by:

$$u_x + iu_y = -\frac{1}{4\pi} \sum_{j=1}^{n} \Omega_j \oint_{\partial A_j} \frac{\mathrm{z} - \mathrm{z}'}{\bar{\mathrm{z}} - \bar{\mathrm{z}}'} \mathrm{dz}' \tag{5.1}$$

where j iterates over all contours. Where the contours are nested, Ω_j represents the jump in ω when crossing the jth contour inwards (Dritschel, 1988*b*; Pullin, 1981). When simulating vortex dipoles, we consider only the case where the flow is symmetric about the x-axis. Therefore, in these cases, n refers to the number of nested contours comprising one of the symmetric vortex cores, usually taken as the positive core.

Similarly, the axisymmetric contour dynamics algorithm of Shariff *et al.* (2008) admits multiple contours by addition of the contributions from individual contours. Therefore, the equation for the velocity induced at a point $\mathbf{x}$ by n regions A_j with a linear distribution of vorticity is given by:

$$\mathbf{u}(\mathbf{x}) = \sum_{j=1}^{n} \Omega_j \oint_{\partial A_j} [(z - z')G(s') \cos\theta' - rH(s') \sin\theta'] \hat{z} + r'H(s') \cos\theta' \hat{r} \mathrm{d}s' \tag{5.2}$$

Where here Ω_j represents the jump in $\xi = \omega/r$ when crossing the jth contour inwards,

and H and G are given by:

$$G(s') = \frac{r'}{\pi\sqrt{C+B}}K(k) \tag{5.3}$$

$$H(s') = \frac{1}{2\pi r}\left(\frac{C}{\sqrt{C+B}}K(k) - E(k)\sqrt{C+B}\right) \tag{5.4}$$

$$k = \sqrt{\frac{2B}{C+B}} \tag{5.5}$$

$$C = (z-z')^2 + r^2 + r'^2, \quad B = 2rr' \tag{5.6}$$

Here too $\theta(s', \alpha)$ is the angle of the outward-pointing normal relative to the symmetry axis, and $K(k)$ and $E(k)$ are the complete elliptic integrals of the first and second kind, respectively (§4.2.3).

These contour dynamics algorithms for multiple contours reduced the evolution problem to tracking the motion of a collection of marker points on the boundary of each contour, by numerical integration of equation 5.1 or equation 5.2. Numerical integration was carried out using the method outlined in §4.2.4. At each time step, additional marker points were inserted in each contour where the linear segments stretched beyond $0.016R$, and removed where segments shrunk below $0.004R$ (Shariff *et al.*, 2008). For nested contours, R was defined as the radial coordinate of the center of the innermost contour in the axisymmetric case, and as the distance from the symmetry axis to the center of the innermost contour in one of the symmetric vortices in the two-dimensional case.

Following Shariff *et al.* (2008), the time step was chosen to satisfy $\Delta t = \frac{0.05}{\Omega_0}$, where Ω_0 is the vorticity at the center of the vortex ring core in the axisymmetric case ($\Omega_0 = \sum_{j=1}^{n} \Omega_j R$), or the vorticity inside the innermost contour of the positively-signed vortex patch in the two-dimensional case ($\Omega_0 = \sum_{j=1}^{n} \Omega_j$). The flow invariants (circulation, impulse, and energy) were monitored and their change was kept below 0.01% over one eddy turnover period for

the impulse and circulation, and 0.02% over the same period for the energy.

5.2.2 Verification

The contour dynamics algorithms described above may be used to simulate the evolution of arbitrary configurations of nested patches, and they have been used extensively to simulate the evolution of "hollow" vortices. That is, vortices with a zero-vorticity patch at their center. In order to verify our implementation of the contour dynamics algorithms described in the previous section, we began by considering the evolution of such hollow vortices.

Dritschel (1986) considered the evolution of several annular vortices, which consisted of a zero-vorticity patch nested within a constant-vorticity patch. Figure 5.1 shows the evolution of one such annular vortex. The vortex consisted of a Kirchhoff elliptic vortex (Kirchhoff, 1876) with an aspect ratio of 1.22, whose major axis initially lay in the horizontal plane, and from which a region of vorticity-carrying fluid was removed. The boundary of the removed region was an ellipse with an aspect ratio of 1.33 and an equivalent diameter of 70% of the outer vortex equivalent diameter. The major axis of the removed region was aligned with the vertical axis (figure 5.1). Dritschel (1986) denoted the ratio of the equivalent diameter of the zero-vorticity patch to that of the constant-vorticity patch by a, and he normalized the time as $\tau = (1 - a^2)t/(1 + a^2)$. The annular vortex in figure 5.1 was found to develop into two elongated vortices which spiraled towards the origin. These results were found to be in excellent qualitative agreement with those of Dritschel (1986).

A similar pattern of breakup into smaller vortices was found when considering the evolution of a pair of symmetric annular vortices, such as those shown in figure 5.2(a). The vortices were constructed by removing regions of vortical fluid from one of the steadily translating dipoles described by Pierrehumbert (1980) and introduced in §4.2.1. Following

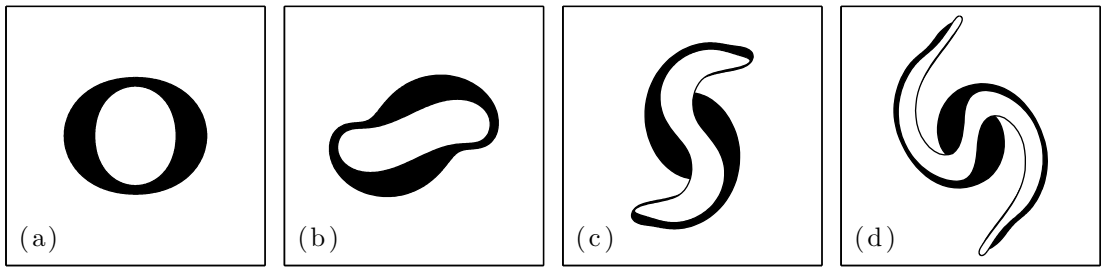

Figure 5.1: Evolution of an annular vortex from Dritschel (1986), at: (a) $\tau = 0$; (b) $\tau = 3$; (c) $\tau = 6$; (d) $\tau = 9$. The vortex was constructed by removing a region of vortical fluid from a Kirchhoff elliptic vortex (Kirchhoff, 1876; Saffman, 1992) of aspect ratio 1.22. The boundary of the removed region is an ellipse with an aspect ratio of 1.33, and an equivalent diameter of 70% of the outer vortex ($a = 0.7$). Time has been normalized by $(1+a^2)/(1-a^2)$, where a is the ratio of the equivalent diameter of the inner ellipse to that of the outer ellipse.

Shariff *et al.* (2008), the boundaries of the removed regions were chosen to be the interior streamlines of the unperturbed dipole where $\psi = \pm 0.25$. Figures 5.2 (b)-(e) show the evolution of the hollow vortex pair into a symmetric arrangement of eight vortices connected by thin filaments. Time $t^* = Ut/R$ was normalized using the speed of the unperturbed dipole (U) and the distance from the symmetry axis of the center to one of the vortices (R), as described in chapter 4.

The evolution of hollow vortices into patches of vorticity connected by thin sheets was also observed to occur in the axisymmetric case by Shariff *et al.* (2008). Therefore, in order to verify our implementation of the axisymmetric contour dynamics algorithm for multiple contours, we considered evolution of a hollow spherical vortex constructed by removing a region of vortical fluid from Hill's spherical vortex of radius $2R$. Following, Shariff *et al.* (2008), the boundary of the region removed was chosen to be an interior streamsurface of the unperturbed Hill's vortex. In our case, the boundary of the removed regions was the streamsurface where $\psi = \frac{\Omega}{10} r^2 \left((2R)^2 - r^2 - z^2\right) = 0.21$. Figure 5.3 shows the breakup of the hollow vortex. Once again time $t^* = Ut/R$ was normalized as in chapter 4: using the speed and radius of the unperturbed Hill's vortex. The results in figure 5.3 agree

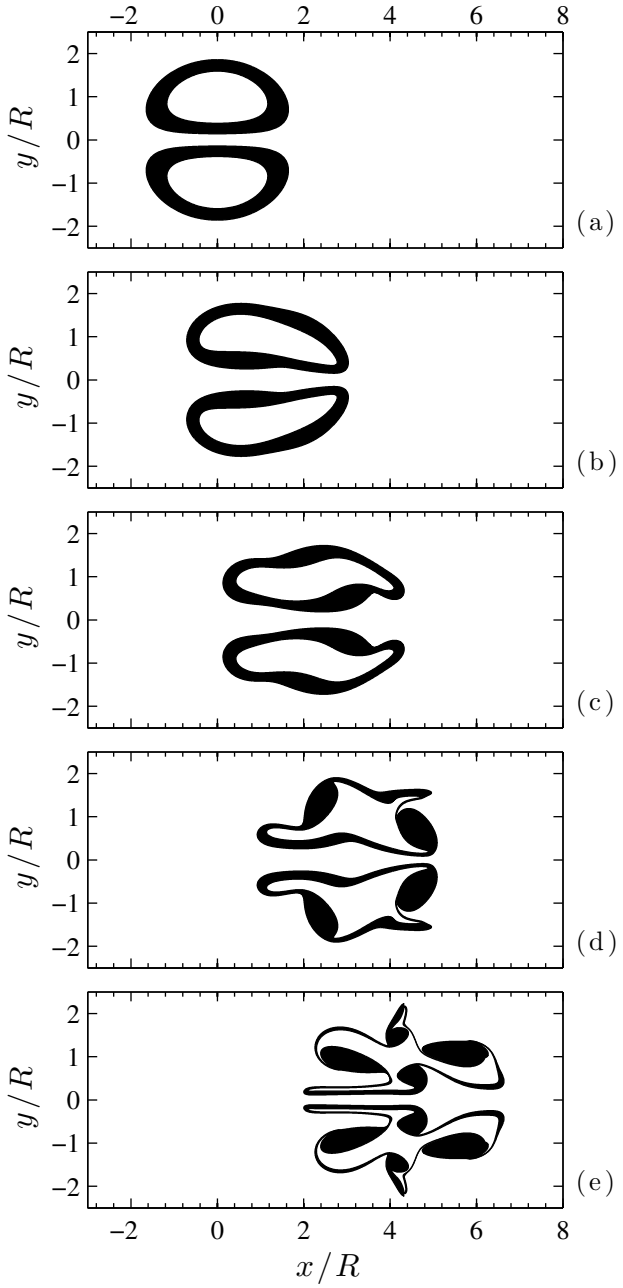

Figure 5.2: Evolution of a pair of annular vortices formed by removing a region of vortical fluid from a Pierrehumbert dipole ($\alpha = 1.2$), at: (a) $t^* = 0$; (b) $t^* = 7.5$; (c) $t^* = 15$; (d) $t^* = 22.5$; (e) $t^* = 30$. The boundaries of the regions removed were the interior streamlines of the unperturbed dipole where $\psi = \pm 0.25$.

qualitatively with the evolution of the vortex described by Shariff *et al.* (2008). However, since Shariff *et al.* (2008) did not indicate the streamsurface they selected for their study, an exact comparison is not possible.

Having verified our implementation of the contour dynamics algorithms for multiple regions of vorticity in the two-dimensional and axisymmetric cases, we proceeded with the construction of model vortex rings and dipoles using nested contours. We began by considering an exact solution of the incompressible Euler equations in two dimensions: the Lamb dipole.

5.3 Example: modeling the Lamb-Chaplygin dipole

The Lamb-Chaplygin dipole is a steadily translating solution to the two-dimensional, incompressible Euler equations, which takes the form of a vortex dipole with a circular boundary and a continuous distribution of vorticity. Inside the circular dipole of radius R, the vorticity and stream function are linearly related by $\omega = b^2(\psi - \lambda)$, where b and λ are constants. This general form of the dipole is due to Chaplygin (Chaplygin (1903) in Russian, Chaplygin (2007) in translation), and was recently brought to the attention of the scientific community by Meleshko & van Heijst (1994). Previously, the special case where $\lambda = 0$ had been described by Sir Horace Lamb, and is known as the Lamb dipole (Lamb, 1895, 1906).

The resulting vorticity field is given by:

$$\omega = \begin{cases} \frac{2Ub}{J_0(bR)} J_1(b\rho) \sin\zeta + \lambda b^2 \left[1 - \frac{J_0(b\rho)}{J_0(bR)}\right] & \rho \leq R \\ 0 & \rho > R \end{cases} \tag{5.7}$$

Where the polar coordinates (ρ,ζ) are those defined in §4.2.1, and J_0 and J_1 are Bessel functions. The constant b is such that bR is the smallest positive root of $J_1(bR) = 0$. When

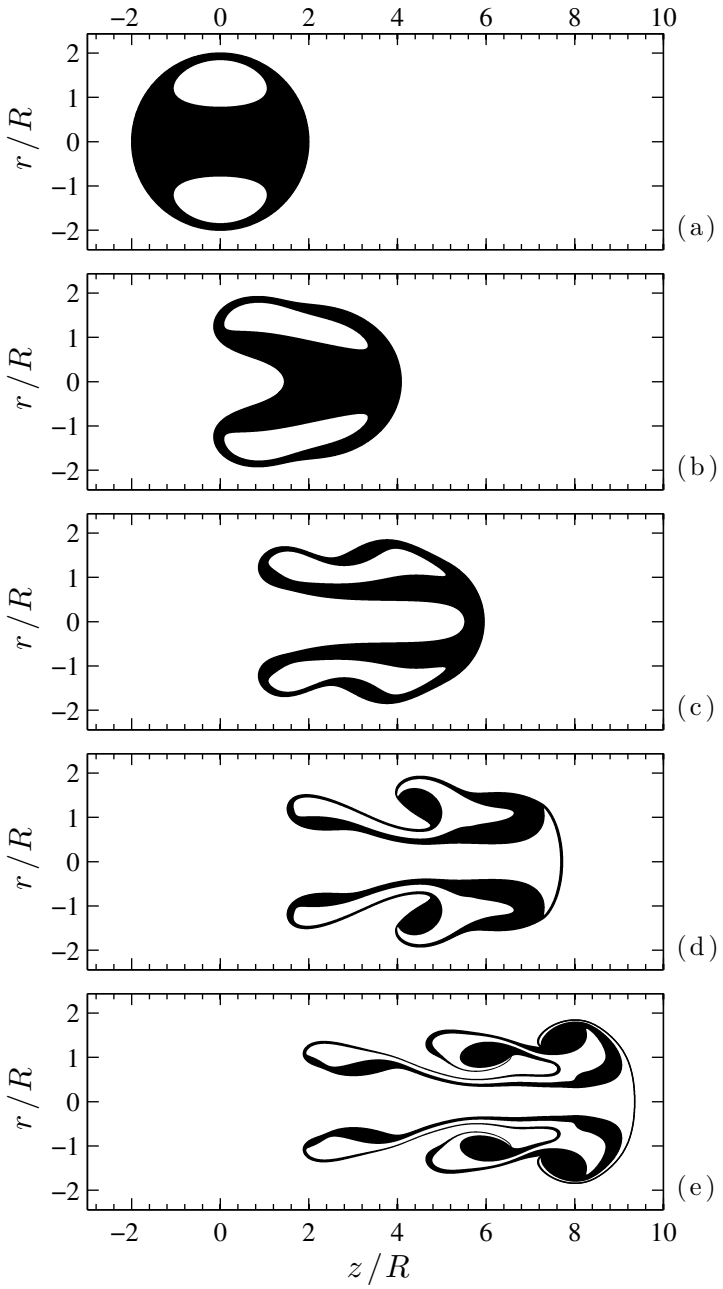

Figure 5.3: Evolution of a hollow spherical vortex formed by removing a region of vortical fluid from Hill's spherical vortex of radius $2R$, at: (a) $t^* = 0$; (b) $t^* = 3.4$; (c) $t^* = 6.8$; (d) $t^* = 10.2$; (e) $t^* = 13.6$. The boundary of the region removed was the interior streamsurface of the unperturbed Hill's vortex where $\psi = \frac{\Omega}{10} r^2 \left((2R)^2 - r^2 - z^2 \right) = 0.21$.

$\lambda = 0$, the two halves of the circular dipole are symmetric, and the vortex is asymmetric when $\lambda \neq 0$. In all cases, however, the dipole translates forward with constant velocity U.

Figure 5.4(a) shows contours of the vorticity distribution inside the circular dipole for the symmetric case ($\lambda = 0$, the Lamb dipole). Since this analytical solution describes an inviscid steadily translating symmetric vortex dipole similar to those described by Pierrehumbert (1980), it is an ideal candidate for modeling using nested contours to achieve a piecewise-constant approximation to a continuous distribution of vorticity. The black lines in figure 5.4(a) show the five contours selected for a nested-contour model of the Lamb dipole. As noted previously, we assumed symmetry of the flow across the x-axis, so that the positively valued half of the core was modeled using five contours, and the contribution from the other half was derived from symmetry. Figure 5.4(b) shows the vorticity distribution along the centerline of the positively valued core of the Lamb dipole (in black), along with the piecewise-constant approximation obtained from the nested-contour model (in red).

Figure 5.5 shows the evolution of the five-nested-contour model of the Lamb dipole, where time and length have been normalized by R/U and R, respectively. Initially, a small amount of irrotational fluid was entrained at the rear of the vortex (figure 5.5(b)). Eventually, the entrained fluid formed a thin cap near the forward stagnation point, which is visible in figure 5.5(d). A small amount of vortical fluid was also detrained into a small filament, which is seen trailing behind the dipole in figure 5.5(e). The formation of this tail of vorticity was also observed by van Geffen & van Heijst (1998) in their viscous numerical simulation of the Lamb dipole, and deemed by the authors to have minimal influence on the motion of the vortex. Despite the formation of these thin filaments, the model dipole retained a shape that closely resembled the analytical Lamb dipole. In addition, the vortex was found to have translated forward by an amount exceeding the expected $5R$ by only

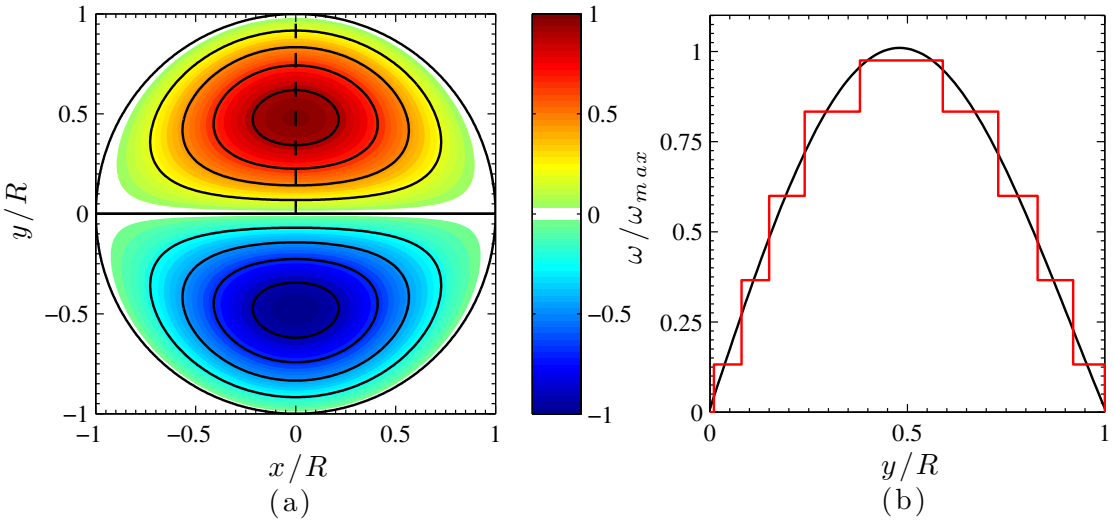

Figure 5.4: The Lamb dipole, and a five-contour approximation to the analytical solution. (a) Contours of ω/ω_{max} for the Lamb dipole. The black lines show the locations of five contours used in a piecewise-constant approximation. The dipole propagates from left to right. (b) Analytical (—) and piecewise-constant (—) vorticity distributions along the centerline of the positively valued vortex. The location of the cross section is shown by a dashed line in (a).

0.6%, at $t^* = Ut/R = 5$ (figure 5.5(e)).

The accuracy of the nested-contour models for the Lamb dipole was found to improve when the number of contours used in the approximation was increased. Figures 5.6 (a-d) show four different nested-contour models at $t^* = 4.7$: a three-nested-contour model, a five-nested-contour model, a ten-nested-contour model, and a fifteen-nested-contour model. The position of the analytical Lamb dipole at the same time instant is shown in figure 5.6(e), for comparison. As the number of contours was increased, the amounts of irrotational fluid entrained by the dipole and rotational fluid detrained by the dipole decreased, and the filaments became less prominent. The black line across all parts of figure 5.6 corresponds to the position, at $t^* = 4.7$, of the forward stagnation point in the analytical solution. It is evident from the figure that as the number of contours was increased, the translation velocity of the nested-contour model approached the analytical value U.

The improved performance of the nested-contour models with increasing number of contours is illustrated by figure 5.7. Figure 5.7(a) shows the circulation in one of the trailing filaments, expressed as a percentage of the circulation in the positive core of the analytical solution, as a function of the number of contours in the model. Similarly, figure 5.7(b) shows a comparison of the average velocity of the model dipole ($\bar{U}$), and velocity of the Lamb solution (U), for increasing number of contours. It is clear from figure 5.7 that the nested-contour models constituted a remarkably faithful approximation to the Lamb dipole even for small numbers of nested contours, and that the accuracy of the models increased with increasing number of contours.

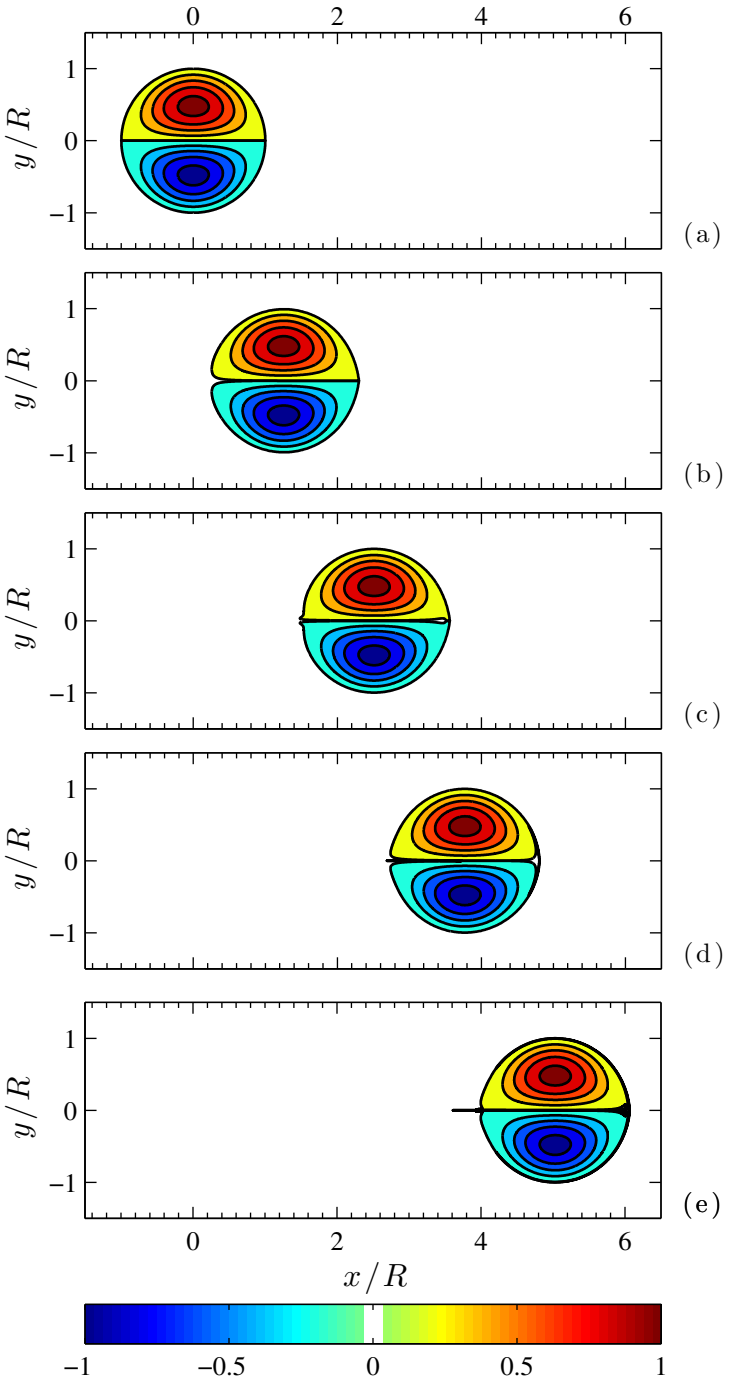

Figure 5.5: Evolution of a five-contour approximation to the Lamb dipole at, at: (a) $t^* = Ut/R = 0$; (b) $t^* = 1.25$; (c) $t^* = 2.5$; (d) $t^* = 3.75$; (e) $t^* = 5$. The interior of the contours has been colored by ω/ω_{max}. Time and length have been normalized by the radius of the circular dipole (R) and the translation velocity of the analytical solution (U).

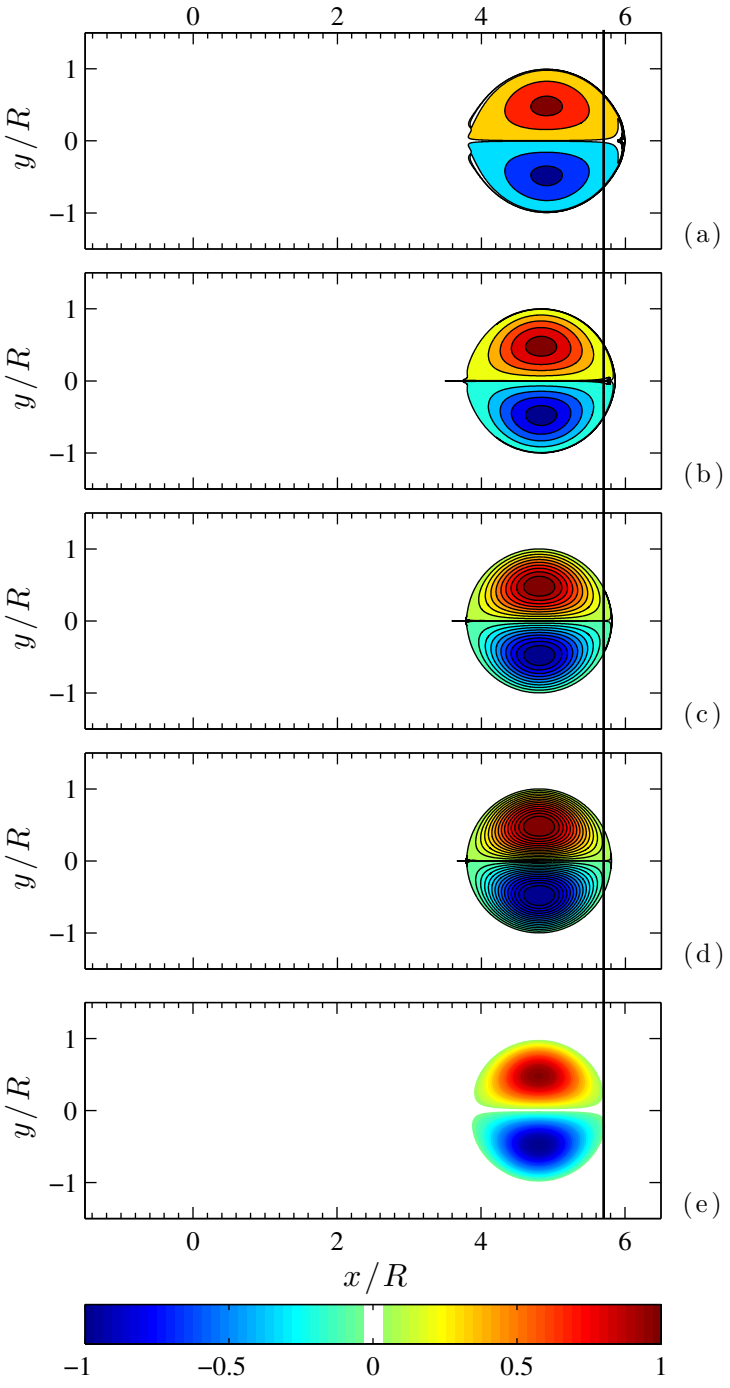

Figure 5.6: Comparison of piecewise-constant models of the Lamb dipole with the analytical solution ((e)) at $t^* = 4.7$. (a) 3-contour model; (b) 5-contour model; (c) 10-contour model; (d) 15-contour model. The x-location of the forward stagnation point in the analytical solution is indicated by the black vertical line.

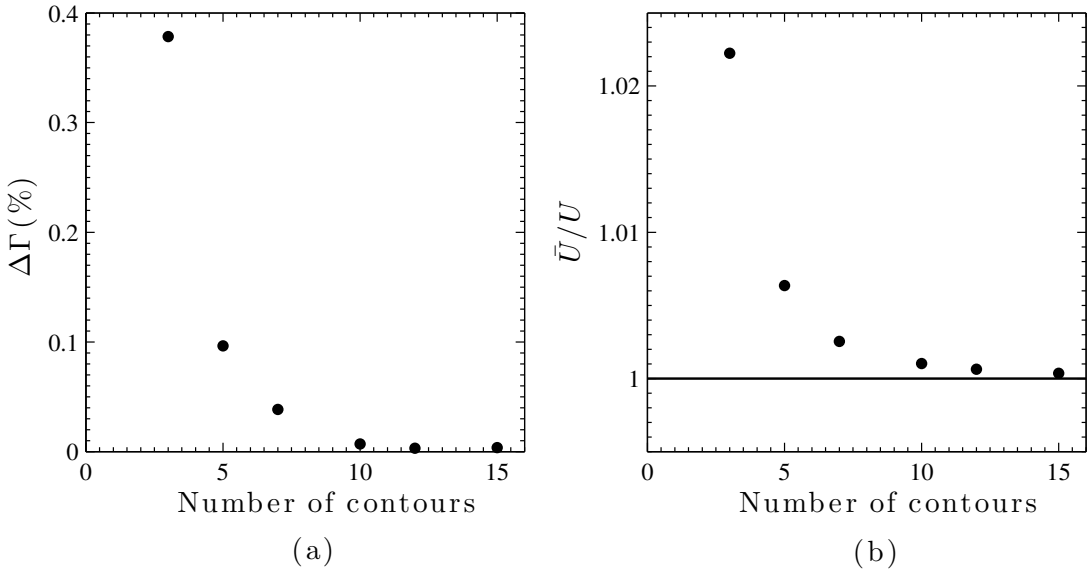

Figure 5.7: Effect of increasing the number of contours on model accuracy. (a) Circulation in the vortex filament, expressed as a percentage of circulation in the analytical solution, as a function of the number of contours. (b) Comparison of the average translating velocity of the model dipole ($\bar{U}$) and the analytical value (U), as a function of number of contours.

5.4 Constructing piecewise-linear models for axisymmetric vortex rings

Multiple nested contours can also be used, in axisymmetric flows, to obtain piecewise-linear approximations to the vorticity distributions inside vortex rings. Unlike in the two-dimensional case, however, no exact solutions to the inviscid Navier-Stokes equations for a vortex ring are known, other than those considered by Hill (1894) and Norbury (1973). Therefore, we used several nested contours to construct models for axisymmetric vortex rings generated using a piston-and-circular-cylinder arrangement.

For this purpose, we considered the vortex rings generated in the long-stroke-ratio ($L/D = 12$) starting jet we described in chapter 2. Our objective was to obtain nested-contour models for the vortex ring at different stages of its growth, up until its satura-

tion and pinch-off. Therefore, we constructed models for vortex rings with stroke ratios $\left(\frac{L}{D}\right)_{desired} = 1, 2, 3$, and 4. Rather than conducting four different experiments to generate isolated vortex rings at these desired stroke ratios, we considered the equivalent vortex rings obtained from different time instants of the $L/D = 12$ data. That is, the vortex rings extracted from the $L/D = 12$ data whose total circulation matched the expected circulation in vortex rings formed using the same experimental parameters, but with the desired stroke ratios.

When looking at the time history of the $L/D = 12$ data, we considered that if fluid ejection were halted at a non-dimensional time of $\hat{T} = \overline{U}_p t/D = \left(\frac{L}{D}\right)_{desired}$, the resulting isolated vortex ring would have a circulation equal to the total circulation ejected by the apparatus up to $\hat{T} = \left(\frac{L}{D}\right)_{desired}$, which we called $\Gamma_{desired}$. However, all of $\Gamma_{desired}$ need not be found in the leading vortex immediately after $\hat{T} = \left(\frac{L}{D}\right)_{desired}$. Figure 5.8 shows the time histories of the total circulation emanating from the apparatus (Γ), as well as the circulation in the leading vortex ring (Γ_{ring}). In the figure, Γ_{ring} is identical to the total circulation until $\hat{T} \approx 2$. For $\hat{T} > 2$, the vortex ring advected away from the nozzle, while remaining attached to the shear layer and continuing to accept circulation from it (Gharib *et al.*, 1998; Gao & Yu, 2010; Domenichini, 2011). As a result of this separation of the vortex ring from the nozzle edge, vortical fluid ejected after $\hat{T} \approx 2$ was not immediately absorbed by the vortex, and Γ_{ring} increased at a rate slower than the total circulation.

Consequently, it was not sufficient to look at instantaneous contours of vorticity at $\hat{T} = \left(\frac{L}{D}\right)_{desired}$ to obtain model vortex rings at these desired stroke ratios. Rather, we compared $\Gamma_{ring}(\hat{T})$ for the $L/D = 12$ data to the time history of the total circulation($\Gamma(\hat{T})$), to find the $\hat{T}_{model}$ at which $\Gamma_{ring}(\hat{T}_{model}) = \Gamma\left(\left(\frac{L}{D}\right)_{desired}\right) = \Gamma_{desired}$. We then used instantaneous contours of vorticity at $\hat{T}_{model}$ to model the vortex ring with $\left(\frac{L}{D}\right)_{desired}$. The annotations

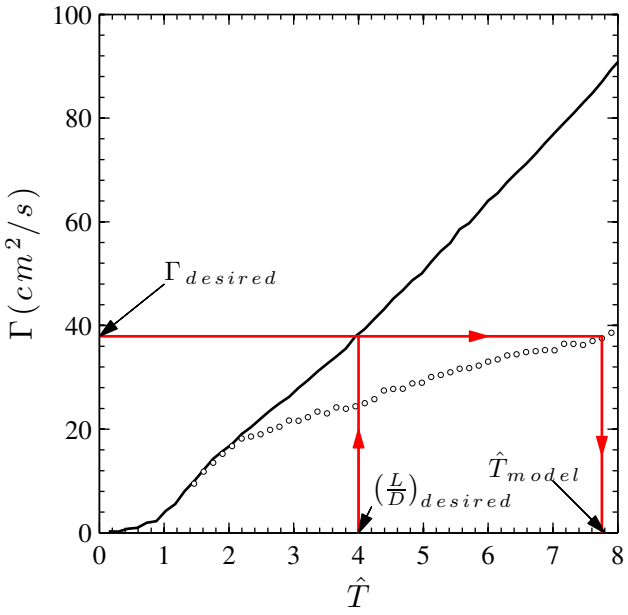

Figure 5.8: Total circulation emanating from the nozzle (—) and vortex ring circulation (∘) as a function of formation time $\hat{T}$ for an experimentally generated vortex ring. The red arrows illustrate the method used to determine $\hat{T}_{model}$ when modeling a vortex ring with a stroke ratio of four. The total circulation emanated from the nozzle at $\hat{T} = 4$ was compared with the time history of the vortex ring, to determine the $\hat{T}$ at which all of the circulation ejected by $\hat{T} = \left(\frac{L}{D}\right)_{desired} = 4$ ($\Gamma_{desired}$) had been absorbed by the vortex ring.

and arrows in figure 5.8 illustrate this process for $\left(\frac{L}{D}\right)_{desired} = 4$, where $\hat{T}_{model}$ was found to be 7.8.

Having determined $\hat{T}_{model}$, we constructed a nested-contour model by extracting contours of the vorticity density ($\xi = \omega/r$) for the leading vortex in the experimental data. Figure 5.9(a) shows contours of vorticity at $\hat{T} = \hat{T}_{model} = 7.8$. In order to apply the axisymmetric contour dynamics algorithm described in §5.2.1, our models were required to consist of nested regions with linear distributions of vorticity $\omega_m = \sum_{j=1}^{m} \Omega_j r$ (where $m \in [1, \ldots, n]$). Therefore, we constructed our models by extracting contours of constant ξ from the experimental data, and assuming the value of ξ within each contour to have a constant value $\xi_m = \sum_{j=1}^{m} \Omega_j$ (where $m \in [1, \ldots, n]$). Figure 5.9(b) shows five instantaneous

contours of vorticity density at $\hat{T} = 7.8$, used to construct a five-nested-contour model for a vortex ring with a stroke ratio of four.

Figure 5.10 shows these same contours of ξ, along with the five-contour model of the vortex which was constructed from these contours (in red). The vorticity density ξ in the leading vortex ring core at $\hat{T} = 7.8$ (shown in figure 5.10) was averaged with the distributions of ξ in the cores at the two adjacent time steps, in order to provide a smoother distribution. The vorticity densities around the cross sections of the ring in the positive r half-plane, and the negative r half-plane, were also averaged to increase the smoothness of the contours in the model. Five contours of constant ξ were then extracted from the averaged vorticity density, and used to construct the model shown in red in figure 5.10. Because the vortex ring remained attached to the shear layer, the rear boundary of the ring was not easily distinguishable. However, isolated laminar vortex rings are known from flow visualization experiments to exhibit high degrees of fore-aft symmetry (Lim & Nickels, 1995). Therefore, we reflected the contour shapes obtained for the front half of the vortex, about the core centerline, and constructed the symmetric core shown in figure 5.10.

A comparison of the distributions of ξ and ω along the centerline of the vortex core, in the experimental and model vortex rings is shown in figure 5.11. Since, in the model vortex ring, the vorticity density was assumed to be constant inside each contour ($\xi_m = \sum_{j=1}^{m} \Omega_j$ where $m \in [1, \ldots, n]$), the experimental distribution of ξ was approximated by a series of steps (figure 5.11(a)) in the model. The vorticity inside each contour in the model vortex, however, was given by $\omega_m = \xi_m r = \sum_{j=1}^{m} \Omega_j r$ (where $m \in [1, \ldots, n]$). Hence, the model vorticity tracked the experimental vorticity well on the half of the core closest to the symmetry axis, where ω had a positive slope in both cases ($r/D < 0.85$ in figure 5.11(b)). However, where the experimental vorticity was decreasing in r, the model ω (which was

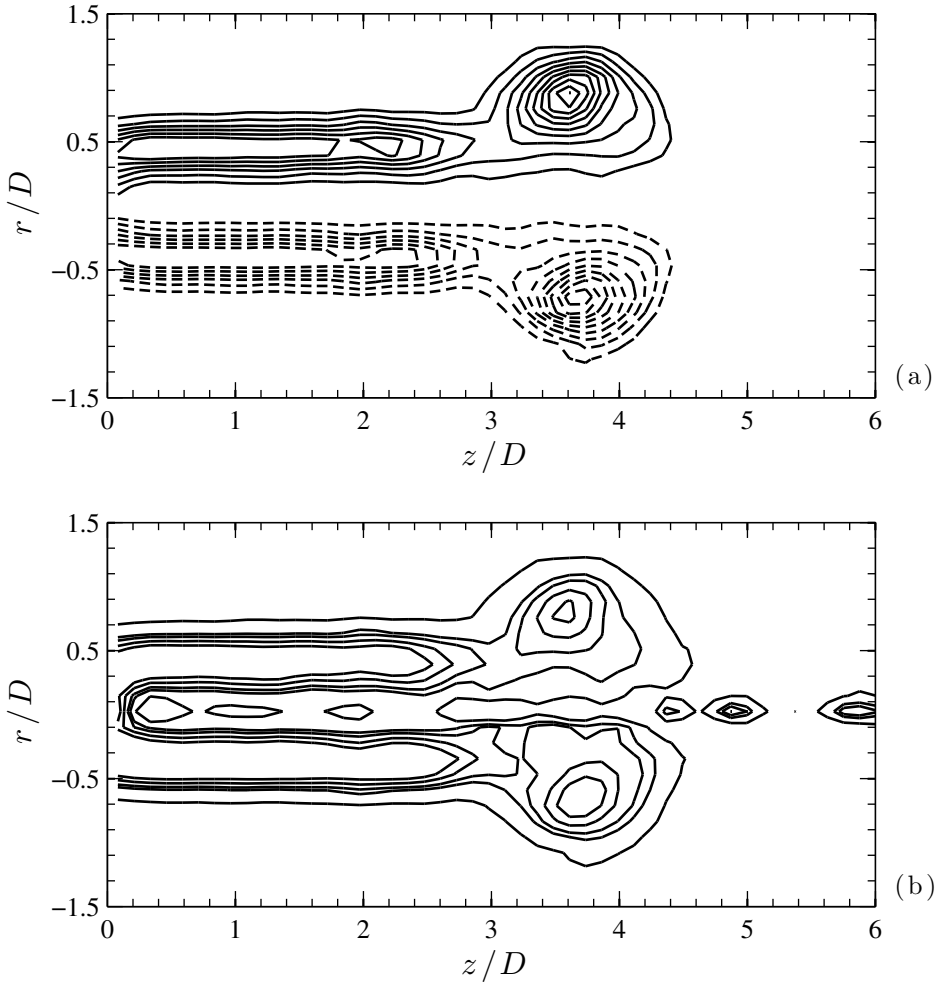

Figure 5.9: Contours of vorticity and vorticity density at $\hat{T} = 7.8$, the time instant at which all of the vorticity generated by $\hat{T} = 4$ had been accepted by the vortex ring. (a) Contours of ω. Levels: min = 10% of ω_{max}, max = 90% of ω_{max}, increment = 10%. Negative values denoted by the dashed lines. (b) Contours of ξ/ξ_{max}, where ξ_{max} is the maximum ξ inside the cores. Levels: 0.09,0.36, 0.49, 0.68, 0.88. Flow is from left to right.

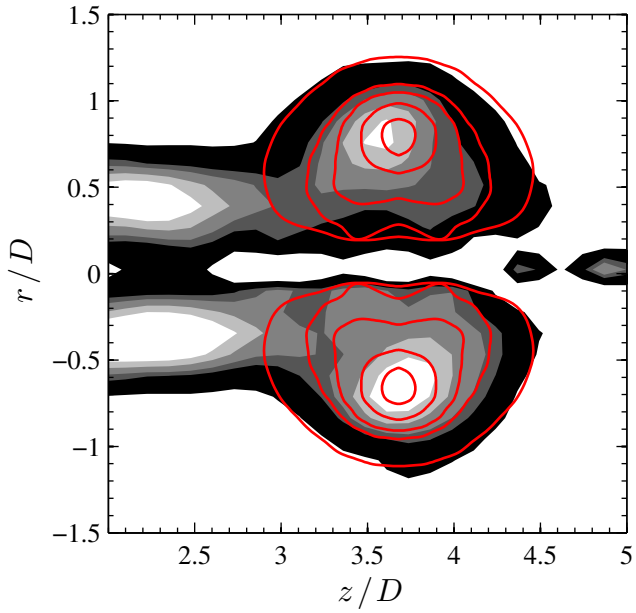

Figure 5.10: Contours of ξ/ξ_{max} at $\hat{T} = 7.8$ and superimposed five-contour model of a vortex ring with a stroke ratio of four (—). Contour levels: 0.09,0.36, 0.49, 0.68, 0.88. The direction of flow and the direction of propagation of the model vortex ring coincide with the direction of increasing z.

constrained to have a positive slope) had a jagged shape ($r/D > 0.85$ in figure 5.11(b)).

5.5 Finding steady state models for experimental vortex rings

Using the numerical scheme described in §5.2.1, we simulated the evolution of the nested-contour model for the vortex ring with a stroke ratio of four shown in figure 5.10. Figure 5.12 shows the evolution of the vortex ring as a function of the normalized time $t^* = \overline{U}_p t/D$, where $\overline{U}_p$ and D are the time-averaged piston velocity and nozzle diameter from the experimental data, respectively. Since the model was seen to detrain circulation into a tail of considerable size, the five contours obtained directly from the experimental data did not comprise a steady solution of the inviscid Navier-Stokes equations. This is not unexpected, for a number of reasons. At least a small amount of detrainment is expected, given our

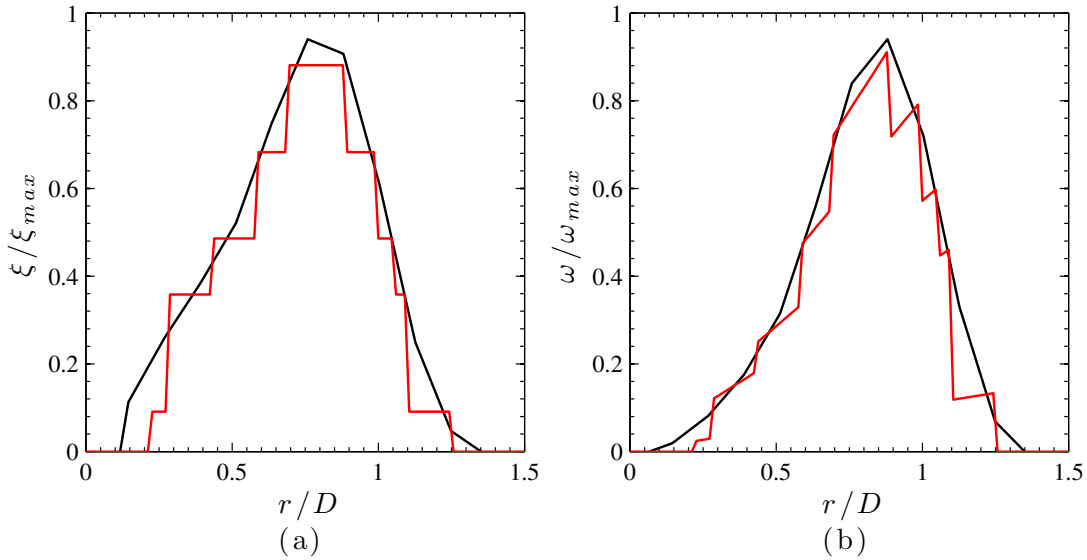

Figure 5.11: (a) Experimental (—) and five-contour model (—) distribution of ξ/ξ_{max} along the centerline of one of the cores of the vortex ring. (b) Experimental (—) and five-contour model (—) vorticity distribution along the centerline of one of the cores of the vortex ring.

findings in modeling the Lamb dipole. In the case of the Lamb dipole, however, the vorticity distribution was an exact solution to the inviscid Navier-Stokes equations. In the axisymmetric case, the vorticity distribution being was obtained from a viscous case ($Re = 1400$), while the contour dynamics algorithm solves the inviscid vorticity equation. Therefore, the contours obtained from the experiment were not expected to closely approximate an inviscid solution.

At the stage shown in figure 5.12(e), the computational costs associated with resolving the stretching of the tail made continuing the simulation prohibitively expensive, in terms of computational costs. Continuing this calculation in its current state would have required implementing the contour surgery algorithm developed by Dritschel (1988*a*), which implied additional computational costs and a large increase in the complexity of the algorithm. As was mentioned in chapter 4, however, Pozrikidis (1986) was able to continue simulating the evolution of perturbed spherical vortices after filament formation, by excision of the vortex

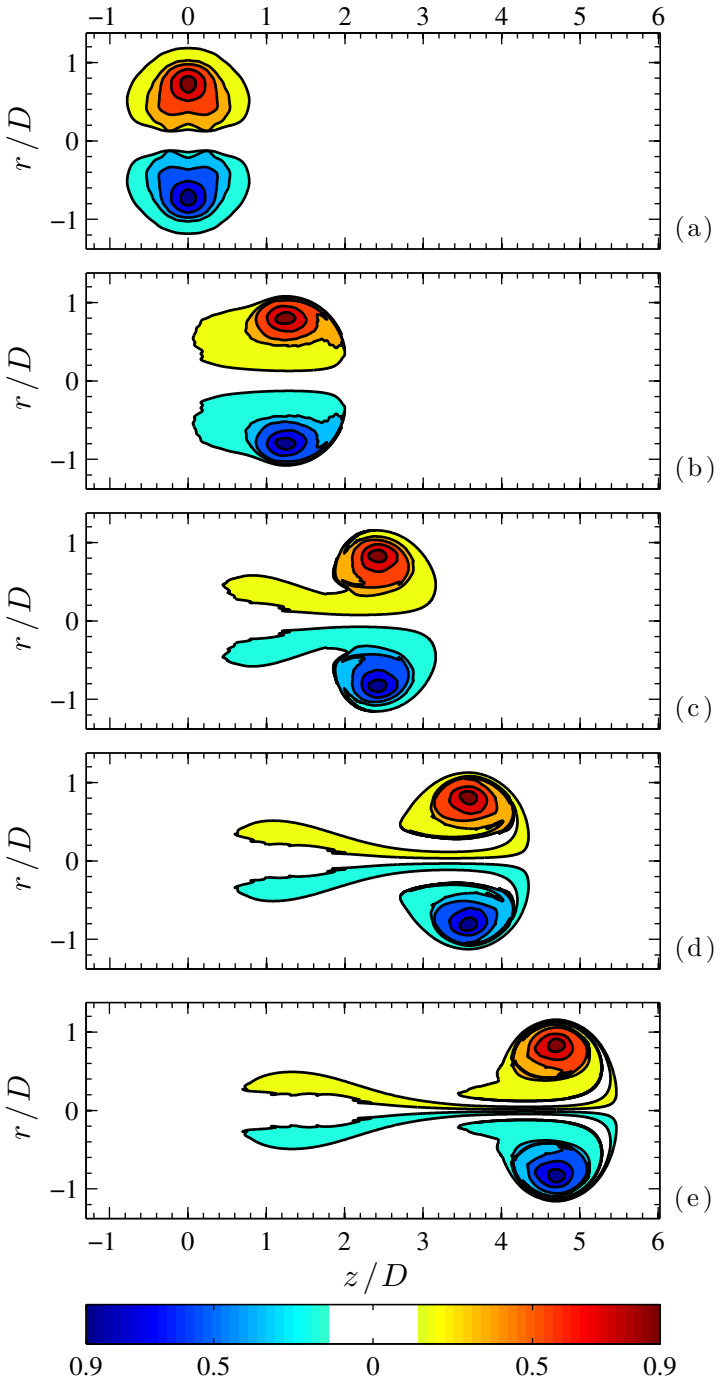

Figure 5.12: Evolution of a five-contour model of a vortex ring with $L/D = 4$, at: (a) $t^* = \overline{U}_p t/D = 0$; (b) $t^* = 2.1$; (c) $t^* = 4.3$; (d) $t^* = 6.5$; (e) $t^* = 8.6$. Inside each contour, $\xi = \omega/r = \Omega_j$ is constant, and the interior of the contours has been colored by ξ/ξ_{max}, where ξ_{max} is the maximum vorticity density in the experimental data.

filaments. Furthermore, Pozrikidis (1986) found this simplification to have a negligible effect on the accuracy of the simulations of the evolution of the remaining vorticity, and the same method was successfully applied in chapter 4. Since the vortex tail in figure 5.12(e) was not of particular interest, we adopted the strategy described in Pozrikidis (1986) and excised the tail at $t^* = 8.6$. We then continued the simulation of the vortex without the tail.

Parts (a) through (e) of 5.13 show the evolution of the model vortex ring after the excision of the tail. Once again, the vortex was found to shed circulation into a tail which trailed behind the ring. However, the amount of circulation shed by the vortex ring in this case was significantly reduced. A second excision of the vorticity in the tail allowed the simulation to continue to longer times. The evolution of the vortex ring after the second excision is shown in parts (f) through (i) of figure 5.13, where the formation of filaments which wrapped around the vortex core was observed, but no vorticity was detrained into a tail. The formation of filaments was observed previously in chapter 4, and is known to occur in contour dynamics simulations wherever there are regions of local concavity in the contour outline.

We repeated this excision process several times, and monitored the evolution of the vortex after each excision. Figure 5.14 shows the decrease in the vortex ring circulation after each excision, expressed as a percentage of the circulation immediately preceding the excision. It is clear from this figure that the amount of circulation shed by the vortex decreased after each excision. Furthermore, the vortex appeared to be approaching an asymptotic steady state, since the decrease in circulation was under 0.1% by the sixth excision. Therefore, we used the configuration of the five-contour-approximation after the sixth excision as our model for vortex rings with a stroke ratio of four.

The method outlined in §5.4 was used to extract nested-contour approximations for

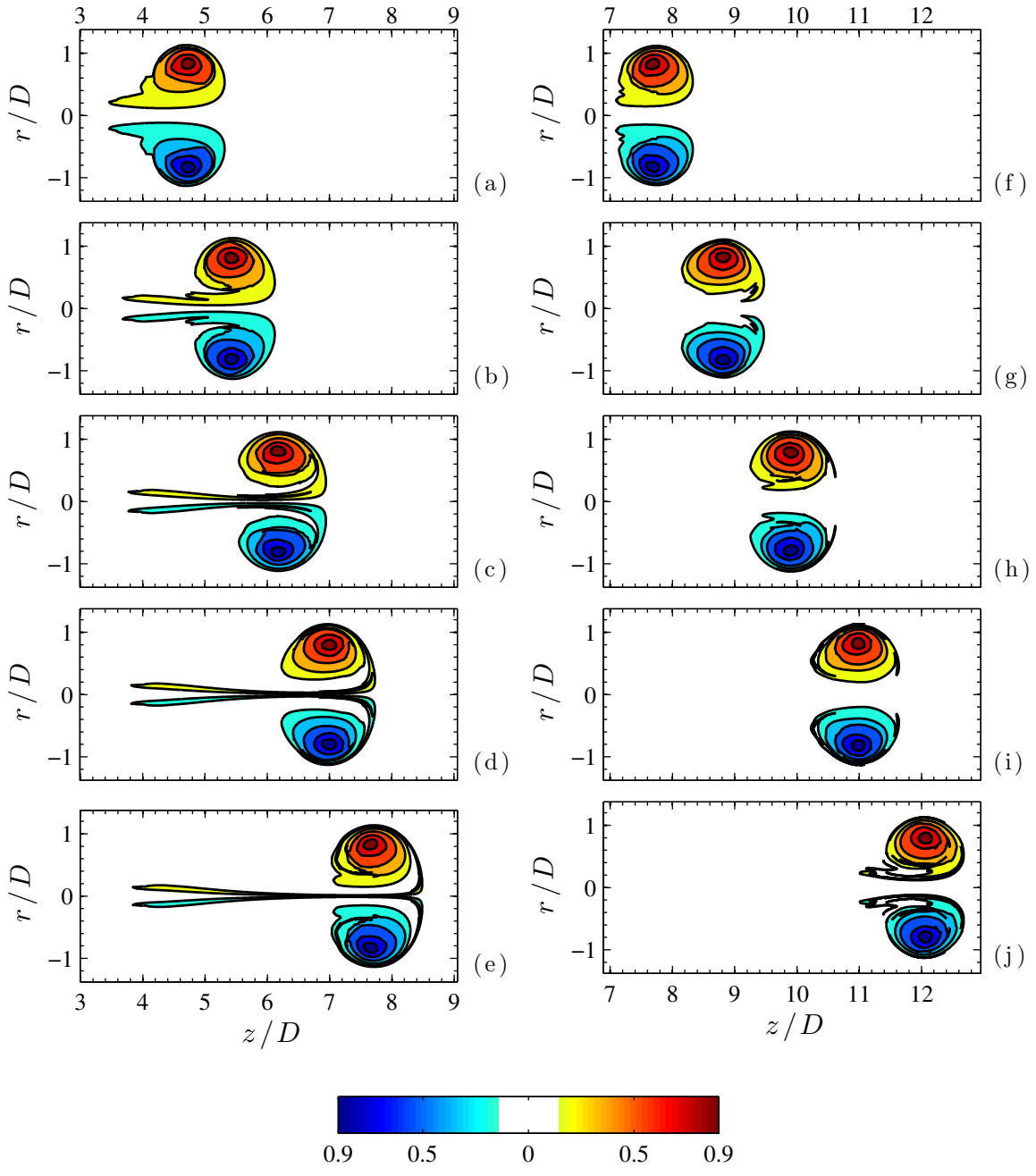

Figure 5.13: Evolution of a five-contour model of a vortex ring with $L/D = 4$ after filament excision, at: (a) $t^* = 8.7$; (b) $t^* = 10.1$; (c) $t^* = 11.6$; (d) $t^* = 13.1$; (e) $t^* = 14.5$. After the second filament excision, at: (f) $t^* = 14.6$; (g) $t^* = 16.7$; (h) $t^* = 18.8$; (i) $t^* = 21$; (j) $t^* = 23.1$. Inside each contour, $\xi = \omega/r = \Omega_j$ is constant, and the interior of the contours has been colored by ξ/ξ_{max}, where ξ_{max} is the maximum vorticity density in the experimental data.

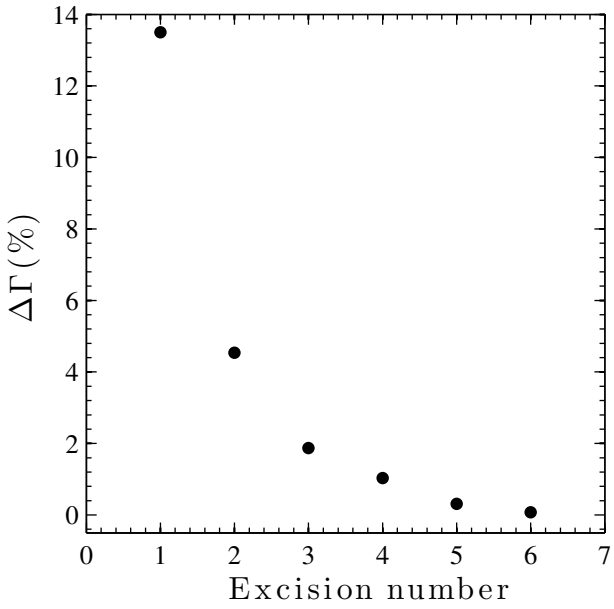

Figure 5.14: Circulation in the vortex filament right before each excision, expressed as a percentage of the vortex circulation before the excision.

vortex rings with stroke ratios of $L/D = 1, 2, 3, 4$ from the experimental data. Each of these models was evolved numerically in time as outlined in the preceding paragraphs, with filaments being excised as needed, until their asymptotic steady shape was determined. Figure 5.15 shows the resulting five-nested-contour models for vortex rings at stroke ratios of one, two, three, and four. These models comprised a family which was used to model vortex rings at different stages of their growth. Following Pozrikidis (1986), Ye & Chu (1995), and our work on the Norbury and Pierrehumbert families of vortices (chapter 4 and O'Farrell & Dabiri (2012)), we therefore investigated the perturbation response of this family of vortex rings.

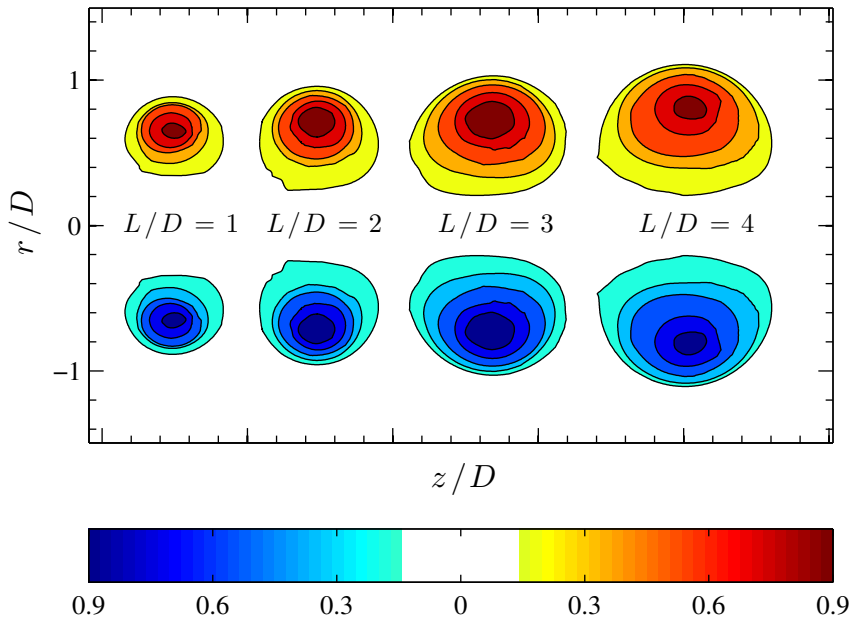

Figure 5.15: Models for vortex rings with $L/D = 1, 2, 3, 4$, constructed using five nested regions of constant $\xi = \omega/r = \Omega_j$. The regions are colored by ξ/ξ_{max}, where ξ_{max} is the maximum vorticity density inside the cores in the experimental data.

5.6 Perturbation response of model vortex rings

In order to study the perturbation responses of model vortex rings in a starting jet at different stages in their growth, and their relationship to pinch-off, we considered a type of perturbation which simulated the addition of vorticity from a trailing shear layer. The perturbation involved adding a small amount of circulation at the rear of the vortex by perturbing the shape of the outermost contour. The perturbation to the outer contour had the following form:

$$z' = \begin{cases} z\left[1 + d\sin\left(\frac{r-r(\pi)}{w}\pi\right)\right] & \pi \leq \eta \leq \eta_w \\ z & \text{elsewhere} \end{cases} \tag{5.8}$$

where z' was the perturbed coordinate, z and r the unperturbed coordinates, and η the polar angle as defined in figure 5.16. The r coordinate was unchanged, so the perturbation amounted to inserting a tail of vorticity of length d and width w at the rear of the vortex. η_w was the polar angle at which $r = r(\pi) + w$, indicated in figure 5.16. We considered perturbations where $w = 2R/3$, and d was varied in order to investigate the change in the perturbation response of the vortices as the amount of circulation introduced was increased.

We introduced perturbations of the form described above to the four model vortices in figure 5.15, and simulated the evolution of the perturbed vortices using the method described in §5.2.1. The size of the perturbations was quantified by the amount of circulation added to the vortex ring by the perturbation, expressed as a percentage of the circulation in the unperturbed vortex ring ($\Delta\Gamma/\Gamma(\%)$). Figure 5.17 depicts the evolution of a model vortex ring with a stroke ratio of two, subjected to a perturbation containing 2% of the unperturbed vortex circulation. The tail introduced by the perturbation was seen to develop into a vortex filament, much like those observed in chapter 4 when perturbing sufficiently

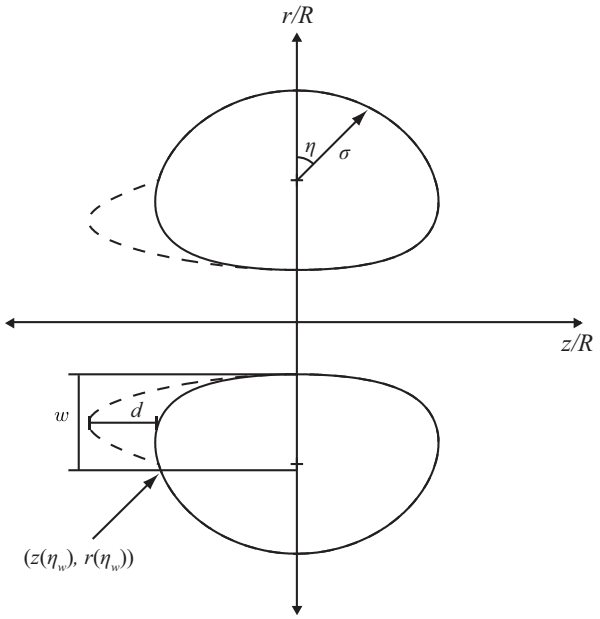

Figure 5.16: Perturbation simulating a trailing shear layer, for a one-contour vortex. The unperturbed vortex (a Norbury vortex with $\alpha = 0.8$ in this case) is depicted by the solid lines. The dashed lines represent a perturbation of the type defined in equation 5.8 to the outer contour of a model vortex. The vortices propagate from left to right.

thin-cored members of the Norbury family, as well as all members of the Pierrehumbert family. Like in those cases, the filament was found to wrap around the vortex core and continue to move with the vortex ring, with no detrainment of vorticity into a tail.

When the size of the perturbation was increased, however, we noticed a change in the response of the stroke-ratio-two model vortex ring. Figure 5.18 shows the evolution of the model vortex ring with a stroke ratio of two, when subjected to a perturbation containing 4% of the unperturbed vortex circulation. In this case, the vortex ring was found to detrain vorticity from the outermost contour into a tail which lingered behind the ring. This difference is indicative of a change in perturbation response, and mirrors the transition identified in our study of the perturbation response of the Norbury family of vortices (chapter 4 and O'Farrell & Dabiri (2012)).

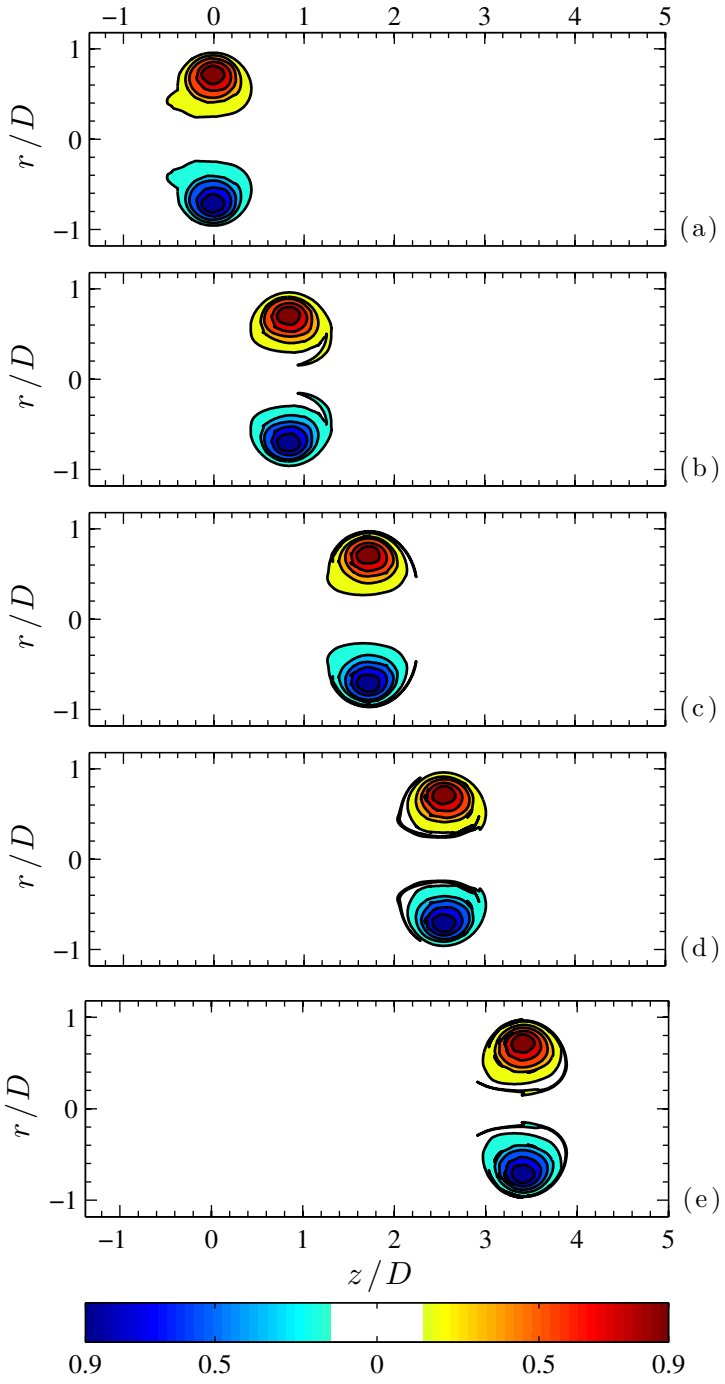

Figure 5.17: Evolution of a five-contour model of a vortex ring with $L/D = 2$, subject to a perturbation containing 2% of the unperturbed circulation, at: (a) $t^* = 0$; (b) $t^* = 2.7$; (c) $t^* = 5.4$; (d) $t^* = 8.1$; (e) $t^* = 10.8$.

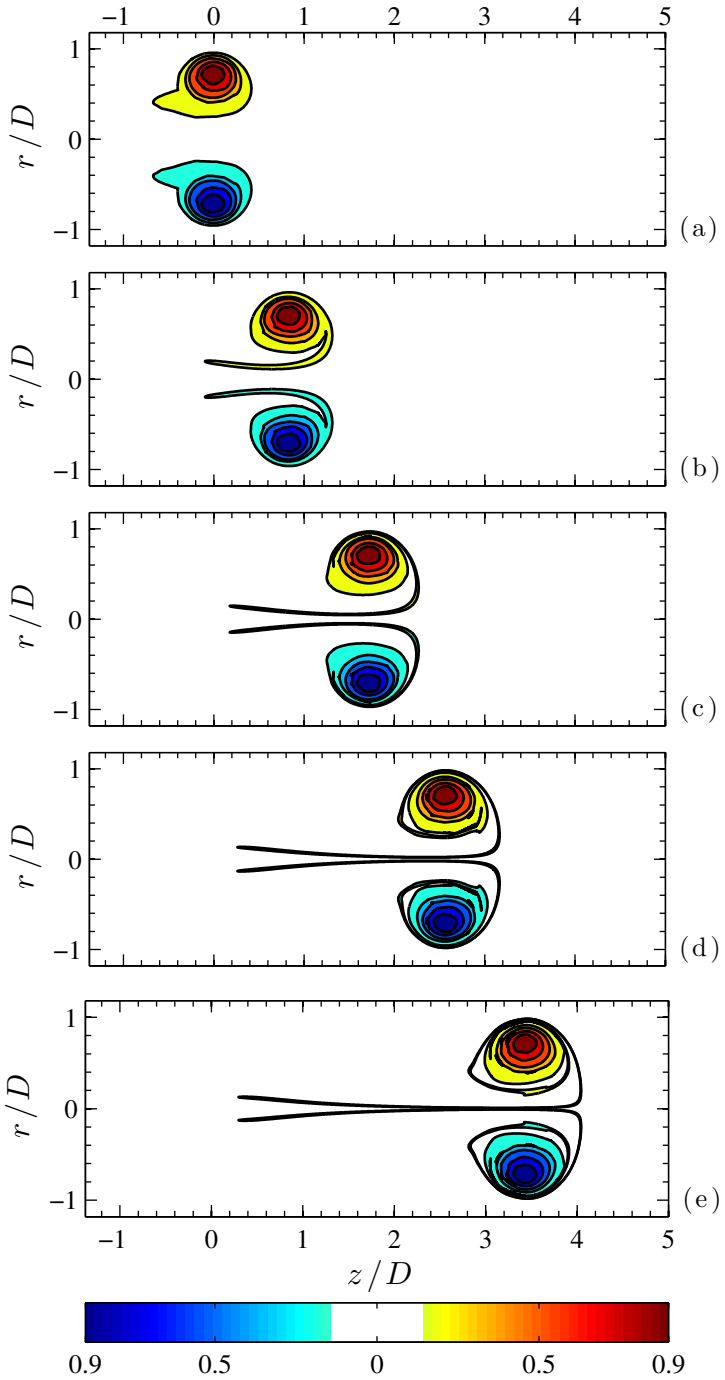

Figure 5.18: Evolution of a five-contour model of a vortex ring with $L/D = 2$, subject to a perturbation containing 4% of the unperturbed circulation, at: (a) $t^* = 0$; (b) $t^* = 2.7$; (c) $t^* = 5.4$; (d) $t^* = 8.1$; (e) $t^* = 10.8$.

For the model vortex ring with a stroke ratio of four, the change in perturbation response was found to occur at a perturbation size smaller than any of those introduced to the stroke-ratio-two vortex. The evolution of a stroke-ratio-four vortex ring subjected to a perturbation containing 2% of the unperturbed vortex circulation is shown in figure 5.19. The shedding of vorticity into a tail was apparent in this vortex even for perturbations containing only 2% of the unperturbed vortex circulation, which had not been observed to lead to tail-shedding in the stroke-ratio-two vortex (figure 5.17).

The fact that the stroke-ratio-two vortex ring was able to withstand larger perturbations than the stroke-ratio-four vortex without detraining vorticity into a tail, suggests that the response of the model vortices to this type of perturbation might be related to the occurrence of pinch-off in starting jets. We therefore determined the maximum perturbation size that all four model vortex rings could accept before detraining vorticity into a tail. These results are shown in figure 5.20, and indicate that the amount of circulation the model vortex rings could accept before shedding a tail decreased with increasing stroke ratio, before leveling off at a stroke ratio of approximately three.

For small stroke ratios, a decrease in the maximum allowable perturbation size before shedding was expected, as the model vortex rings grew closer to a limiting size known to exist from the experiments of Gharib *et al.* (1998) and others (Dabiri & Gharib, 2004*a*; Krueger *et al.*, 2006; Pawlak *et al.*, 2007). At a stroke ratio of approximately three, this decrease in the maximum perturbation size stopped, indicating that the stroke-ratio-three and -four vortex rings were comparably close to the limiting size. This similarity suggests that, in our family of model vortex rings, "pinch-off" occurred near a stroke ratio of three.

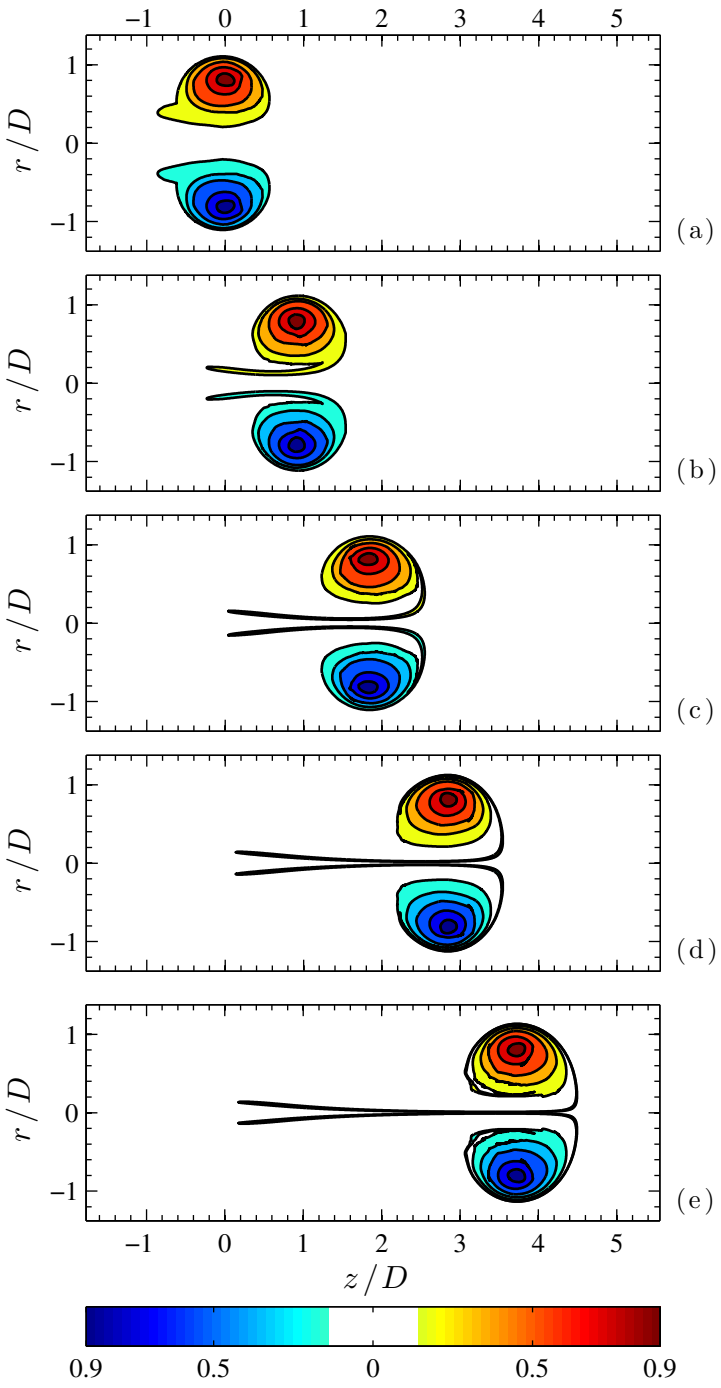

Figure 5.19: Evolution of a five-contour model of a vortex ring with $L/D = 4$, subject to a perturbation containing 2% of the unperturbed circulation, at: (a) $t^* = 0$; (b) $t^* = 1.9$; (c) $t^* = 3.8$; (d) $t^* = 5.7$; (e) $t^* = 7.6$.

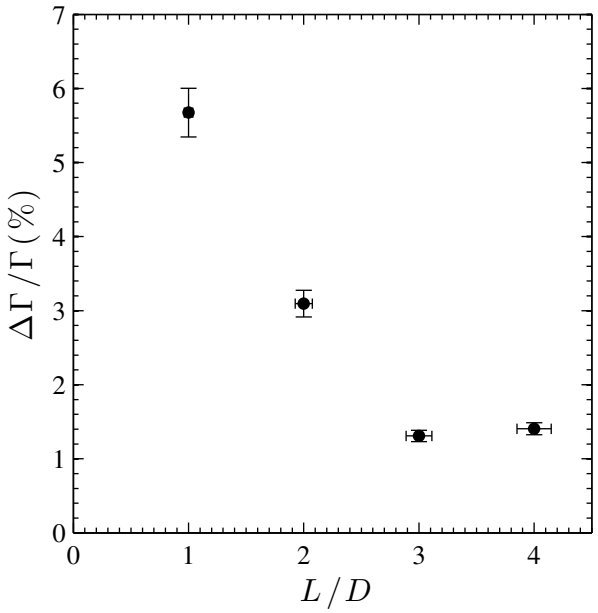

Figure 5.20: Maximum perturbation size accepted by the model vortex, as a function of the vortex stroke ratio. The perturbation size was quantified by the circulation added to the vortex ($\Delta\Gamma$), expressed as a percentage of the vortex circulation.

5.7 Conclusions

This chapter was concerned with the modeling of vortex rings and vortex dipoles using several nested patches of vorticity, and their simulation using contour dynamics methods. The use of nested contours allowed us to construct more realistic approximations to vortex rings and dipoles, while retaining the computational simplicity of the inviscid contour dynamics method.

In two dimensions, we constructed nested-contour models for the Lamb dipole, and found their agreement with the analytical solution to to be excellent, even for models consisting of as few as five contours. In our contour dynamics simulations, we demonstrated that nested regions of vorticity can be used to approximate dipolar solutions to the inviscid Navier-Stokes equations with high fidelity. The contour dynamics models for dipolar vortices

presented here are of great interest, given the widespread use of the Lamb dipole and Lamb-like vortices in studies of two-dimensional turbulence. In addition to the Lamb dipole, nested contours could be used to model the families of deformed vortices derived from the Lamb dipole by Boyd & Ma (1990), Kizner & Khvoles (2004), and Khvoles *et al.* (2005), which have also been used to model the dipolar vortices found in two-dimensional turbulence and geophysical flows.

In the case of axisymmetric vortex rings flows, we obtained nested-contour models for the vortex rings formed in starting jets. These models were constructed using contours of vorticity density from experimental data from a piston-cylinder experiment with a long stroke ratio, and were then allowed to asymptote to a steady state. From these steady states, we were able to construct a family of model vortex rings at different stroke ratios.

We considered the perturbation response of the model vortex rings to physically pertinent shape perturbations, which simulated the addition of a small amount of circulation to the rear of a vortex ring by the feeding shear layer. The results of the perturbation study suggest that there is a transition in the behavior of the vortices at a stroke ratio of approximately three. For stroke ratios below three, we found that the relative amount of circulation a model vortex ring could accept before shedding vorticity into a tail decreased with increasing stroke ratio. This suggests that the model vortex rings of increasing stroke ratio were progressively closer to the saturation size. After a stroke ratio of three, however, the relative amount of circulation the vortex rings could accept leveled off. This change in behavior was believed to be in agreement with pinch-off: vortex rings of increasing stroke ratio were found to be increasingly sensitive to perturbation by addition of vorticity, until a stroke ratio of three. Model vortex rings with a stroke ratio of three and four were found to be approximately equally sensitive to perturbation, suggesting they are quite similar in

structure and perturbation response, and perhaps indicating that pinch-off occurs when experimental vortex rings reach a size comparable to these two models.

The change in behavior in the model vortices at a stroke ratio of approximately three reported here differs from the occurrence of pinch-off at a stroke ratio of four reported by Gharib *et al.* (1998) for circular starting jets, and at $\hat{T} = 4.2 \pm 0.2$ for this particular data set (chapter 2 and O'Farrell & Dabiri (2010)). However, given that the inviscid models were constructed from viscous experimental data and allowed to shed vorticity until they reached a steady state which differed from the experimental vorticity contours, the agreement is encouraging. The present results show that only instantaneous shape perturbations to low-order models for vortex rings are required to produce a change in response which is consistent with pinch-off. However, the perturbations experienced by experimentally generated vortex rings during formation differ from those introduced to steady-state models in this chapter. Avenues for future work on contour dynamics models, including those for constructing more physically pertinent perturbations, are presented in the final chapter of this thesis. In this final chapter, we also present conclusions and suggestions for future work pertaining to the entire thesis.

Chapter 6

Conclusions and future work

6.1 Conclusions

Vortex rings, whether they be nearly axisymmetric or visibly non-circular, are found in the wakes of all manner of swimming and flying animals (Dickinson *et al.*, 2000; Dabiri & Gharib, 2005*a*; Kokshaysky, 1979; Drucker & Lauder, 1999). It is thought that, by harnessing the propulsive advantages that vortex rings provide over steady jets, animals have achieved propulsive efficiencies that exceed those of engineered vehicles. Thus, swimming and flying organisms have captured the attention of engineers attempting to improve the efficiency of current underwater vehicles. However, it is believed that vortex pinch-off and the existence of a limiting size for vortex rings govern the shedding of vortices by animals during locomotion, by means not yet fully understood or characterized. The aim of this thesis was therefore to shed additional light on those aspects of vortex formation and vortex pinch-off that are relevant to biological propulsion, and to provide future researchers with tools to assist in identifying pinch-off in biological flows, as well as understanding and predicting its occurrence. It is hoped that these tools will aid in uncovering the mechanisms by which vortex formation shapes swimming and flying behaviors in nature, as well as aiding in the design and evaluation of the next generation of underwater vehicles which incorporate

our understanding of optimal vortex formation.

In chapter 2 we introduced a criterion for identifying pinch-off in starting jets, based on the Lagrangian coherent structures in the flow. This method provides an alternative to the circulation criterion of Gharib *et al.* (1998), which we believe will prove useful in identifying pinch-off in complex biological flows where the vorticity field can obscure pinch-off and make the circulation criterion difficult to apply. The proposed LCS criterion has the disadvantage of being more computationally intensive than existing methods, but it possesses the advantages associated with LCS of being dependent on the velocity field only, robust to errors in the velocity field, and frame-invariant.

Since most naturally occurring vortex rings are not circular, and the effect of departure from axisymmetry on the vortex formation number had not been previously characterized, in chapter 3 we considered the formation of vortex rings from non-axisymmetric nozzles. The results of our experimental study suggested that the local curvature does not influence the vortex formation number to a large degree, at least for vortex rings with moderate departure from axisymmetry. Instead, the definition of the vortex formation number can be extended to vortex rings of this kind by considering the equivalent diameter of the nozzle (the diameter of a circular nozzle with identical area). These findings have potentially far-reaching implications for the study of biological flows where non-circular vortex rings are the norm. In particular, the results of our investigations into the formation of non-circular vortices suggest that vortex rings with moderate departure from axisymmetry can be reduced to circular vortex rings by means of the equivalent diameter.

This reduction has the potential to aid significantly in the modeling and prediction of pinch-off in biological flows. However, even when the results of chapter 3 are considered, modeling pinch-off in many biological flows is at this stage difficult and often impractical.

This difficulty arises from the reliance of existing models on approximations for the rates of injection of circulation, impulse, and energy by a feeding shear layer into the vortex ring. In complex biological flows, such as those generated by swimming and flying animals, such approximations are often difficult to obtain, as the shear layers themselves are difficult to characterize. In these cases, a framework for identifying, understanding, and predicting pinch-off based on the properties of the vortex rings generated by the animal alone would be beneficial.

In chapters 4 and 5 we developed such a framework by studying the perturbation response of model vortex rings. In chapter 4, we considered the response of the Norbury family of vortex rings to prolate shape perturbations, using contour dynamics methods. We identified a change in response as we considered members of the family of increasing core radius, which was analogous to pinch-off. In chapter 5, on the other hand, we considered the response of more realistic models for vortex rings constructed from experimental data using nested contours, to perturbations which more closely resembled those encountered by forming vortex rings. These simulations were also conducted using contour dynamics algorithms, and once again resulted in the identification of a shedding behavior analogous to pinch-off.

6.2 Avenues for future work

Throughout this thesis, we presented a set of tools for identifying and predicting pinch-off in biological flows. In this final section, we therefore suggest future research directions relating primarily to the application of these tools to biological flows. In chapter 2 we introduced a criterion for identifying pinch-off, which we believe will prove useful in complex biological flows. Therefore, characterizing the performance of this criterion in biological flows in the

field and in the lab would be a useful next step.

Our analysis of pinch-off in non-axisymmetric vortex rings covered a class of vortices with moderate departure from axisymmetry. While the extent to which our findings are applicable to vortex rings outside of this class is not known, such highly non-circular vortex rings are not relevant to applications in biological propulsion. However, given the differences between the results presented in chapter 3 and those of Domenichini (2011), determining the extent to which the equivalent diameter is the relevant length scale in defining a global formation number is of interest from the perspective of vortex dynamics. Further studies on the formation of vortices outside of the biologically relevant class might enable us to define a (possibly locally varying) analogue to the formation number of Gharib *et al.* (1998), which extends to a large class of vortex ring geometries and recovers the asymptotic behavior of circular vortex rings and two-dimensional vortex dipoles.

In chapters 4 and 5, we introduced two families of models for the vortex rings found in the wakes of swimming and flying animals. Future work could focus on improving the accuracy of the contour dynamics models, to develop increasingly realistic models for naturally occurring vortices. To this end, nested-contour models could be constructed using a larger class of experimental data sets, as well as for numerical data, which has the advantage of providing smoother vorticity contours from which to extract models. The accuracy of the vortex models could also potentially be improved by increasing the number of nested contours which comprise them.

At this stage, the greatest impediments to carrying out studies with increased number of contours or on a larger class of data sets, are those expenses associated with obtaining the asymptotic shapes of the vortex rings. In the present study, the contour shapes obtained directly from the experimental data were not found to correspond to steadily-translating

shapes. As a result, these shapes were allowed to approach their asymptotic states by simulating them for times up to $t^* = 60$. This necessitated costly long-time simulations, as well as labor-intensive excisions of filaments. However, these simulations suggested that steady solutions to the incompressible Euler equations in the form of vortex rings with nested contours exist, since our vortices were found to approach such steady states asymptotically. Future work in developing a numerical method for finding equilibrium shapes using nested contours similar to Norbury's scheme (Norbury, 1973), could sharply reduce these costs. The work of Aref & Vainchtein (1998) on finding asymmetric point vortex equilibria, starting from previously known symmetric equilibria, is suggested as a basis for finding nested-contour solutions, starting from existing single-contour solutions.

In addition to developing vortex models of increasing accuracy and complexity, there is ample opportunity for future work on applying the models introduced in this thesis to the vortices shed by swimming and flying animals. The perturbation response framework developed here can then be applied towards predicting pinch-off in the wakes of specific animals, where existing models prove difficult to apply.

Bibliography

Adhikari, D. 2009 Some experimental studies on vortex ring formation and interaction. Master's thesis, National University of Singapore, available online at http://scholarbank.nus.edu.sg/handle/10635/16569.

Adrian, R.J. 1991 Partpart-imaging techniques for experimental fluid mechanics. *Annu. Rev. Fluid Mech.* **23**, 261–304.

Afanasyev, Y.D. 2006 Formation of vortex dipoles. *Phys. Fluids* **18**, 037103.

Ahuja, A., Manes, J. & Massey, K. 1990 An evaluation of various concepts of reducing jet noise. *AIAA Paper 90-3982* .

Akhmetov, D.G. 1980 Extinguishing gas and oil well fires by means of vortex rings. *Combust. Explos. Shock Waves* **16**, 490–494.

Akhmetov, D.G. 2009 *Vortex Rings*. Springer.

Albrecht, T.R. 2011 Steady vortex dipoles with general profile functions. *J. Fluid Mech* **670**, 85–95.

Anderson, E.J. & DeMont, M.E. 2000 The mechanics of locomotion in the squid *Loligo pealei*: locomotory function and unsteady hydrodynamics of the jet and intramantle pressure. *J. Exp. Biol.* **203**, 2851–2863.

Anderson, E.J. & Grosenbaugh, M.A. 2005 Jet flow in steadily-swimming adult squid. *J. Exp. Biol.* **208**, 2851–2863.

Aref, J. & Vainchtein, D.L. 1998 Point vortices exhibit asymmetric equilibria. *Nature* **392**, 769–770.

Arms, R.J. & Hama, F.R. 1965 Localized-induction concept on a curved vortex and motion of an elliptic vortex ring. *Phys. Fluids* **8** (4), 553–559.

Arzani, A. & Shadden, S.C. 2012 Characterization of the transport topology in patient-specific abdominal aortic aneurysm models. *Phys. Fluids* **24**, 081901.

Auerbach, D. 1987 Experiments on the trajectory and circulation of the starting vortex. *J. Fluid Mech* **183**, 185–198.

Auerbach, D. 1991 Stirring properties of vortex rings. *Phys. Fluids A* **3**, 1351–55.

Baird, M.H.I., Wairegi, T. & Loo, H.J. 1977 Velocity and momentum of vortex rings in relation to formation parameters. *Can. J. Chem. Eng.* **55**, 19–26.

Bartol, I.K., Krueger, P.S., Stewart, W.J. & Thompson, J.T. 2009 Pulsed jet dynamics of squid hatchlings at intermediate Reynolds numbers. *J. Exp. Biol.* **212**, 1506–18.

Bartol, I.K., Krueger, P.S., Thompson, J.T. & Stewart, W.J. 2008 Swimming dynamics and propulsive efficiency of squids throughout ontogeny. *Integr. Comp. Biol.* **48**, 720–733.

Bartol, I.K., Patterson, M.R. & Mann, R. 2001 Swimming mechanics and behavior of the shallow-water brief squid. *J. Exp. Biol.* **204**, 3655–3682.

Batchelor, G.K. 1967 *An Introduction to Fluid Dynamics*. Cambridge University Press.

Bellhouse, B.J. 1972 Fluid mechanics of a model mitral valve and left ventricle. *Cardiovas. Res.* **6**, 199–210.

Benjamin, T.B. 1976 The alliance of practical and analytical insights into the nonlinear problems of fluid mechanics. In *Applications of Methods of Functional Analysis to Problems in Mechanics* (ed. P. Germain & B. Nayroles), pp. 8–28. Springer.

Beron-Vera, F.J, Olascoaga, M.J., Brown, M.G. & Koçak, H. 2012 Zonal jets as meridional transport barriers in the subtropical and polar lower stratosphere. *Journal of the Atmospheric Sciences* **69** (2), 753–767.

Beron-Vera, F.J, Olascoaga, M.J., Brown, M.G., Koçak, H. & Rypina, I.I 2010 Invariant-tori-like Lagrangian coherent structures in geophysical flows. *Chaos* **20**, 017514.

Boyd, J.P. & Ma, H. 1990 Numerical study of elliptical modons using a spectral method. *J. Fluid Mech* **221**, 597–611.

Chahine, G.L. & Genoux, P.F. 1983 Collapse of a cavitating vortex ring. *J. Fluids. Eng.* **105**, 400–405.

Chaplygin, S.A. 1903 One case of vortex motion in a fluid. *Trans. Phys. Sect. Imperial Moscow Soc. Friends of Natural Sciences* **11** (2), 11–14.

Chaplygin, S.A. 2007 One case of vortex motion in a fluid. *Regul. Chaotic. Dyn.* **12** (2), 219–231.

Cone, C.D. 1962 Thermal soaring of birds. *Am. Sci.* **50** (1), 180–209.

Corcos, G.M. & Lin, S.J. 1984 The mixing later: deterministicmodels of a turbulent flow. Part 2. The origin of three-dimensional motion. *J. Fluid Mech.* **139**, 67–95.

Corcos, G.M., Sherman, F.S. & Lin, S.J. 1984 The mixing later: deterministicmodels of a turbulent flow. Part 1. Introduction and two-dimensional flow. *J. Fluid Mech.* **139**, 29–65.

Couder, Y. & Basdevant, C. 1986 Experimental and numerical study of vortex couples in two-dimensional flows. *J. Fluid Mech* **173**, 225–251.

Crowdy, D. & Surana, A. 2007 Contour dynamics in complex domains. *J. Fluid Mech* **593**, 235–254.

Dabiri, J.O. 2009 Optimal vortex formation as a unifying principle in biological propulsion. *Ann. Rev. Fluid Mech.* **41**, 17–33.

Dabiri, J.O., Colin, S.P. & Costello, J.H. 2006 Fast-swimming hydromedusae exploit velar kinematics to form an optimal vortex wake. *J. Exp. Biol.* **209**, 2025–33.

Dabiri, J.O., Colin, S.P., Katija, K. & Costello, J.H. 2010 A wake-based correlate of swimming performance and foraging behavior in seven co-occurring jellyfish species. *J. Exp. Biol.* **213**, 1217–1225.

Dabiri, J.O. & Gharib, M. 2004*a* Delay of vortex ring pinch-off by an imposed bulk counerflow. *Phys. Fluids* **16** (L), 28–30.

Dabiri, J.O. & Gharib, M. 2004*b* Fluid entrainment by isolated vortex rings. *J. Fluid Mech* **511**, 311–331.

Dabiri, J.O. & Gharib, M. 2004*c* A revised slug model boundary layer correction for starting jet vorticity flux. *Theoretical and Computational Fluid Dynamics* **17** (4), 293–295.

Dabiri, J.O. & Gharib, M. 2005*a* The role of optimal vortex formation in biological fluid transport. *Proc. R. Soc. B* **272**, 1557–60.

Dabiri, J.O. & Gharib, M. 2005*b* Starting flow through nozzles with temporally variable exit diameter. *J. Fluid Mech* **538**, 111–36.

Deem, G.S. & Zabusky, N.J. 1978 Vortex waves: stationary 'V states', interactions, recurrence and breaking. *Phys. Rev. Letters* **40**, 859–62.

Delbende, I. & Rossi, M. 2009 The dynamics of a viscous vortex dipole. *Phys. Fluids* **21**, 073605.

Dewey, P.A., Carriou, A. & Smits, A.J. 2012 On the relationship between efficiency and wake structure of a batoid-inspired oscillating fin. *J. Fluid Mech.* **691**, 245–266.

Dhanak, M.R. & de Bernardinis, B. 1981 The evolution of an elliptic vortex ring. *J. Fluid Mech.* **109**, 189–216.

Dickinson, M.H., Farley, C.T., Full, R.J., Koehl, M.A.R., Kram, R. & Lehman, S. 2000 How animals move: an integrative view. *Science* **288** (5463), 100–106.

Dickinson, M.H. & Götz, K.G. 1996 The wake dynamics and flight forces of the fruit fly *Drosophila melanogaster*. *J. Exp. Biol.* **199**, 2085–2104.

Didden, N. 1979 On the formation of vortex rings: rolling-up and production of circulation. *Z. Angew. Math. Phys.* **30**, 101–116.

Domenichini, F. 2011 Three-dimensional impulsive vortex formation from slender orifices. *J. Fluid Mech.* **666**, 506–520.

Domenichini, F., Pedrizzetti, G. & Baccani, B. 2005 Three-dimensional filling flow into a model left ventricle. *J. Fluid Mech.* **539**, 179–198.

Dritschel, D.G. 1986 The nonlinear evolution of rotating configurations of uniform vorticity. *J. Fluid Mech.* **172**, 157:182.

Dritschel, D.G. 1988*a* Contour surgery: A topological reconnection scheme for extended integrations using contour dynamics. *J. Comp. Phys.* **77**, 240–266.

Dritschel, D.G. 1988*b* The repeated filamentation of two-dimensional vorticity interfaces. *J. Fluid Mech.* **194**, 511–47.

Dritschel, D.G. 1989 Contour dynamics and contour surgery: numerical algorithms for extended high-resolution modelling of vortex dynamics in two dimensional, inviscid, incompressible flows. *Comput. Phys. Rep.* **10**, 79–146.

Dritschel, D.G. 1995 A general theory for two-dimensional vortex interactions. *J. Fluid Mech.* **293**, 269–303.

Dritschel, D. G. 1985 The stability and energetics of corotating uniform vortices. *J. Fluid Mech.* **157**, 95–134.

Drucker, E.G. & Lauder, G.V. 1999 Locomotor forces on a swimming fish: three-dimensional vortex wake dynamics quantified using digital particle image velocimetry. *J. Exp. Biol.* **202**, 2393–2412.

Du Toit, P.C. 2010 Transport and separatrices in time-dependent flows. PhD thesis, California Institute of Technology.

Du Toit, P.C. & Marsden, J.E. 2010 Horseshoes in hurricanes. *Journal of Fixed Point Theory and Applications* **7** (2), 351–384.

Duran-Matute, M., Albagnac, J., Kamp, L.P.J. & van Heijst, G.J.F. 2010 Dynamics and structure of decaying shallow dipolar vortices. *Phys. Fluids* **22**, 116606.

Eldredge, J.D. & Chong, K. 2010 Fluid transport and coherent structures of translating and flapping wings. *Chaos* **20**, 017509.

Ellington, C.P. 1984 The aerodynamics of hovering insect flight.V. A vortex theory. *Phil. Trans. Roy. Soc. London, B* **305**, 115–144.

Fernandez, V.M., Zabusky, N.J. & Gryanik, V.M. 1995 Vortex intensification and collapse of the Lissajous-elliptic ring: single- and multi-filament Biot-Savart simulations and visiometrics. *J. Fluid Mech.* **299**, 289–331.

Fish, F., Smits, A.J., Haj-Hariri, H., Iwasaki, T. & Bart-Smith, H. 2011 *Biomimetics: Nature-Based Innovation*, chap. Biomimetic swimmer inspired by the manta ray, pp. 495–523. CRC Press.

Flór, J.B. & van Heijst, G.J.F. 1994 An experimental study of dipolar vortices in a stratified fluid. *J. Fluid Mech.* **279**, 101–133.

Fraenkel, L.E. 1972 Examples of steady vortex rings of small cross-section in an ideal fluid. *J. Fluid Mech.* **51**, 119–135.

Fukumoto, Y. & Kaplanski, F. 2008 Global time evolution of an axisymmetric vortex ring at low Reynolds numbers. *Phys. Fluids* **20**, 053103.

Gao, L. & Yu, S.C.M. 2010 A model for the pinch-off process of the leading vortex ring in a starting jet. *J. Fluid Mech.* **656**, 205–222.

van Geffen, J.H.G.M. & van Heijst, G.J.F. 1998 Viscous evolution of 2D dipolar vortices. *Fluid. Dyn. Res.* **22**, 191–213.

Gharib, M., Rambod, E., Kheradvar, A., Sahn, D.J. & Dabiri, J.O. 2006 Optimal vortex formation as an index for cardiac health. *Proc. Natl. Acad. Sci. USA* **103**, 6305–08.

Gharib, M., Rambod, E. & Shariff, K. 1998 A universal time scale for vortex ring formation. *J. Fluid Mech.* **360**, 121–140.

Glezer, A. & Coles, D. 1990 An experimental study of a turbulent vortex ring. *J. Fluid Mech.* **221**, 243–283.

Green, M.A, Rowley, C.W. & Haller, G. 2007 Detection of Lagrangian coherent structures in 3D turbulence. *J. Fluid Mech.* **572**, 111–120.

Green, M.A, Rowley, C.W. & Smits, A.J. 2010 Using hyperbolic Lagrangian coherent structures to investigate vortices in bio-inspired fluid flows. *Chaos* **20**, 017510.

Grinstein, F.F. 1995 Self-induced vortex ring dynamics in subsonic rectangular jets. *Phys. Fluids* **7** (10), 2519–2521.

Grinstein, F.F. 2001 Vortex dynamics and entrainment in rectangular free jets. *J. Fluid Mech* **437**, 69–101.

Grinstein, F.F., Glauser, M.N. & George, W.K. 1995 Vorticity in jets. In *Fluid Vortices* (ed. S.I. Green). Kluwer Academic Publishers.

Gutmark, E.J. & Grinstein, F.F. 1999 Flow control with noncircular jets. *Annu. Rev. Fluid Mech.* **31**, 239–272.

Haller, G. 2000 Finding finite-time invariant manifolds in two-dimensional velocity fields. *Chaos* **10**, 99.

Haller, G. 2001*a* Distinguished material surfaces and coherent structures in three-dimensional flows. *Physica D* **149**, 1851–61.

Haller, G. 2001*b* Lagrangian structures and the rate of strain in a partition of two-dimensional turbulence. *Phys. Fluids* **13**, 3365.

Haller, G. 2002 Lagrangian coherent structures for approximate velocity data. *Phys. Fluids.* **14** (6), 1851–61.

Haller, G. & Poje, A.C. 1998 Finite time transport in aperiodic flows. *Physica D* **119**, 352.

Haller, G. & Yuan, G. 2000 Lagrangian coherent structures and mixing in two-dimensional turbulence. *Physica D* **147**, 352–70.

van Heijst, G.J.F. & Flór, J. B. 1989 Dipole formation and collisions in a stratified fluid. *Nature* **340**, 212–215.

Helmholtz, H. 1858 Über integrale der hydrodynamischen gleichungen, welche den wirbelbewegungen entsprechen. *Journal fr die reine und angewandte Mathematik* **55**, 25–55.

Hendabadi, S., del Alamo, J.C., Benito, Y., Bermejo, J. & Shadden, S. 2012 Characterization of human left ventricle flow patterns using ultrasound and Lagrangian coherent structures. In *Bulletin of the American Physical Society*, , vol. 57.

Hill, M. J. M. 1894 On a spherical vortex. *Phil. Trans. Roy. Soc. London, A,* **185**, 213–245.

Ho, C.-M. & Gutmark, E. 1987 Vortex induction and mass entrainment in a small-aspect-ratio jet. *J. Fluid Mech* **179**, 383–405.

Ho, C-M. & Huerre, P. 1984 Perturbed free shear layers. *Ann. Rev. Fluid Mech.* **16**, 365–424.

Hsieh, S.T. & Lauder, G.V. 2004 Running on water: Three-dimensional force generation by basilisk lizards. *Proc. Natl. Acad. Sci. U. S. A.* **101** (48), 16784–16788.

Hu, D.L., Chan, B. & Bush, J.W.M. 2003 The hydrodynamics of water strider locomotion. *Nature* **424** (6949), 663–666.

Husain, H.S. & Hussain, F. 1993 Elliptic jets. Part 3. Dynamics of preferred mode coherent structure. *J. Fluid Mech* **248**, 315–361.

Hussain, A..K.M.F. & Zaman, K.B.M.Q. 1980 Vortex pairing in a circular jet under controlled excitation. Part 2. Coherent structure dynamics. *J. Fluid Mech.* **101**, 493–544.

Hussain, F. & Husain, H.S. 1989 Elliptic jets. Part 1. Characteristics of unexcited and excited jets. *J. Fluid Mech.* **208**, 257–320.

Hussain, H.S. & Hussain, F. 1991 Elliptic jets. Part 2. Dynamics of coherent structures: pairing. *J. Fluid Mech.* **233**, 439–482.

Jacobs, P.A. & Pullin, D.I. 1989 Multiple-contour-dynamic simulation of eddy scales in the plane shear layer. *J. Fluid Mech* **199**, 89–124.

Jeon, D. & Gharib, M. 2004 On the relationship between the vortex formation process and and cylinder wake vortex patterns. *J. Fluid Mech* **519**, 161–81.

Johnston-Lavis, H.J. 1890 The state of the active Sicilian volcanoes in September 1889. *The Scottish Geographical Magazine* **6** (3), 145–149.

Kambe, T. & Takao, T. 1971 Motion of distorted vortex rings. *J. Phys. Soc. Japan* **31** (2), 591–599.

Kaplanski, F.B. & Rudi, Y.A. 2005 A model for the formation of "optimal" vortex rings taking into account viscosity. *Phys. Fluids* **17**, 087101.

Kelvin, Lord 1867 The translatory velocity of a circular vortex ring. *Phil. Mag.* **33**, 511–512.

Kelvin, Lord 1880*a* On the vibrations of a columnar vortex. *Philos. Mag.* **10**, 155–168.

Kelvin, Lord 1880*b* Vortex statics. *Philos. Mag.* **10**, 97–109.

Kern, S. & Koumoutsakos, P. 2006 Simulations of optimized anguilliform swimming. *J. Exp. Biol.* **209**, 4841–4857.

Kheradvar, A. & Gharib, M. 2007 Influence of ventricular pressure drop on mitral annulus dynamics through the process of vortex ring formation. *Ann. Biomed. Eng.* **35** (12), 2050–2064.

Khvoles, R., Berson, D. & Kizner, Z. 2005 The structure and evolution of elliptical barotropic modons. *J. Fluid Mech.* **530**, 1–30.

Kim, D. & Gharib, M. 2011 Flexibility effects on vortex formation of translating plates. *J. Fluid Mech.* **677**, 255–271.

Kimura, Y. 2006 Motion of an elliptic vortex ring and particle transport. In *IUTAM Symposium on Hamiltonian Dynamics, Vortex Structures, Turbulence* (ed. A.V Borisov, V.V Kozlov, I.S. Mamaev & M.A. Sokolovskiy), pp. 119–124. Springer.

Kirchhoff, G. 1876 *Vorlesungen ber mathematische Physik*. Leipzig: B. G. Teubner.

Kiya, M. & Ishii, H. 1991 Deformation and splitting of pseudo-elliptic vortex rings. In *Advances in Turbulence 3* (ed. A.V. Johansson & P.H. Alfredsson), pp. 52–60. Springer.

Kiya, M., Toyoda, K., Ishii, H., Kitamura, M. & Ohe, T. 1992 Numerical simulation and flow-visualization experiments on deformation of pseudo-elliptic vortex rings. *Fluid Dyn. Res.* **10**, 117–131.

Kizner, Z. & Khvoles, R. 2004 Two variations on the theme of Lamb-Chaplygin: Supersmooth dipoles and rotating multipoles. *Regul. Chaotic. Dyn.* **4**, 509–518.

Kizner, Z., Khvoles, R. & Kessler, D.A. 2010 Viscous selection of an elliptical dipole. *J. Fluid Mech* **658**, 492–508.

Kokshaysky, N.V. 1979 Tracing the wake of a flying bird. *Nature* **279**, 146–148.

Krueger, P.S. 2001 The significance of vortex ring formation and nozzle exit overpressure to pulsatile jet propulsion. PhD thesis, California Institute of Technology.

Krueger, P.S., Dabiri, J.O. & Gharib, M. 2006 The formation number of vortex rings in uniform background coflow. *J. Fluid Mech.* **556**, 147–66.

Krueger, P.S. & Gharib, M. 2003 The significance of vortex ring formation to the impulse and thrust of a starting jet. *Phys. Fluids* **15**, 1271–81.

Lamb, H. 1895 *Hydrodynamics*, 2nd edn. Cambridge University Press.

Lamb, H. 1906 *Hydrodynamics*, 3rd edn. Cambridge University Press.

Lamb, H. 1932 *Hydrodynamics*, 6th edn. Cambridge University Press.

Leonard, A. 1985 Computing three-dimensional incompressible flows with vortex elements. *Annu. Rev. Fluid Mech.* **17**, 523–59.

Lewin, G.C. & Haj-Hariri, H. 2003 Modelling thrust generation of a two-dimensional heaving aerofoil in a viscous flow. *J. Fluid Mech.* **492**, 339–362.

Lim, T.T. 1997 A note on the leapfrogging between two coaxial vortex rings at low Reynolds numbers. *Phys. Fluids* **9** (1), 239–241.

Lim, T.T. & Nickels, T.B. 1995 Vortex rings. In *Fluid Vortices*. Kluwer Academic Publishers.

Lin, S.J. & Corcos, G.M. 1984 The mixing later: deterministic models of a turbulent flow. Part 3. The effects of plane strain on the dynamics od streamwise vortices. *J. Fluid Mech* **141**, 139–178.

Linden, P.F. & Turner, J.S. 2001 The formation of 'optimal' vortex rings, and the efficiency of propulsive devices. *J. Fluid Mech.* **427**, 61–72.

Linden, P.F. & Turner, J.S. 2004 'Optimal' vortex rings and aquatic propulsion mechanisms. *Proc. R. Soc. B* **271**, 647–53.

Lipinski, D. & Mohseni, K. 2009 Flow structures and fluid transport for the hydromedusa *Sarsia tubulosa* and *Aequorea victoria*. *J. Exp. Biol.* **212**, 2436–2447.

Lugt, H.J. 1995 *Vortex Flow in Nature and Technology*. Krieger Publishing Company.

Luzzatto-Fegiz, P. & Williamson, C.H.K. 2010*a* Stability of conservative flows and new steady-fluid solutions from bifurcation diagrams exploting a variational argument. *Phys. Rev. Lett.* **104**, 044504.

Luzzatto-Fegiz, P. & Williamson, C.H.K. 2010*b* Stability of elliptical vortices from "Imperfect-Velocity-Impulse" diagrams. *Theor. Comput. Fluid Dyn.* **24**, 181–188.

Luzzatto-Fegiz, P. & Williamson, C.H.K. 2012*a* Determining the stability of steady two-dimensional flows through imperfect velocity-impulse diagrams. *J. Fluid Mech.* **706**, 323–350.

Luzzatto-Fegiz, P. & Williamson, C.H.K. 2012*b* Structure and stability of the finite-area von Kármán street. *Phys. Fluids* **24** (6), 066602.

Makarov, V.G. & Kizner, Z. 2011 Stability and evolution of uniform-vorticity dipoles. *J. Fluid Mech.* **672**, 307–325.

Mathur, M., Haller, G., Peacock, T., Ruppert-Felsot, J.E. & Swinney, H.L. 2007 Uncovering the Lagrangian skeleton of turbulence. *Phys. Rev. Lett.* **98**, 144502.

Maxworthy, T. 1972 The structure and stability of vortex rings. *J. Fluid Mech.* **51** (1), 15–32.

Maxworthy, T. 1977 Some experimental studies of vortex rings. *J. Fluid Mech.* **81**, 465–495.

McWilliams, J.C. 1984 The emergence of isolated coherent vortices in turbulent flow. *J. Fluid Mech* **146**, 21–43.

Meleshko, V.V. & van Heijst, G.J.F. 1994 On Chaplygin's investigations of two-dimensional vortex structures in an inviscid fluid. *J. Fluid Mech.* **272**, 157–182.

Mellander, M.V., McWilliams, J.C. & Zabusky, N.J. 1987 Axisymmetrization and vorticitity-gradient intensification of an isolated two-dimensional vortex through filamentation. *J. Fluid Mech.* **178**, 137–158.

Milano, M. & Gharib, M. 2005 Uncovering the physics of flapping flat plates with artificial evolution. *Proc. R. Soc. B* **543**, 403–9.

Moffatt, H.K. & Moore, D.W. 1978 The response of Hill's spherical vortex to a small axisymmetric disturbance. *J. Fluid Mech.* **168**, 337–367.

Mohseni, K. 2001 Statistical equilibrium theory for axisymmetric flows: Kelvins variational principle and an explanation for the vortex ring pinch-off process. *Phys. Fluids* **13** (13), 1924–1931.

Mohseni, K. & Gharib, M. 1998 A model for universal time scale of vortex ring formation. *Phys. Fluids* **10**, 2436–2438.

Mohseni, K., Ran, H. & Colonius, T. 2000 Numerical experiments on vortex ring formation. *J. Fluid Mech.* **430**, 267–282.

Moored, K.W. private communication .

Moored, K.W., Dewey, P.A., Smits, A.J. & Haj-Hariri, H. 2012 Hydrodynamic wake resonance as an underlying principle of efficient unsteady propulsion. *J. Fluid Mech.* **708**, 329–348.

Moslemi, A.A. & Krueger, P.S. 2010 Propulsive efficiency of a biomorphic pulsed-jet underwater vehicle. *Bioinspir. Biomim.* **5**, 036003.

Nguyen Duc, J.-M. & Sommeria, J. 1998 Experimental characterization of two-dimensional vortex couples. *J. Fluid Mech* **192**, 1175–192.

Nitsche, M. 2001 Self-similar shedding of vortex rings. *J. Fluid Mech.* **435**, 397–407.

Norbury, J. 1973 A family of steady vortex rings. *J. Fluid Mech.* **57**, 417–431.

O'Dor, R.K. 1988 The forces acting on swimming squid. *J. Exp. Biol.* **137**, 421–442.

O'Farrell, C. & Dabiri, J.O. 2010 A Lagrangian approach to vortex pinch-off. *Chaos* **20**, 017513.

O'Farrell, C. & Dabiri, J.O. 2012 Perturbation response and pinch-off of vortex rings and dipoles. *J. Fluid Mech.* **704**, 280–300.

Olascoaga, M.J. & Haller, G. 2012 Forecasting sudden changes in environmental pollution patterns. *Proc. Natl. Acad. Sci. U. S. A.* **109** (13), 4738–4743.

Olcay, A.B. & Krueger, P.S. 2007 Measurements of ambient fluid entrainment during laminar vortex formation. *Exps. Fluids* **44**, 235–247.

Olcay, A.B. & Krueger, P.S. 2010 Momentum evolution of ejected and entrained fluid during laminar vortex ring formation. *Theor. Comput. Fluid Dyn.* **24**, 465–482.

Oshima, Y. 1972 Motion of vortex rings in water. *J. Phys. Soc. Japan* **32** (4), 1125–1131.

Oshima, Y., Izutsu, N., Oshima, K. & Hussain, A.K.M.F. 1988 Bifurcation of an elliptic vortex ring. *Fluid Dyn. Res.* **3**, 133–139.

Oshima, Y., Kambe, T. & Asaka, S. 1975 Interaction of two vortex rings moving along a common axis of symmetry. *J. Phys. Soc. Japan* **38**, 1159–1166.

Overman, E.A. & Zabusky, N.J 1983 Evolution and merger of isolated vortex structures. *Phys. Fluids* **25**, 1297–1395.

Pawlak, G., Cruz, C. M., Bazan, C. M. & Hrdy, P.G. 2007 Experimental characterization of starting jet dynamics. *Fluid Dyn. Res.* **39**, 711–730.

Pedrizzetti, G. 2010 Vortex formation out of two-dimensional orifices. *J. Fluid Mech.* **655**, 198–216.

Peng, J. & Dabiri, J.O. 2009 Transport of inertial particles by Lagrangian coherent structures: application to predator-prey interactions in jellyfish feeding. *J. Fluid Mech* **623**, 75–84.

Peng, J., Dabiri, J.O., Madden, P.G. & Lauder, G.V. 2007 Non-invasive measurement of instantaneous forces during aquatic locomotion: a case study of the bluegill sunfish pectoral fin. *J. Exp. Biol.* **210** (4), 685–698.

Pennycuick, C.J. 1971 Soaring behaviour and performance of some East African birds, observed from a motor glider. *Ibis* **114** (2), 178–218.

Petersen, R. .A. 1978 Influence of wave dispersion on vortex pairing in a jet. *J. Fluid Mech.* **89**, 469–495.

Pierrehumbert, R.T. 1980 A family of steady, translating vortex pairs with distributed vorticity. *J. Fluid Mech.* **99**, 129–144.

Pozrikidis, C. 1986 The nonlinear instability of Hill's vortex. *J. Fluid Mech.* **168**, 337–367.

Prandtl, L. & Tietjens, O.G. 1934 *Applied Hydro- and Aeromechanics*. McGraw-Hill.

Pullin, D.I. 1979 Vortex ring formation at tube and orifice openings. *Phys. Fluids* **22**, 401–403.

Pullin, D.I. 1981 The nonlinear behavour of a constant vorticity layer at a wall. *J. Fluid Mech.* **108**, 401–421.

Pullin, D.I. 1992 Contour dynamics methods. *Annu. Rev. Fluid Mech.* **24**, 84–115.

Pullin, D.I. & Jacobs, P.A. 1986 Inviscid evolution of stretched vortex arrays. *J. Fluid Mech* **171**, 377–406.

Rayner, J.M.V. 1979 A vortex theory of animal flight. Part2: The forward flight of birds. *J. Fluid Mech.* **91**, 731–763.

Reul, H., Talukder, N. & Muller, W. 1981 Fluid mechanics of the natural mitral valve. *J. Biomech.* **14**, 361–372.

Reynolds, O. 1876 On the resistance encountered by vortex rings and the relation between the vortex rings and the streamlines of a disk. *Nature* **14**, 477.

Ringuette, M.J., Milano, M. & Gharib, M. 2007 Role of the tip vortex in the force generation of low-aspect-ratio normal flat plates. *J. Fluid Mech.* **581**, 453–68.

Roper, M., Seminara, A., Bandi, M.M., Cobb, A., Dillard, H.R. & Pringle, A. 2010 Dispersal of fungal spores on a cooperatively generated wind. *Proc. Natl. Acad. Sci. U. S. A.* **107** (41), 17414–17479.

Rosenfeld, M., Rambod, E. & Gharib, M. 1998 Circulation and formation number of laminar vortex rings. *J. Fluid Mech.* **376**, 297–318.

Ruiz, L.A., Whittlesey, R.W. & Dabiri, J.O. 2011 Vortex-enhanced propulsion. *J. Fluid Mech.* **668**, 5–32.

Ryu, K.-W. & Lee, D.-J. 1997 Sound radiation from elliptic vortex rings: evolution and interaction. *J. Sound Vibrat.* **200** (3), 281–301.

Saffman, P.G. 1978 The number of waves on unstable vortex rings. *J. Fluid Mech* **84**, 625–639.

Saffman, P.G. 1992 *Vortex Dynamics*. Cambridge University Press.

Saffman, P.G. & Szeto, R. 1980 Equilibrium shapes of a pair of equal uniform vortices. *Phys. Fluids* **23**, 2339–42.

Saffman, P.G. & Szeto, R. 1981 Structure of a linear array of uniform vortices. *Stud. Appl. Math.* **65**, 223–248.

Saffman, P.G. & Tanveer, S. 1982 The touching pair of equal and opposite uniform vortices. *Phys. Fluids* **25**, 1929–30.

Shadden, S.C., Astorino, M. & Gerbeau, J.F. 2010 Computational analysis of an aortic valve jet with Lagrangian coherent structures. *Chaos* **20**, 017512.

Shadden, S..C., Dabiri, J.O. & Marsden, J.E. 2006 Lagrangian analysis of fluid transport in empirical vortex ring flows. *Phys. Fluids.* **18**, 047105.

Shadden, S.C., Katija, K., Rosenfeld, M., Marsden, J.E. & Dabiri, J.O. 2007 Transport and stirring induced by vortex formation. *J. Fluid Mech.* **593**, 315–331.

Shadden, S.C., Lekien, F. & Marsden, J.E. 2005 Definition and properties of Lagrangian coherent structures from finite-time Lyapunov exponents in two-dimensional aperiodic flows. *Physica D* **212**, 271–304.

Shadden, S.C. & Taylor, C.A. 2008 Characterization of coherent structures in the cardiovascular system. *Ann. Biomed. Eng.* **36**, 1152–1162.

Shariff, K. & Leonard, A. 1992 Vortex rings. *Annu. Rev. Fluid Mech.* **24**, 235–79.

Shariff, K., Leonard, A. & Ferziger, J.H. 2008 A contour dynamics algorithm for axisymmetric flow. *J. Comp. Phys.* **227**, 9044–9062.

Shusser, M. & Gharib, M. 2000 Energy and velocity of a forming vortex ring. *Phys. Fluids* **12**, 618–21.

Stanaway, S., Cantwell, B.J. & Spalart, P.R. 1988 A numerical study of viscous vortex rings using a spectral method. *Tech. Rep.*. NASA TM -101041.

Steen, T. & Steen, S. 1994 Filling of a model left ventricle studied by colour M mode Doppler. *Cardiovas. Res.* **28**, 1821–1827.

Taylor, G.K., Nudds, R.L. & Thomas, A.L.R. 2003 Flying and swimming animals cruise at a Strouhal number tuned for high power efficiency. *Nature* **425**, 707–711.

Triantafyllou, G.S., Triantafyllou, M.S. & Grosenbaugh, M.A. 1993 Optimal thrust development in oscillating foil with application to fish propulsion. *J. Fluids Struct.* **7** (2), 205–224.

Triantafyllou, M.S. & Triantafyllou, G.S. 1995 An efficient swimming machine. *Sci. Am.* **272** (3), 64–70.

Trieling, R., Santberg, R., van Heijst, G.J.F. & Kizner, Z. 2010 Barotropic elliptical dipoles in a rotating fluid. *Theor. Comput. Fluid Dyn.* **24**, 111–115.

Turner, J.S. 1960 On the intermittent release of smoke from chimneys. *Mech. Engng. Sci.* **2**, 356.

Velasco Fuentes, O.U. & van Heijst, G.J.F. 1994 Experimental study of dipolar vortices on a topographic β-plane. *J. Fluid Mech* **259**, 79–106.

Vétel, J., Garon, A. & Pelletier, D. 2009 Lagrangian coherent structures in the human carotid artery bifurcation. *Exp. Fluids* **46**, 1067–1079.

Viets, H. & Sforza, P.M. 1972 Dynamics of bilateraly symmetric vortex rings. *Phys. Fluids* **13** (2), 230–240.

Villanueva, A., Smith, C. & Priya, S. 2011 A biomimetic robotic jellyfish (Robojelly) actuated by shape memory alloy composite actuators. *Bioinspir. Biomim.* **6**, 036004.

Wan, Y.-H. 1988 Variational principles for Hiill's spherical vortex and nearly spherical vortices. *Trans. Am. Math. Soc.* **308**, 299–312.

Weigand, A. & Gharib, M. 1997 On the evolution of laminar vortex rings. *Exp. Fluids* **22**, 447–457.

Weihs, D. 1977 Periodic jet propulsion of aquatic creatures. *Fortschr. Zool.* **24**, 171–175.

Whitaker, D.L. & Edwards, J. 2010 *Sphagnum* moss disperses spores with vortex rings. *Science* **329** (5990), 406.

Whittlesey, R.W. 2013 Dynamics and scaling of self-excited passive vortex generators for underwater propulsion. PhD thesis, California Institute of Technology, Pasadena, CA.

Wieting, D.W. & Stripling, T.E. 1984 Dynamics and fluid dynamics of the mitral valve. In *Recent Progress in Mitral Valve Disease* (ed. C. Duran, W.W. Angell, A.D. Johnson & J.H. Oury), pp. 13–46. Butterworths.

Willert, C.E. & Gharib, M. 1991 Digital particle image velocimetry. *Exps. Fluids* **10**, 181–193.

Wilson, M. M., Peng, J., O.Dabiri, J. & Eldredge, J. D. 2009 Lagrangian coherent structures in low Reynolds number swimming. *J. Phys.: Condens. Matter* **21** (20), 204105.

Winant, C.D. & Browand, F.K. 1974 Vortex pairing: the mechanism of turbulent mixing-layer growth at moderate Reynolds number. *J. Fluid Mech.* **63** (2), 237–255.

Yamada, H. & Matsui, T. 1979 Mutual slip-through of a pair of vortex rings. *Phys. Fluids* **22** (2), 1245–1249.

Ye, Q.Y. & Chu, C. K. 1995 Unsteady evolutions of vortex rings. *Phys. Fluids* **7**, 795–801.

Yule, A.J. 1978 Large-scale structure in the mixing layer of a round jet. *J. Fluid Mech.* **879** (3), 413–432.

Zabusky, N.J., Hughes, M.H. & Roberts, K.V. 1979 Contour dynamics for the Euler equations in two dimensions. *J. Comp. Phys.* **30**, 96–106.